The Oxidative Destruction of Volatile Organic Compounds Using Heterogeneous Catalysis

Thesis submitted in accordance with the requirement of Cardiff University for the degree of Doctor of Philosophy

David Richard Sellick

November 2011

CardiffCatalysisinstitute

CARDIFF UNIVERSITY

PRIFYSGOL CAERDYD

UMI Number: U585508

UMI U585508

Chapter 1 – Introduction

Chapter 2 – Experimental

Chapter 3 – CeZrO₂ Catalysts for Naphthalene Total Oxidation

Chapter 4 – Investigating the Preparation Conditions of Pt/SiO₂ for the Total Oxidation of Naphthalene

Chapter 5 – The Total Oxidation of Naphthalene and Propane Using Catalysts Prepared in Non-Aqueous Solvents

Chapter 6 – Conclusions & Further Work

Acknowledgements

The production of this thesis would not have been possible without the help of many people. Firstly I must thank my supervisors, Drs. Stuart Taylor and Albert Carley for their invaluable help and guidance over the last three years. I would also like to thank Drs. Tom Davies, Kieran Cole, Matt House and Mathew Davies for all their help with setting up equipment, useful discussions and generally around the lab. I wouldn't have done it without you! Tom in particular has been a lifesaver on more than one occasion. I would also like to thank Dr. Bin Gao for his patience and assistance with the supercritical work presented in this thesis. Thanks also to Cardiff University for the financial support.

Special thanks must also go to Suni Aranda who stayed in Cardiff for three months as part of her PhD. Some of the work that we collaborated on is presented in this thesis. She also taught me how to be a better chemist and that work can be fun.

I would also like to thank Steve Morris, Alun Davies, John Cavanagh, Richard Breeze and Ricky Fearne for all their help and assistance in helping me build and maintain various pieces of equipment. Without their help, nothing in the lab would have worked. Gary Coleman, Jamie Cross, Mal Bryant and Sham Ali have also been invaluable colleagues in the Stores department.

I have also been lucky enough to be surrounded by a very good group of colleagues who I now consider very good friends, especially when things were not going to plan. There are too many to list here; they know who they are. Two people that stand out however are Simon and Cat who started their PhD studies at the same time as I and without them, life would have been very boring.

Finally, heartfelt thanks to my family for their unyielding support particularly when things got tough, even when they could not understand what was causing me grief. I owe you a lot.

Abstract

The preparation, testing and characterisation of catalysts for the total oxidation of two volatile organic compounds (VOCs) have been studied. These two VOCs were naphthalene and propane. Naphthalene was the main focus of this study.

CeZrO$_2$ with varied Ce:Zr ratios and preparation methods was investigated for the total oxidation of naphthalene. These preparation methods were all precipitation methods using different precipitating agents (urea, sodium carbonate and supercritical CO$_2$). Zr contents as low as 1 molar percent enhanced activity for both urea and sodium carbonate precipitated catalysts compared to CeO$_2$. A supercritical analogue was found to be less active.

Pt/SiO$_2$ as a catalyst for naphthalene total oxidation was studied with a view to optimise an existing impregnation technique. A Pt loading of 2.5wt% with a calcination regime of 550°C for 12h in static air with a ramp rate of 5°C/min was found to be optimal. These preparation conditions were found to increase the proportion of metallic Pt which was found to exist as large crystallites with low dispersion. Other catalyst features were probed in this study. The type of silica used as a support was changed to novel hollow sphere silica then nanopore silica but no improvement in activity was found. Pt was then substituted for Pd which again did not improve activity. It was found that the Pd existed as Pd oxide hence Pd oxide is not as active for naphthalene oxidation as metallic Pt.

The preparation of impregnated catalysts using non-aqueous solvents on so-called 'hydrophobic' materials was also investigated. These were tested for both naphthalene and propane total oxidation. It was found that Pt and Pd based catalysts afforded the most active catalysts. Several supports were studied which interacted with the impregnated metals in different ways. This affected the nature of the impregnated metals and therefore the activities of these catalysts. Some of the more active catalysts used supports that were of a low surface area. A high surface area SnO$_2$ support was produced and impregnated with Pd. The high surface area SnO$_2$ was found to be more active than the original Pd/SnO$_2$ catalyst for propane total oxidation.

Abstract (Microfiche)

Catalysts have been tested for their activities towards the catalytic total oxidation of naphthalene. It was found that $CeZrO_2$ catalysts were active for naphthalene total oxidation. Experiments were undertaken in an attempt to explain this activity. The preparation of an impregnated Pt/SiO_2 catalyst was investigated in a study to determine optimal preparation conditions. These conditions included Pt loading, calcination regime and silica type. The most active catalysts favoured predominantly metallic Pt crystallites which were large and poorly dispersed. A Pd/SiO_2 analogue was also prepared for comparative purposes. The preparation of impregnated catalysts with non-aqueous solvents is also reported. The activities for the total oxidation of naphthalene and the total oxidation of propane are reported. It was found that the strength of the interaction of the impregnated metal with the support can play a role in a catalyst's activity for total oxidation of hydrocarbons. The influence of support surface area was also probed for one of these 'hydrophobic' catalysts, Pd/SnO_2 for the total oxidation of naphthalene and propane.

Chapter 1 - Introduction

1.1   Introduction

The focus of this study is to utilise heterogeneous catalysis as a means to reduce the emission of two volatile organic compounds (VOCs). The reasoning for reducing VOC levels is discussed. Although other techniques exist for emission abatement, justification is given for using catalysis. Some background information on catalysis theory is given, as is a review of the published literature available.

1.1.1   Volatile Organic Compounds and Their Environmental Effects

Volatile Organic Compounds (VOCs) are a class of chemicals which are known to contribute to atmospheric pollution and are defined as substances of low volatility, which can then be easily released into the atmosphere. For example chlorofluorocarbons (CFCs) have been found to destroy ozone via a photochemical radical mechanism. The problem was compounded by its widespread use in both commercial and domestic situations (as a refrigerant). Relatively large release of CFCs resulted in sufficient depletion of ozone to create a hole in the southern hemisphere. As a result, the use of CFCs was prohibited. This prohibition had a positive effect on ozone levels as it has been reported that levels will increase to eventually reach 1980 levels[1]. One other noticeable atmospheric polluting effect is the formation of photochemical smog in urban settings[2].

1.1.2   Classes of VOCs

There are several classes of VOCs e.g. short chain alkanes, dioxins etc. One class in particular creates the main basis of this project; polyaromatic hydrocarbons (PAHs). These are all based on multiple ring molecules (naphthalene is the most simplistic PAHs possible hence its use as a model PAH) and are regarded as being very difficult to destroy via oxidation due to their high thermal stability[3].

1

1.1.2.1 Why Study Naphthalene?

Naphthalene specifically has been identified as a constituent of wood burning stoves[4] and diesel exhaust emissions[5-8]. It has also been a by-product of some industrial processes e.g. plastic production. Also, when one wishes to study the chemistry of PAHs, naphthalene is an ideal candidate for study. It is the simplest PAH available. It also has relatively low toxicity and is relatively cheap to purchase. This makes it ideal for R&D use.

1.1.2.2 Why Study Propane?

Propane has been attributed to LPG based heating systems and has also been identified in vehicle emissions[9, 10], especially as liquid petroleum gas powered internal combustion engines are commonplace.

1.1.3   Current Legislation

Due to the polluting nature of VOCs, several legislative measures have been introduced. Two of the most prominent of these are the Gothenburg Protocol of 1999 and European Union Directive 2004/42/CE.

1.1.3.1 The 1999 Gothenburg Protocol to Abate Acidification, Eutrophication and Ground-level Ozone

The 1999 Protocol was adopted in November 1999 by a number of European countries including the UK. The USA and Canada have also signed the Protocol. The basis of the Protocol was to establish lower emission ceilings (compared to 1990 figures) for four groups of atmospheric pollutants; sulphur oxides (63% reduction), nitrogen oxides (NOx) (41% reduction), VOCs (40% reduction) and ammonia (17% reduction). The target for these reductions was 2010. For the UK specifically, 2555 thousand tonnes of VOCs were produced in 1990. A reduction of 53% to 1200 thousand tonnes per year was agreed. The sources of these pollutants were considered, e.g. VOC emissions from the paint/coating industries and revised abatement levels set. For new pharmaceutical installations, for

example, a limit of 5% of the solvent input can be emitted as NMVOCs (non methane VOCs) was imposed.

1.1.3.2 EU Directives 1999/13/EC and 2004/42/CE

The 1999/13/CE directive considers the VOC emissions of EU countries, e.g. one EU country's VOCs emissions affecting the atmospheric quality of another EU country. VOCs which are classified under particular risk phrases were postulated to be reduced or replaced fully by less hazardous materials (if possible). Halogenated VOCs were limited to 20mg/Nm^3 if the mass flow met or exceeded 100g/h.

In terms of other new emission ceilings, the values mirror that of the Gothenburg Protocol already mentioned. For example, a maximum of 25g of solvent is allowed to be emitted per pair of shoes manufactured.

In 2004, this Directive was additionally supplemented with the Directive 2004/42/CE. This Directive centred on issues concerning VOC emissions from automotive refinishing and general paint products. The limits for paints were designed to be introduced over a two stage implementation plan (stage 1 in 2007; stage 2 from 2010 onwards). For example, solvent based interior matt paints were limited to 400g/l of VOC in 2007. This was then limited to 30 g/l in 2010. For automotive refinishing, the limits were introduced in a single stage (2007). Topcoat paints, for example, were limited to 420g/l of VOC content.

1.2   Routes for Treating VOCs

There are several possible routes for the treatment of VOCs. Some of these are outlined here.

Thermal incineration. Thermal incineration is where the target chemical is subjected to a high enough temperature to enable total combustion to occur. There are, however, several disadvantages to this method. Firstly, very high temperatures (they can be in excess of 1000°C) are required to achieve total combustion. This introduces a large energy penalty, hence this method is neither particularly cheap or energy efficient. It is also not a very selective technique in that many partial oxidation products are formed. Some of these by-products, e.g. dioxins are extremely hazardous to human health and their formation is not desirable.

Absorption. Here, the VOC is absorbed by a liquid e.g. water and a centrifuge based packed bed[11]. Commercial applications also exist worldwide. However, no chemical change occurs during the absorption process. Therefore, a clean-up regime is still required to treat the contaminated fluids.

Adsorption. Adsorption requires the VOC pollutant to be adsorbed on a suitable solid material. Ceria has been reported to be a good adsorption material[12]. Activated carbon has been reported to be effective for benzene adsorption[13]. However, the same problem of treating the contaminated adsorbent occurs as mentioned for absorption.

This technology could be useful for treating VOC contamination in areas where thermal incineration would not be feasible by trapping the VOC then transferring the adsorbed VOC to a separate facility for further treatment. However, this route can be time consuming and the transportation of the adsorbed VOCs could be problematic (due to health and safety concerns) or expensive (if a suitable facility is not local to the original site where the VOCs were first adsorbed).

Biological treatment. Several technologies exist where microbes are used to remove VOC effluents from gas streams, such as biofilters and bioscrubbers[14]. The exact nature of these microbes does depend on the specific VOC and the reaction pathway to be used[15]. Products tend to be simple hydrocarbons (i.e. methane[16]) or CO_2.

Catalytic combustion. An alternative method is to lower the activation energy of the combustion reaction by means of a catalyst. Another advantage of using a catalyst is that it is possible to achieve very high or complete selectivity for a desired product. As vastly reduced temperatures are required compared to thermal incineration, the energy penalty is significantly reduced. This means that the use of catalysts to reduce naphthalene emissions is the most suitable avenue to pursue, especially if these catalysts can be produced economically and can be used over a large time scale.

1.3   Introduction to Catalysis

1.3.1   Basic Concepts

Catalysts are an intrinsic part of everyday life; many substances used by mankind require some form of catalysis at some point during its production, e.g. pharmaceutical preparations, fine chemical synthesis, plastic production and environmental control. According to some sources, approximately 90% of all chemical products require a catalysed reaction[17] with an annual turnover of approximately US$900 billion[18].

The term catalysis was first used by J.J. Berzelius where catalysts are described as materials which 'produce decomposition in bodies, and form new compounds into the composition of which they do not enter'[17, 19].

A contemporary definition of catalysis can be considered to be a process where a substance enhances the rate of a given reaction but undergoing no net change itself. It does this by offering an alternative pathway for a reaction to proceed which requires a lower overall activation barrier (E_a). A typical energy profile illustrating this is shown in figure 1.1. In order to offer this alternative pathway, it may be necessary to form extra or different transition state species from the non-catalysed reaction pathway. Also, the energy changes/requirements of adsorbing and desorbing species onto the catalyst need to be considered. If the standard Gibb's free energy change of a reaction is considered, i.e.

$$-\Delta G^{\circ} = RT\ln K$$

It can be seen that one value of ΔG° will give only one value of K for a given reaction. This means that if a reversible reaction is considered, the overall equilibrium rate constant, K must contain rate constant terms for both the forward and the reverse reaction in its expression, i.e.

$$K = \frac{k(\text{Reverse})}{k(\text{Forward})}$$

This is also true for a catalysed reaction at equilibrium. The expression for ΔG° is the same regardless of if the non-catalysed or catalysed reaction is considered; therefore the expression of the rate constant, K, must be the same for both the catalysed and non-

5

catalysed reactions. The value of K would be greater for the catalysed reaction. In other words, a catalyst is only effective whilst a reaction is under 'kinetic control'[17].
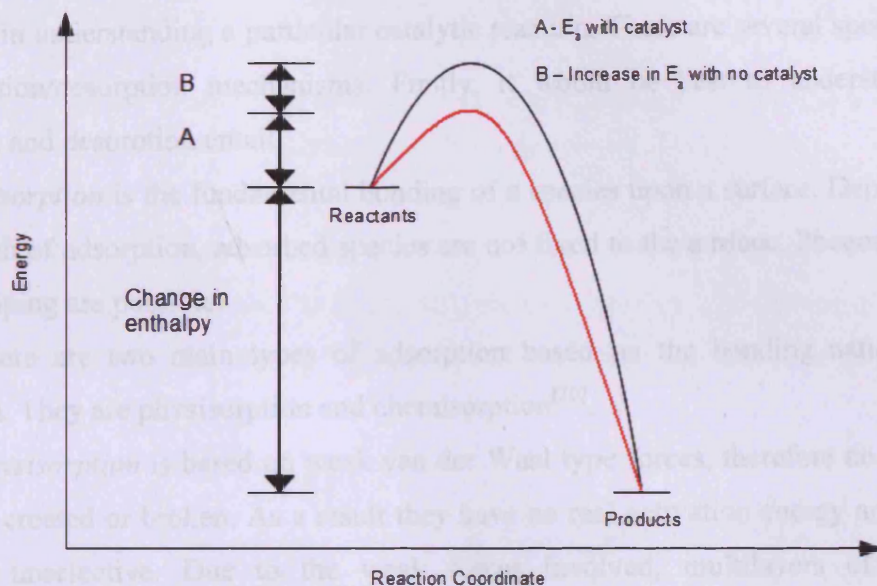
Figure 1.1. Reaction profile for a catalysed and a non-catalysed reaction highlighting the difference in activation energy (E_a). The catalysed pathway is highlighted in red.

1.3.2 Homogeneous and Heterogeneous Catalysis

Catalysts can be split into two broad groups; homogeneous and heterogeneous. This distinction is made by comparing the phase of the catalyst with the phase of the reactants.

Homogeneous catalysis involves reactants and catalysts in the same phase (e.g. liquid/liquid). These catalysts do have the advantage of easier catalyst/reactant interaction and these systems tend to have high product selectivity. However, they tend to have relatively modest catalytic activity. Also, it can be difficult to separate the catalyst from the reactant/product mixture. An example of homogeneous catalysis is polymerisation of olefins (such as propylene) using Ziegler – Natta catalysts.

Heterogeneous catalysis is where the catalyst is in a different phase to the reactants. These catalysts can have relatively poor selectivity compared to homogeneous catalysts and activity can occur at much higher temperatures. However, product/catalyst separation is much simpler. In this work, all further discussion will be focussed on heterogeneous catalysts (specifically gas/solid systems).

6

1.3.3 Adsorption at a Surface

Knowledge of the mechanisms of adsorption and the opposite phenomena, desorption can be crucial in understanding a particular catalytic reaction. There are several specific types of adsorption/desorption mechanisms. Firstly, it would be best to understand what adsorption and desorption entail.

Adsorption is the fundamental bonding of a species upon a surface. Depending on the strength of adsorption, adsorbed species are not fixed to the surface. Phenomena such as site hopping are possible.

There are two main types of adsorption based on the bonding nature of this adsorption. They are physisorption and chemisorption[20].

Physisorption is based on weak van der Waal type forces, therefore no molecular bonds are created or broken. As a result they have no real activation energy and they are relatively unselective. Due to the weak forces involved, multilayers of adsorbate molecules can form. Adsorbed molecules can also 'hop' between active sites. This is caused by the energy of physisorption being absorbed by the adsorbate lattice until there is not enough energy for motion to occur any longer. This allows full adsorption onto the substrate surface.

Chemisorption involves stronger molecular-surface interactions i.e. bonds are created or broken. Due to this, an activation energy barrier exists and therefore chemisorption occurs more selectively than physisorption. Fragmentation of the adsorbed species can occur if there is a high degree of valency deficiency. Due to the activation energy required, multilayer adsorption does not occur.

Desorption is where adsorbed products leave the surface of the catalyst/material. Desorption can occur if the thermal energy of the adsorbed species is high enough and if the dissociation energy of the adsorbed species is not breached.

1.3.3.1 Common Catalytic Mechanisms Employing Adsorption and Desorption

Langmuir/Hinschelwood[20]. For oxidation reactions, this mechanism is based on the simultaneous adsorption of both the oxidant species and the reactant species. The products then desorb simultaneously. Reactions occur on the adsorbate surface via site hopping as described in the previous section.
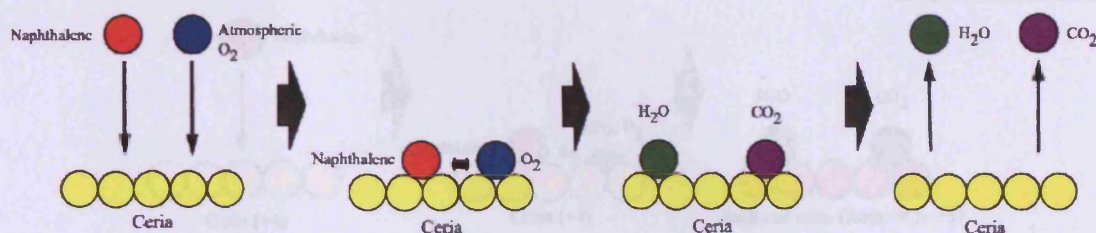
Figure 1.2. Langmuir – Hinschelwood mechanism for adsorption/desorption using naphthalene for the adsorbate and ceria as the substrate.

Eley-Rideal[20]. For oxidation reactions using this mechanism, the reactant adsorbs onto the surface. The oxidant (i.e. oxygen) is still gaseous and attacks the adsorped reactant. After product formation, they can then desorb from the surface of the catalyst.
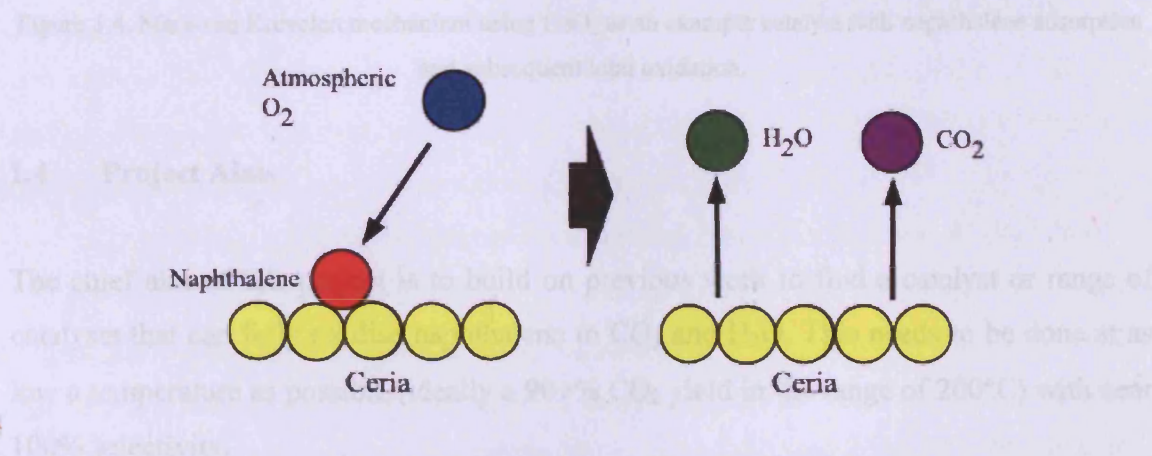
Figure 1.3. Eley-Rideal mechanism of adsorption/desorption using naphthalene as the adsorbate and ceria as the substrate.

Mars van Krevelen (MvK)[20]. The MvK mechanism has been previously reported to be involved in naphthalene total oxidation[21]. In this mechanism, the reactant adsorbs onto the surface. Interaction with facile oxygen within the substrate lattice is used as the oxidising species. This leads to a reduction in the catalyst oxidation state, which is restored to its original value via chemisorption (i.e. oxidation) via oxygen from the gaseous atmosphere. Hence, this sort of mechanism can only be seen for oxide based catalysts. A radical transfer mechanism could occur between the oxide O atoms and the adsorbed reactant to produce the reaction products. One of the chief disadvantages of catalysts using this mechanism is that constant reduction then subsequent oxidation of the oxide support could lead to premature degradation and possible deactivation of the catalyst.
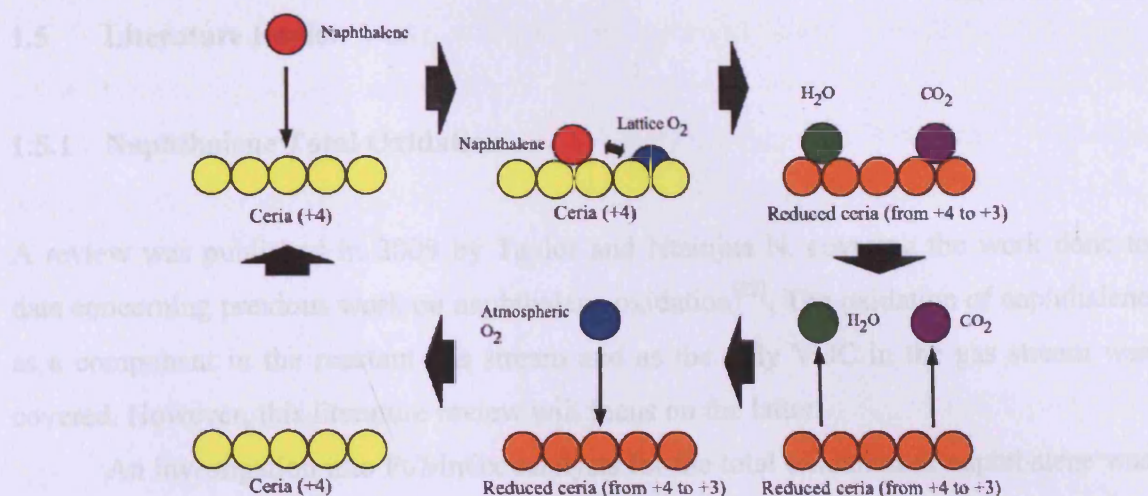
Figure 1.4. Mars-van Krevelen mechanism using CeO_2 as an example catalyst with naphthalene adsorption and subsequent total oxidation.

1.4   Project Aims

The chief aim of this project is to build on previous work to find a catalyst or range of catalysts that can fully oxidise naphthalene to CO_2 and H_2O. This needs to be done at as low a temperature as possible (ideally a 90+% CO_2 yield in the range of 200°C) with near 100% selectivity.

Ideally, these catalysts will use a relatively simple preparation method using commonly available materials. The preparations of these catalysts will also be investigated in an attempt to optimise them.

Some catalysts will also be probed for their catalytic activities for the total oxidation of propane. The catalysts chosen will be dictated by two factors. Firstly, the reviews of current literature will shine light on what catalysts have been tested for the total oxidation of propane (most of the work involving propane concerns its partial oxidation). Secondly, the focus of this project is naphthalene oxidation. Hence the propane oxidation work will be of a lower priority.

The second aim of this project is to correlate the catalytic activities mentioned above with the catalysts' features. These features include, for example, the physical parameters of the active sites and the supports. The aim of doing this is to attempt to explain any trends found within similar catalyst sets. Typical characterisation analyses include chemisorption, surface area determination and catalyst reducibility studies.

1.5   Literature Review

1.5.1   Naphthalene Total Oxidation

A review was published in 2009 by Taylor and Ntainjua N. covering the work done to date concerning previous work on naphthalene oxidation[22]. The oxidation of naphthalene as a component in the reactant gas stream and as the only VOC in the gas stream was covered. However, this literature review will focus on the latter.

An investigation into Pt/MnOx catalysts for the total oxidation of naphthalene was reported in 1997[23]. Small loadings of Pt had a positive influence on the catalytic activity and this activity increased with increasing Pt loading. However, pure Pt catalysts were more active. The reason for this was cited to be the encapsulation of Pt by MnOx. Another observation was that high calcination temperatures (800°C) could produce more active catalysts compared to a lower calcination temperature (500°C).

Some of the other earlier papers investigating the total oxidation of naphthalene were published by Ferrandon *et al.*[4, 24, 25]. These included Pt and Pd catalysts supported on γ-Al$_2$O$_3$ which required temperatures of 288-395°C to achieve 50% naphthalene destruction[4]. Surface areas were reported to be as high as 150m^2/g which were reduced to 15m^2/g with high temperature hydrothermal treatment. Scanning Electron Microscopy revealed the formation of alumina whiskers, which could be changed when the preparation conditions were varied.

Ntainjua N. and Taylor described the work of Zhang *et al.*[5, 26] in some detail in their 2009 review[22]. In 2003[5], Zhang *et al.* studied 1% Pt, 1% Pd, 1% Ru, 5% Co, 5% Mo and 5% W on γ-Al$_2$O$_3$. BET studies indicated that the metal impregnation caused a reduction in surface area compared to the bare Al$_2$O$_3$ support. This was proposed to be due to large metal particles filling the pores of the support. From XRD analysis, the impregnated metals were found to be oxidised rather than metallic. In the case of Pd and Ru, these M oxide crystallites were observed to be fairly large. In terms of activity, the Pd and Pt catalysts were the most active, followed by Ru and Co and finally the least active were Mo and W. Zhang *et al.* also discovered that the naphthalene consumption and the CO$_2$ yields at a given temperature did not always correlate. This suggested that by-product formation was occurring. Kinetic studies were also reported and the authors reported that the Langmuir-Hinschelwood mechanism applied.

The following year, Zhang *et al.* released a second paper[26] where an attempt was made to probe the mechanistic details of naphthalene oxidation over 1% Pt/γ-Al_2O_3 and 5% Co/γ-Al_2O_3. They reported that Pt caused a greater degree of by-product formation due to the stronger chemisorption of naphthalene on Pt. The by-products were found to be oxygenated and non-oxygenated polycyclic aromatic hydrocarbons (due to naphthalene growth prior to decomposition), alkyl and oxygenated naphthalene derivatives (due to methylation and dimerisation) and naphthalene decomposition fragments (due to the formation of phthalic anhydride and subsequent oxidation). Since Co and naphthalene experienced a weaker chemisorption interaction compared to Pt, Zhang *et al.* proposed that a weaker adsorption favoured naphthalene oxidation.

The work of Zhang *et al.* led to a publication by Shie *et al.* in 2005[27]. In this paper, 1% Pt/γ-Al_2O_3 was studied to optimise reaction conditions and to determine mechanistic details. They showed that the Eley-Rideal mechanism with Arrhenius behaviour fitted the pseudo-first order kinetic data. In terms of improving catalyst activity, a relatively low GHSV of less than $35000h^{-1}$ with 600vppm of naphthalene produced a 95% CO_2 yield at approximately 150°C. A temperature of 727°C was required to reach the same CO_2 yield if no catalyst was present.

The next step was to try and improve the activity of the Pt/γ-Al_2O_3 catalyst. Ndifor *et al.* published a paper where the addition of V to Pt/γ-Al_2O_3 catalysts were investigated. The combination of V and Pd in the same catalyst was not a new one.

TiO_2 based catalysts were tested by Garcia *et al.* previously where $Pd/V/TiO_2$ was compared to Pd/TiO_2 and V/TiO_2. In that paper there is evidence that different cyclic VOCs could give rise to different adsorption mechanisms. 0.5% Pd/3% V/TiO_2 was the most active catalyst for the total oxidation of benzene. 0.5% Pd/TiO_2 was more active than all investigated $Pd/V/TiO_2$ catalysts for the total oxidation of naphthalene at higher temperatures (i.e. above 250°C).

Upon analysing the characterisation data for these catalysts (with respect to naphthalene oxidation), it was found that

1   Pd/V/TiO$_2$ catalysts underwent an increase in polyvanadate and V$_2$O$_5$ species compared to V/TiO$_2$

2   Increasing the vanadium loading increased the CO chemisorption uptake

3   The catalyst surface area was reduced when the loadings of Pd and V were increased

4   The reducibility of V sites increased in the presence of Pd

5   The inclusion of Pd increased the concentration of paramagnetic V^{4+} ions but the vanadium oxide structures were not altered.

When the reactivity profiles for the total oxidation of naphthalene were considered, it was found that V/TiO$_2$ did not give very active or selective catalysts. At 300°C, naphthalene consumption was noted to be 100% but the CO$_2$ yields were only 55% (approximately). This could be observed regardless of V loading. The authors attributed this to a carbon balance deficit from naphthalene adsorption and by product formation. In order to eliminate the effects of naphthalene adsorption, the reaction was allowed to reach adsorption equilibrium. Analysis of the reaction by-products (where naphthalene consumption was high but CO$_2$ yields were low) revealed substances such as trimethyl benzene, benzaldehyde, phthalic anhydride and benzoic acid were present.

It was noted that there was a general trend between V content and naphthalene consumption; higher (3%) V loadings gave higher naphthalene consumptions. However, this trend was not carried over to CO$_2$ yields. It was proposed that the oxidation mechanism proceeded via nucleophillic attack to adsorb the naphthalene to the catalyst surface. It then underwent electrophillic substitution to the total oxidation products. However, it was found that naphthalene appears to be more easily adsorbed on the catalyst surface than benzene but naphthalene was the more difficult to oxidise fully at lower temperatures, possibly due to the formation of very stable oxygenated intermediates.

If the most active Pd/TiO$_2$, V/TiO$_2$ and Pd/V/TiO$_2$ catalysts were considered, it was shown that whilst 3% V/TiO$_2$ gave higher naphthalene consumption than 0.5% Pd/TiO$_2$, the CO$_2$ yield was higher for Pd/TiO$_2$. It had been previously reported that if there is weak physisorption between the adsorbed naphthalene and the catalyst, the oxidation of the second naphthalene ring can be oxidised more easily after the oxidation of the first ring. Hence, it was postulated that V active sites produced stronger naphthalene-catalyst bonds compared to Pd active sites. It was also stated that V active sites had an affinity for attacking C-H bonds via selective nucleophillic oxygen species,

producing partial oxidation products such as those noted above. Pd was postulated to contain non selective electrophillic oxygen species, hence a higher CO_2 yield.

The paper published by Ndifor *et al.* on catalysts designed in a similar vein to the paper by Garcia *et al.* above had a different outcome with respect to the total oxidation of naphthalene. A small amount (0.5wt%) of V incorporated into 0.5wt% Pt/γ-Al_2O_3 was found to enhance the activity for the total oxidation of naphthalene. Larger loadings of V decreased activity compared to 0.5wt% Pt/γ-Al_2O_3. This decrease in activity was identified to be due to the formation of crystalline V_2O_5 for these higher V loadings (up to 12wt%). The addition of 0.5wt% V caused an easily reducible V species to be formed (identified as a unique peak in TPR analysis). BET and CO chemisorption data also indicated that both the textural properties and the Pt distribution were altered upon the inclusion of V.

An advance was made during 2005/2006 when Garcia *et al.* reported the comparison of various metal oxides for the total oxidation of naphthalene[28]. These oxides were Fe_2O_3, CoOx, CeO_2, MnOx, CuOx, ZnO and CuZnO. Two different forms of CeO_2 were reported, denoted CeO_2 and CeO_2 (U). The U designation refers to a co-precipitation preparation using urea as the precipitating agent.

If the temperatures required for each catalyst to produce a 90% CO_2 yield are considered, it was reported that the urea precipitated ceria required a temperature of 210°C. The next active catalyst was MnOx (250°C). ZnO was the least active (a temperature of 340°C was required for a 90% CO_2 yield). The urea precipitated ceria was also reported to have 100% selectivity to CO_2 as a 90% consumption of naphthalene was observed at 210°C. The only other catalyst that displayed this behaviour was reported to be CoOx (a temperature of 270°C was required for a 90% CO_2 yield and 90% naphthalene consumption). All other catalysts (Fe_2O_3, CeO_2, MnOx, CuOx, ZnO and CuZnO) were reported to achieve a 90% CO_2 yield at a higher temperature than 90% naphthalene consumption (e.g. Fe_2O_3 displayed a 90% naphthalene conversion at 295°C whereas a CO_2 yield of 90% was reached at 300°C). This suggests that some by-products were being produced[5, 29].

It was reported that the urea precipitated ceria had one of the largest surface areas of all the investigated catalysts (171m²/g). With the exception of Al_2O_3 (180m²/g), all other surface areas were reported to be less than 90m²/g. Therefore it appeared that a high surface area was a key requirement for an active ceria catalyst.

If the reported Temperature Programmed Desorption (TPD) data is considered, it was reported that a relatively low temperature was required to desorb naphthalene from CeO_2 (U). It was suggested that naphthalene was bonded relatively weakly to ceria (U) and that partial oxidation would be less facile, hence the 100% selectivity to CO_2.

A further advantage of using ceria as a catalyst was the reduced cost of catalyst preparation compared to supported precious metal catalysts[22].

As ceria was now known to be the most active catalyst for the total oxidation of naphthalene, the focus was then turned to improving its catalytic activity. As previously mentioned, the most active catalyst reported is that of urea precipitated ceria (CeO_2 (U)), which was reported to afford a 100% yield of CO_2 at approximately 190°C. Two key features of CeO_2 (U) were proposed to be a small crystallite size and a high surface area. CeO_2 precipitated via aqueous sodium carbonate (CeO_2 (P)) was not as active as CeO_2 (U), with 100% CO_2 yield at approximately 325°C. CeO_2 (P) had a larger crystallite size (5.2nm compared with 4.7nm) and a smaller surface area ($87m^2/g$ compared with $171m^2/g$). It was also noted that CeO_2 (U) underwent a morphological change during reaction by Garcia *et al.*; the globular/spherical morphology transformed into regular prismatic forms during reaction. The CeO_2 (P) sample exhibited the same globular/spherical morphology as CeO_2 (U) but this did not change during reaction[12]. The authors proposed that defects within the prismatic forms upon which naphthalene could adsorb could be responsible. They also proposed that the pore size distribution could be 'optimised' so that naphthalene adsorption is maximised and that this effect was not observed for other preparation methods[12].

When CeO_2 (U) was compared with other catalysts that were known to be very active for the total oxidation of naphthalene, it was shown that CeO_2 (U) was the most active. Now that CeO_2 (U) was established as the most active catalyst for the total oxidation of naphthalene, the focus turned to improving and optimising the preparation conditions of CeO_2 (U). This was investigated as part of a recent Ph.D. thesis[30]. In that thesis, the preparation of ceria was optimised and various characterisation techniques were performed in order to determine what structural features were necessary for a catalyst that was highly active for the total oxidation of naphthalene. The preparation conditions (e.g. using a precipitation method with urea as the precipitating agent) were discussed and it was proposed that a cerium salt to urea ratio of 1:4 with an ageing time of 24h, followed by drying then calcination at 500°C for 6h produced nanocrystalline ceria that was the most active for the total oxidation of naphthalene. In terms of characterisation

(via N_2 adsorption coupled with the BET method and X-ray diffraction using the Scherrer equation) it was determined that a small crystallite size and a high surface area were paramount for an active catalyst, which is in agreement with the published literature.

One other important key feature was determined to be the presence of surface defects in the catalyst. Higher concentrations of surface defects were observed with larger surface areas. Also, surface defects enable more catalyst molecules to be open to the adsorption of naphthalene. This should lead to a greater number of successful reactions, hence an increase in the reaction rate being observed. These surface defects were reported to increase in number when urea precipitated ceria was used in a catalytic reaction.

One of the observations made during the study of ceria catalysts was that the redox properties of the catalyst appeared to be important. This implies that the oxidation reactions could proceed via redox mechanisms such as that proposed by Mars and van Krevelen[31]. One of the main features of CeO_2 that benefits catalytic activity is that it is an efficient store of oxygen and that its surface is easily reducible[32]. In the literature, there are examples of cerium zirconium dioxide catalysts that are a more efficient store of oxygen than CeO_2[33]. The activity of $CeZrO_2$ for the total oxidation of naphthalene was probed in 2008 by Bampenrat *et al.*[21]. They prepared catalysts via urea hydrolysis and Ce^{3+} nitrate. In terms of catalytic activity, it was reported that high Ce content $CeZrO_2$ catalysts were more active than either CeO_2 or ZrO_2. These more active catalysts contained Ce:Zr ratios of 75:25 and 50:50. These catalysts reached naphthalene conversions of 100% at approximately 600°C. Zr contents above 50% resulted in changes in the catalyst reducibility, agreeing with previous studies that the catalyst reducibility was an important factor.

The kinetics of the oxidation for the most active catalyst, Ce75Zr25 was probed using the initial rates at a temperature where less than 20% naphthalene conversion was observed. The data produced suggested reaction orders of approximately 0.5 with respect to oxygen and naphthalene. The best fit was obtained by applying the Mars van Krevelen rate expression to the data hence the proposal that the oxidation of naphthalene occurred via the MvK mechanism.

Pt/SiO_2 was recently probed for its activity for the total oxidation of naphthalene in a study by Edwin *et al.* amongst a wide range of catalysts consisting of 0.5wt% Pt supported on a range of supports[34]. Out of all the supports tested, the most active support was SiO_2.

The supports tested in this study were SiO_2, Al_2O_3, TiO_2, CeO_2 and SnO_2. When they were tested for their activity for the total oxidation of naphthalene, all of the catalysts were less active than urea precipitated CeO_2 (denoted as CeO_2 (U)) except for 0.5wt% Pt/SiO_2. This exhibited higher activity than CeO_2 (U) at low temperatures (i.e. below CO_2 yields of 100%). When the CO chemisorption data was examined, it revealed that the less active catalysts had higher Pt dispersions, larger Pt surface areas and smaller Pt crystallite sizes compared with the more active Pt based catalysts (i.e. Pt/SiO_2). Therefore it was postulated that poorly dispersed, larger Pt particles were necessary for active catalysts for the total oxidation of naphthalene. It was also suggested that since the more active supported Pt catalysts (Pt/SiO_2 and Pt/Al_2O_3) were known to only have significantly weaker metal-support interactions (due to their inherent non-reducibility) compared with the other supports, strong Pt-support interactions were undesirable. XPS analysis also revealed that metallic Pt was present in Pt/SiO_2 rather than an oxide.

SnO_2 was used as a support and exhibited the largest Pt crystallite sizes and the least dispersion, despite being relatively inactive for the total oxidation of naphthalene. As SnO_2 is hydrophobic, using an aqueous impregnation method would cause poor deposition of Pt on the surface (poor surface wetting). This may have caused the Pt particles to have more bulk-like behaviour rather than the 'surface-like' behaviour of smaller nanoscale particles. In short, the data presented in that paper may not represent the true activity and characteristics of Pt/SnO_2 prepared to account for the hydrophobicity of SnO_2. It would be useful to repeat this study to see if a more active catalyst can be prepared. This paper presents two potential avenues of research:

1   Optimisation of the Pt/SiO_2 catalyst preparation in a similar way to that investigated by Edwin *et al.* with regards to ceria and naphthalene total oxidation.

2   Modification of the Pt/SnO_2 catalyst preparation taking into account the hydrophobicity of the SnO_2 support and its effect on metal deposition/impregnation on the surface.

1.5.2   Propane Total Oxidation

The total oxidation of propane has been reported several times in the literature, although partial propane decomposition (e.g. dehydrogenation) has received more extensive coverage. There are more examples to be found than that for naphthalene total oxidation.

One of the earliest published studies of propane combustion was published by Yazawa and co-workers[35]. The Pd oxidation state of Pd/SiO_2-Al_2O_3 was studied. It was found that in varying $C_3H_8:O_2$ stoichiometric ratios, the oxidation states of the Pd varied. It was found that more oxidative atmospheres gave rise to a greater proportion of the Pd existing as Pd oxides. The authors reported that an optimum stoichiometric ratio was found for optimum propane conversion and that the palladium was found in both the oxidised and metallic states. It was reported that the Pd dispersion did not change with the $C_3H_8:O_2$ stoichiometric ratio.

The activity of Pt/γ-Al_2O_3 towards propane oxidation was reported to be enhanced by the promotion of SO_2 in propane oxidation[36]. The effect was reported to be reversible, although recovery to the original activities was reported to be slow after the SO_2 was removed from the reaction. Water was reported to inhibit propane oxidation. These effects could not be repeated for a Pt/SiO_2 analogue; no significant change in activity was observed. Surface sulphates were observed on the Pt/γ-Al_2O_3 catalyst which the authors proposed allowed additional reaction pathways for propane oxidation to occur.

Yoshida *et al.* reported the catalytic activities and oxidation state of a variety of promoted Pt catalysts on different supports (MgO, Al_2O_3 and SiO_2-Al_2O_3)[37]. It was found that the more acidic supports gave more active catalysts. In terms of Pt oxidation state, the Pt catalysts that exhibited higher degrees of metallic Pt were the more active. The degree of metallic Pt was controlled by the electrophillic or electrophobic properties of the supports and the promoting additives used in the catalyst preparation. More electrophillic supports and promoters gave rise to the formation of more metallic Pt. This was proposed to be due to the Pt oxo-anion being stabilised by electrophobic cations.

Chambers and Cant reported that the introduction of NO in propane oxidation over Pt/SiO_2 reduced catalytic activity[38]. This reduction was observed with less than 1ppm of NO in the gas stream. The rate of reaction was reported to decrease by a factor greater than 20 when 1000ppm of NO was introduced into the gas stream. At 1ppm NO concentration, it was observed that the NO adsorbs weakly on the catalyst surface under reaction conditions. The authors attributed the decrease in activity to the cyclic oxidation

of some of the NO to NO_2 followed by NO_2 decomposition on the propane oxidation active sites.

Garcia *et al.* reported the use of vanadium modified Pd/TiO_2 catalysts for propane total oxidation[39]. It was reported that the co-impregnation of the V and Pd enhanced catalytic activities, with 0.5% Pd/1.5% V/TiO_2 reported to be the most active. It was found that Pd dispersion and surface site concentration decreased upon the addition of V. A greater concentration of polymeric V species were observed in the presence of palladium. The concentration of V^{4+} species was found to increase in the presence of Pd, thereby changing the redox properties of the catalysts and therefore affecting the activities. The reducibility of these catalysts were also enhanced.

The effect of Nb modifiers in Pd/TiO_2 catalysts was reported by Taylor *et al.* in 2008[40]. It was reported that the inclusion of niobium provided an increase in catalytic activity. This was found to be due to an increase in oxygen mobility after Nb addition. The nature of the Pd was also altered; oxidised Pd was observed. The activity was also found to increase with increasing Nb and Pd loading. The most active catalyst was found to be 0.5% Pd/6% Nb_2O_5/TiO_2.

The activities of Au catalysts on a variety of different supports were reported in 2006[41]. CoOx was reported to be the most active catalyst out of the range tested (CoOx, MnOx, CuO, Fe_2O_3 and CeO_2) with a T_{50} temperature of 180°C. CeO_2 and TiO_2 needed temperatures in excess of 400°C to reach T_{50}. When Au was included in a co-precipitation catalyst preparation, the activity of CoOx was enhanced. Au/CoOx achieved T_{50} at a temperature of 165°C. An impregnated analogue was less active, where a T_{50} temperature of 220°C was reported. The inclusion of Au was found to enhance the reducibility of the CoOx support.

Au/CoOx was the subject of a TAP study in 2009[42]. In that paper, it was reported that the previous observation of Au enhancing propane total oxidation was repeatable. The Mars-van Krevelen mechanism was reported to operate using isotopically labelled oxygen in the catalyst testing experiments. The presence of Au was reported to enhance the speed of cobalt oxide reoxidation. The Au catalyst contained a higher concentration of oxygen vacancies which was the reason behind this increased reoxidation speed. It was also proposed, in a separate work, that the redox properties of the catalyst was a key feature in producing an active catalyst for propane total oxidation[28].

Further work was reported with regards to Co oxide in propane combustion[43]. A nanocrystalline cobalt oxide catalyst was found to give 100% propane conversion at

18

200°C. Pd/Al_2O_3 was found to require a temperature of 450°C to display similar propane conversions. The nanocrystallinity of the cobalt oxide was proposed to be the important factor in enhancing catalytic activity by providing new catalytically active surfaces. Another paper compared this nanocrystalline cobalt oxide as a bulk catalyst with the same nanocrystalline cobalt oxide supported on alumina[44]. The alumina supported cobalt oxide was found to be less active than the bulk cobalt oxide for the total oxidation of propane. The bulk cobalt oxides which had high surface areas were the most active and were the most reducible due to low Co-O bond strengths and increased defect concentration.

Harrison *et al.* reported that the activity of tin (IV) oxide towards propane oxidation was not improved with the inclusion of rare earth metals during a co-precipitation preparation method[45]. However, Cr promoted SnO_2 catalysts were found to be more active for propane oxidation than a commercial Pt/Al_2O_3 catalyst.

Song *et al.* performed kinetic studies using a perovskite based catalyst[46]. The best fit of the kinetic data was achieved by fitting the Mars Van Krevelen kinetic model to the data. It was also observed that the addition of water and carbon dioxide to the gas feed had an inhibiting effect, which corresponds with the observations of Skoglundh and co-workers[36]. The Mars-van Krevelen mechanism was reported to operate in several other works.

Heynderickx *et al.* proposed that propane oxidation operated via the Mars van Krevelen mechanism using vanadia-titania catalysts on porous silica and non-porous SiO_2-ZrO_2 supports[47]. A similar conclusion with regards to the mechanism was reached in a later paper[48], but for a different catalyst system (CuO-CeO_2/γ-Al_2O_3). A more detailed kinetic study on CuO-CeO_2/γ-Al_2O_3 was performed in another paper[49]. A Langmuir-Hinschelwood mechanism gave the best fit to the activity data when CO_2 and water are present in the reaction. The overall catalytic activity was reported to decrease when water was present. The same effect was observed when CO_2 was present, although the effect was less pronounced.

Another recent paper was published by Alexopoulos *et al.* who studied CuO-CeO_2/Al_2O_3 for the total oxidation of propane[50]. It was found that the Cu was oxidised (Cu^{2+}) during the propane oxidation. If the catalyst was subjected to 2% C_3H_8/He and then reoxidised in 10% O_2/He, then the Cu was found to be in the metallic, +1 and +2 oxidation states in a two step mechanism. After reoxidation the Cu was found to be in the +2 oxidation state hence the original state of the catalyst was recovered. The reoxidation

of the catalyst was more facile than the reduction, indicating that the Mars-van Krevelen mechanism operated.

1.6 Glossary; Basic Terminology

There are a number of phrases that can be used when discussing catalysis and catalytic processes. Some of these are given here.

Active site. The portion of a catalyst surface where reaction actually takes place e.g. CO oxidation occurs on the surface of Au nanoparticles and immediately at the metal/support interface rather than on bulk Au particles or exclusively on the surface of the support.

Promoter. A promoter is a substance which can be incorporated into a catalyst of known activity in order to try and improve said activity. An example of this is the incorporation of V in Pt/Al_2O_3 catalysts to give $Pt/V/Al_2O_3$ for naphthalene total oxidation[51].

Support. A support is a material which provides an 'anchor' for the active component of a catalyst. The support can have an influence on the catalytic properties of the active component(s). For example, the metal-support interaction (MSI) strength could affect a metal active site when exposed to high temperatures (i.e. the support could encourage or prevent changes in metal crystallite size or the degree of sintering). Some catalysts can be self supporting (e.g. CeO_2).

Poison. A substance that inhibits catalytic activity by blocking the catalytic active sites. This can include adsorption of gaseous poisons (e.g. sulphur) onto the active sites or the formation of a solid film over the active sites e.g. catalyst coking.

Deactivation. Deactivation is the decrease in catalytic activity for a given catalyst. This can be induced via the reaction atmosphere or physical damage to the catalyst structure (e.g. repeated heat cycle treatment). It can also be propagated by using an active site poison.

Inhibitor. An inhibitor is most commonly seen in biochemical situations, particularly enzymes. For enzymes an inhibitor is a substance that will partially block amino acid sites within the enzyme's active site, preventing the binding of the original target molecule. This sort of behaviour is found in a wide range of pharmaceutical therapies.

Impregnation. A catalyst preparation technique. A solution of metal salt (usually aqueous, although the use of non-aqueous solutions has been reported) is stirred at a set temperature (depending on the solvent used). The support material is then added and the solution stirred for a given length of time. It is then dried and usually calcined/thermally treated to give the finished catalyst.

Co-precipitation. Another catalyst preparation technique. Usually performed in aqueous conditions, this preparation can be used for self supporting catalyst synthesis. A solution of starting material is refluxed with a precipitating agent for a set amount of time at a set temperature. The solvent is then removed (e.g. by filtration) then the finished catalyst is produced by calcination.

Calcination. A thermal heat treatment process used for 'finishing' a catalyst in an oxidative atmosphere. Calcination can be used to remove solvent or starting material fractions, change support morphologies or change active metal oxidation states. Samples can also be treated in other atmospheres (such as He or H_2) at elevated temperatures in a similar fashion, although it would be incorrect to call these processes calcinations.

Light off temperature. This is the temperature/temperature range where catalytic activity significantly increases from a low product yield to a much higher value.

Metal Support Interaction (MSI). The term used to describe the behaviour between the metal clusters on the surface and the surface of the support. The strength of this interaction could have beneficial or detrimental effects on catalyst activity, or could have important mechanistic effects, e.g. Bond and Thompson's CO oxidation model[52].

Mass transfer[53]. As described previously, catalytic mechanisms require the diffusion of chemical species from the gaseous atmosphere to a catalyst-bound state. If the rate of diffusion of the reactants to the catalyst surface is exceeded by the rate of reaction from reactants to products, then the system is described as 'mass transfer limited'. In other words, the activity of a catalyst would not be limited to how quickly adsorbed species can react to form products, but by how quickly the initial adsorption onto the catalyst can occur.

1.7 References

1. P. A. Newman, E. R. Nash, S. R. Kawa, S. A. Montzka, S. M. Schauffler, *Geophysical Research Letters*, **33**, (2006), Article No. L12814.

2. *Chemistry in Britain*, 1997.

3. A. Sorokin, B. Meunier, *European Journal of Inorganic Chemistry*, **1998**, (1998), 1269-1281.

4. M. Ferrandon, M. Berg, E. Bjornbom, *Catalysis Today*, **53**, (1999), 647-659.

5. X. W. Zhang, S. C. Shen, L. E. Yu, S. Kawi, K. Hidajat, K. Y. S. Ng, *Applied Catalysis A: General*, **250**, (2003), 341–352.

6. H. Li, R. Westerholm, J. Almen, K. Gragg, *Fuel*, **73**, (1994), 11-16.

7. H. Li, C. D. Banner, G. G. Mason, R. N. Westerholm, J. J. Rafter, *Atmospheric Environment*, **30**, (1996), 3537-3543.

8. W. O. Siegl, R. H. Hammerle, H. M. Herrmann, B. W. Wenclawiak, B. Luers-Jongen, *Atmospheric Environment*, **33**, (1999), 797-805.

9. F. H. Geng, C. J. Cai, X. X. Tie, Q. Yu, J. L. An, L. Peng, G. Q. Zhou, J. M. Xu, *Journal of Atmospheric Chemistry*, **62**, (2009), 229-247.

10. L. Jaimes, J. Sandoval, *Science Of The Total Environment*, **289**, (2002), 243-247.

11. Y. S. Chen, H. S. Liu, *Industrial & Engineering Chemistry Research*, **41**, (2002), 1583-1588.

12. T. Garcia, B. Solsona, S. H. Taylor, *Catalysis Letters*, **105**, (2005), 183-189.

13. Y. C. Chiang, P. C. Chaing, C. P. Huang, *Carbon*, **39**, (2001), 523-534.

14. S. Mudliar, B. Giri, K. Padoley, D. Satpute, R. Dixit, P. Bhatt, R. Pandey, A. Juwarkar, A. Vaidya, *Journal of Environmental Management*, **91**, (2010), 1039-1054.

15. K. Min, S. J. Ergas, *Water, Air and Soil Pollution: Focus*, **6**, (2006), 83–96.

16. M. D. S. Hossain, M. A. Haque, *Waste Management*, **29**, (2009), 1568-1576.

17. M. Bowker, *The Basis and Applications of Heterogeneous Catalysis*, Oxford University Press, 1998.

18. *U.S. Climate Change Technology Program – Technology Options for the Near and Long Term*, August 2005, 1.4-9.

19. J. J. Berzelius, *Edinburgh New Philosophical Journal*, **21**, (1836), 223.

20. P. W. Atkins, J. de Paula, *Physical Chemistry*, Oxford University Press, 2002.

21. A. Bampenrat, V. Meeyoo, B. Kitiyanan, P. Rangsunvigit, T. Rirksomboon, *Catalysis Communications*, **9**, (2008), 2349-2352.

22. E. Ntainjua, S. H. Taylor, *Topics in Catalysis*, **52**, (2009), 528-541.

23. J. Carno, M. Ferrandon, E. Bjornbom, S. Jaras, *Applied Catalysis A-General*, **155**, (1997), 265-281.

24. M. Ferrandon, J. Carno, S. Jaras, E. Bjornbom, *Applied Catalysis A-General*, **180**, (1999), 153-161.

25. M. Ferrandon, E. Bjornbom, *Catalyst Deactivation 1999*, **126**, (1999), 423-426.

26. X. W. Zhang, S. C. Shen, K. Hidajat, S. Kawi, L. E. Yu, K. Y. S. Ng, *Catalysis Letters*, **96**, (2004), 87-96.

27. J. L. Shie, C. Y. Chang, J. H. Chen, W. T. Tsai, Y. H. Chen, C. S. Chiou, C. F. Chang, *Applied Catalysis B-Environmental*, **58**, (2005), 289-297.

28. T. Garcia, B. Solsona, S. Taylor, *Applied Catalysis B-Environmental*, **66**, (2006), 92-99.

29. R. Weber, T. Sakurai, H. Hagenmaier, *Applied Catalysis B-Environmental*, **20**, (1999), 249-256.

30. E. N. Ndifor, *The Catalytic Oxidation of Volatile Organic Compounds, PhD Thesis*, 2007.

31. P. Mars, D. W. van Krevelen, *Chemical Engineering Science*, **3**, (1954), 41-58.

32. A. Trovarelli, *Catalysis by Ceria and Related Materials*, Imperial College Press, London, 2002.

33. J. F. Lamonier, S. P. Kulyova, E. A. Zhilinskaya, B. G. Kostyuk, V. V. Lunin, A. Aboukais, *Kinetics and Catalysis*, **45**, (2004), 429-435.

34. N. N. Edwin, A. F. Carley, S. H. Taylor, *Catalysis Today*, **137**, (2008), 362-366.

35. Y. Yazawa, H. Yoshida, N. Takagi, S. Komai, A. Satsuma, T. Hattori, *Applied Catalysis B-Environmental*, **19**, (1998), 261-266.

36. M. Skoglundh, A. Ljungqvist, M. Petersson, E. Fridell, N. Cruise, O. Augustsson, E. Jobson, *Applied Catalysis B-Environmental*, **30**, (2001), 315-328.

37. H. Yoshida, Y. Yazawa, T. Hattori, *Catalysis Today*, **87**, (2003), 19-28.

38. D. C. Chambers, N. W. Cant, *Applied Catalysis B-Environmental*, **41**, (2003), 61-70.

39. T. Garcia, B. Solsona, D. M. Murphy, K. L. Antcliff, S. H. Taylor, *Journal of Catalysis*, **229**, (2005), 1-11.

40. M. Taylor, E. N. Ndifor, T. Garcia, B. Solsona, A. F. Carley, S. H. Taylor, *Applied Catalysis A-General*, **350**, (2008), 63-70.

41. B. E. Solsona, T. Garcia, C. Jones, S. H. Taylor, A. F. Carley, G. J. Hutchings, *Applied Catalysis A-General*, **312**, (2006), 67-76.

42. B. Solsona, T. Garcia, G. J. Hutchings, S. H. Taylor, M. Makkee, *Applied Catalysis A-General*, **365**, (2009), 222-230.

43. B. Solsona, I. Vazquez, T. Garcia, T. E. Davies, S. H. Taylor, *Catalysis Letters*, **116**, (2007), 116-121.

44. B. Solsona, T. E. Davies, T. Garcia, I. Vazquez, A. Dejoz, S. H. Taylor, *Applied Catalysis B-Environmental*, **84**, (2008), 176-184.

45. P. G. Harrison, C. Bailey, W. Azelee, *Journal of Catalysis*, **186**, (1999), 147-159.

46. K. S. Song, D. Klvana, J. Kirchnerova, *Applied Catalysis A-General*, **213**, (2001), 113-121.

47. P. M. Heynderickx, J. W. Thybaut, H. Poelman, D. Poelman, G. B. Marin, *Applied Catalysis B-Environmental*, **90**, (2009), 295-306.

48. P. M. Heynderickx, J. W. Thybaut, H. Poelman, D. Poelman, G. B. Marin, *Journal of Catalysis*, **272**, (2010), 109-120.

49. M. P. Heynderickx, J. W. Thybaut, H. Poelman, D. Poelman, G. B. Marin, *Applied Catalysis B-Environmental*, **95**, (2010), 26-38.

50. K. Alexopoulos, M. Anilkumar, M. F. Reyniers, H. Poelman, S. Cristol, V. Balcaen, P. M. Heynderickx, D. Poelman, G. B. Marin, *Applied Catalysis B-Environmental*, **97**, (2010), 381-388.

51. E. N. Ndifor, T. Garcia, S. H. Taylor, *Catalysis Letters*, **110**, (2006), 125-128.

52. G. C. Bond, D. T. Thompson, *Gold Bulletin*, **33**, (2000), 41-51.

53. K. Arnby, J. Assiks, P. A. Carlsson, A. Palmqvist, M. Skoglundh, *Journal of Catalysis*, **233**, (2005), 176-185.

Chapter 2 - Experimental

2.1   Catalyst Preparation

2.1.1   Preparation of Cerium Zirconium Dioxide Catalysts via Urea Co-precipitation

Urea (Aldrich, ACS reagent, 99–100.5%, 40g), distilled water (200mL) and the appropriate amounts of ammonium cerium (IV) nitrate (Aldrich, 99.99+%) and zirconyl nitrate hydrate (Aldrich, 99%) were aged with stirring in a round-bottomed flask for 24h at 120°C. The resulting slurry was filtered, washed with deionised water and dried at 110°C overnight. This was followed by calcination in static air at 500°C for 6h with a ramp rate of 10°C/min. The following catalysts were prepared:

- ZrO_2 (no ammonium cerium (IV) nitrate was used in this preparation)
- Ce50Zr50
- Ce60Zr40
- Ce70Zr30
- Ce80Zr20
- Ce90Zr10
- Ce99Zr1
- CeO_2 (no zirconyl nitrate hydrate was used in this preparation)

The Ce:Zr ratios relate to percentage atomic weights rather than wt% and these catalysts are henceforth denoted NH_4-U.

2.1.2   Preparation of Cerium Zirconium Dioxide Catalysts via Carbonate Co-precipitation

0.25M solutions of zirconyl nitrate hydrate (Aldrich, 99%) and ammonium cerium (IV) nitrate (Aldrich, 99.99+%) (proportions were dependent on the desired Ce:Zr ratio) were combined and heated to 80°C with stirring. Aqueous sodium carbonate solution (0.25M) was then added dropwise until a pH of 8 – 9 was reached. This was then aged at 80°C

with stirring for 1h. The precipitate was filtered, washed with distilled water then dried at 110°C overnight. The dried precursors were calcined for 3h at 400°C in static air with a ramp rate of 10°C/min. These catalysts are henceforth denoted NH$_4$-C.

A third series of catalysts were produced which are denoted NIT-C. The preparation method used is as described in the previous paragraph except that cerium (III) nitrate hexahydrate (Aldrich, 99.99%) was used instead of the ammonium cerium (IV) nitrate as described above.

2.1.3 Preparation of Cerium Zirconium Dioxide Catalysts via Supercritical Fluids

The supercritical CeZrO$_2$ was prepared by Dr. Bin Gao of this research group via the SAS (supercritical anti solvent) method. Figure 2.1 (below) is a schematic of the apparatus used for the sample preparation. Solutions of Ce(acac)$_3$ (Aldrich) in MeOH (Fisher) (concentration = 6.03×10^{-5} mol/mL) and Zr(acac)$_4$ (Aldrich, 98%) in MeOH (Fisher) (concentration = 6.13×10^{-7} mol/mL) were combined. This solution was introduced into a precipitation vessel via pumping through a fine capillary as part of a coaxial nozzle system. At the same time CO$_2$ (BOC) was introduced into the precipitation vessel through the outer part of the same coaxial nozzle via pumping using a HPLC pump. A CO$_2$ pressure of 110bar and temperature of 40°C ensured that the CO$_2$ was kept in the supercritical phase. The temperature was controlled by fitting the precipitation vessel into a GC oven. The Ce/Zr/MeOH solution and supercritical CO$_2$ were flowed concurrently for 16h at flow rates of 0.1mL/min and 10mL/min respectively. After this 16h period, MeOH and supercritical CO$_2$ were flowed for 1h followed by supercritical CO$_2$ only for 1h. After collection of the product, it was calcined in static air at 500°C for 6h with a ramp rate of 10°C/min to give the finished catalyst.
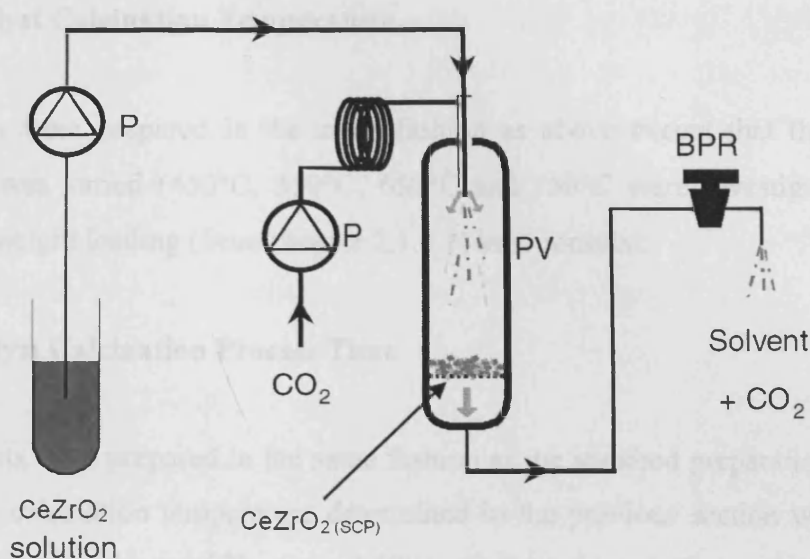
Figure 2.1. Schematic of the type of supercritical apparatus used to prepare sc-Ce99Zr1O$_2$. BPR: back pressure regulator; P: pump; PV: precipitation vessel. Schematic adapted from reference[1].

2.1.4 Preparation of Pt/SiO$_2$ Catalysts

All of the Pt/SiO$_2$ catalysts were prepared via an impregnation method as follows: an appropriate amount of the Pt salt, hexachloroplatinate (IV) hydrate (Aldrich, $\geq$99.9% metals basis) was dissolved in distilled water (100mL) then heated to 80°C with stirring. SiO$_2$ (3g, Silica 60Å, Fisher) was added. This was then stirred at 80°C until a paste was formed. This paste was dried at 110°C overnight before calcination. Calcination conditions were static air at 550°C for 6h (ramp rate of 10°C/min) to give the finished catalyst after cooling to room temperature.

2.1.4.1 Pt Loading on Catalyst

The Pt/SiO$_2$ catalysts were synthesised to contain differing percentage weights of Pt, namely 0.1, 0.5, 1, 2.5 and 5 weight percent Pt on the 60Å pore SiO$_2$ support.

27

2.1.4.2 Catalyst Calcination Temperature

The catalysts were prepared in the same fashion as above except that the calcination temperature was varied (450°C, 550°C, 650°C and 750°C were investigated) and the optimum Pt weight loading (from chapter 2.1.4.1) kept constant.

2.1.4.3 Catalyst Calcination Process Time

These catalysts were prepared in the same fashion as the standard preparation except that the optimum calcination temperature determined in the previous section was taken into account. Calcination times of 3h, 6h and 12h were investigated. The optimum Pt weight loading and calcination temperature were kept constant.

2.1.4.4 Catalyst Calcination Process Ramp Rate

These catalysts were calcined using a ramp rate of 5, 10 or 20°C/min using the optimum conditions determined thus far.

2.1.4.5 Catalyst Calcination Atmosphere

Using the optimised calcination regime determined thus far, these catalysts were calcined in either static or flowing air for the entire calcination procedure.

2.1.4.6 Nature of SiO₂ Support

After optimising the Pt weight loading, calcination temperature, timeframe, ramp rate and atmosphere, the nature of the SiO_2 support was changed from the Silica 60Å used thus far to nanopowder SiO_2 (Aldrich, 5-15nm (BET), 99.5% metals basis). SiO_2 hollow spheres which used this nanopowder as a precursor were also used as a support. The nanopowder was used as supplied from Aldrich. The hollow spheres were prepared by Asuncion Aranda using the following method[2].

Sodium silicate, $Na_2SiO_3.9H_2O$ (47.3g), was added dropwise into a nanosized carbonate suspension (details in reference[3]) with stirring at 80°C within a 1h time period. The pH was adjusted to 9-10 by use of 10wt% HCl solution. This solution was then

stirred for 2h at 80°C. A molar $SiO_2/CaCO_3$ ratio of 1/10 was desired. After 2h, the solid was filtered and washed with distilled water, followed by ethanol. This was then dried at 110°C overnight prior to calcination at 700°C for 5h in static air. The $CaCO_3$ template was then removed by dissolving the composite in 10wt% HCl solution overnight. The gel was then filtered and washed with distilled water and ethanol before being dried overnight at 110°C. The material was then milled to give the finished product.

2.1.5 Preparation of Pd/SiO₂ Catalysts

This preparation was identical to that reported in section 2.1.3 except that sodium tetrachloropalladate (II) hydrate (Alfa Aesar, 99.95% metals basis, 30% Pd content) substituted the hexachloroplatinate (IV) hydrate. The calcination regime used was based on the optimum calcination determined using the catalysts synthesised in section 2.1.3.

2.1.6 Preparation of Hydrophobic Supporting Catalysts with Non-Aqueous Solvents

The hydrophobic catalysts studied were initially prepared using a modified procedure that was described elsewhere[4-6]. An appropriate amount of the metal acetylacetonate salt was dissolved in its corresponding solvent (100mL) and stirred until the salt had dissolved. The support was then added (3g) and the resulting slurry stirred at room temperature for 24h. The solvent was removed via rotary evaporation and the solid dried overnight. The solid was then treated with flowing He (500°C, 2h, ramp rate = 10°C/min). The sample was then treated with flowing air (350°C, 2h, ramp rate = 10°C/min) and flowing 5% H_2/Ar (500°C, 2h, ramp rate = 10°C/min). These samples were allowed to cool after each 2h calcination period. The catalysts were then finished with flowing He (room temperature, 30min).

The following starting materials, solvents and supports used are described in the tables below. Different solvents were required due to the differing nature of the metal acetylacetonate salts. Ag and Cu acetylacetonate are polar (in the case of Ag, very polar) hence a highly polar solvent was required (i.e. DMSO which has a dielectric constant of 46.7). Ethyl acetate has a higher dielectric constant than toluene (6.02[7] versus 2.38[8]) and hence is more polar. Ni acetylacetonate is a relatively polar compound compared to the Pd and Pt analogues; therefore a more polar solvent is required.

2.1.6.1 Metal Salts Used in Preparations

Table 2.1. Metal salts and their corresponding solvents used in all preparations.

Salt	Reaction solvent
Pd acetylacetonate (Aldrich, 99%)	Toluene (Fisher, lab. reagent grade)
Ag acetylacetonate (Aldrich, 98%)	Dimethylsulfoxide (DMSO) (Aldrich)
Cu acetylacetonate (Aldrich, 98%)	Dimethylsulfoxide (DMSO) (Aldrich)
Ni acetylacetonate (Merck, ≥ 98%)	Ethyl acetate (Fisher, lab. reagent grade)
Pt acetylacetonate (Aldrich, 97%)	Toluene (Fisher, lab. reagent grade)

2.1.6.2 Supports Used in Preparations

- Boron nitride (Aldrich, powder, ~1 micron, 98%)

- Silicon nitride (Aldrich, nanopowder, <50nm particle size (spherical), ≥98.5% trace metals basis)

- Silicon carbide (Aldrich, nanopowder <100nm particle size)

- Tin (IV) oxide (Aldrich, 325 mesh, 99.9% trace metals basis)

The metal loadings were kept constant at 0.5wt%. The following catalysts were prepared:

- 0.5wt% Ni/BN
- 0.5wt% Ni/Si$_3$N$_4$
- 0.5wt% Ni/SiC
- 0.5wt% Ni/SnO$_2$
- 0.5wt% Cu/BN
- 0.5wt% Cu/Si$_3$N$_4$
- 0.5wt% Cu/SiC
- 0.5wt% Cu/SnO$_2$
- 0.5wt% Pd/BN
- 0.5wt% Pd/Si$_3$N$_4$

- 0.5wt% Pd/SiC
- 0.5wt% Pd/SnO$_2$
- 0.5wt% Ag/BN
- 0.5wt% Ag/Si$_3$N$_4$
- 0.5wt% Ag/SiC
- 0.5wt% Ag/SnO$_2$
- 0.5wt% Pt/BN
- 0.5wt% Pt/Si$_3$N$_4$
- 0.5wt% Pt/SiC
- 0.5wt% Pt/SnO$_2$

30

2.1.6.3 Aqueous Analogue Preparation

An aqueous analogue of 0.5wt% Pd/BN was prepared using a similar technique described in section 2.1.7. However the Pd acetylacetonate was substituted with tetrachloropalladate (II) hydrate (Alfa Aesar, 99.95% metals basis, 30% Pd content) and water was used as the reaction solvent. The impregnation was performed at room temperature for 24h as in section 2.1.7. The calcination regime also remained unchanged.

2.1.6.4 High Surface Area SnO_2 Support Preparation

The preparation of a high surface area SnO_2 support was also performed based on the work of Wang *et al.*[9].

Di-n-butyltin dilaurate (Alfa Aesar, 95%) was dissolved in toluene (Fisher, laboratory reagent grade) (100mL) with stirring. An appropriate mass of SiO_2 (Fisher, 60Å pore size) was added. The resulting solution was aged with stirring for 24h at RTP. Then solvent was then removed with rotary evaporation and dried at 120°C for 2h. It was then calcined in static air for 4h at 600°C to give the finished support. A theoretical Sn content of 16wt% was prepared. This support is henceforth denoted SnO_2-SiO_2.

2.2   Reactor Design

2.2.1   Naphthalene Oxidation

2.2.1.1 Reactor Schematic

The catalytic activities of the materials synthesised were probed using a laboratory micro-scale reactor coupled with a gas chromatograph (Varian 3400 GC) fitted with inline thermal conductivity and flame ionisation detectors. The analytes were separated using OV-17 (naphthalene) and Carbosphere 80/100 mesh (O_2 and CO_2) packed columns. A schematic of the whole reactor is displayed in figure 2.2 and figure 2.3 is a photograph of the reactor. The reactor was composed of a 0.25 inch O.D. 316 stainless steel tube which was heated using a 'clam shell' type furnace. Helium and oxygen flows totalling 50 mL/min (20% O_2 content) and 100vppm of naphthalene were used. The catalyst was

31

packed in such a way to provide the desired GHSV (defined where necessary in this text). All the lines from the naphthalene source onwards were heated by external heating tapes to prevent condensation of the gaseous naphthalene within the reactor. Activity tests were performed in the range of 100-350°C and the catalyst temperature was controlled via a thermocouple fitted in the catalyst bed.

NAPHTHALENE TOTAL OXIDATION REACTOR SCHEMATIC
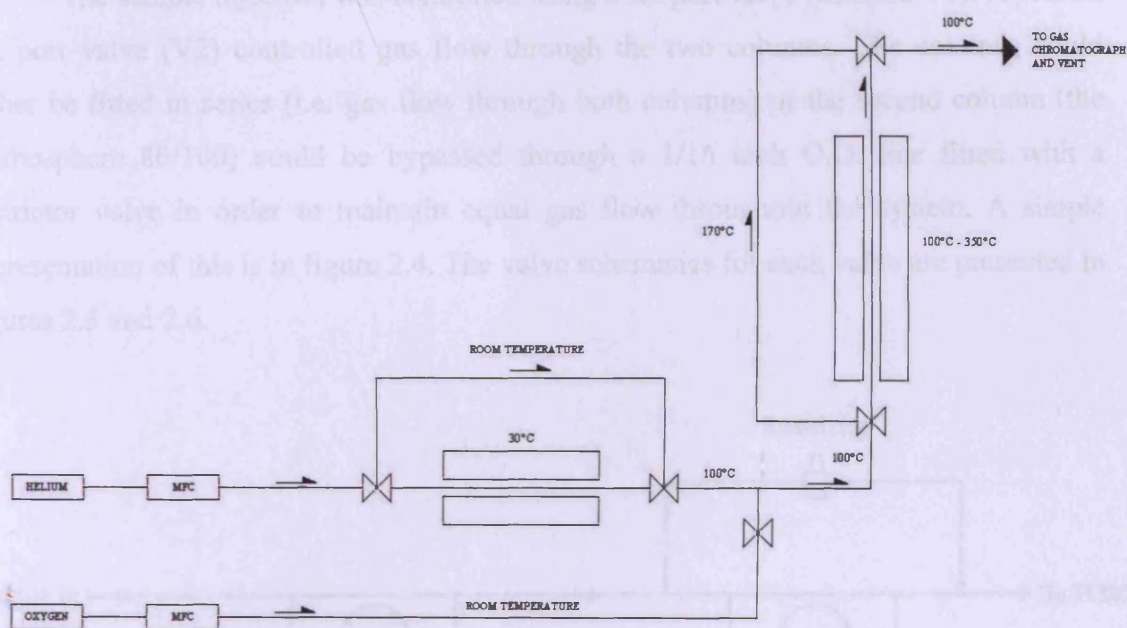
Figure 2.2. Schematic of apparatus used to probe catalytic activities for the total oxidation of naphthalene. Arrows denote direction of gas flow. Temperatures denote temperature of the respective section of gas line. MFC denotes mass flow controller.

Figure 2.3. Photograph of the reactor set-up used to investigate the total oxidation of naphthalene.

2.2.1.2 Sample Delivery

In order to separate the hydrocarbons produced (i.e. partial oxidation products) the column temperatures would need to be altered in order to separate each hydrocarbon. For example, phthalic anhydride can have a similar retention time to naphthalene and can also be a partial oxidation product from incomplete (partial) naphthalene combustion[10-12].

The sample injection was controlled using a six port valve (denoted V1). A second six port valve (V2) controlled gas flow through the two columns. The columns could either be fitted in series (i.e. gas flow through both columns) or the second column (the Carbosphere 80/100) could be bypassed through a 1/16 inch O.D. line fitted with a restrictor valve in order to maintain equal gas flow throughout the system. A simple representation of this is in figure 2.4. The valve schematics for each valve are presented in figures 2.5 and 2.6.
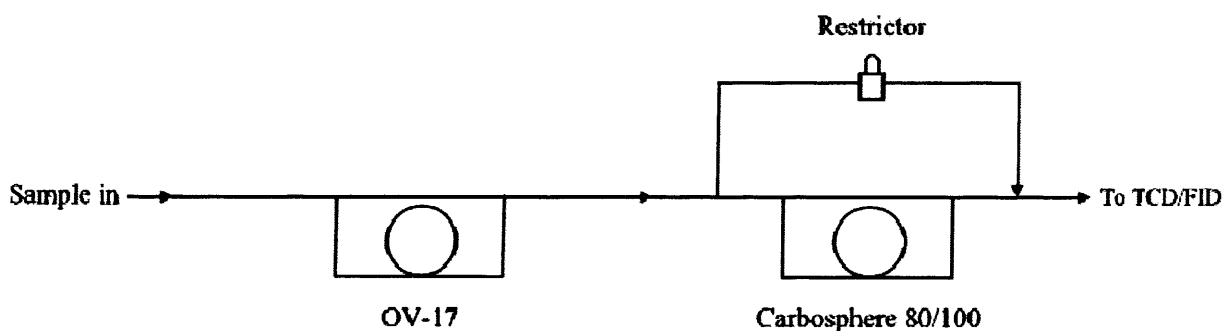
Figure 2.4. Diagram of GC column set-up. The Carbosphere 80/100 column can be bypassed via a pneumatic valve which is described in detail in figure 2.6.
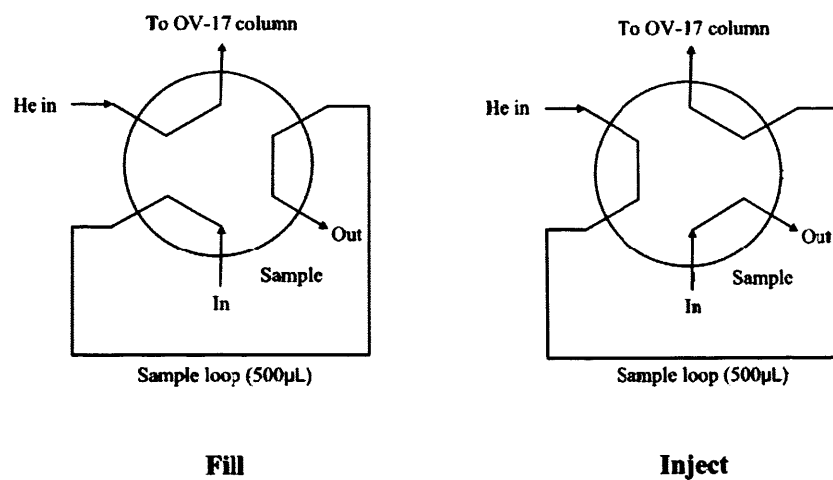
Figure 2.5. Schematic of valve 1 in all possible positions; fill (+) and inject (-).
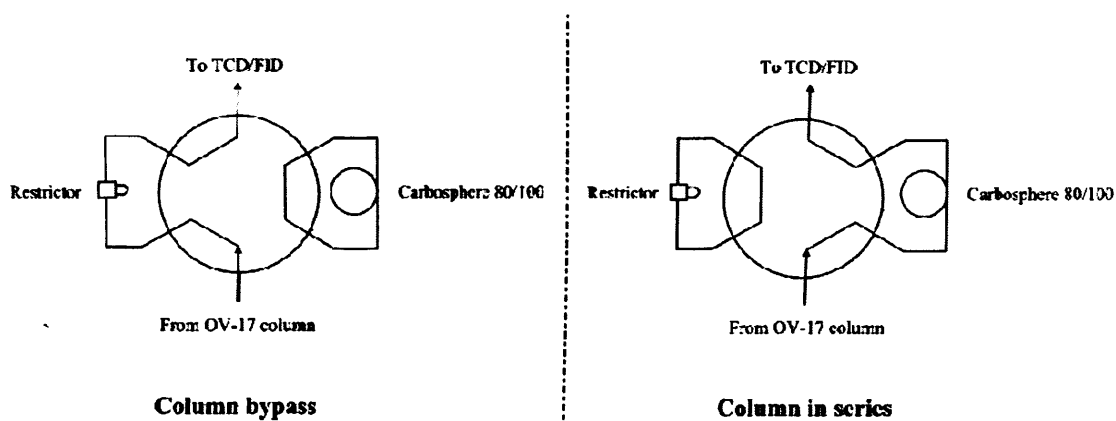
Figure 2.6. Schematic of valve 2 in both positions. Column bypass (+) allows gas flow through restrictor bypassing Carbosphere column. Column series (-) allows separated gas mixture components to be analysed via TCD and FID.

Table 2.2. Valve event timings of sample injection and column switching.

Time (min)	Valve event
Initial	+1, -2
0.01	-1, -2
1.25	+1, -2
12.00	+1, +2

Valve 1 controlled sample injection and valve 2 controlled the bypassing of the Carbosphere column. (+) denotes filling the sample loop for valve 1 and bypassing the Carbosphere column for valve 2. (–) denotes injecting the contents of the sample loop into the column system for valve 1 and switching the Carbosphere column in series for valve 2.

2.2.1.3 Temperature Program

Using a Carbosphere column allows efficient and fast separation of O_2 and CO_2 at a relatively low temperature (100°C). However, naphthalene and associated products need a higher temperature in order to have acceptable retention times. Therefore the temperature program given in the table below was used.

Table 2.3. Temperature program used for GC runs.

Time (min)	Temperature (°C)	Ramp rate (°C/min)
Initial	100	N/A
12.00	200	50

2.2.1.4 Data Analysis

Two detectors were employed to analyse gas quantity from a given reaction. These were thermal conductivity and flame ionisation detectors (denoted as TCD and FID respectively). Both detectors were fitted inline directly after analyte separation from the column system. Due to the destructive nature of the FID, it was fitted after the TCD. For this project, the TCD was used for detection of O_2 and CO_2 and the FID for hydrocarbon detection.

A TCD is based on thermal conductivity changes of the analyte gas stream compared to a reference flow (usually the gas is the same as the carrier gas within the GC; in this case, He was used). A tungsten wire element at an elevated temperature will undergo changes in its resistance as the thermal conductivity of the surrounding analyte gas changes. This resistance (or a derivative measurement, such as voltage) can be measured at a known electrical power as a function of time to produce a workable plot. The analyte flow does not undergo any chemical change during the detection, so it is free to be analysed by other detectors; in this case, a FID.

A FID is based on combustion to analyse the gas flow; therefore it is the last detector to be used. The analyte is ignited in an oxidative atmosphere, producing ionised analyte and electrons. A current can then be produced if voltage is applied across the burner and electrode. It is this current that is detected. FID is mass sensitive (i.e. the number of C atoms is detected as a function of time) so the analyte flow rate has a small effect on the detector's measurements. The elution times were as follows:

Thermal Conductivity Detector

- O_2. Elution time = 2 min (approx).
- CO_2. Elution time = 9 min (approx).

Flame Ionisation Detector

- *Naphthalene*. Elution time = 14 min (approx).

MFCs were calibrated prior to performing any analyses. This was done by producing a calibration plot of known (unitless) MFC values and the corresponding gas flow this produced. This was produced for both helium and oxygen flows and it was checked and updated if necessary throughout the course of the project.

2.2.1.5 Calculating CO₂ Yields

CO_2 yields were calculated using a reference catalyst that was known to give 100% activity with 100% selectivity at a given temperature. The raw counts that this catalyst gave were averaged over several runs to give a raw count that equalled a 100% yield of CO_2. This raw count was checked and updated (if necessary) periodically due to column aging etc. The relationship for calculating this is thus simple:

$$\frac{\text{Number of raw counts observed}}{\text{Number of raw counts relating to }100\% \text{ } CO_2 \text{ yield}} \times 100$$

The vast majority of the catalytic data presented in this thesis is based on CO_2 production/yields rather than naphthalene consumption. The reason for this is based on reports such as the one published by Zhang *et al.*[13] where naphthalene consumption and CO_2 production did not correlate at lower temperatures. For example, the Pt catalysts reported by Zhang *et al.* catalysed half of the naphthalene available (i.e. the naphthalene consumption was 50%) at 200°C. However, very little CO_2 was measured (a 10% CO_2 yield was reported to occur at 240°C). This suggested that partial oxidation was occurring and GC-MS analysis revealed that several reaction pathways were operating and that there was a number of partial oxidation products produced. Also, it could be assumed that different catalysts will have different adsorption affinities towards naphthalene, i.e. the interaction strength between a catalyst and adsorbed naphthalene varied from catalyst to catalyst. This meant that as Mo and W based catalysts displayed stronger metal-solid interactions (MSIs) than the other catalysts studied, the destruction of the second naphthalene ring could be more difficult compared to a system where the MSIs are weaker. Therefore, the Mo and W catalysts could produce a smaller number of total oxidation products due to the partially decomposed naphthalene remaining adsorbed on the catalyst surface. This could have increased the deficit between high naphthalene consumption and low CO_2 yields.

2.2.2 Propane Oxidation

2.2.2.1 Reactor Schematic

The total oxidation of propane was probed using a similar reactor to that described above for the naphthalene total oxidation reactor. The specific schematic is in figure 2.7 and figure 2.8 is a photograph of the reactor apparatus. The reactor was composed of 0.25 inch O.D. stainless steel tubing heated using a tubular Carbolite furnace. The temperature of the catalyst bed was controlled via a thermocouple placed within the bed. 4000vppm of propane was used in synthetic air (20% O_2 content, He make up gas) with a total flow of 50 mL/min. The reactor flow was analysed using a Varian 3800 GC fitted with inline TCD and FID detectors. The reactor flow components were separated using Hayesep Q (separated hydrocarbons and CO_2) and Molsieve 13X (separated N_2, CO and O_2) packed columns. The activities were tested over a temperature range of 100°C to 550°C.

PROPANE TOTAL OXIDATION REACTOR SCHEMATIC

Figure 2.7. Schematic of apparatus used to probe catalytic activities for the total oxidation of propane. Arrows denote direction of gas flow. Temperatures denote temperature of the respective section of gas line. MFC: mass flow controller.

Figure 2.8. Photograph of the set-up used to investigate the total oxidation of propane.

2.2.2.2 Sample Delivery and Temperature Program

The key point in designing the sample delivery program is that CO_2 can adsorb irreversibly on the Molsieve 13X column (hence causing deactivation). Therefore the Molsieve column needs to be bypassed during the elution of CO_2 to prevent it from entering the column. The following tables show the temperature and valve switching programs used during analysis.

Table 2.4. Sample injection and column switching timing programs for the propane oxidation reactor.

Time (min)	V1 (sample injection)	V2 (column bypass)
Initial	Fill (-)	Series (-)
0.01	Inject (+)	Series (-)
1.00	Inject (+)	Bypass (+)
2.00	Inject (+)	Series (-)
5.00	Inject (+)	Bypass (+)

Table 2.5. Temperature regime for a typical GC run for the propane oxidation reactor.

Step	Temperature (°C)	Rate (°C/min)	Hold time (min)	Total (min)
Initial	50	-	2.50	2.50
1	140	20	0	7.00
2	180	30	0	8.33
3	220	60	4.00	13.00

The following two figures detail the valve configuration for sample injection and bypassing of the Molsieve 13X column. The set-up is very similar to that already described for the naphthalene oxidation reactor above.
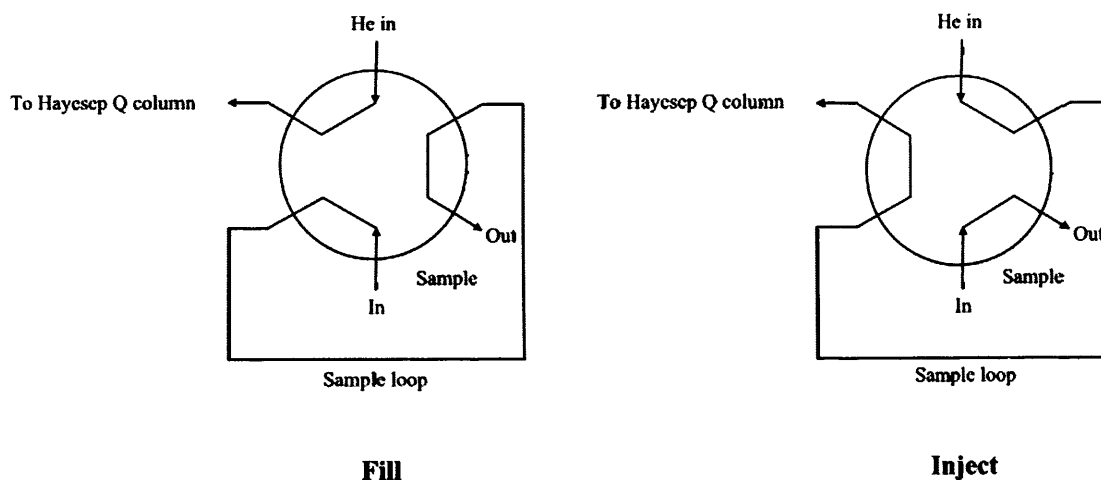
Figure 2.9. Sample injection valve (valve 1) in all possible configurations.
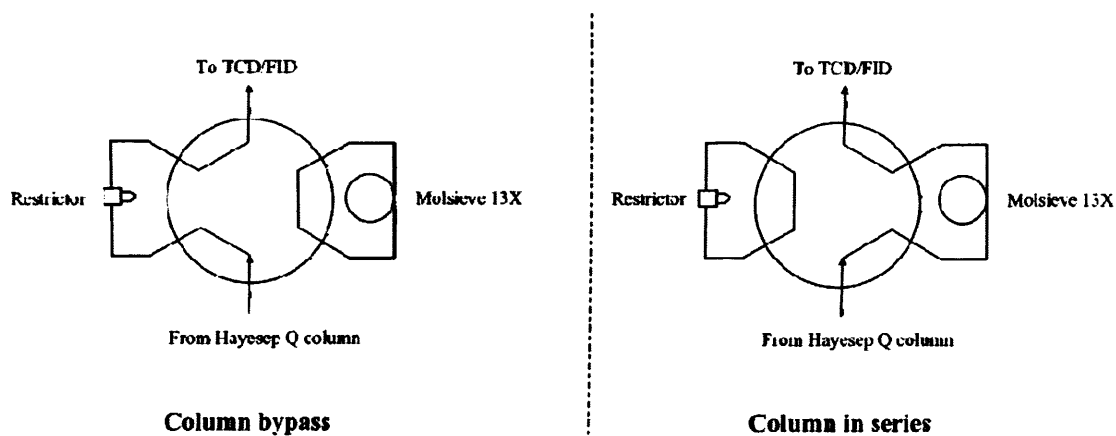
Figure 2.10. Molsieve 13X column bypass control via valve 2.

2.2.2.3 Data Analysis

Prior to performing any analysis, the GC was calibrated for both gas flow and for correlating raw counts (i.e. GC trace peak areas) to percentage CO_2 yields. Gas flow calibration was performed as described in section 2.2.1.4. The latter calibration was performed as described for the naphthalene total oxidation apparatus.

The GC was fitted with a TCD and FID in an identical set-up to that described for the naphthalene oxidation reactor. The elution times were as follows:

40

Thermal Conductivity Detector

- O_2. Elution time = 1 min (approx).

- CO_2. Elution time = 1.5 min (approx).

Flame Ionisation Detector

- *Propane*. Elution time = 6.5 min (approx).

2.3   Characterisation

2.3.1.1 Brunauer, Emmett and Teller (BET) Isotherm for Surface Area Determination

The BET isotherm is considered to be an extension of the Langmuir isotherm, i.e.

$$\theta = \frac{Kp}{1 + Kp} \quad \text{where} \quad K = \frac{k_a}{k_d}$$

The Langmuir isotherm has several assumptions, one being that values of $\theta < 1$ are considered, i.e. it only considers monolayer formation. The BET isotherm improves on this by considering values of $\theta > 1$, i.e. multilayer formation. The BET equation if written to mimic the Langmuir isotherm is:

$$v = \frac{\left(\dfrac{v_m c}{p_0} p \right)}{\left(1 + \dfrac{c}{p_0} p \right)}$$

It can be re-arranged to the following equation in the form of y = m x + c (straight line plot).

41

$$\frac{p}{v(p_0 - p)} = \frac{1}{v_m c} + \left(\frac{c-1}{v_m c}\right)\left(\frac{p}{p_0}\right) \text{ and } c = \exp\left(\frac{E_1 - E_L}{RT}\right)$$

where

p   analyte pressure

v   volume of adsorbed gas

p_0 saturation pressure

v_m molar volume of gas to form a complete monolayer (i.e. $\theta=1$) at STP

E_1 heat of adsorption for monolayer formation

E_L heat of adsorption for multilayer formation (equals to the heat of liquefaction)

R   universal gas constant

T   temperature (in degrees Kelvin)

Hence a plot of $\frac{p}{v(p_0 - p)}$ and $\left(\frac{p}{p_0}\right)$ should yield a straight line graph of intercept

$\frac{1}{v_m c}$ and gradient $\left(\frac{c-1}{v_m c}\right)$. With the value of v_m known, it is possible to calculate the specific surface area using the relationship

$$S = (N)(v_m)(A)$$

where

S   specific surface area

N   Avogadro's number

v_m molar volume of gas to form a complete monolayer (i.e. $\theta=1$) at STP

A   cross sectional area of adsorbent gas ($N_2 = 16\text{Å}^2$)

S can then be divided by the sample mass used in the analysis to normalise surface areas to units of m^2/g. There are five general isotherm forms (type I through to type V) and the BET isotherm is based on either the type II or type III isotherm, dependant on the observed c value[14]. The type II describes a gradual monolayer formation followed by increasing multilayer formation (i.e. the volume of adsorbed gas increases in an

accelerated fashion) with increasing pressure up towards the saturation pressure, p_0. The type II isotherm is the most common observed isotherm.

As the isotherm plots are based on pressure, multilayer formation is infinite as there are an infinite number of multilayers possible for type II and III isotherms.
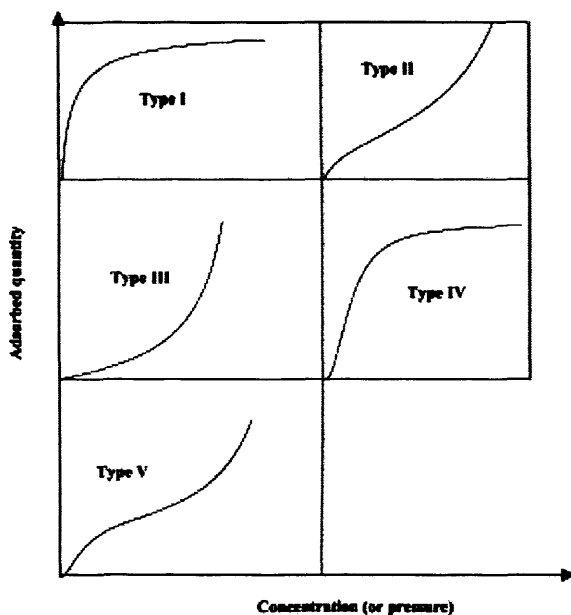
Figure 2.11. The 5 different types of adsorption/desorption isotherm as defined by Brunauer, Emmett and Teller. Taken from reference[15].

2.3.1.2 Experimental Procedure

As the BET isotherm is dependent on knowing the volume of gas adsorbed onto the surface, recording the changes in adsorbate pressure is essential. It is therefore also essential that the active sites on the catalyst are free from contaminants.

Analyses were performed using a Micromeritics Gemini 2360 analyser coupled with a Micromeritics FlowPrep for sample pretreatment. The surface was first cleaned via N_2 flow at 120°C for 45 minutes. A five point analysis was performed for each sample between $\frac{p}{p_0}$ values of 0.05 and 0.35 (as the BET isotherm plot is only linear between these two values[16]). Each data point was obtained using N_2 as the analysis gas (assumed surface area of 16Å^2 per molecule) at -196°C (i.e. the sample was immersed in liquid N_2).

43

2.3.2.1 Chemisorption for Metal Analysis[17]

The principal aim with undertaking chemisorption analysis is to determine the nature of a supported metal in a given catalyst. This includes calculating parameters such as the surface area of the active sites, the percentage dispersion and crystallite size of the investigated metal. All of these calculations can be based on determining the amount of gas required to form one complete chemisorbed monolayer.

The calculations focus on quantifying surface metal atoms. This is essential as the active sites for reaction would be found at the surface rather than in the bulk of the metal particle. Therefore, knowing the character of the active sites would be very useful in explaining the observed catalytic activities.

2.3.2.2 Active Surface Area

The active surface area (ASA) corresponds to the number of metal active sites in a given sample that can interact with the chemisorbing gas. The relationship is as follows

$$\text{Active Surface Area (m}^2/\text{g)} = \frac{(N_m)(S)(A_m)}{166}$$

where

N_m number of gas molecules adsorbed on the surface

S adsorption stoichiometry

A_m active surface atom cross sectional area

The adsorption stoichiometry relates to how many surface atoms are covered by a single chemisorbed gas molecule.

2.3.2.3 Metal Dispersion

The determination of the fraction of active metal atoms that are exposed to the surface can be linked to the active surface area in the following expression:

$$D = \frac{(N_m)(S)(M)}{100L}$$

where

D Metal dispersion, i.e. the percentage of metal atoms in a metal particle that are exposed at the surface

N_m number of gas molecules adsorbed on the surface

S adsorption stoichiometry

M molecular weight of investigated metal

L Metal loading within sample (represented as a percentage of the entire material being investigated)

2.3.2.4 Crystallite Size

It is possible to use the data calculated above to determine the average crystallite size of a given sample of metal particles using the following equation:

$$\text{Average crystallite size} = \frac{100(N)(f)}{(ASA)(Z)}$$

where

N Mass of investigated metal

f Shape correction factor

ASA Active surface area

Z Density of investigated metal

The assumption that crystallites are generally spherical (and hence f=6) can give the crystallite size based on the volume (determined by the mass and density of the metal) and the surface area of the crystallite to give its crystallite size.

2.3.2.5 Experimental Procedure

All chemisoprtion data were obtained using a Quantachrome ChemBET-3000 analyser. The samples were pre-treated in H_2 at either 200°C or 400°C depending on the catalyst's calcination temperature for 1h. The samples were then exposed to 50μL pulses of analyte gas at a specific temperature (or temperature range). The aim of the experiment was to gradually chemisorb the analyte gas onto the active sites over a number of pulses in order to collect as many data points as possible. The concentration of analyte gas that was not chemisorbed was analysed using a thermal conductivity detector. It was from this TCD profile that the required characterisation parameters were obtained.

For Pt and Pd, CO was used as the chemisorption gas at room temperature following pretreatment in H_2 for 1 hour at an elevated temperature[18] (defined in the text as necessary).

2.3.3.1 Raman Spectroscopy

When a sample is irradiated with electromagnetic radiation, photons can be emitted. This is termed emission spectroscopy. When the rotation-vibration character of a molecule is irradiated, Raman emission occurs[19].

Not all molecules are Raman active; there are some selection rules which must be followed. For example, a molecule must possess no centres of symmetry in order to have Raman active modes. Raman active species must also have a changeable polarisability.

When a molecule is irradiated, the interaction and the consequent scattering can be put into one of two groups; elastic and inelastic scattering.

If the scattering is elastic, then the kinetic energy of the scattered photon is of a similar energy to the incident radiation (hence the frequencies are similar). This phenomenon is termed Rayleigh scattering. In terms of virtual energy states, it can be considered as excitation to a higher virtual energy level from the ground state followed by relaxation back to the ground state. This is described in figure 2.12.

If the scattering is inelastic, then a more significant change in the kinetic energy of the scattered photon occurs. If the molecule loses energy (hence the scattered photon gains kinetic energy) then anti-Stokes frequencies are observed. If the opposite applies

(the molecule gains energy, the scattered photon loses kinetic energy) then Stokes frequencies are observed. These are also described in figure 2.12.

Excited state

V=1

V=0

Raylcigh   Stokes   Anti-Stokes
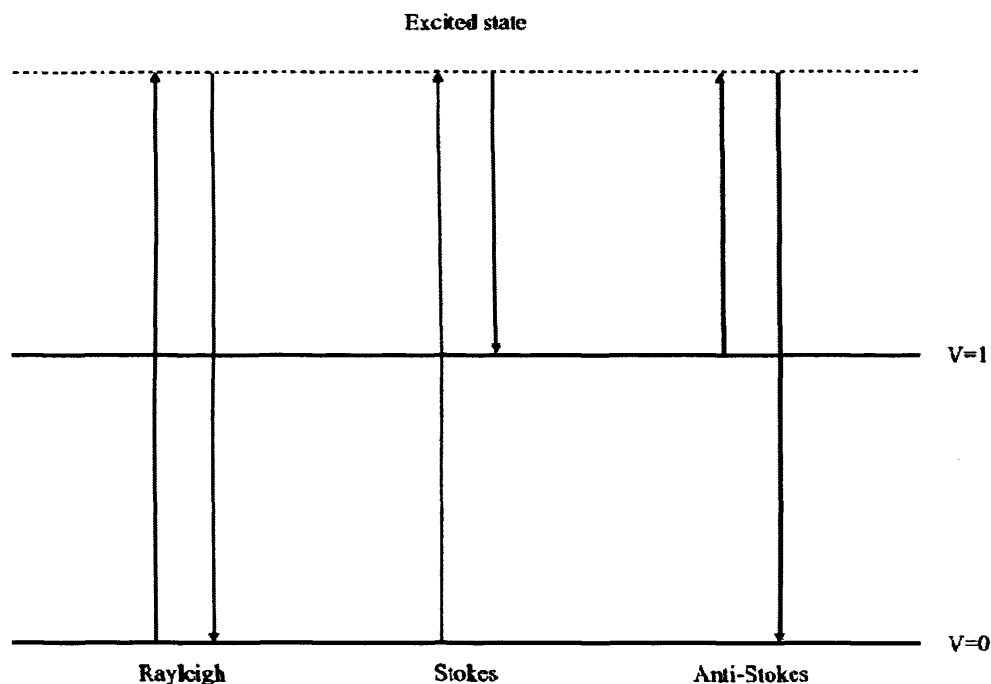
Figure 2.12. Pictorial representation of excitation and relaxation of molecular energy states possible during Raman scattering.

Lasers are the most common source of incident radiation. The two main reasons for this are

- a high intensity light source is required due to the amount of scattering being very low

- a highly monochromatic light source is required as the change in incident to scattered light frequencies can be small.

2.3.3.2 Experimental Procedure

Raman spectra were obtained using a Renishaw Ramascope fitted with a Spectraphysics argon ion laser (λ=514nm) at a power of 20mW. An Olympus BH2-UMA microscope was used for laser focussing. Sample mass was unimportant.

2.3.4.1 Scanning Electron Microscopy (SEM) and Backscattered Electron Detection (BSD)

SEM involves the irradiation of a sample with an electron beam in order to produce a topographical image. This can be used to identify morphological changes for example between fresh and used catalysts.

Images are produced by using an electron beam with a diameter on the nanoscale. This electron beam can interact with surface atoms and several effects can be observed, depending on the strength of the electron beam. Some of these effects will be discussed below.

Common electron beam sources are tungsten or LaB_6 cathodes. When the electron beam interacts with the sample, scattering occurs immediately below the surface, known as the interaction volume, which is teardrop shaped. The size of the interaction volume depends on factors such as electron acceleration voltage. These scattered electrons then travel from the interaction volume to the detector, where they are recorded.

When the electron beam interacts with the sample, the scattering can be elastic or inelastic. Elastic scattering involves changes in beam trajectory with a negligible loss in beam energy. High atomic number elements when irradiated with relatively low energy electron beams give rise to elastic scattering[20].

Inelastic scattering involves a noticeable loss in kinetic energy as well as a change in trajectory. Several inelastic scatterings can occur, but two of these are of particular interest; secondary electron emission and core electron ejection.

Secondary electron emission occurs via conduction electron excitation, or the ejection of conduction band electrons which are loosely bound. These can be used to produce a topographical image using higher energy electron beams than normally used in SEM imaging. Core electron ejection provides the basis for energy dispersive X-ray analysis which is described in the next section.
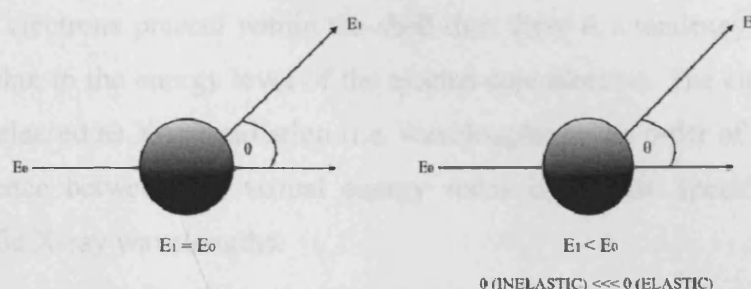
Figure 2.13. Elastic (left) and inelastic (right) scattering models.

2.3.4.2 Back Scattered Electron (BSE) Imaging

Back scattered electrons are a product of elastic scattering of the incident electron beam within the interaction volume of the analysed sample. Elemental distribution can be determined via BSEs. This is due to a given element's atomic (Z) number. A higher number means that the concentration of BSEs can be higher compared to an element with a lower atomic number. This manifests itself on an image as bright spots in the case of higher Z number elements.

2.3.4.3 Energy Dispersive X-ray (EDX) Analysis

EDX analysis allows for elemental composition of a solid mixture and can be used to identify if a solid solution has discrete elemental regions. However, the identification of the area of these discrete regions would be limited by the resolution of the SEM, i.e. regions only a few nanometres in size would not be identifiable using the equipment available.

Another related application of EDX is that quantification of the elements present is possible. Therefore, this analysis could be used to investigate if a given catalyst prepared with a desired atomic ratio (or impregnated metal loading) does possess this atomic ratio/metal loading.

Elements are identified by analysing the wavelengths of the X-rays generated when atoms are struck by high energy electron beams. Each element has a specific wavelength or set of wavelengths attributed to it due each element having specific

49

differences between the core and higher energy electron energies. When an atom is irradiated with an electron beam, a core electron is ejected from the atom. If there are higher energy electrons present within the shell then there is a tendency for one of these electrons to relax to the energy level of the ejected core electron. The energy lost by this relaxation is released as X-ray radiation (i.e. wavelengths of the order of $x10^{-10}$m). As the energy difference between the virtual energy states is element specific, this leads to element specific X-ray wavelengths.

2.3.4.4 Experimental Procedure

Images were obtained using a Carl Zeiss EVO 40 scanning electron microscope fitted with backscattered and secondary electron detectors. For image collection using these detectors, variable working distances and probe currents were used. An EHT of 25KeV was used for all sample imaging. All samples were mounted on carbon Leit adhesive discs.

For EDX analysis, the same microscope was used. However, the working distance was fixed at 9mm. An EHT value of 25KeV was used. High probe currents (up to 25nA) were required in order for X-ray production to occur. The data was collected using an Oxford EDX analyser coupled to the EVO 40 SEM.

2.3.5.1 Temperature Programmed Reduction (TPR)

In a temperature programmed reduction experiment, the analysed sample's propensity to undergo reduction is measured as a function of temperature. Obviously, the sample must be reducible in order for one to follow its reduction. It is of course, possible to follow the opposite of this; the oxidation of a reduced sample as a function of temperature; temperature programmed oxidation (TPO).

In physical terms, the oxide is reduced by flowing reducing gas (e.g. a H_2/inert gas mixture) while systematically increasing the temperature of the sample. The initial concentration of the reducing gas is known before the start of the experiment and any subsequent decrease in this concentration is monitored during the temperature increase. Thus, a plot of reducing gas concentration as a function of temperature can be produced. A relatively large uptake of reducing gas by the sample at a given temperature indicates

that the sample is easily reducible at that temperature. This information can then be correlated with catalytic activity data in order to explain any observations for the activity of a given catalyst (e.g. light-off temperature).

2.3.5.2 Experimental Procedure

A Thermo TPDRO1100 was used to obtain the temperature programmed reductions presented in this text (unless otherwise stated). Samples were first pre-treated in flowing Ar (a flow of 20mL/min was used) at 110°C for 45 minutes with a heating ramp of 20°C/min. For experiments, a temperature range of ambient to 700°C was used unless otherwise stated. A 10% H_2/Ar flow of 13mL/min was used with a heating ramp of 5°C/min. Approximately 100 - 110mg of catalyst was used per analysis.

2.3.6.1 Powder X-ray Diffraction (XRD)

XRD is a bulk sensitive technique where the crystal structure of a given material is analysed. A crystalline material is considered to be made up of a regular arrangement of atoms ordered in such a way to form planes as described in figure 2.14.
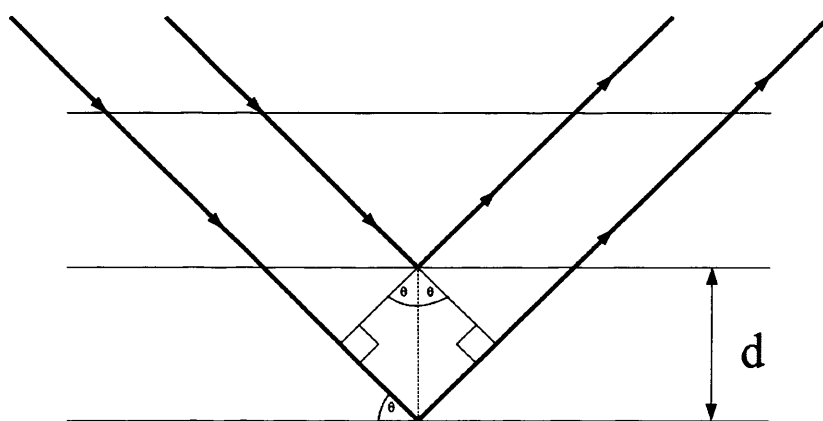
Figure 2.14. Reflection of X-rays in a crystalline solid as defined by Bragg's Law

If electromagnetic radiation interacts with a crystalline substance, then reflection of the incident light occurs. Using monochromatic X-rays, it is possible to have

constructive and destructive interference of the reflected X-rays if reflections of X-rays on more than one plane are considered. Constructive interference occurs if the wavelengths of the reflected radiation have a difference of an integer number. Constructive interference results in a signal, hence a response, being detected. The angle of the monochromatic radiation and the crystal plane and the wavelength of the monochromatic radiation are related by Bragg's Law;

$$n\lambda = 2d\sin\theta$$

where

n   order of reflection, an integer number of path length differences between two different rays in terms of complete wavelengths

λ wavelength of incident X-ray radiation

d   inter planar spacing

θ angle of diffraction between incident and scattered radiation (usually plotted as 2θ)

By observing the ratio of constructive to destructive interference as a function of the angle of the radiation to the crystal plane, it is possible to create a pattern of the amount of constructive interference as a function of angle. The patterns produced are unique to the material; hence it is possible to build a database to use as a reference.

2.3.6.2 Crystallite Size Determination via the Scherrer Method[21]

The crystallite size of a given phase within a material can be quantified using the Debye-Scherrer equation given below.

$$\beta_k = \frac{k\lambda}{d_{hkl}\cos\theta}$$

where

β_k peak width where $\beta_k = B_{obs} - B_{std}$

B_{obs} overall peak width

B_{std} instrument line broadening component

k   shape factor (e.g. cubic structures have a value of 0.899)

λ wavelength of radiation used

d_{hkl} crystallite size

θ peak position

The Scherrer equation relies on the phenomena of peak broadening as a function of the observed crystallite size, i.e. broad peaks give rise to smaller crystallites. However, the method does have its limitations. The FWHM of broad peaks (hence smaller crystallites) can sometimes be difficult to accurately quantify as it is more difficult to determine where the investigated peak begins and finishes, especially if the pattern has a relatively low signal to noise ratio (SNR). Also, as uniform crystallites are considered, there is an upper and lower limit on the crystallite sizes that the method can accurately determine.

Both the instrument and the lattice strain within the crystalline system contribute to line broadening along with the crystallite size. The effect of instrument broadening can be quantified by use of a crystalline silicon standard which contains no lattice strain and a large crystallite size (hence the resultant peak width is due only to instrument broadening).

The lattice strain contribution to line broadening was calculated using the following algorithm

$$\text{Lattice strain} = \frac{B}{4\tan\theta}$$

where

$$B = \sqrt{(B_{obs}^{2} - B_{std}^{2})}$$

θ peak position

B_{obs} overall peak width

B_{std} instrument line broadening component

2.3.6.3 Experimental Procedure

Patterns were obtained using a PANalytical X'pert Pro diffractometer equipped with a Cu Kα X-ray source. An analysis tension of 40kV and current of 40mA were used for all analyses. Runs were performed between angles of $10 - 80°2\theta$ unless otherwise specified in the text. The resultant patterns were compared against reference patterns contained in the JCPDS database.

Crystallite sizes were also calculated using the same software package used for running the diffractometer mentioned above. A highly crystalline reference silicon sample was used to calculate peak broadening values. Hence a reference FWHM value of $0.0925°2\theta$ was used for all calculations.

2.3.7.1 X-ray Photoelectron Spectroscopy (XPS)

The principal aim of XPS analysis is the identification of metal oxidation states on the surface of a material and their resultant energy levels. To do this, atoms are irradiated with monochromatic X-rays producing weak electron ejection. The kinetic energy of these ejected electrons can be measured to give the binding energy of an electron in a given atomic orbital of a given element. The relationship is described as

$$E_{BINDNG} = E_{X-RAY} - E_{KINETIC}$$

where

E_{BINDNG} binding energy

E_{X-RAY} energy of incident X-ray photon

$E_{KINETIC}$ kinetic energy of emitted electron

Each binding energy (and hence the kinetic energy of an electron) is characteristic of a given atom. As most elements contain several electron shells, there can be a set of characteristic binding energies for one given element.

As with energy dispersive X-ray (EDX) analysis discussed earlier in this chapter, X-ray irradiation can cause vacancies in core electron shells. This allows a higher energy electron to relax to this core energy level and the excess energy needs to be released. This can be released as an X-ray (as in EDX analysis) or transfer of the energy to another electron in the same atom can occur. This can cause the electron to be ejected if the transferred energy exceeds the binding energy of that electron. This second ejected electron is known as an Auger electron and the detection of this second electron is the basis of Auger Electron Spectroscopy (AES).

2.3.7.2 Experimental Procedure

Spectra were obtained using a Kratos Axis Ultra DLD photoelectron spectrometer fitted with a monochromatic Al source (photon energy = 1486.6eV). Pass energies of 40eV (high resolution scans) and 160eV (survey spectra) were used over an analysis area of 700x300 microns. All spectra were calibrated to C (1s) of adventitious carbon (binding energy = 284.7eV).

2.4 References

1. G. J. Hutchings, J. A. Lopez-Sanchez, J. K. Bartley, J. M. Webster, A. Burrows, C. J. Kiely, A. F. Carley, C. Rhodes, M. Hävecker, A. Knop-Gericke, R. W. Mayer, R. Schlögl, J. C. Volta, M. Poliakoff, *Journal of Catalysis*, **208**, (2002), 197–210.

2. J. F. Chen, H. M. Ding, J. X. Wang, L. Shao, *Biomaterials*, **25**, (2004), 723–727.

3. J. F. Chen, Y. H. Wang, F. Guo, X. M. Wang, C. Zheng, *Industrial & Engineering Chemistry Research*, **39**, (2000), 948-954.

4. I. Kurzina, F. J. Cadete Santos Aires, G. Bergeret, J. C. Bertolini, *Chemical Engineering Journal*, **107**, (2005), 45–53.

5. G. Garcia Cervantes, F. J. Cadete Santos Aires, J. C. Bertolini, *Journal of Catalysis*, **214**, (2003), 26–32.

6. F. Monnet, Y. Schuurman, F. Cadete Santos Aires, J. C. Bertolini, C. Mirodatos, *Catalysis Today*, **64**, (2001), 51–58.

7. *Handbook of Chemistry and Physics*, 77th Edn., CRC Press, 1996, 6-157.

8. *Handbook of Chemistry and Physics*, 77th Edn., CRC Press, 1996, 6-166.

9. S. Wang, X. Ma, J. Gong, X. Yang, H. Guo, G. Xu, *Industrial & Engineering Chemistry Research*, **43**, (2004), 4027-4030.

10. A. Aranda, J. M. Lopez, R. Murillo, A. M. Mastral, A. Dejoz, I. Vazquez, B. Solsona, S. H. Taylor, T. Garcia, *Journal of Hazardous Materials*, **171**, (2009), 393-399.

11. T. Garcia, B. Solsona, D. Cazorla-Amoros, A. Linares-Solano, S. H. Taylor, *Applied Catalysis B-Environmental*, **62**, (2006), 66-76.

12. T. Garcia, B. Solsona, S. H. Taylor, *Applied Catalysis B-Environmental*, **66**, (2006), 92-99.

13. X. W. Zhang, S. C. Shen, L. E. Yu, S. Kawi, K. Hidajat, K. Y. S. Ng, *Applied Catalysis A: General*, **250**, (2003), 341–352.

14. M. Khalfaoui, S. Knani, M. Hachicha, A. Ben Lamine, *Journal of Colloid and Interface Science*, **263**, (2003), 350-356.

15. C. Tien, *Adsorption Calculations and Modeling (Butterworth-Heinemann Series in Chemical Engineering)*, Butterworth–Heinemann, 1994.

16.   S. Brunauer, P. Emmett, E. Teller, *Journal of the American Chemical Society*, **60**, (1938), 309-319.

17.   Quantachrome Instruments, *Autosorb-1 Operating Manual*, Quantachrome Instruments, 2006.

18.   British Standards Institute, *BS 4359-4:1995. Determination of the specific surface area of powders. Recommendations for methods of determination of metal surface area using gas adsorption techniques*, British Standards Institute, 1995.

19.   D. A. Skoog, D. M. West, F. J. Holler, *Fundamentals of Analytical Chemistry*, Seventh Edn., Saunders College Publishing, 1996.

20.   R. D. Evans, *The Atomic Nucleus*, McGraw-Hill New York, 1955.

21.   K. Bobzin, E. Lugscheider, M. Maes, P. Immich, S. Bolz, *Thin Solid Films*, **515**, (2007), 3681-3684.

Chapter 3 – CeZrO$_2$ Catalysts for Naphthalene Total Oxidation

3.1   Introduction

One of the main features of CeO$_2$ that benefits catalytic activity is that it is an efficient store of oxygen and that its surface is easily reducible[1]. In the literature, there are examples of cerium zirconium dioxide catalysts which are a more efficient store of oxygen than CeO$_2$[2]. The focus of this study is to ascertain whether this can be applied to catalysts for the total oxidation of naphthalene.

Here, varying Ce:Zr ratios will be investigated using the preparation methods described in Chapter 2. The first preparation method (co-precipitation using urea with (NH$_4$)$_2$Ce(NO$_3$)$_6$ as the cerium source, denoted NH$_4$-U) has been previously reported to be effective[3] for the production of active CeO$_2$ catalysts for the total oxidation of naphthalene.

Another preparation method was also employed for comparative purposes. This involved the use of sodium carbonate as the precipitating agent and is denoted NH$_4$-C. The same theoretical Ce:Zr ratios were prepared for all preparation methods.

The effect of preparing CeZrO$_2$ via precipitation using supercritical CO$_2$ as a solvent was also investigated. Due to the length of time required to obtain sufficient quantities of sample, only one CeZrO$_2$ ratio (Ce99Zr1) was investigated and compared against the carbonate and urea precipitated catalysts. This was done to ascertain whether observations made elsewhere[4] comparing urea precipitated and supercritically precipitated CeO$_2$ agreed with those made in this study.

3.2   Catalytic Activity

3.2.1   Catalyst Comparison

Figure 3.1 (below) shows the activity data obtained for the NH$_4$-U series of catalysts. Here, one of the most active catalysts is Ce99Zr1 (i.e. a Ce:Zr molar ratio of 99:1). The majority of the catalysts seemed to experience mass transport limitations, which may have limited activity at higher temperatures. There was no clear trend observed between Ce:Zr ratio and activity. Pure ZrO$_2$ showed no catalytic activity. Higher Zr content catalysts

(Ce50Zr50) appeared to be less active than CeO_2. All other $CeZrO_2$ catalysts were found to be more active than CeO_2.

Activity Data - NH₄-U Series
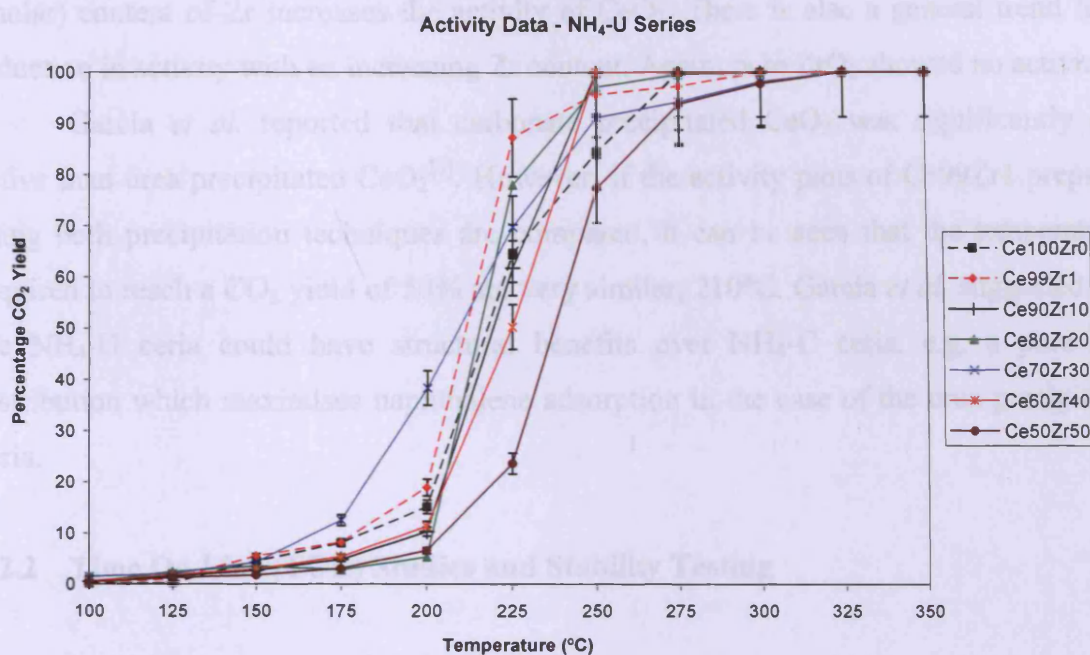
Figure 3.1. NH₄-U CeZrO₂ catalytic activities for the total oxidation of naphthalene. Temperature range: 100 – 350°C. GHSV = 135,000h⁻¹, 100vppm naphthalene, total flow = 50mL/min. Numbers in the legend refer to Ce:Zr atomic weight ratios. Error bars are ± 6.7%.

Activity Data - NH₄-C Series
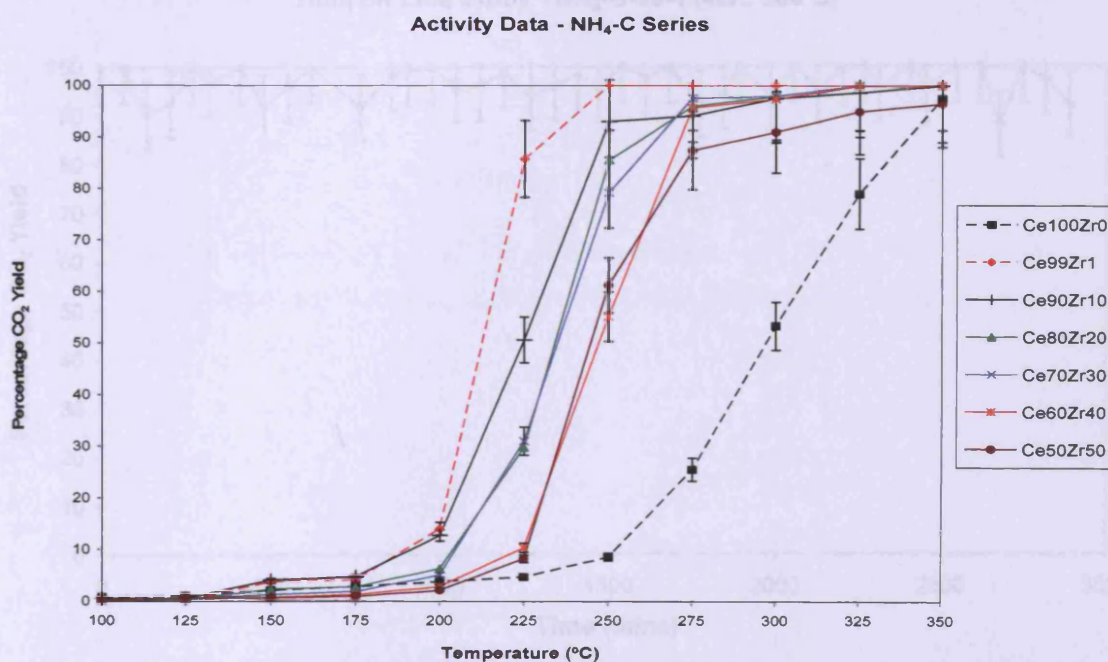
Figure 3.2. NH₄-C CeZrO₂ catalytic activities for the total oxidation of naphthalene. Temperature range: 100 – 350°C. GHSV = 135,000h⁻¹, 100vppm naphthalene, total flow = 50mL/min. Numbers in the legend refer to Ce:Zr atomic weight ratios. Error bars are ± 6.7%.

59

Figure 3.2 displays the catalytic activities of the same Ce:Zr ratio catalysts prepared using sodium carbonate as the precipitating agent (i.e. the NH_4-C series). A 1% (molar) content of Zr increases the activity of CeO_2. There is also a general trend for a reduction in activity with an increasing Zr content. Again, pure ZrO_2 showed no activity.

Garcia *et al.* reported that carbonate precipitated CeO_2 was significantly less active than urea precipitated CeO_2[3]. However, if the activity plots of Ce99Zr1 prepared using both precipitation techniques are compared, it can be seen that the temperatures required to reach a CO_2 yield of 50% are very similar; 210°C. Garcia *et al.* suggested that the NH_4-U ceria could have structural benefits over NH_4-C ceria, e.g. a pore size distribution which maximises naphthalene adsorption in the case of the urea precipitated ceria.

3.2.2 Time On Line (TOL) Studies and Stability Testing

The Ce99Zr1 catalyst prepared using both precipitating agents were subjected to a TOL study for 48h at 300°C. The results for the NH_4-U series are presented in figure 3.3.

Time on Line Study - NH₄-U-99-1 (48h, 300°C)

Figure 3.3. TOL study for NH_4-U Ce99Zr1 for the total oxidation of naphthalene over a 48h period at 300°C. GHSV = 135,000h⁻¹, 100vppm naphthalene, total flow = 50mL/min. Error bars are ± 6.7%.

Here, it can be seen that a negligible decrease in activity occurs over the 48 hour testing period. If the catalyst is subjected to three LOT (light off temperature) analyses it can be seen (in figure 3.4) that the light off curve temperature range has a negligible change. This behaviour has been reported to occur for CeO_2 prepared in the same way[3], so this resilience could be expected. In a LOT analysis, the sample is heated through the light off curve temperature range then cooled. The same sample is then taken through the same LOT temperature range again to see if any decrease in activity is observed for a given temperature. This can be repeated as often as necessary.
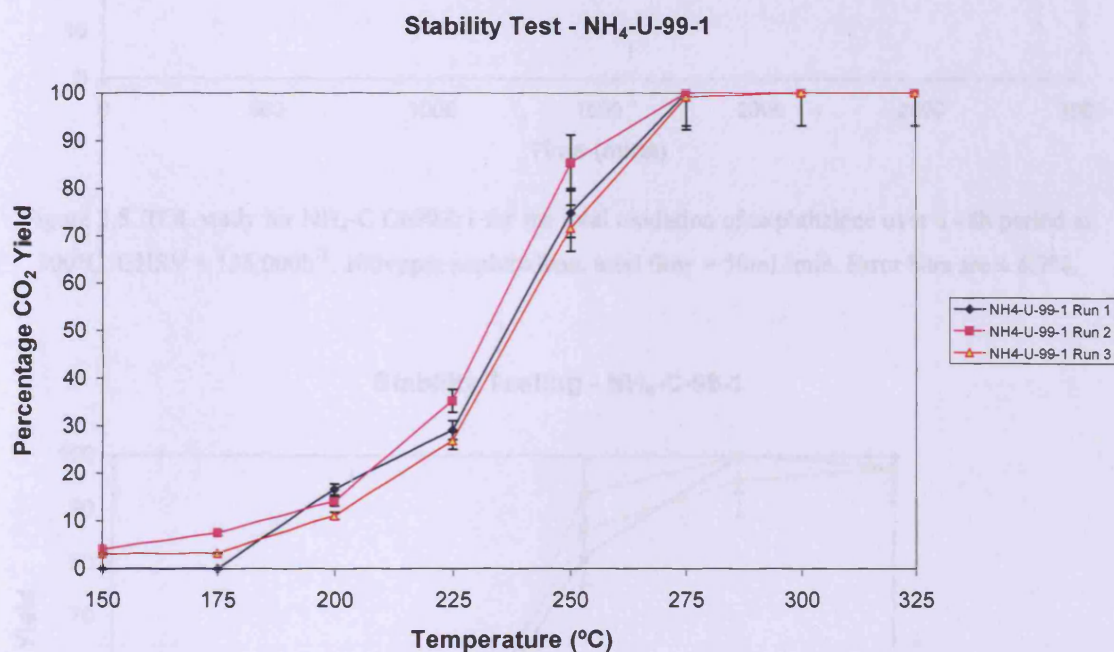
Figure 3.4. LOT study for NH_4-U Ce99Zr1. Temperature range: 150 – 325°C. GHSV = 135,000h⁻¹, 100vppm naphthalene, total flow = 50mL/min. Error bars are ± 6.7%.

Time on Line Study - NH$_4$-C-99-1 (48h, 300°C)
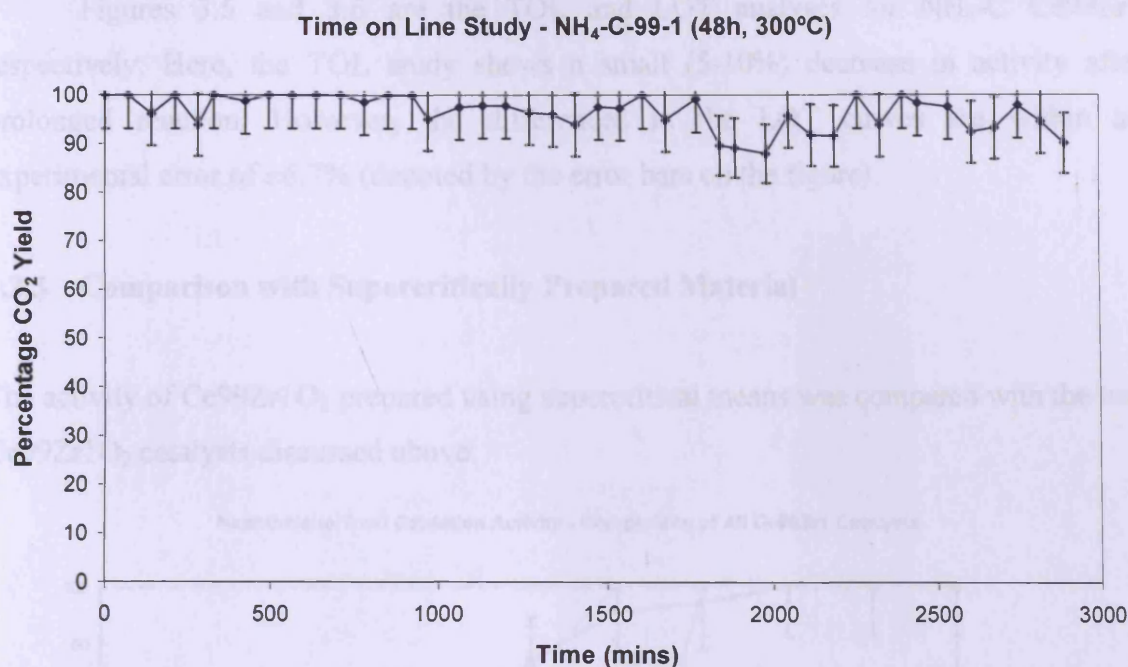
Figure 3.5. TOL study for NH$_4$-C Ce99Zr1 for the total oxidation of naphthalene over a 48h period at 300°C. GHSV = 135,000h^{-1}, 100vppm naphthalene, total flow = 50mL/min. Error bars are ± 6.7%.

Stability Testing - NH$_4$-C-99-1

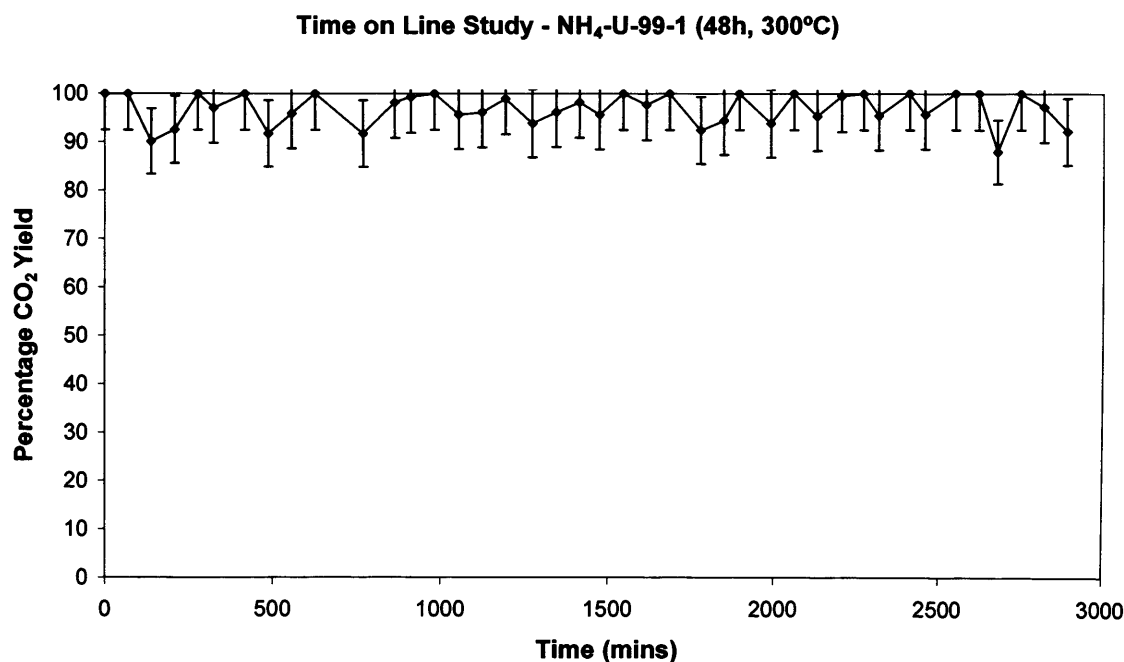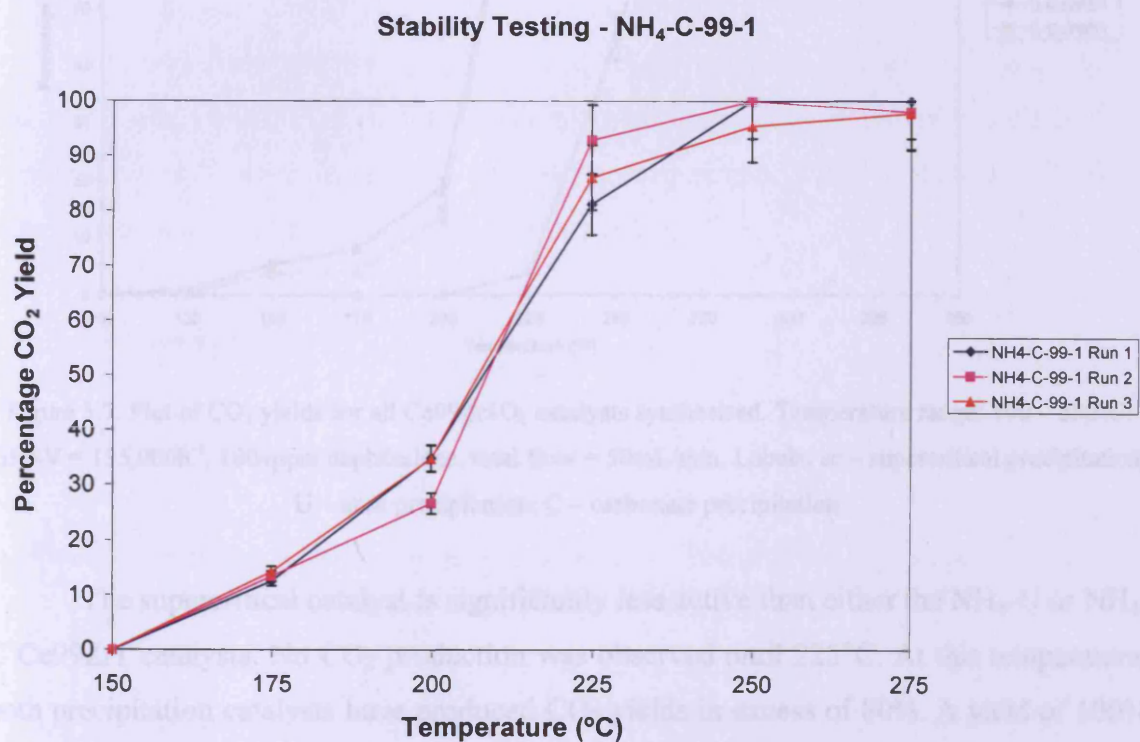Figure 3.6. LOT study for NH$_4$-C Ce99Zr1. Temperature range: 150 – 275°C. GHSV = 135,000h^{-1}, 100vppm naphthalene, total flow = 50mL/min. Error bars are ± 6.7%.

Figures 3.5 and 3.6 are the TOL and LOT analyses for NH$_4$-C Ce99Zr1 respectively. Here, the TOL study shows a small (5-10%) decrease in activity after prolonged reaction. However, the differences in the LOT curves are within an experimental error of ±6.7% (denoted by the error bars on the figure).

3.2.3 Comparison with Supercritically Prepared Material

The activity of Ce99Zr1O$_2$ prepared using supercritical means was compared with the two Ce99Zr1O$_2$ catalysts discussed above.

Naphthalene Total Oxidation Activity - Comparison of All Ce99Zr1 Catalysts
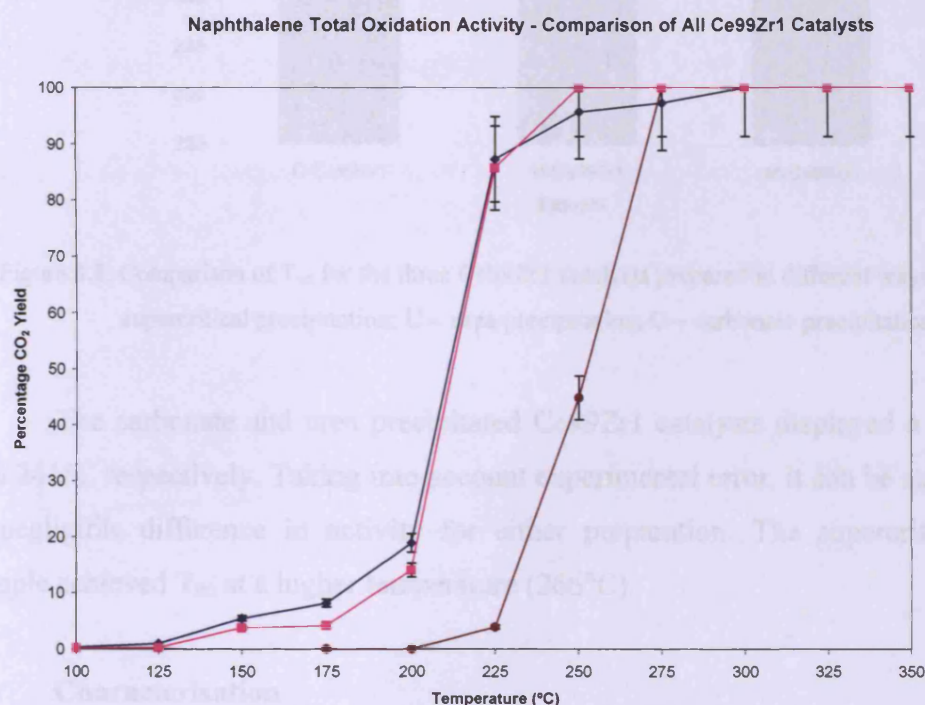
Figure 3.7. Plot of CO$_2$ yields for all Ce99Zr1O$_2$ catalysts synthesised. Temperature range: 100 – 350°C. GHSV = 135,000h^{-1}, 100vppm naphthalene, total flow = 50mL/min. Labels: sc – supercritical precipitation; U – urea precipitation; C – carbonate precipitation.

The supercritical catalyst is significantly less active than either the NH$_4$-U or NH$_4$-C Ce99Zr1 catalysts. No CO$_2$ production was observed until 225°C. At this temperature, both precipitation catalysts have produced CO$_2$ yields in excess of 80%. A yield of 100% was achieved at 275°C for the supercritical catalyst. The NH$_4$-U and NH$_4$-C precipitation catalysts displayed 100% CO$_2$ yields at 250°C. The carbonate precipitation catalyst is as active as the urea precipitated catalyst. This contradicts what has been previously reported for CeO$_2$ catalysts for naphthalene total oxidation[3]. As the following figure shows, the

temperature at which a 90% CO_2 yield is required (termed T_{90}) was similar for the NH_4-U and NH_4-C catalysts.

Temperature Required for 90% CO₂ Yield - Ce99Zr1
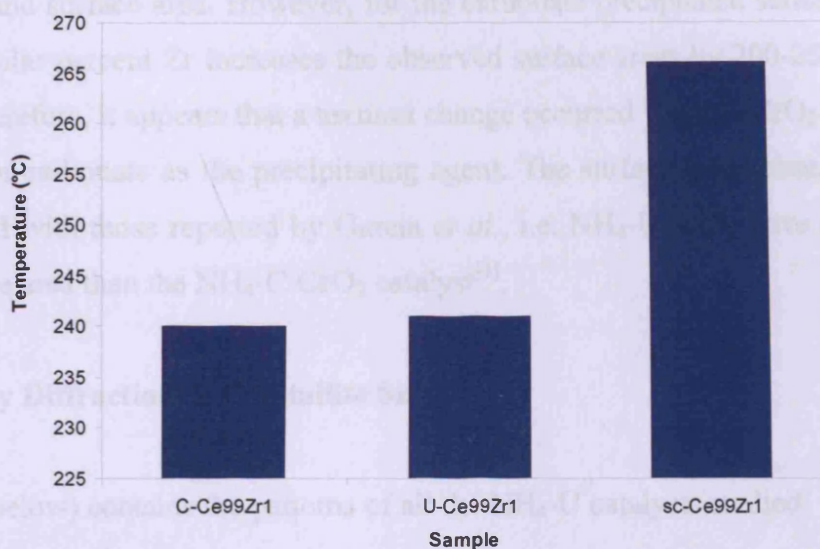
Figure 3.8. Comparison of T_{90} for the three Ce99Zr1 catalysts prepared in different ways. Labels: sc - supercritical precipitation; U – urea precipitation; C – carbonate precipitation.

The carbonate and urea precipitated Ce99Zr1 catalysts displayed a T_{90} of 240°C and 241°C respectively. Taking into account experimental error, it can be stated that there is negligible difference in activity for either preparation. The supercritical Ce99Zr1 sample achieved T_{90} at a higher temperature (266°C).

3.3   Characterisation

3.3.1   Surface Area Analysis

Table 3.1. Surface areas of the two $CeZrO_2$ catalyst series. Determined by N_2 adsorption at 77K.

Sample	Surface Area (m^2/g) (NH_4-U)	Surface Area (m^2/g) (NH_4-C)
Ce50Zr50	111	131
Ce60Zr40	134	148
Ce70Zr30	104	127
Ce80Zr20	142	112
Ce90Zr10	135	125
Ce99Zr1	117	144
CeO₂	123	56

64

Table 3.1 shows the surface areas obtained for both of the preparation series investigated. For the urea precipitated series, it is apparent that the variance of the Ce:Zr ratio does not have a clear effect on the observed surface areas, or that there is a correlation between Ce:Zr ratio and surface area. However, for the carbonate precipitated series, the addition of even 1 molar percent Zr increases the observed surface areas by 200-250% compared to CeO_2. Therefore, it appears that a textural change occurred when $CeZrO_2$ was produced using sodium carbonate as the precipitating agent. The surface areas observed for CeO_2 corresponded with those reported by Garcia *et al.*, i.e. NH_4-U CeO_2 gave a significantly larger surface area than the NH_4-C CeO_2 catalyst[3].

3.3.2   X-ray Diffraction & Crystallite Size

Figure 3.9 (below) contains the patterns of all the NH_4-U catalysts studied.
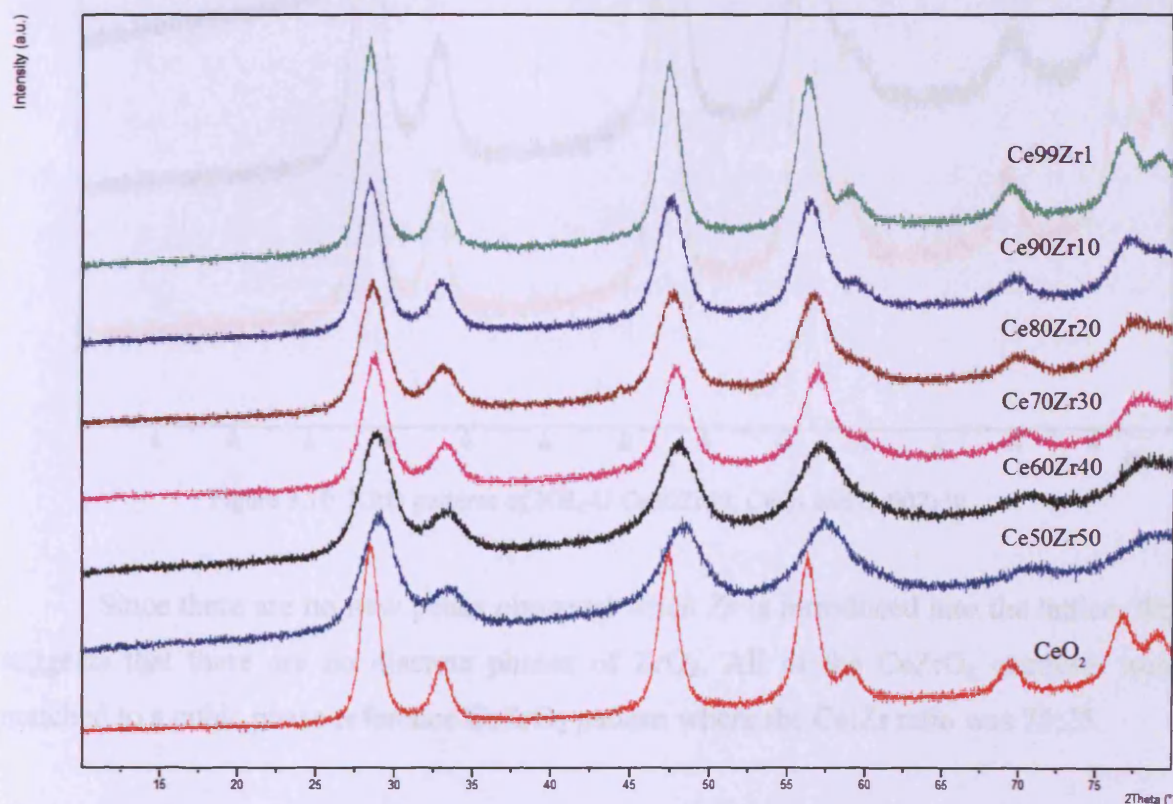
Figure 3.9. XRD patterns obtained for all NH_4-U catalysts.

The patterns for the cerium zirconium oxide catalysts appear similar. As the Zr content increased, the resulting peak positions shifted to higher angles. A loss in crystallinity was also observed when Zr content was increased.

A second peak at approximately 57°2θ can be clearly seen for higher Ce loadings. When the Zr content was increased, this peak was not observed in the resulting patterns. This suggests that the lattice was modified, i.e. Zr is being incorporated into the CeO$_2$ lattice. This is shown in the following figure.
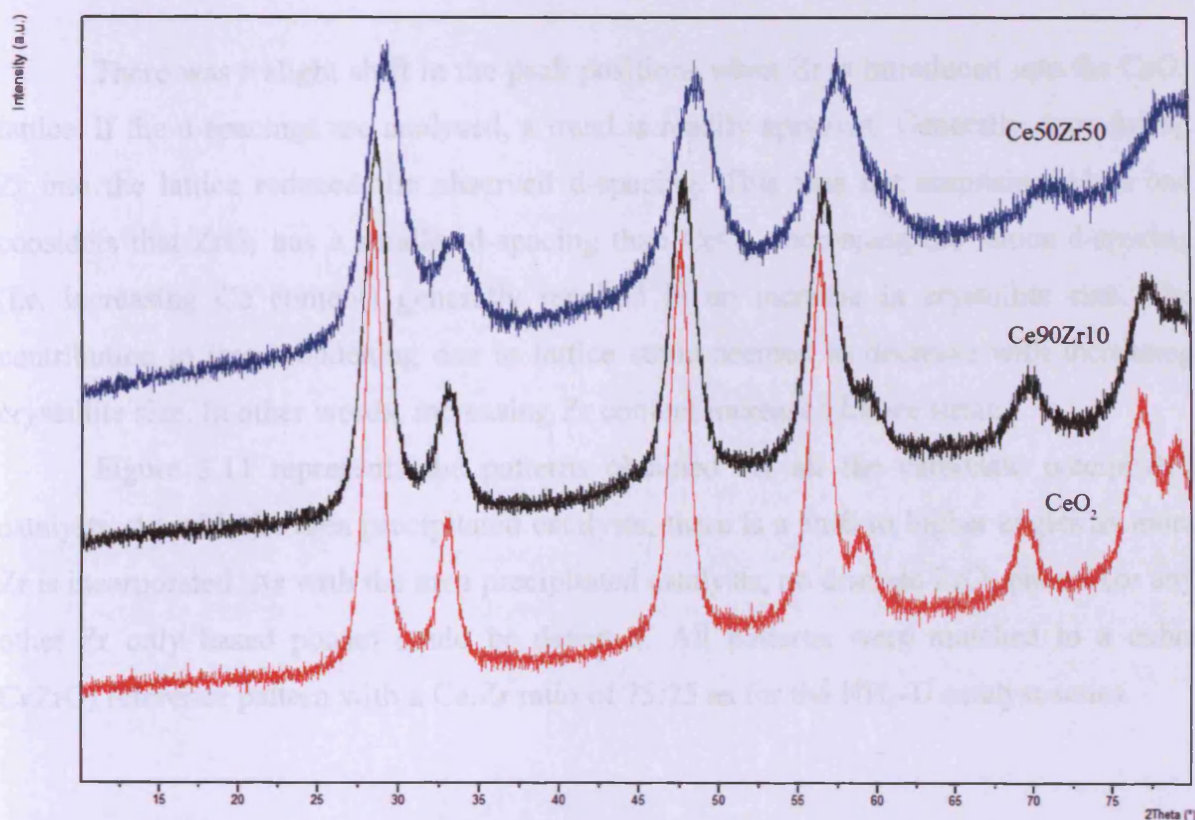
Figure 3.10. XRD patterns of NH$_4$-U Ce50Zr50, CeO$_2$ and Ce90Zr10.

Since there are no new peaks observed when Zr is introduced into the lattice, this suggests that there are no discrete phases of ZrO$_2$. All of the CeZrO$_2$ catalysts were matched to a cubic phase reference CeZrO$_2$ pattern where the Ce:Zr ratio was 75:25.

Table 3.2. Crystallite size, lattice strain and d-spacing data for all NH₄-U catalysts studied using the Scherrer method. All readings were taken from a peak with 100% relative intensity.

Sample	Crystallite size (Å)	Lattice strain (%)	d-spacing (Å)
Ce50Zr50	23	6.260	3.05981
Ce60Zr40	35	4.119	3.08234
Ce70Zr30	60	2.460	3.09844
Ce80Zr20	50	2.943	3.10805
Ce90Zr10	55	2.698	3.11962
Ce99Zr1	68	2.229	3.12416
CeO₂	74	2.056	3.12954

There was a slight shift in the peak positions when Zr is introduced into the CeO₂ lattice. If the d-spacings are analysed, a trend is readily apparent. Generally, introducing Zr into the lattice reduced the observed d-spacing. This was not surprising when one considers that ZrO₂ has a smaller d-spacing than CeO₂. Increasing the lattice d-spacing (i.e. increasing Ce content) generally resulted in an increase in crystallite size. The contribution to line broadening due to lattice strain seemed to decrease with increasing crystallite size. In other words, increasing Zr content increased lattice strain.

Figure 3.11 represents the patterns obtained for all the carbonate precipitated catalysts. As with the urea precipitated catalysts, there is a shift to higher angles as more Zr is incorporated. As with the urea precipitated catalysts, no discrete ZrO₂ phases (or any other Zr only based phase) could be detected. All patterns were matched to a cubic CeZrO₂ reference pattern with a Ce:Zr ratio of 75:25 as for the NH₄-U catalyst series.
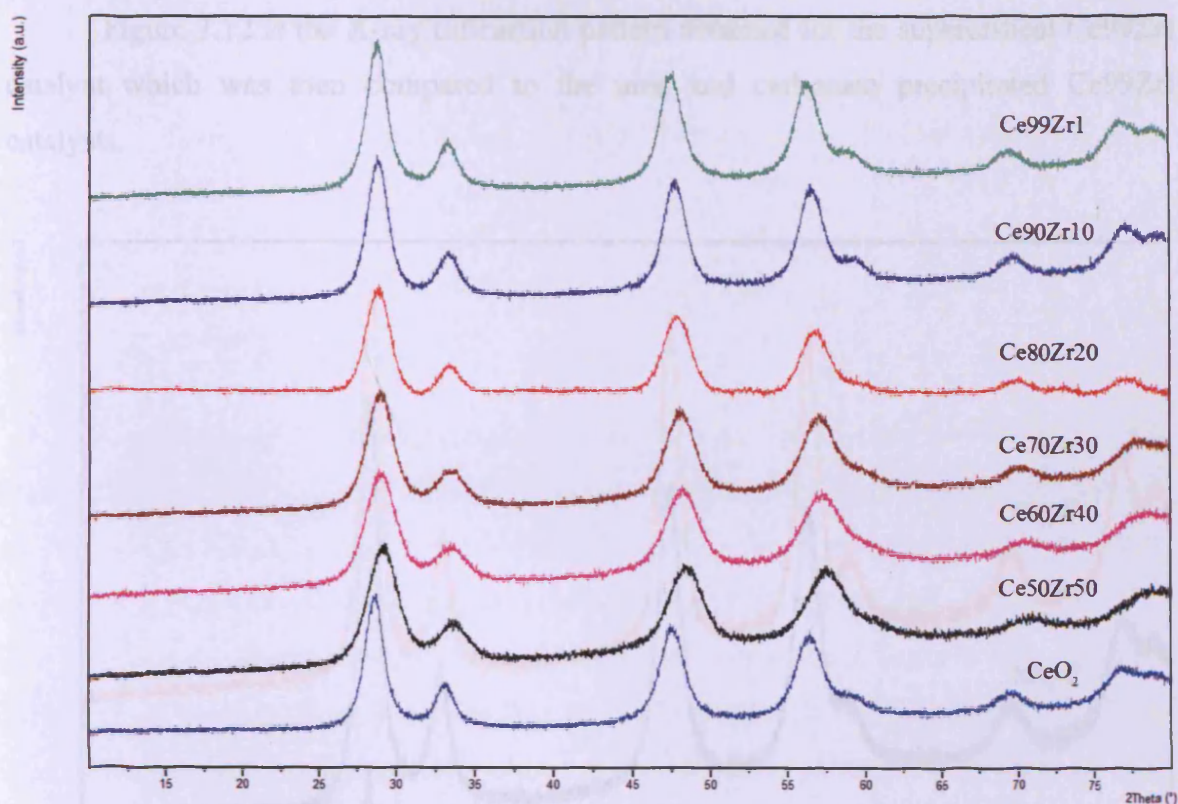
Figure 3.11. XRD patterns for carbonate precipitated CeZrO$_2$ (NH$_4$-C) catalysts.

If the d spacing of each catalyst is analysed as before, it is apparent that the same trend applies to the NH$_4$-C catalysts as it did to the NH$_4$-U catalysts. In other words, increasing Zr content caused a decrease in the observed d spacing. The NH$_4$-C catalysts also exhibited the same trends as the NH$_4$-U catalysts with regards to crystallite size and lattice strain.

Table 3.3. Lattice strains and d-spacing data for all CeZrO$_2$ NH$_4$-C catalysts. Lattice strains were calculated using the Scherrer method and a Si reference pattern.

Catalyst	Crystallite size (Å)	Lattice strain (%)	D spacing (Å)
Ce50Zr50	44	3.267	3.07325
Ce60Zr40	44	3.345	3.08826
Ce70Zr30	47	3.088	3.09612
Ce80Zr20	69	2.182	3.10497
Ce90Zr10	62	2.412	3.12112
Ce99Zr1	62	2.433	3.13150
CeO$_2$	65	2.330	3.12851

Figure 3.12 is the X-ray diffraction pattern obtained for the supercritical Ce99Zr1 catalyst which was then compared to the urea and carbonate precipitated Ce99Zr1 catalysts.
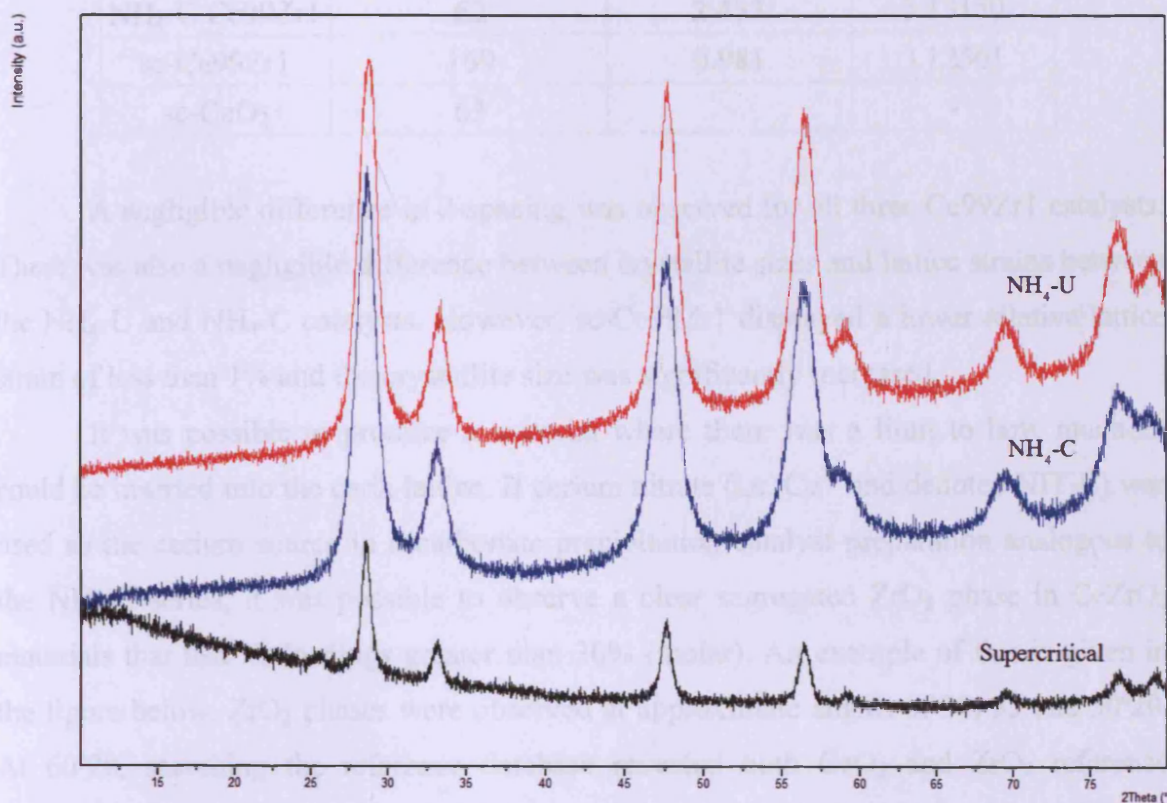
Figure 3.12. XRD patterns of Ce99Zr1 prepared supercritically and via precipitation using ammonium Ce^{4+} nitrate.

Matching the sc-Ce99Zr1 pattern with the reference database revealed a match for the same $CeZrO_2$ reference pattern as reported for the NH₄-U and NH₄-C series (i.e. cubic phase). No separate ZrO_2 reflections could be observed. However, this is not surprising as the Zr content is very low (1 molar percent), therefore any detection would be extremely difficult.

A d-spacing of 3.12561Å was observed at the most intense reflection at 28°2θ for sc-Ce99Zr1. Table 3.4 compares the XRD characteristics for NH₄-U, NH₄-C and sc-Ce99Zr1.

Table 3.4. Lattice strain and d-spacing data for sc, NH₄-U and NH₄-C Ce99Zr1. sc-CeO₂ crystallite size taken from reference[4].

Sample	Crystallite size (Å)	Lattice strain (%)	D spacing (Å)
NH₄-U	68	2.229	3.12416
NH₄-C Ce99Zr1	62	2.433	3.13150
sc-Ce99Zr1	169	0.981	3.12561
sc-CeO₂	63	-	-

A negligible difference in d-spacing was observed for all three Ce99Zr1 catalysts. There was also a negligible difference between crystallite sizes and lattice strains between the NH₄-U and NH₄-C catalysts. However, sc-Ce99Zr1 displayed a lower relative lattice strain of less than 1% and the crystallite size was significantly increased.

It was possible to produce a material where there was a limit to how much Zr could be inserted into the ceria lattice. If cerium nitrate (i.e. Ce^{3+} and denoted NIT-C) was used as the cerium source in a carbonate precipitation catalyst preparation analogous to the NH₄-C series, it was possible to observe a clear segregated ZrO_2 phase in $CeZrO_2$ materials that had Zr loadings greater than 30% (molar). An example of this is given in the figure below. ZrO_2 phases were observed at approximate angles of 30, 35 and 50°2θ. At 60°2θ, searching the reference database revealed both CeO_2 and ZrO_2 reference patterns with a reflection at this angle. Both phases were cubic. This reflection could also be matched with a reference $CeZrO_2$ pattern. Again, this was a cubic phase.
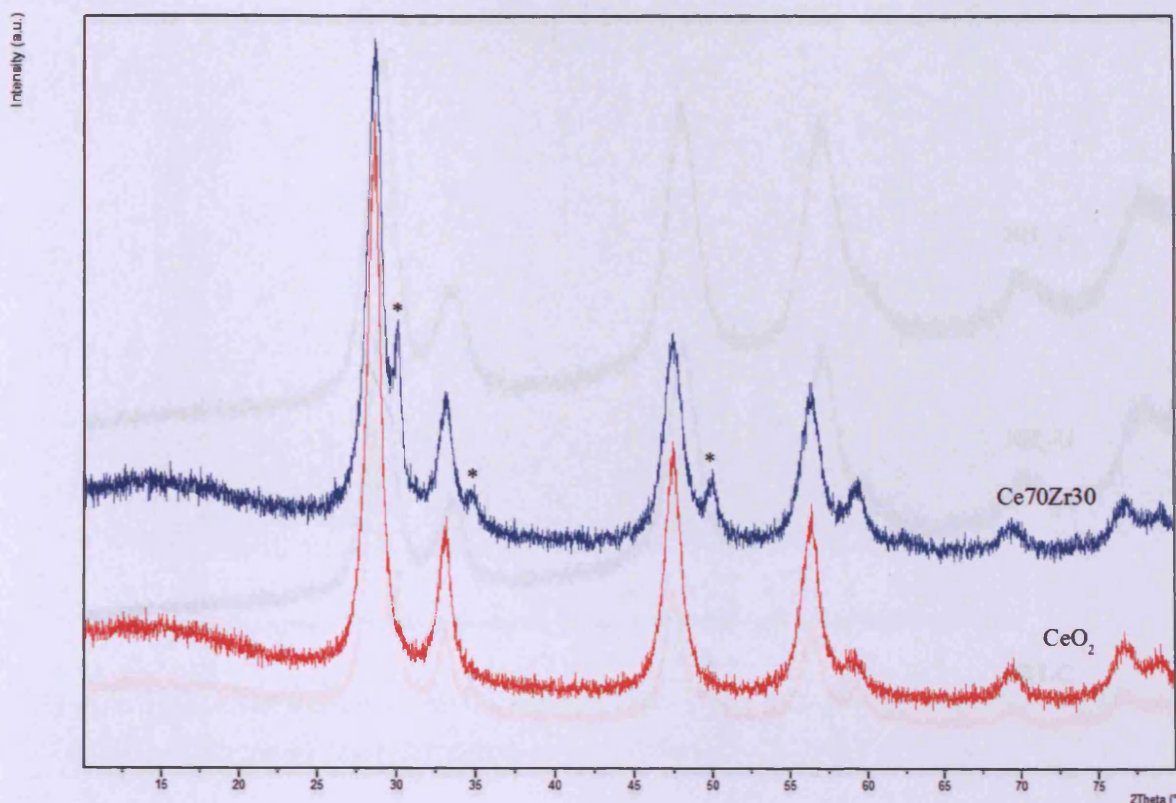
Figure 3.13. Comparison of Ce70Zr30 and CeO$_2$ prepared using carbonate precipitation and Ce^{3+} nitrate as the Ce source. * denotes cubic ZrO$_2$ phase.

Figure 3.14 is a comparison of Ce70Zr30 prepared via carbonate precipitation using both Ce^{3+} nitrate and ammonium Ce^{4+} nitrate (NIT-C and NH$_4$-C series respectively) and also prepared via urea precipitation (NH$_4$-U) . It is clear from figure 3.14 that the segregated ZrO$_2$ cubic phase occurs only for the NIT-C series. It should be noted that pure ZrO$_2$ displayed no catalytic activity for the total oxidation of naphthalene, therefore oxidation would be unlikely to occur on the separate ZrO$_2$ phase.
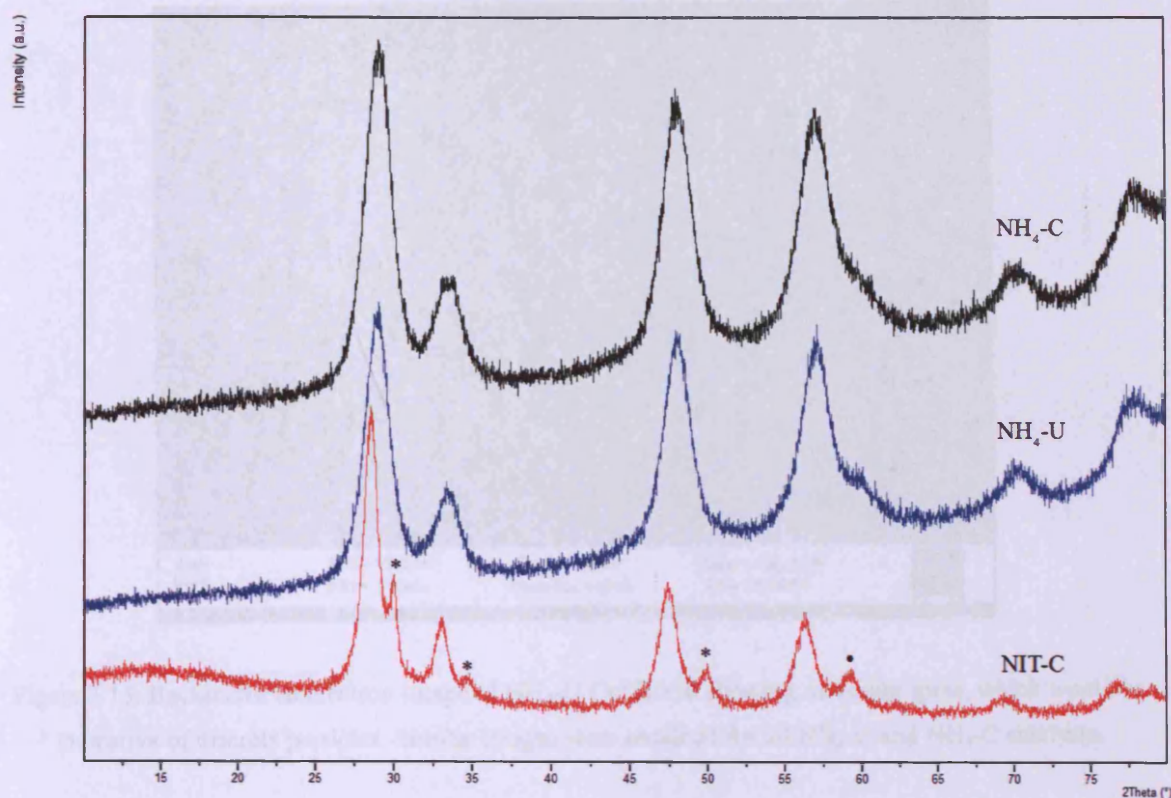
Figure 3.14. XRD patterns of Ce70Zr30 of all three precipitation series (NH₄-U, NH₄-C and NIT-C). * denotes segregated cubic ZrO₂ phase. • denotes reflection which was matched to both cubic ZrO₂ and cubic CeO₂.

3.3.3 Scanning Electron Microscopy/Energy Dispersive X-ray Analysis

The BSD (backscattered electron detection) method was used to see if Ce and Zr exist as discrete particles or if there is a more homogeneous mixture of the two. Due to cerium's larger atomic mass, Ce particles would appear as relatively bright spots.

Figure 3.15 is representative of what was observed for all CeZrO₂ catalysts; no bright spots (therefore no discrete particles) were observed, which agrees with the observations made with during the XRD pattern analysis earlier in this text.
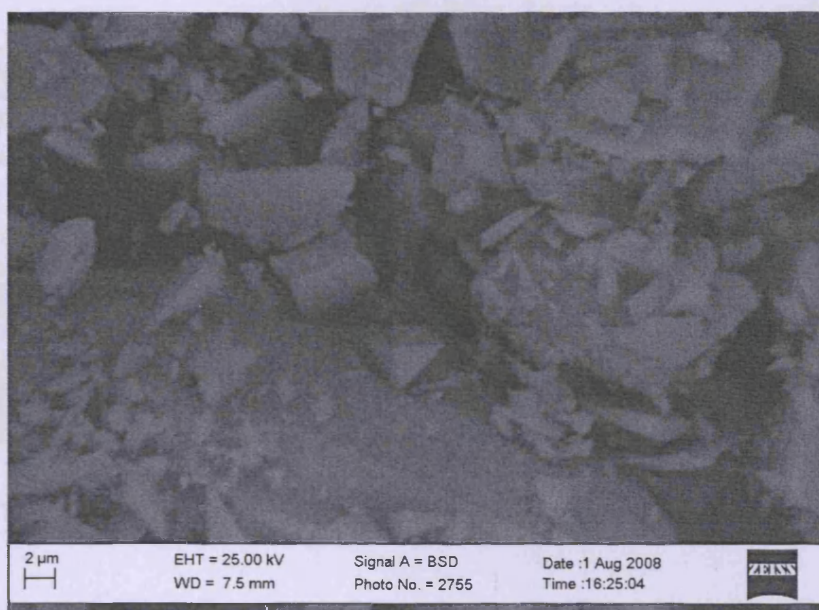
Figure 3.15. Backscattered electron image of NH$_4$-U Ce50Zr50 showing no bright spots, which would be indicative of discrete particles. Similar images were obtained for all NH$_4$-U and NH$_4$-C catalysts.

The most active catalyst (Ce99Zr1) from each series was imaged in both its fresh and used forms in order to try and explain the loss in activity after extended use. These images are shown in the following two figures.
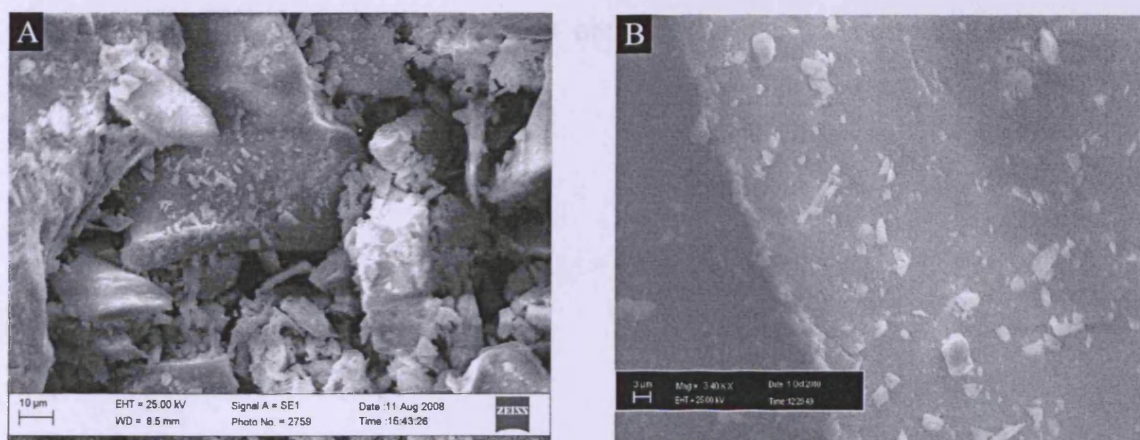
Figure 3.16. NH$_4$-U 99-1 catalyst before (A) and after use (B) for the total oxidation of naphthalene.

If the images obtained for fresh and used NH$_4$-U 99-1 CeZrO$_2$ are compared, it can be seen that a change has taken place. Some of the defects on the surface have disappeared/decomposed.
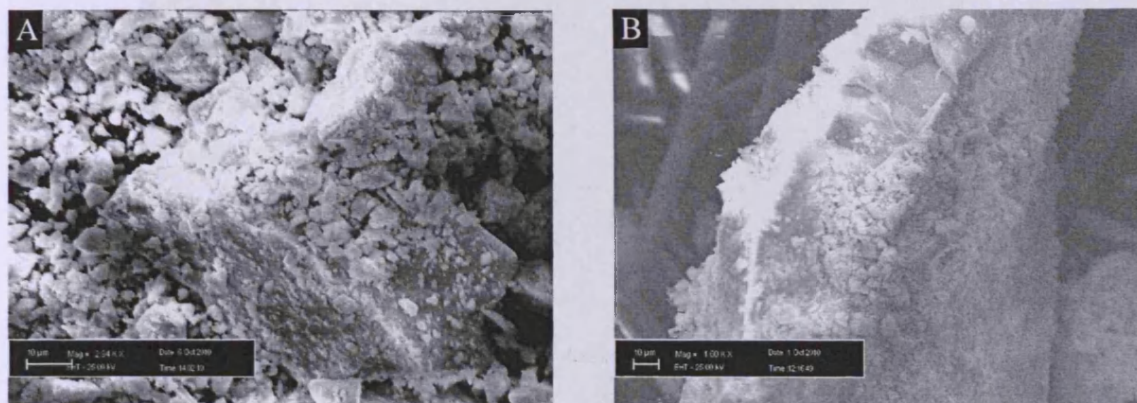
Figure 3.17. NH$_4$-C 99-1 catalyst before (A) and after (B) use for the total oxidation of naphthalene.

If the two used Ce99Zr1 catalysts are compared, it can be seen that there is a greater degree of agglomeration in the case of the NH$_4$-C catalyst. The used NH$_4$-C also appeared to undergo no real morphological change compared to its fresh counterpart. There may be a small degree of agglomeration after using the catalyst for reaction. This sort of observation has been made previously for carbonate precipitated ceria. The urea precipitated ceria analogue underwent a morphological change. A change of this sort was noticeable, but not to the same degree as reported in the literature. In other words, the observations made by Garcia *et al.* were replicated to a degree in this study.

Figure 3.18 represents the images obtained for the supercritical Ce99Zr1 after calcination but prior to reaction.
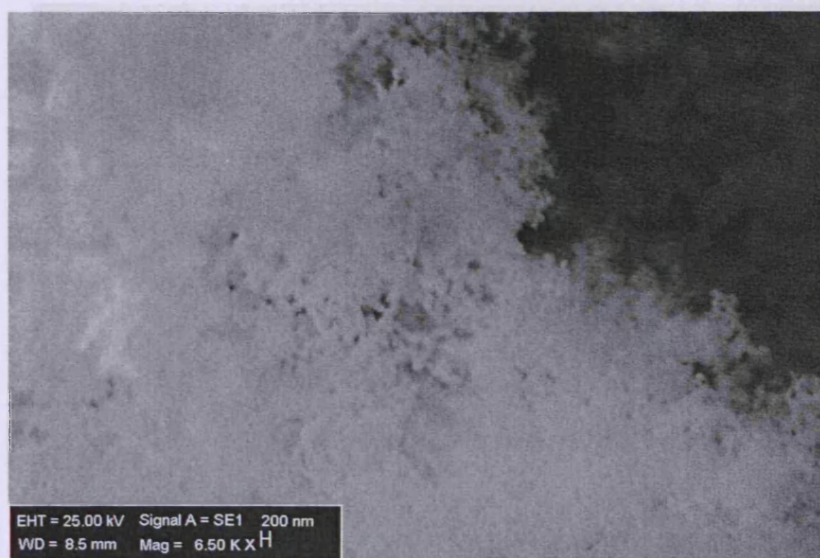
Figure 3.18. SEM image obtained for calcined sc-Ce99Zr1 prior to being used in reaction.

The image clearly shows a different morphology compared to the urea or carbonate precipitated $CeZrO_2$. The supercritical preparation afforded a morphology that is coral-like. There was little point in analysing the sample (via BSE imaging) for discrete Ce and Zr based phases as there was a minimal amount of Zr present (1 molar percent).

As the following figure shows, it can be seen that the morphology had changed after use in the reactor in a similar way to that reported previously for carbonate precipitated ceria[3]. Agglomeration of the previous coral like particles occurred during reaction. However, this agglomeration was not complete as figure 3.20 shows.

Figure 3.19. SEM image of sc-Ce99Zr1 after being used for the total oxidation of naphthalene.
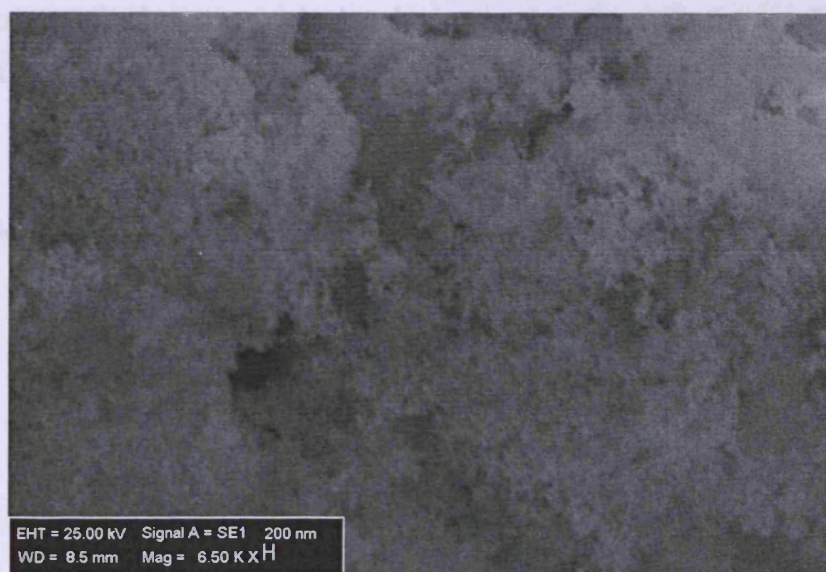
Figure 3.20. A second SEM image of used sc-Ce99Zr1 showing the previous morphology before reaction.

This image was taken from a second particle of the catalyst batch that was used in the same oxidation experiment as figure 3.19. There is a negligible difference between the morphology shown in figure 3.20 and the morphology observed in the unused sample.

Due to the amount of sample available, it was not possible to test multiple reaction experiments on the same catalyst batch to determine whether this change in morphology

has a positive or negative effect on activity over a long time period or through repeated reaction cycles (as performed in chapter 3.2).

EDX analysis was employed to determine the catalysts' Ce:Zr ratios and compare them against the theoretical ratios. Table 3.5 shows the EDX data for the NH_4-U series.

Table 3.5. Ce, Zr and O ratios of all NH_4-U $CeZrO_2$ catalysts tested with the calculated Ce:Zr ratios.

Sample	Ce:Zr ratio (atomic %)
Ce50Zr50	42:58
Ce60Zr40	59:41
Ce70Zr30	74:26
Ce80Zr20	85:15
Ce90Zr10	93:7
Ce99Zr1	99.7:0.3

As the table shows, the Zr loadings are slightly less than intended, particularly for lower Zr loadings, with one exception. However an error of approximately ±5% can be attributed to the Ce:Zr ratios calculated above, therefore all the catalysts with the exception of Ce50Zr50 have a Ce:Zr loading ratio within this error. The following table contains the Ce:Zr ratio data obtained for the NH_4-C series of catalysts.

Table 3.6. EDX data obtained for all NH_4-C $CeZrO_2$ catalysts investigated in this study.

Sample	Ce:Zr ratio (atomic %)
Ce50Zr50	61:39
Ce60Zr40	67:33
Ce70Zr30	77:23
Ce80Zr20	83:17
Ce90Zr10	92:8
Ce99Zr1	99:1

As with the NH_4-U series, the Zr loadings were found to be generally less than the intended amounts. The data presented in the above tables will need to be compared with the x-ray photoelectron spectroscopy (XPS) data at a later point in this chapter.

Table 3.7. Atomic weight percentages of the Ce:Zr ratio determined by EDX analysis for all Ce99Zr1 catalysts investigated in this study.

Sample	Ce:Zr ratio (atomic %)
NH_4-U Ce99Zr1	99.7:0.3
NH_4-C Ce99Zr1	99.3:0.7
sc-Ce99Zr1	99.3:0.7

As the above table shows, the Ce:Zr ratio is similar for sc-Ce99Zr1 as it is for the other two series, i.e. a fraction of 1% was observed for the Zr loading. This therefore suggests that the Zr was inserted into the ceria lattice as intended during the catalyst preparation regardless of the specific technique.

3.3.4 Temperature Programmed Reduction
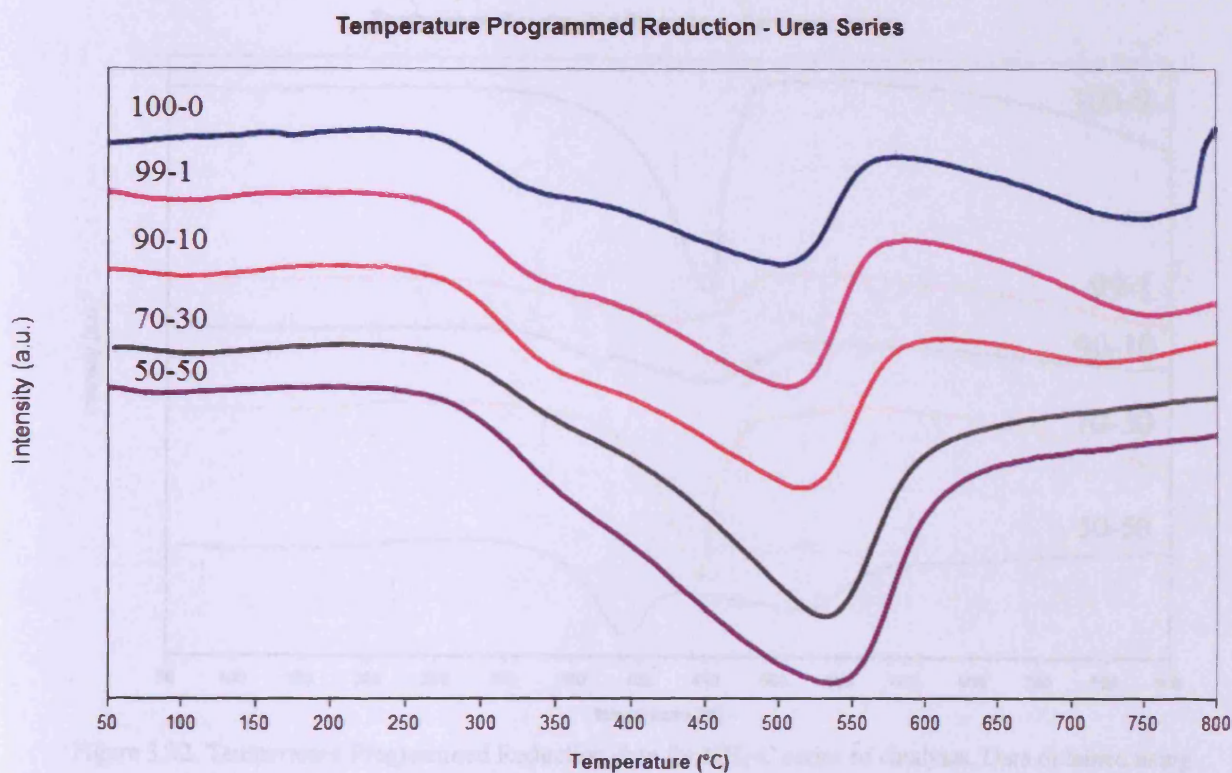
Figure 3.21. Temperature Programmed Reduction data for NH₄-U series of catalysts. Data obtained using Micromeritics Autochem II, 10% H_2/Ar at 50mL/min, temperature range of RT – 850°C studied. Sample mass – *ca*. 100mg per run.

The TPR profiles for the NH₄-U series of catalysts show two general trends. Firstly, the incorporation of Zr caused an increase in the amount of H_2 take-up as peak intensity for all $CeZrO_2$ catalysts were higher than that observed for CeO_2. Secondly, increasing Zr content caused an increase in the temperature required for maximum reduction, i.e. the maxima of the reduction peak shifted to higher temperatures. This implied that increasing the Zr content caused the ease of reducibility within the catalyst to decrease. However, the quantity of H_2 take-up appeared to increase with increasing Zr incorporation. One of the

most active catalysts, Ce99Zr1, displayed one of the lowest temperature when reducibility was at its peak (505°C) of all the CeZrO$_2$ catalysts. However, the peak intensity was one of the smaller intensities observed.

The reduction peaks at higher temperatures (in excess of 700°C) were due to reduction of the bulk ceria[5], which explains why the higher Zr content catalysts (Ce70Zr30 and Ce50Zr50) did not display this reduction peak and why the Ce99Zr1 catalyst experienced a greater quantity of H$_2$ uptake compared to the Ce90Zr10 catalyst.

Temperature Programmed Reduction - Carbonate Series
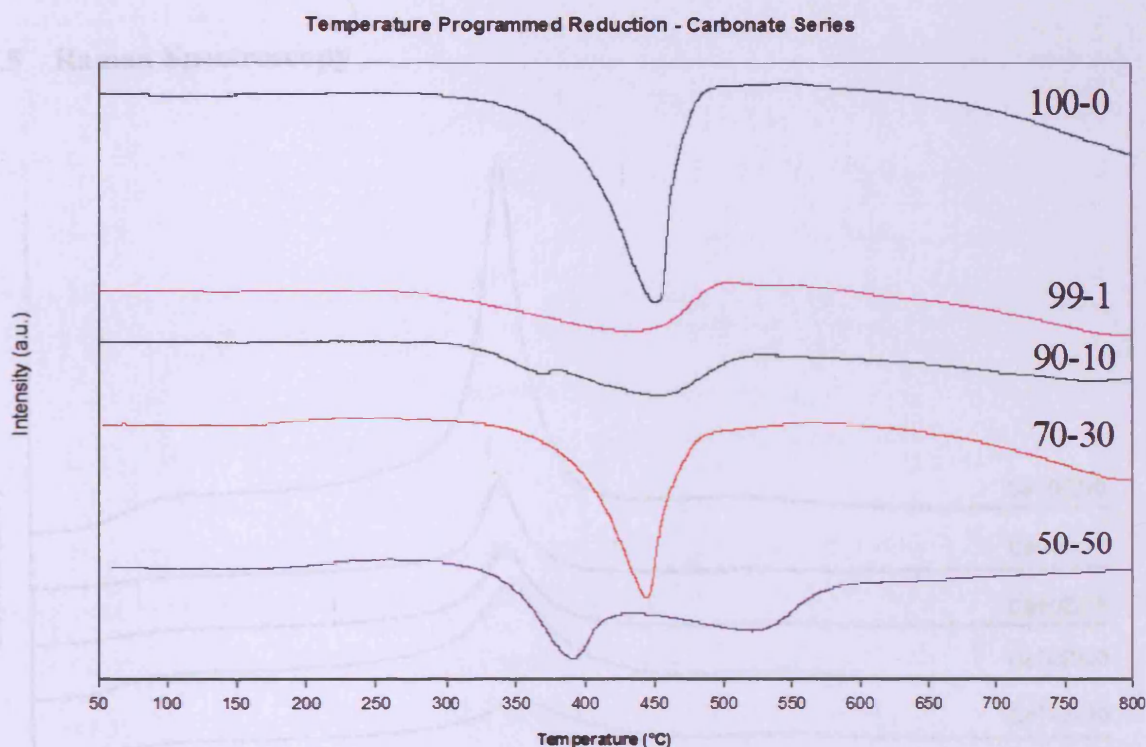
Figure 3.22. Temperature Programmed Reduction data for NH$_4$-C series of catalysts. Data obtained using Micromeritics Autochem II, 10% H$_2$/Ar at 50mL/min, temperature range of RT – 850°C studied. Sample mass – *ca*. 100mg per run.

There was no real trend between catalytic activity and the temperature at which H$_2$ consumption was at its highest (i.e. the temperature at which the reduction peak was at its maximum). What is clearer is the relationship between the reduction peak intensities and catalytic activity. Generally, peak intensity increased with decreasing catalytic activity. The most active catalyst, Ce99Zr1, was amongst the least reducible catalysts.

For the Ce50Zr50 sample, it appears that two different reductions are taking place. It is possible that the reduction peaks relate to two different oxidation states of Ce; Ce^{3+} and Ce^{4+}. Garcia *et al.* reported that carbonate precipitated ceria did contain a mixture of

Ce^{3+} and Ce^{4+}. As Ce^{4+} has been reported to be the more easily reducible than Ce^{3+}, it was likely that the reduction at approximately 400°C is due to Ce^{4+}, with the Ce^{3+} reducing at approximately 540°C.

It is unlikely that reduction of the Zr component occurred as the double reduction profile observed for NH₄-C Ce50Zr50 was not replicated for the NH₄-U analogue. The reduction peaks at higher temperatures (in excess of 700°C) were due to reduction of the bulk ceria, as observed for the NH₄-U series of catalysts[5].

3.3.5 Raman Spectroscopy
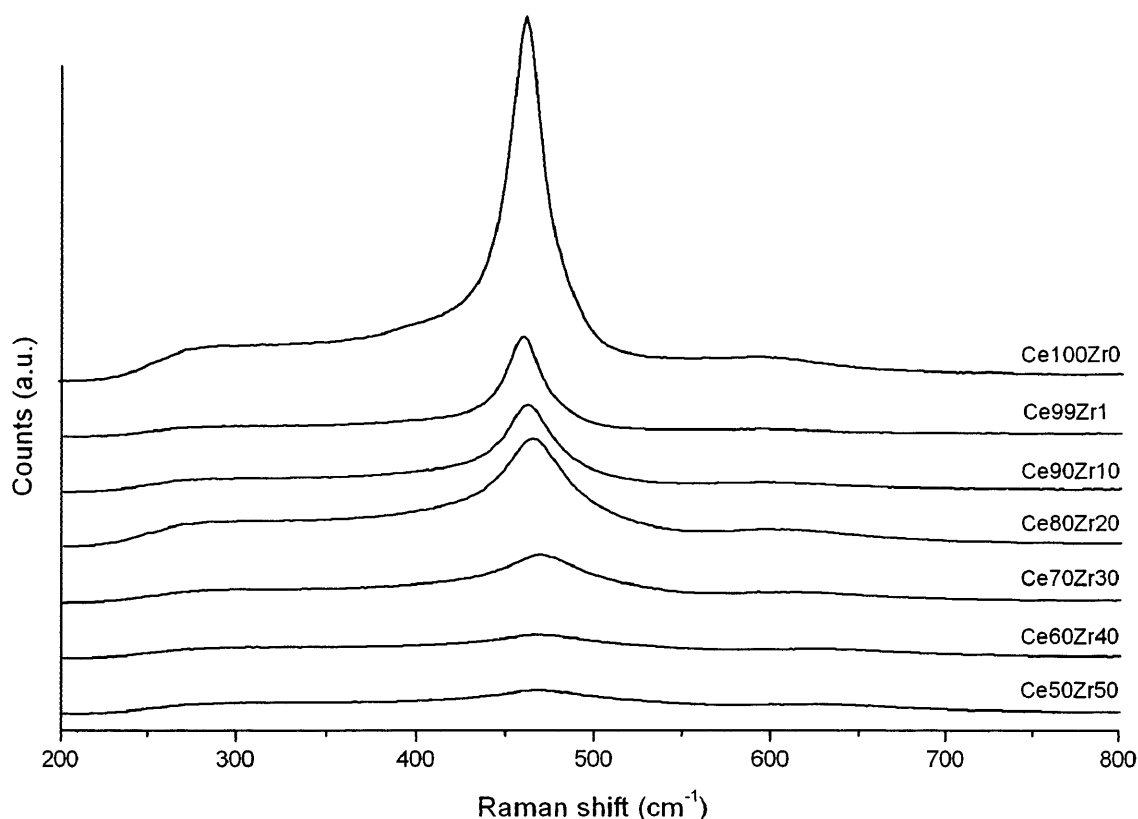
Figure 3.23. Raman spectra of NH₄-U series of CeZrO₂ catalysts. Laser λ=514nm. Intensity of CeO₂ (i.e. 100-0) spectrum halved for clarity of other other less intense spectra.
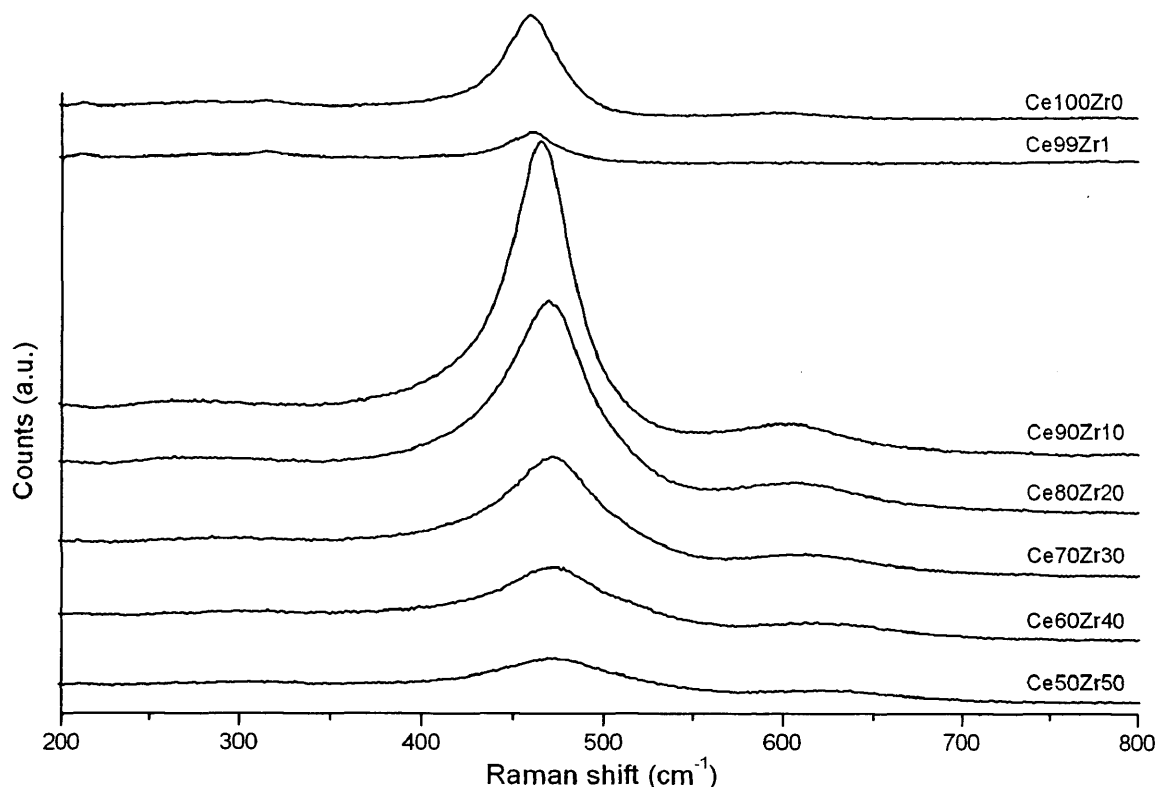
Figure 3.24. Raman spectra for NH_4-C series of catalysts. Laser λ=514nm.

Two bands were observed for all catalysts; CeO_2 F2g vibrational stretching[6] at 460cm⁻¹ and tetragonal ZrO_2 A1g+2B1g+3Eg vibrational stretches[7] at 600cm⁻¹. It should be noted that tetragonal ZrO_2 also displays a vibrational stretch at 460cm⁻¹. However, due to the larger relative quantity of CeO_2, this peak would be immeasurable. There was no clear trend observed in terms of peak intensity and Ce:Zr ratio, especially when the NH_4-U series is considered. The exception is that for the NH_4-C series, the higher Zr loadings gave rise to progressively less intense CeO_2 stretching. One would expect this as the cerium content is much lower. It is more useful to look at the full width half maximum (FWHM) values of each CeO_2 stretch as shown in table 3.8. A trend is readily apparent.

Table 3.8. FWHM values derived from figures 3.23 and 3.24 for both NH₄-U and NH₄-C catalyst series.

Sample	Raman FWHM (NH₄-U) (cm⁻¹)	Raman FWHM (NH₄-C) (cm⁻¹)
Ce50Zr50	71	70
Ce60Zr40	66	68
Ce70Zr30	56	59
Ce80Zr20	43	55
Ce90Zr10	35	42
Ce99Zr1	24	31
Ce100Zr0	20	36

For both series, it is clear that an increase in FWHM occurred when Zr content was increased, which has been reported previously[5]. This broadening implies that crystallite sizes would then also decrease. By comparing tables 3.2 and 3.3, it can be seen that this was the case; increasing Zr content caused a decrease in crystallite size[8 - 9].

Teng, Luo and Yang[6] have reported that Raman peak broadening occurs when incorporating higher Zr content into the CeZrO₂ catalysts. This was due to a reported reduction in unit cell size (as Zr^{4+} has a smaller ionic radius than Ce^{4+}) and that crystal defects would therefore be more noticeable. They also reported that these crystal defects occur due to oxygen vacancies in CeO_2.

The FWHM values could also be affected by internal strain (in much the same way as XRD) as explained by Rosenblatt and co-workers[10]. In this study, it was found that increasing Zr content caused an increase in lattice strain and therefore an increase in the Raman FWHM values. This applied to both the NH₄-C and NH₄-U series. The Raman FWHM values experience precisely the same changes (with respect to strain and crystallite size) as observed in XRD analysis[8 - 9].

3.3.6 X-ray Photoelectron Spectroscopy

Table 3.9. Ce:Zr ratios observed for both NH₄ catalyst series via XPS. Orbitals analysed: Ce 4d, Zr 3d.

Sample (theoretical Ce:Zr ratio)	Observed Ce:Zr ratio (atomic %) by XPS analysis	
	NH₄-U series	NH₄-C series
Ce50Zr50	64:36	62:38
Ce60Zr40	73:27	71:29
Ce70Zr30	80:20	77:23
Ce80Zr20	88:12	87:13
Ce90Zr10	94:6	94:6
Ce99Zr1	99:1	99:1

As with the bulk EDX analysis, the surface Ce:Zr ratios for the NH_4-U series were observed to be approximately correct (in relation to the intended Ce:Zr ratios) for high Ce content catalysts. Larger than intended Ce contents were observed for high Zr content catalysts (i.e. Ce70Zr30, Ce60Zr40 and Ce50Zr50).

The NH_4-C series displayed a similar XPS trend to that of the NH_4-U series. The Ce contents were higher than intended, particularly for the larger Zr content catalysts. However, if any given Ce:Zr ratio was compared between the NH_4-U and NH_4-C series, it can be seen that the Ce:Zr ratios are similar (within a reasonable error margin) at both the surface and in the bulk. For example, the NH_4-U and NH_4-C Ce80Zr20 displayed Ce:Zr ratios of 88:12 and 87:13 respectively.

The XPS analysis was also used to investigate if Ce^{3+} was present in any of the samples. A larger quantity of Ce^{3+} instead of Ce^{4+} has been previously proposed in the literature as detrimental to a ceria catalyst's activity for the total oxidation of naphthalene[3].

Whilst it is possible in theory to determine the ratio of Ce^{3+} and Ce^{4+}, in practice it can be much more problematic. As the spectra for pure Ce^{4+} and Ce^{3+} coincide in terms of binding energy peaks, effects such as charging and line broadening make it difficult to quantify the amounts of both oxidation states with any great certainty.

If the spectra obtained for pure Ce^{3+} and Ce^{4+} are compared, it was observed that all the catalysts contained some residual Ce^{3+} content. Figure 3.25 shows an example comparison of the spectra obtained during XPS analysis. The first of the spectra in that figure corresponds to pure Ce^{3+} and Ce^{4+} overlaid each other to illustrate how the characteristic peaks occur at very similar binding energies. All the samples analysed were observed to contain Ce^{4+} due to the presence of a characteristic peak at a binding energy of 917eV. The second spectrum was obtained for NH_4-C Ce80Zr20. The presence of Ce^{4+} can be seen clearly at 917eV. At 880eV, a binding energy characteristic of Ce^{3+} was apparent. Therefore NH_4-C Ce80Zr20 contained both Ce^{4+} and Ce^{3+}.
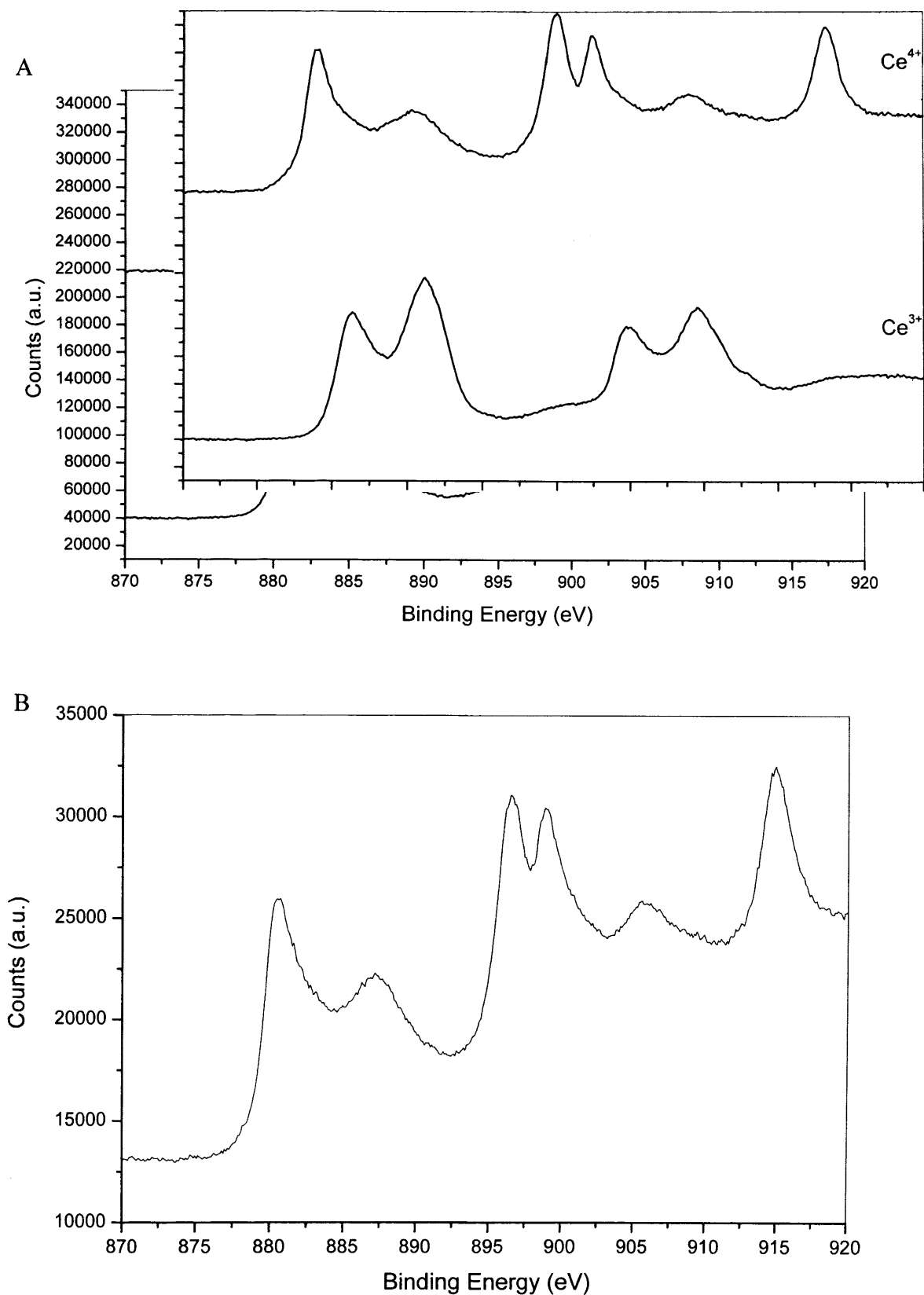
Figure 3.25. A) XPS spectra of pure Ce^{3+} and Ce^{4+}. B) XPS spectrum of NH$_4$-C Ce80Zr20 displaying an amalgamation of both pure spectra.

For the NH₄-C series, all of the catalysts displayed a very small amount of Ce^{3+}. It must be noted that the spectra implied (through peak intensities) that the Ce^{3+} was the rarer oxidation state; very strong relative binding energies at 913eV (specific to Ce^{4+}) were observed for all samples. A peak at 880eV was observed for all catalysts. Pure Ce^{3+} spectra contain a peak at 881eV with pure Ce^{4+} displaying a peak at 879eV. Therefore, it can be suggested that the binding energy of this peak observed for the CeZrO₂ samples were influenced by both Ce oxidation states.

For the NH₄-U series, similar observations were made. All the catalysts contained a very small amount of Ce^{3+}, but the vast majority of the cerium was found to be Ce^{4+}. However, by looking at the extent of the shift in some of the binding energies, an attempt was made to try and link the XPS data with the catalytic activity data to try and tentatively establish a trend between the two. The less active catalysts were observed to generally have a smaller shift away from the pure Ce^{4+} binding energies towards the pure Ce^{3+} binding energies. The more active catalysts generally appeared to experience a larger shift in binding energies from the pure Ce^{4+} towards the pure Ce^{3+} spectrum. This implied that the Ce^{3+} content relative to Ce^{4+} was higher. Therefore, the implication is that a very small amount of Ce^{3+} could be beneficial to catalytic activity, however larger amounts of Ce^{3+} would be detrimental, or that the Ce^{3+} may come from the cerium starting material and the apparent trend was coincidental. In order to investigate this, a pure Ce^{4+} CeZrO₂ catalyst would have to been synthesised, tested and compared. However, as quantification of the oxidation state ratio was extremely difficult, these observations would need further investigation to confirm them.

The Zr 3d spectra were also analysed for both NH₄-U and NH₄-C series. All CeZrO₂ catalysts displayed two binding energy peaks at approximately 182eV and 184eV. Both peaks have been observed previously to be due to Zr oxides for the Zr $3d_{5/2}$ and Zr $3d_{3/2}$ spectra respectively. The peak positions did not experience a significant shift of any kind when the Ce:Zr ratio was altered. The ratio of the two Zr peak areas was also consistent (approximately 60:40 in favour of the Zr $3d_{5/2}$ binding energy).

The oxygen 1s spectra of the NH₄-U and NH₄-C series all displayed O binding energies of 529eV, which has been observed to exist for CeZrO₂ previously[11].However, NH₄-C CeO₂ and Ce99Zr1 each displayed a second peak at 531.3eV. Barr[12] reported this to be due to cerium hydroxides, therefore can be attributed to incomplete oxidation of the cerium starting material during the catalyst preparations.

3.4   Further Discussion & Conclusions

It has been shown that the addition of a very small amount of Zr (1 molar percent) in a co-precipitation catalyst preparation can improve the catalytic activity. It was shown that if $CeZrO_2$ was prepared using sodium carbonate as the precipitating agent (i.e. the NH_4-C catalysts), a clear trend between Ce:Zr ratio and activity was apparent. All NH_4-C catalysts were more active than the CeO_2 analogue. Increasing the Zr content of the NH_4-C catalysts caused a reduction in activity. In the case of NH_4-U $CeZrO_2$, no trend between Ce:Zr ratio and activity could be established. The majority of the catalysts were observed to be as, or more, active than the CeO_2 catalyst prepared in the same way.

TOL and LOT experiments of Ce99Zr1 showed that the NH_4-U analogue was resistant to deactivation over repeated use and during an extended period of time at high temperature. The NH_4-C analogue showed a slight deactivation after prolonged reaction at high temperature, but no significant deactivation occurred when the same catalyst sample was used repeatedly across the experimental temperature range.

A supercritical analogue was also prepared and tested for the total oxidation of naphthalene to see if an improvement in activity over urea and carbonate precipitated $CeZrO_2$ could be found; however it was significantly less active than either the NH_4-U or NH_4-C analogue.

In terms of a mechanism, a redox mechanism such as the Mars van Krevelen (MvK) appears to be the most likely candidate. A previous kinetic study published by Bampenrat *et al.* came to this conclusion[13]. Their study focussed on $CeZrO_2$ and naphthalene total oxidation. However, the Ce precursor used in their preparation was Ce^{3+} nitrate using urea[14]. A kinetic study on both the NH_4-U and NH_4-C catalysts studies in this chapter would be useful future work to see if the results agree with the findings of Bampenrat *et al.*, or if different Ce precursor materials (i.e. using a Ce^{3+} or Ce^{4+} starting material) influence the reaction mechanism followed during naphthalene total oxidation.

It has also been previously proposed that a redox reaction operates for ceria with regards to naphthalene total oxidation[15]. These conclusions were drawn from the correlation of activity data with previously published redox turnover frequencies[16]. Therefore catalyst reducibility should be a crucial characteristic. An oxygenated atmosphere would also be required to ensure both the complete combustion of naphthalene and for the regeneration of the reduced support.

The findings made during TPR analysis, i.e. a general increase in H_2 consumption with increasing Zr content confirmed the reasoning behind the project aims; the reducibility of these catalysts was improved. This agreed with the findings of Bampenrat *et al*. However, there was a trade-off; the temperature at which H_2 consumption reached its maximum (i.e. the maxima of the reduction peaks in the TPR profiles) increased. One might wonder why the improvement in reducibility did not manifest itself as increasing the catalytic activities. The reason may lie with the testing parameters employed in this study. Since a small amount of naphthalene was used in the reactant gas stream (100vppm) with a set mass of catalyst (50mg), it is possible that the relatively slight (compared to the other CeZrO₂ catalysts with larger Zr contents) increase in reducibility for the lower Zr content catalysts was sufficient to be effectively reduced by the concentration of naphthalene available. What this implies is that the increased reducibility of the higher Zr content catalysts was not required by the concentration of naphthalene available. Therefore, the increased reducibility of the higher Zr content catalysts was not required for the testing parameters employed in this study; the higher temperatures at which these high Zr content catalysts began to reduce had a greater (negative) influence on catalyst activity. One may suppose that there would be a point where a particular naphthalene gas stream content and catalyst mass would utilise the increased reducibility of the higher Zr content catalysts. This may be a simplistic view; other factors such as mass transfer effects may have a significant influence on the kinetics of the naphthalene adsorption on the catalyst surface.

As a final note, if the temperature ranges of both sets of catalysts are analysed, the NH₄-C series displayed reductions 50-75°C (typically) lower than their NH₄-U series analogues. Therefore, despite being more difficult to reduce, the NH₄-U series of catalysts still have comparable catalytic activities to the NH₄-C catalysts, as discussed in the text above (chapter 3.1). It could therefore be suggested that there are other catalytic features which are at least as important than the catalyst reducibility.

It was found that the inclusion of Zr caused a significant increase in surface area for the NH₄-C series catalysts. No significant change occurred for the NH₄-U series. The XRD data showed that no separate zirconia phase existed for any NH₄-U or NH₄-C catalyst. The crystallite sizes from XRD showed that the NH₄-C catalysts were composed of smaller crystallites than the NH₄-U series. A general trend of decreasing crystallite size with increasing Zr content was found. The supercritical catalyst's crystallite size was

significantly larger than all other investigated catalysts. Crystallite sizes were also probed via Raman spectroscopy, the data from which was shown to agree with the XRD analysis data. The FWHM values were found to increase with increasing Zr content. A larger FWHM inferred a smaller crystallite size.

The crystallite sizes can be explained by the differences between the ionic radii of Ce^{4+} and Zr^{4+}; Zr^{4+} has the smaller ionic radius (0.084nm and 0.097nm for Zr^{4+} and Ce^{4+} respectively). Since no discrete ZrO_2 phases could be observed via XRD, it can be said that the Zr was contained within the ceria lattice. Increasing the concentration of Zr within the crystal lattice would cause an increased concentration of M-O bond lengths to be altered. These bonds can then be reduced more easily and this can be demonstrated by TPR analysis data where high Zr content $CeZrO_2$ displayed higher H_2 consumptions than low Zr content $CeZrO_2$.

SEM/EDX studies displayed agreement with the raw XRD patterns obtained during this study; no discrete phases could be detected. Imaging studies suggested that the morphological change already reported to occur in the literature for ceria catalysts also applied here, albeit to a lesser degree. A NH$_4$-U catalyst appeared to undergo a morphological change upon use, but this change was not observed for the NH$_4$-C series analogue. The supercritical analogue displayed agglomeration of a proportion of the catalyst's coral-like structure after use.

If the Ce oxidation states were analysed via XPS, it was found that accurate quantification of the ratio of Ce^{4+} to Ce^{3+} was impossible without further investigation and high resolution scanning. This was due to the binding energies of both Ce oxidation states occurring at similar values and XPS phenomena such as sample charging and line broadening. However, qualitative analysis was attempted. For the NH$_4$-U series, it was tentatively proposed that a general link between the amount of Ce^{3+} compared to Ce^{4+} and the observed catalytic activities existed. The more active catalysts generally appeared to have slightly more Ce^{3+} than Ce^{4+} compared with the lesser active catalysts. For the NH$_4$-C series, a trend could not be established as with the NH$_4$-U series. However, Ce^{3+} was observed in all catalysts. The most prevalent oxidation state was still Ce^{4+}.

Comparing EDX and XPS analyses gave rise to some conflicting data. The EDX analysis suggested that the NH$_4$-U catalyst series had similar Ce:Zr ratios to that originally intended. XPS analysis disagreed with this for higher Zr content catalysts; higher Ce loadings than originally intended were observed. XPS also displayed higher

than intended Ce loadings for high Zr content NH₄-C catalysts. However, this was in agreement with the EDX analysis data.

NH₄-U Ce50Zr50, Ce60Zr40 and Ce70Zr30 displayed a higher Ce surface content than bulk content. If the Ce-O bond strength is reduced through increased lattice strain (due to the presence of Zr), then the susceptibility of the catalyst to reduce would increase. If the reduction of Zr oxide is less facile than Ce oxide, then an increased surface concentration of Ce would further increase the reducibility of the catalyst surface. This would then manifest itself as an increased H₂ uptake during TPR experiments.

3.5   References

1.   A. Trovarelli, *Catalysis by Ceria and Related Materials*, Imperial College Press, London, 2002.

2.   J. F. Lamonier, S. P. Kulyova, E. A. Zhilinskaya, B. G. Kostyuk, V. V. Lunin, A. Aboukais, *Kinetics and Catalysis*, **45**, (2004), 429-435.

3.   T. Garcia, B. Solsona, S. H. Taylor, *Catalysis Letters*, **105**, (2005), 183-189.

4.   E. N. Ndifor, *The Catalytic Oxidation of Volatile Organic Compounds, PhD Thesis*, 2007.

5.   D. Andreeva, R. Nedyalkova, L. Ilieva, M. V. Abrashev, *Applied Catalysis B-Environmental*, **52**, (2004), 157-165.

6.   M. L. Teng, L. T. Luo, X. M. Yang, *Microporous and Mesoporous Materials*, **119**, (2009), 158-164.

7.   S. Askrabic, R. Kostic, Z. Dohcevic-Mitrovic, Z. V. Popovic, *12th International Conference on Phonon Scattering in Condensed Matter (Phonons 2007)*, **92**, (2007), 12042-12042.

8.   E. N. Ndifor, T. Garcia, B. Solsona, S. H. Taylor, *Applied Catalysis B-Environmental*, **76**, (2007), 248-256.

9.   B. Puertolas, B. Solsona, S. Agouram, R. Murillo, A. M. Mastral, A. Aranda, S. H. Taylor, T. Garcia, *Applied Catalysis B-Environmental*, **93**, (2010), 395-405.

10.   J. W. Ager, D. K. Veirs, G. M. Rosenblatt, *Physical Review B*, **43**, (1991), 6491-6499.

11.   A. Galtayries, R. Sporken, J. Riga, G. Blanchard, R. Caudano, *Journal of Electron Spectroscopy and Related Phenomena*, **88**, (1998), 951-956.

12. T. L. Barr, *Journal of Physical Chemistry*, **82**, (1978), 1801-1810.

13. A. Bampenrat, V. Meeyoo, B. Kitiyanan, P. Rangsunvigit, T. Rirksomboon, *Catalysis Communications*, **9**, (2008), 2349-2352.

14. S. Pengpanich, V. Meeyoo, T. Rirksomboon, K. Bunyakiat, *Applied Catalysis A-General*, **234**, (2002), 221-233.

15. T. Garcia, B. Solsona, S. H. Taylor, *Applied Catalysis B-Environmental*, **66**, (2006), 92-99.

16. M. Badlani, I. E. Wachs, *Catalysis Letters*, **75**, (2001), 137-149.

Chapter 4 – Investigating the Preparation Conditions of Pt/SiO₂ for the Total Oxidation of Naphthalene

4.1   Introduction

A recent investigation by Edwin *et al.* has revealed that precious metal supported catalysts can be very active for the total oxidation of naphthalene. Pt/SiO_2 catalysts were found to be significantly more active than self supporting nanoparticular CeO_2, which was considered to be one of the most active catalysts known thus far[1, 2]. The SiO_2 support also gave the most active catalysts out of the range of supports tested in the paper published by Edwin *et al.* They postulated that large, metallic Pt crystallites with low dispersion were desirable features in a catalyst for the total oxidation of naphthalene[1]. As the focus of that paper was to investigate the influence of the support used, a constant loading of Pt was used (0.5wt%). The next stage in investigating these catalysts is to vary the preparation method of Pt/SiO_2 in terms of Pt content and calcination regime (calcination temperature, time frame, ramp rate, calcination atmosphere and the nature of the SiO_2 support). This was done with the aim to improve the activity of Pt/SiO_2 in terms of catalyst light-off based on CO_2 yields.

Palladium has been demonstrated to be an ideal metal for the preparation of active catalysts for hydrocarbon oxidation,[3-6] as well as other reaction types[7]. Once the optimum Pt weight loading and calcination regime were established, a Pd analogue was synthesised. This was to compare the activities for the total oxidation of naphthalene of Pt/SiO_2 and Pd/SiO_2 prepared in the same way.

4.2   The Effect of Varying Pt Content on the Total Oxidation of Naphthalene

4.2.1   Activity Data

Figure 4.1 represents the catalytic activities (based on CO_2 yields as a function of temperature) of the 5 different Pt weight Pt/SiO_2 catalysts investigated. Larger Pt loadings (i.e. 2.5 and 5 weight percent) gave rise to increased activity. What should be noted is that the temperature range from low to very high activity was quite short (i.e. over

approximately 20 - 30°C) for all the investigated catalysts. A calcination regime of 550°C for 6h in static air with a ramp rate of 10°C/min was used.
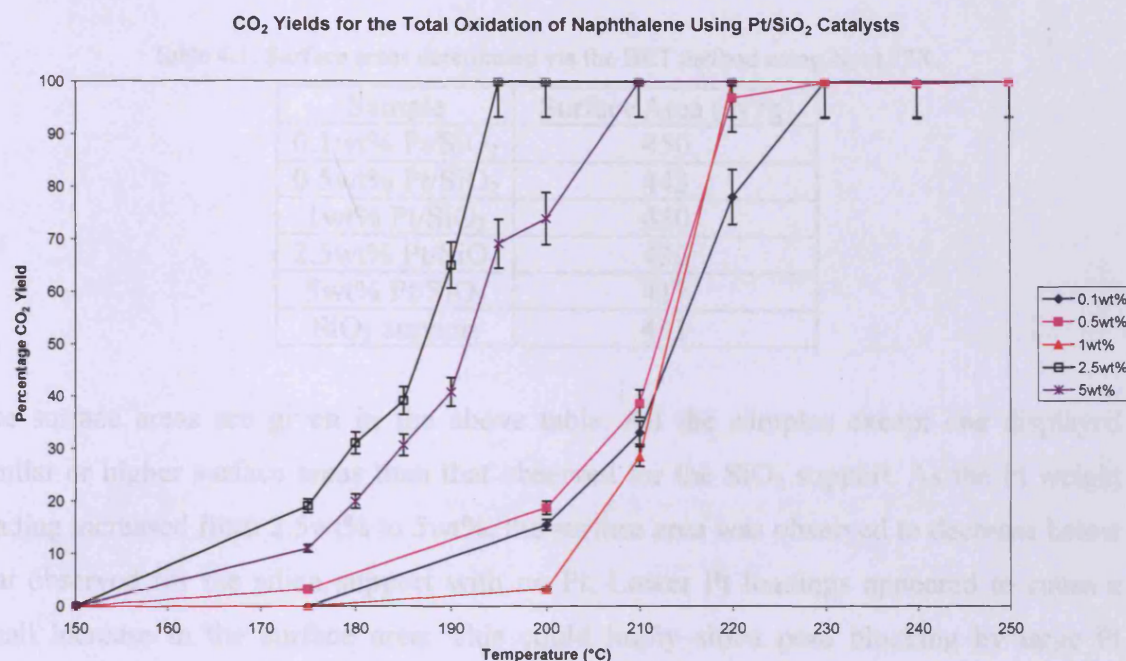
Figure 4.1. CO_2 yields for all the investigated catalysts obtained via the apparatus described in Chapter 2. Temperature range: 150 – 250°C. GHSV = 45,000h^{-1}, 100vppm naphthalene, total flow = 50mL/min. The numbers in the legend refer to Pt percentage weights. Error bars are ± 6.7%.

Another way of considering catalytic activity is to investigate the temperature at which a catalyst is active for a given CO_2 yield. If the temperatures required for a 50% CO_2 yield (T_{50}) are considered, 2.5 and 5 wt% Pt/SiO₂ required a lower temperature to attain a 50% CO_2 yield compared to the other catalysts. The 5wt% Pt/SiO₂ Pt dispersion may be higher than the 2.5wt% Pt/SiO₂ which would reduce the catalytic activity of 5wt% Pt/SiO₂ according to Edwin *et al.*[1], which could explain why 2.5wt% was slightly more active than 5wt% Pt/SiO₂. Repeat experiments using fresh 2.5wt% and 5wt% Pt/SiO₂ showed the same trend as the original testing experiments, i.e. 2.5wt% Pt/SiO₂ was more active than 5wt% Pt/SiO₂.

4.2.2 Characterisation

4.2.2.1 Surface Area Analysis

Table 4.1. Surface areas determined via the BET method using N_2 at 77K.

Sample	Surface Area (m^2/g)
0.1wt% Pt/SiO₂	450
0.5wt% Pt/SiO₂	443
1wt% Pt/SiO₂	430
2.5wt% Pt/SiO₂	436
5wt% Pt/SiO₂	417
SiO₂ support	431

The surface areas are given in the above table. All the samples except one displayed similar or higher surface areas than that observed for the SiO_2 support. As the Pt weight loading increased from 2.5wt% to 5wt%, the surface area was observed to decrease below that observed for the silica support with no Pt. Lower Pt loadings appeared to cause a small increase in the surface area. This could imply silica pore blocking by large Pt clusters on the surface in the case of higher (5wt%) Pt loadings.

4.2.2.2 X-Ray Diffraction

Figure 4.2 represents all the XRD patterns taken during this study. The poorly defined peak at approximately 23°2θ is due to an amorphous SiO_2 phase. The 3 peaks at approximately 40, 46 and 68°2θ can be assigned as a cubic Pt phase. The concentration of the Pt phase increases with Pt loading which can be seen from the increased peak intensity.
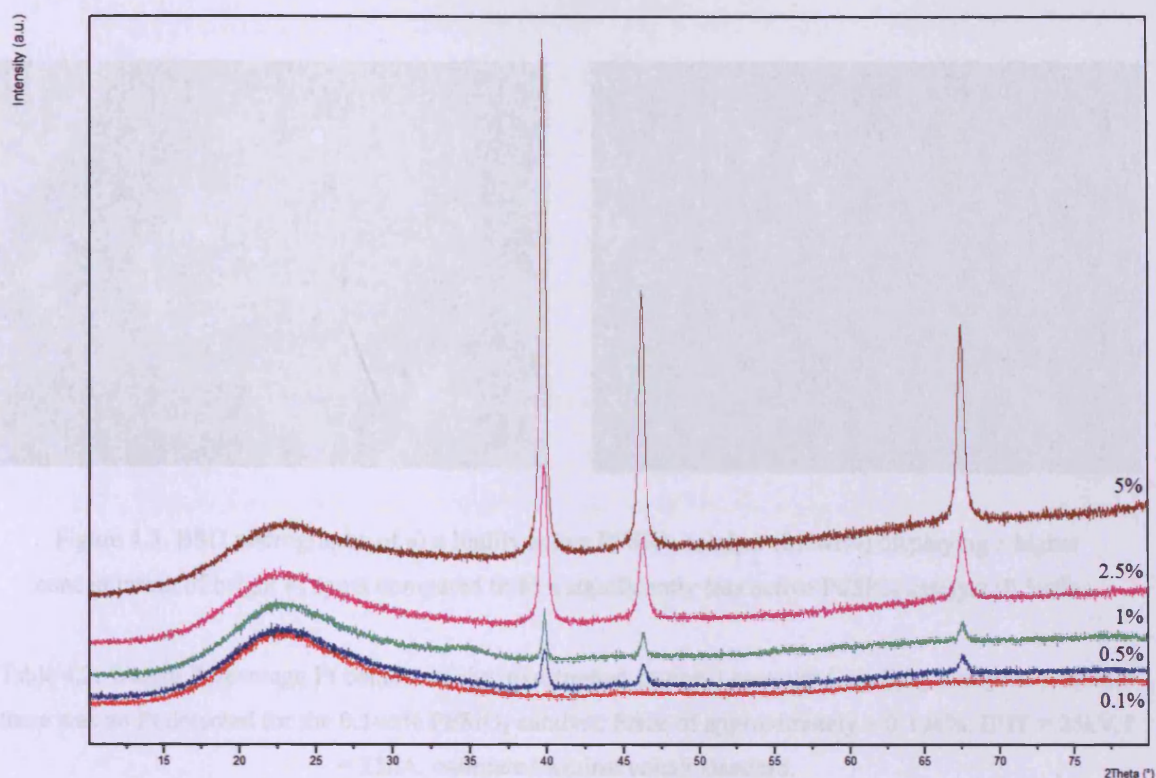
Figure 4.2. XRD patterns of all the investigated Pt/SiO$_2$ catalysts of varying Pt content.

4.2.2.3 Scanning Electron Microscopy & Energy Dispersive X-Ray Analysis

The bright white spots on the following image indicate the presence of Pt particles on the surface. The micrograph in the following figure suggests that the Pt particles are relatively large and are poorly dispersed, two features which were postulated by Edwin *et al.* as important features for an active catalyst[1]. Conversely 0.5wt% Pt/SiO$_2$, one of the poorer catalysts, displayed no noticeable large Pt particles.

Figure 4.3. BSD micrographs of a) a highly active Pt/SiO₂ catalyst (2.5wt%) displaying a higher concentration of bright Pt spots compared to b) a significantly less active Pt/SiO₂ catalyst (0.5wt%).

Table 4.2. Weight Percentage Pt content of the investigated catalysts measured via EDX analysis. Note that there was no Pt detected for the 0.1wt% Pt/SiO₂ catalyst. Error of approximately ± 0.1wt%. EHT = 25kV, I = 25nA, calibrated against cobalt standard.

Sample	Weight percentage Pt content
0.1wt% Pt/SiO₂	N/A
0.5wt% Pt/SiO₂	0.5
1wt% Pt/SiO₂	1.0
2.5wt% Pt/SiO₂	2.5
5wt% Pt/SiO₂	5.0

As the above table shows, the observed Pt loadings coincide with the theoretical Pt loadings. This could be expected as impregnation techniques can give accurate precious metal loadings[8]. Spot analyses on the bright spots confirmed them to be Pt.

4.2.2.4 CO Chemisorption

Table 4.3. Pt surface area measurements determined by CO chemisorption. Pretreatment conditions: 400°C, 1h, 20mL/min H₂ flow. Analysis performed at RT. Sample mass used *ca.* 400-500mg.

Pt content (wt%)	Av. crystallite size (Å)	Dispersion (%)	Pt surface area (m²/g)
0.1	41	28	0.1
0.5	61	19	0.2
1	91	12	0.3
2.5	276	4	0.3
5	736	2	0.2

From the data presented in table 4.3 it can be seen that larger loadings of Pt (i.e. the more active catalysts) gave rise to larger Pt particles that had a lower degree of dispersion. This agrees with the findings of Edwin *et al*[1]. If the chemisorption data reported by Edwin *et al.* is compared to the analogous data given in table 4.3 (i.e. the data for 0.5wt% Pt/SiO₂), it can be seen that the values are similar. Two different analysers were used (Edwin *et al.* used a Quantachrome Autosorb-1, the data presented in this thesis was obtained using a Quantachrome ChemBET-3000). Also, the pretreatment regimes differed; therefore a small variance in the quantitative data could be expected.

Table 4.4. Comparison of the 0.5wt% Pt/SiO₂ synthesised during this study and the same Pt properties reported by Edwin *et al.* respectively.

Sample	Av. Crystallite Size (Å)	Dispersion (%)	Surface area (m²/g)
0.5% Pt/SiO₂	61	19	0.2
0.5% Pt/SiO₂[a]	49	12	0.3

[a]: Data taken from reference[1].

The Pt surface areas increased with increasing Pt content for lower Pt contents, followed by a decrease in the case of 5 wt% Pt/SiO₂. It therefore appears that although a relatively high Pt surface area was required, the effect of this property was less than the effect of Pt crystallite size and dispersion on catalyst activity.

4.2.2.5 X-Ray Photoelectron Spectroscopy

X-ray Photoelectron Spectroscopy - Pt/SiO₂
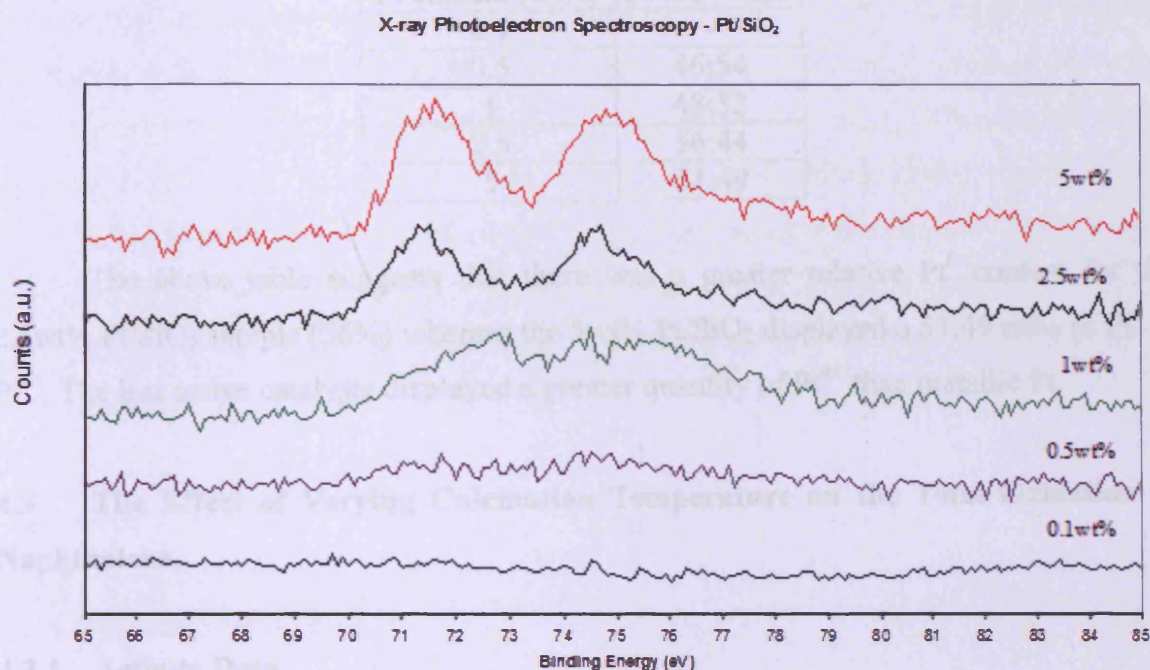
Figure 4.4. Pt 4f spectra of Pt/SiO₂. Legend labels refer to Pt percentage content.

No Pt signal could be observed for the 0.1wt% Pt/SiO₂ catalyst. This was not surprising due to the very low Pt content. The XPS data showed that in the case of 0.5 and 1wt% Pt/SiO₂, little evidence of Pt^{2+} was observed. Edwin *et al.*[1] reported that a broad peak between 70 and 77eV was observed for 0.5wt% Pt/SiO₂. This peak covered the binding energies where the three main Pt oxidation states (Pt^{0}, Pt^{2+} and Pt^{4+} at binding energies of 71, 72 and 74eV respectively) occur. They also reported that subtracting the Pt^{2+} component from the spectrum obtained for 0.5wt% Pt/SiO₂ revealed a doublet peak at 71 and 74eV (therefore Pt^{0} [1, 9-12] and Pt^{4+} respectively[1, 11]). In this study, the higher Pt loading catalysts revealed this doublet in greater intensity with increasing Pt loading. Therefore, the observations of Edwin *et al.* were replicated. The ratio of Pt^{0} to Pt^{4+} was examined where possible and the results are presented in the table below.

Table 4.5. Pt^0:Pt^{4+} ratio for Pt/SiO₂ determined by XPS spectra peak analysis. 0.1wt% Pt/SiO₂ sample displayed no quantifiable Pt 4f peaks therefore the Pt^0:Pt^{4+} ratio could not be quantified.

Pt content (wt%)	Pt^0:Pt^{4+} ratio
0.1	-
0.5	46:54
1	48:52
2.5	56:44
5	51:49

The above table suggests that there was a greater relative Pt^0 content for the 2.5wt% Pt/SiO₂ sample (56%) whereas the 5wt% Pt/SiO₂ displayed a 51:49 ratio of Pt^0 to Pt^{4+}. The less active catalysts displayed a greater quantity of Pt^{4+} than metallic Pt.

4.3 The Effect of Varying Calcination Temperature on the Total Oxidation of Naphthalene

4.3.1 Activity Data
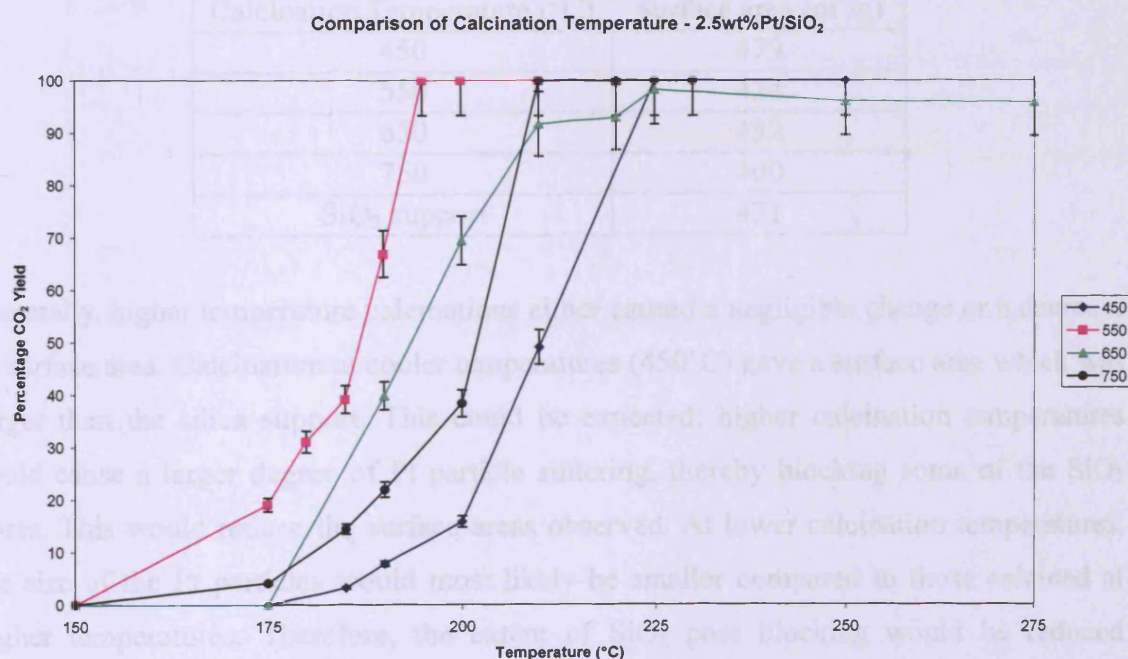
Figure 4.5. Comparison of 2.5wt%Pt/SiO₂ calcined at different temperatures. Temperature range: 150 – 275°C. GHSV = 45,000h⁻¹, 100vppm naphthalene, total flow = 50mL/min. The numbers in the legend refer to the calcination temperature used. Other calcination parameters: 6h, 10°C/min, static air. Error bars are ± 6.7%.

The above figure compares the activity of 2.5wt% Pt/SiO$_2$ catalysts calcined at different temperatures. All other calcination parameters were kept constant. The 550°C calcination produced the most active catalyst. Also, it appears that the 650°C calcination sample significantly suffered from the effects of mass transfer due to a more gradual increase in activity at higher CO$_2$ yields. Therefore one could argue that, when experimental error was considered, the 650°C calcination and 750°C calcination afforded catalysts of similar activity. It can also be argued that the 650°C calcination sample can attain a CO$_2$ yield of 100%. This is due to the plateau like behaviour of the plot at higher temperatures. Again, this in all likelihood is due to mass transfer. Calcination at 450°C produced the least active catalyst.

4.3.2 Characterisation

4.3.2.1 Surface Area Analysis

Table 4.6. Surface areas determined via the BET method using N$_2$ at 77K.

Calcination Temperature (°C)	Surface area (m^2/g)
450	479
550	424
650	432
750	400
SiO$_2$ support	431

Generally, higher temperature calcinations either caused a negligible change or a decrease in surface area. Calcination at cooler temperatures (450°C) gave a surface area which was larger than the silica support. This could be expected; higher calcination temperatures could cause a larger degree of Pt particle sintering, thereby blocking some of the SiO$_2$ pores. This would reduce the surface areas observed. At lower calcination temperatures, the size of the Pt particles would most likely be smaller compared to those calcined at higher temperatures. Therefore, the extent of SiO$_2$ pore blocking would be reduced allowing the surface area to be greater.

4.3.2.2 X-ray Diffraction

All of the unknown reflections observed for each catalyst were matched to cubic Pt metal phases. The most crystalline material observed was the 750°C calcined sample. The least crystalline was the 450°C calcined material. The angles of reflection for each catalyst are similar.
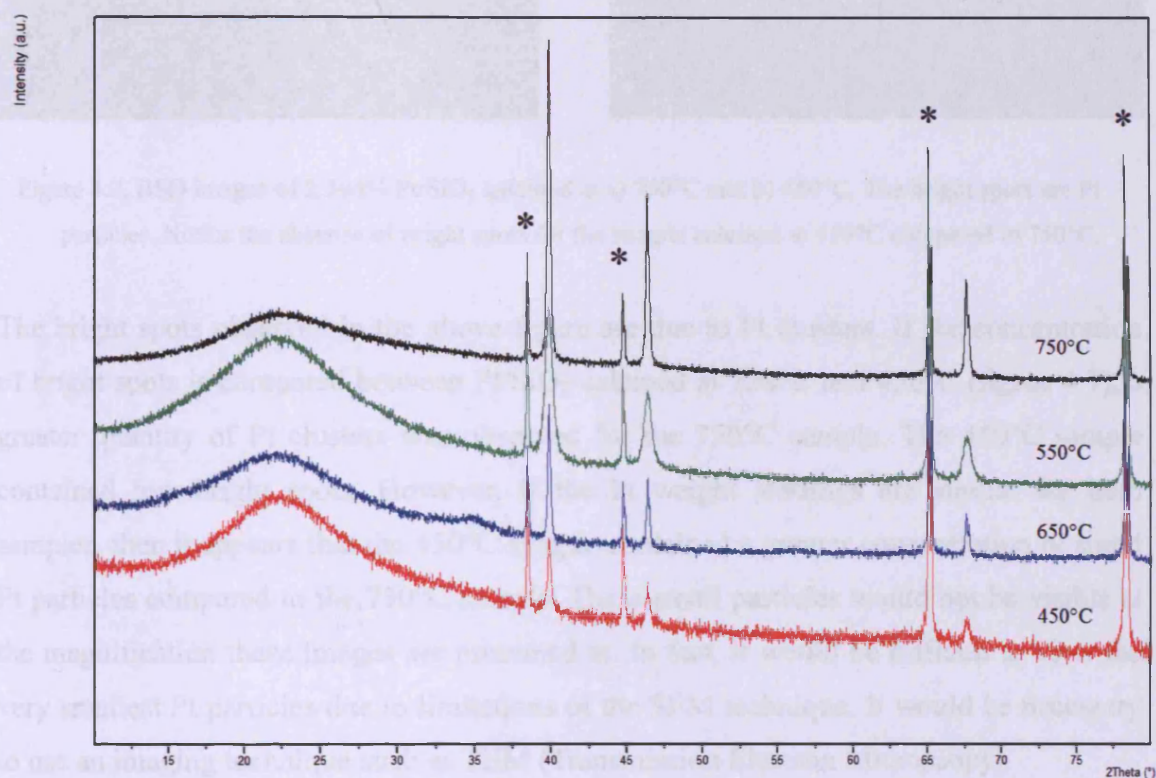
Figure 4.6. XRD patterns of 2.5wt% Pt/SiO₂ calcined at different temperatures. The reflections marked with an asterisk refer to a crystalline sample mounting plate and can therefore be disregarded.

4.3.2.3 Scanning Electron Microscopy & Energy Dispersive X-ray Analysis

Figure 4.7. BSD images of 2.5wt% Pt/SiO$_2$ calcined at a) 750°C and b) 450°C. The bright spots are Pt particles. Notice the absence of bright spots for the sample calcined at 450°C compared to 750°C.

The bright spots observed in the above figure are due to Pt clusters. If the concentration of bright spots is compared between Pt/SiO$_2$ calcined at 750°C and 450°C (figure 4.7), a greater quantity of Pt clusters was observed for the 750°C sample. The 450°C sample contained few bright spots. However, if the Pt weight loadings are similar for both samples, then it appears that the 450°C sample contained a greater concentration of small Pt particles compared to the 750°C sample. These small particles would not be visible at the magnification these images are presented at. In fact, it would be difficult to view the very smallest Pt particles due to limitations of the SEM technique. It would be necessary to use an imaging technique such as TEM (Transmission Electron Microscopy).

These images help support the earlier postulation (from the surface area and XRD analyses) that the lower calcination temperatures generally afforded smaller Pt particles than those calcined at higher temperatures.

4.3.2.4 CO Chemisorption

Table 4.7. CO chemisorption data for 2.5wt% Pt/SiO$_2$ calcined at different temperatures. Pretreatment conditions: 400°C, 1h, H$_2$. CO chemisorption performed at RT using 50μL pulses of CO . Sample mass used *ca.* 300mg.

Temperature (°C)	Av. Crystallite Size (Å)	Dispersion (%)	Surface area (m^2/g)
450	52	21	1.3
550	70	16	1
650	81	14	0.9
750	107	11	0.7

101

As the above table shows, an increase in calcination temperature caused an increase in Pt crystallite size, thereby causing a decrease in Pt dispersion and surface area. This implied that the Pt sintered during the catalyst calcination.

4.3.2.5 X-ray Photoelectron Spectroscopy

X-ray Photoelectron Spectroscopy - Pt/SiO₂
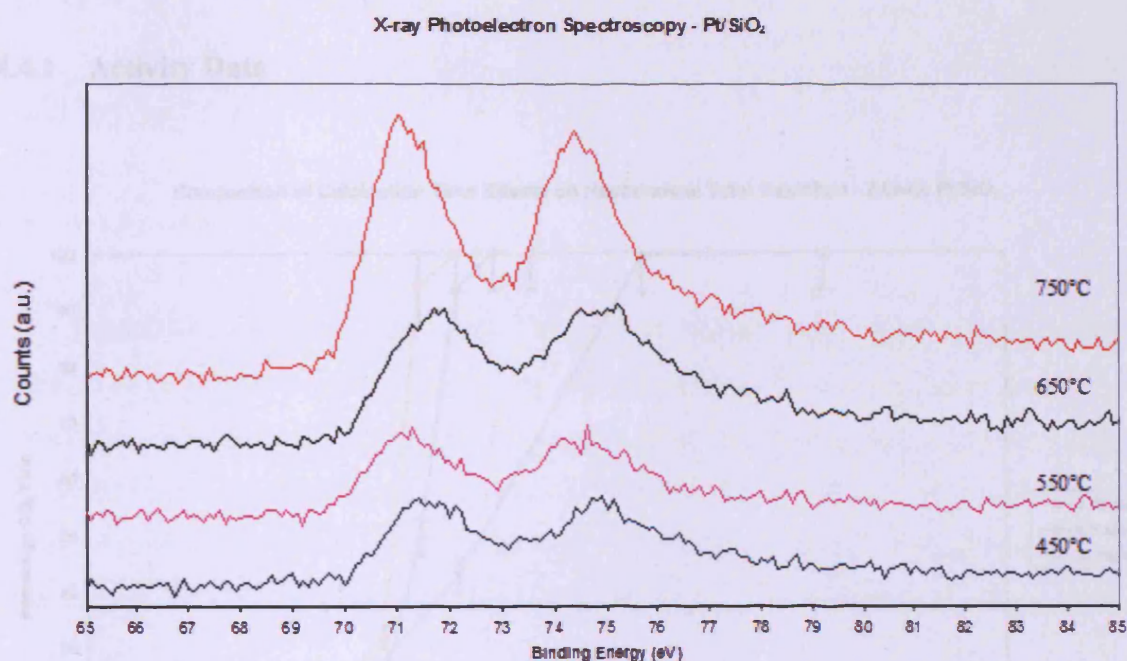
Figure 4.8. Pt 4f spectra of 2.5wt% Pt/SiO₂ calcined at different temperatures.

All the catalysts were observed to compose of Pt^0 and Pt^{4+} as previously observed (binding energies of 71eV and 74eV respectively). A binding energy peak corresponding to Pt^{2+} was not observed. The following table shows the Pt^0:Pt^{4+} ratio for the Pt/SiO₂ catalysts calcined at different temperatures for 6h in static air with a ramp rate of 10°C/min.

Table 4.8. Pt^0:Pt^{4+} ratio for 2.5wt% Pt/SiO₂ calcined at different temperatures determined by XPS spectra peak analysis.

Sample calcination temperature (°C)	Pt^0:Pt^{4+} ratio
450	57:43
550	59:41
650	52:48
750	56:44

102

The most active catalyst (the 550°C calcination) was found to have the highest proportion of Pt^0 of all the catalysts (59%). However, a definitive trend could not be established as the least active catalyst (the 450°C calcination) contained the second highest relative Pt^0 content (57%).

4.4 The Effect of Varying Calcination Time on the Total Oxidation of Naphthalene

4.4.1 Activity Data
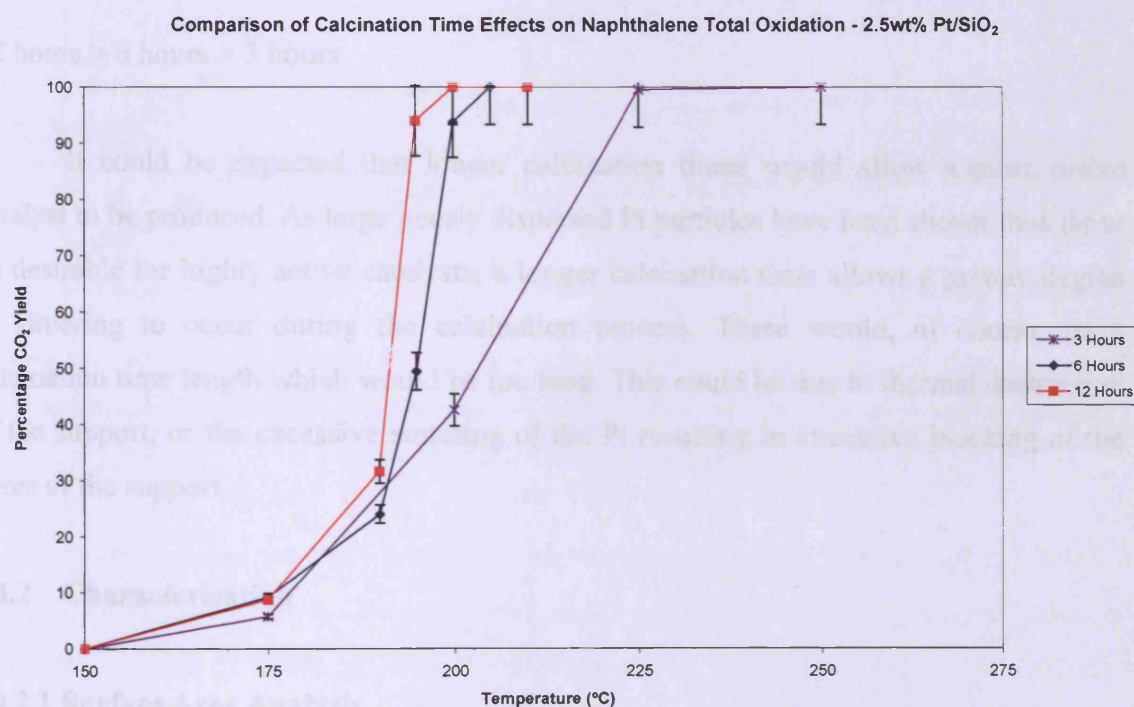
Figure 4.9. 2.5wt% Pt/SiO$_2$ catalysts calcined for different periods of time. Temperature range: 150 – 275°C. GHSV = 45,000h^{-1}, 100vppm naphthalene, total flow = 50mL/min. All other calcination parameters were kept constant (550°C, ramp rate = 10°C/min, static air). Error bars are ± 6.7%.

The most active catalyst was the one calcined for 12 hours. A 100% yield of CO_2 was obtained at 200°C. It was significantly more active than the catalyst calcined for the shortest amount of time (3 hour calcination) which required a temperature of 225°C to reach a 100% CO_2 yield. The T_{50} temperatures replicated the T_{100} trend.

One could argue that there may be mass transfer effects occurring with respect to the 3 hour calcination sample. When repeat experiments were performed, identical trends

in respect of both the T_{50} and overall activity analyses was observed. The T_{50} values from the repeat experiments, for example, were within 2°C of the respective original experiment for each sample. Therefore, the catalytic activities can be listed as (in terms of decreasing activity) as follows.

T_{50} analysis

12 hours > 6 hours > 3 hours

Overall activity (T_{100})

12 hours > 6 hours > 3 hours

It could be expected that longer calcination times would allow a more active catalyst to be produced. As large poorly dispersed Pt particles have been shown thus far to be desirable for highly active catalysts, a longer calcination time allows a greater degree of sintering to occur during the calcination process. There would, of course, be a calcination time length which would be too long. This could be due to thermal destruction of the support, or the excessive sintering of the Pt resulting in excessive blocking of the pores of the support.

4.4.2 Characterisation

4.4.2.1 Surface Area Analysis

Table 4.9. Surface areas determined via the BET method using N_2 at 77K.

Sample	Surface Area (m^2/g)
3h	421
6h	427
12h	426

The surface areas do not vary a great deal as a function of calcination time and are not significantly different to the bare support surface area. This implies that any Pt sintering that might have occurred was not extensive enough to significantly block the pores of the 60Å pore support. The bare support was observed to have a surface area of $431m^2/g$.

4.4.2.2 X-ray Diffraction
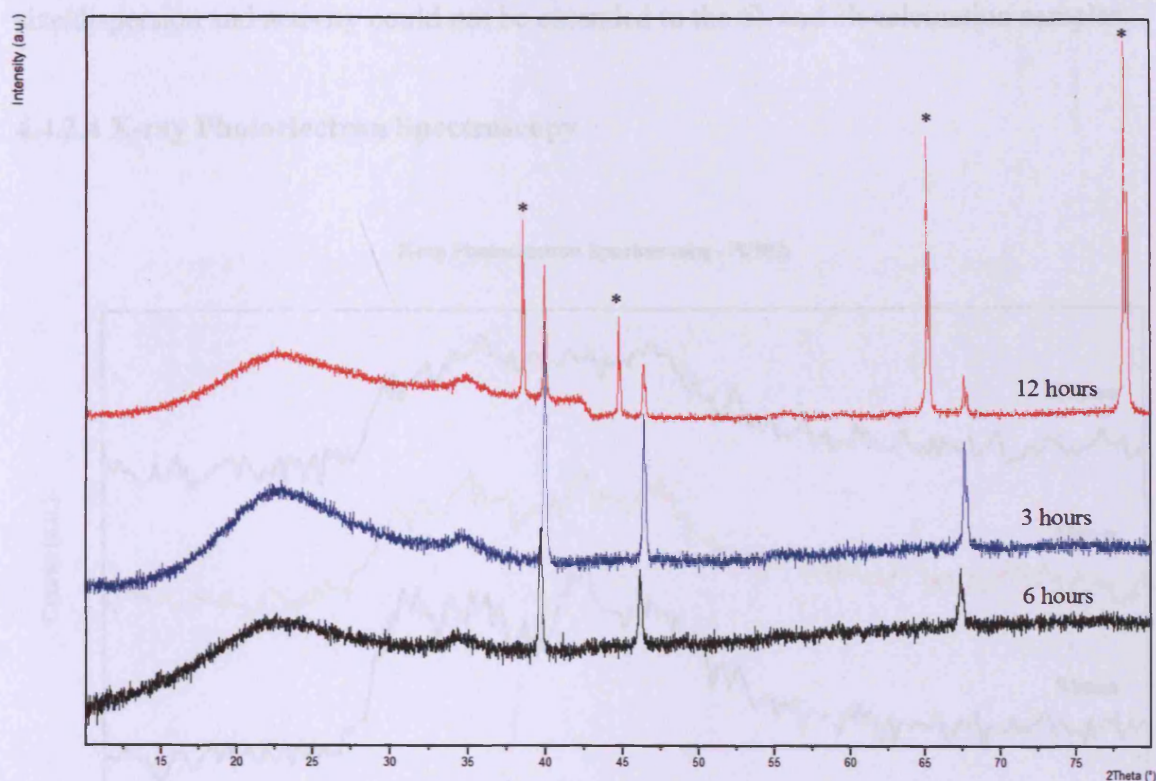
Figure 4.10. XRD patterns obtained for 2.5wt% Pt/SiO$_2$ calcined for 3, 6 and 12h at 550°C in static air with a ramp rate of 10°C/min. The reflections marked with an asterisk refer to a crystalline sample mounting plate and can therefore be disregarded.

All three reflections for each sample occur at similar angles. The amorphous hump at approximately 23°2θ is due to amorphous silica. All the phases (except at 35 °2θ) were matched to cubic Pt metal phase. The reflection at 35 °2θ has been reported to occur for Pt^{4+} based oxides[13].

4.4.2.3 CO Chemisorption

Table 4.10. CO chemisorption data for 2.5wt% Pt/SiO$_2$ calcined for different times. Pretreatment conditions: 400°C, 1h, H$_2$. CO chemisorption performed at RT using 50μL pulses of CO. Sample mass used *ca.* 600mg.

Time (h)	Av. Crystallite Size (Å)	Dispersion (%)	Pt surface area (m^2/g)
3	293	4	0.2
6	219	5	0.3
12	316	4	0.2

105

The most active catalyst (calcination for 12h) displayed similar Pt properties as before, i.e. low dispersion and large crystallite size. The same correlation between Pt crystallite size/dispersion and activity could not be extended to the 6h and 3h calcination samples.

4.4.2.4 X-ray Photoelectron Spectroscopy
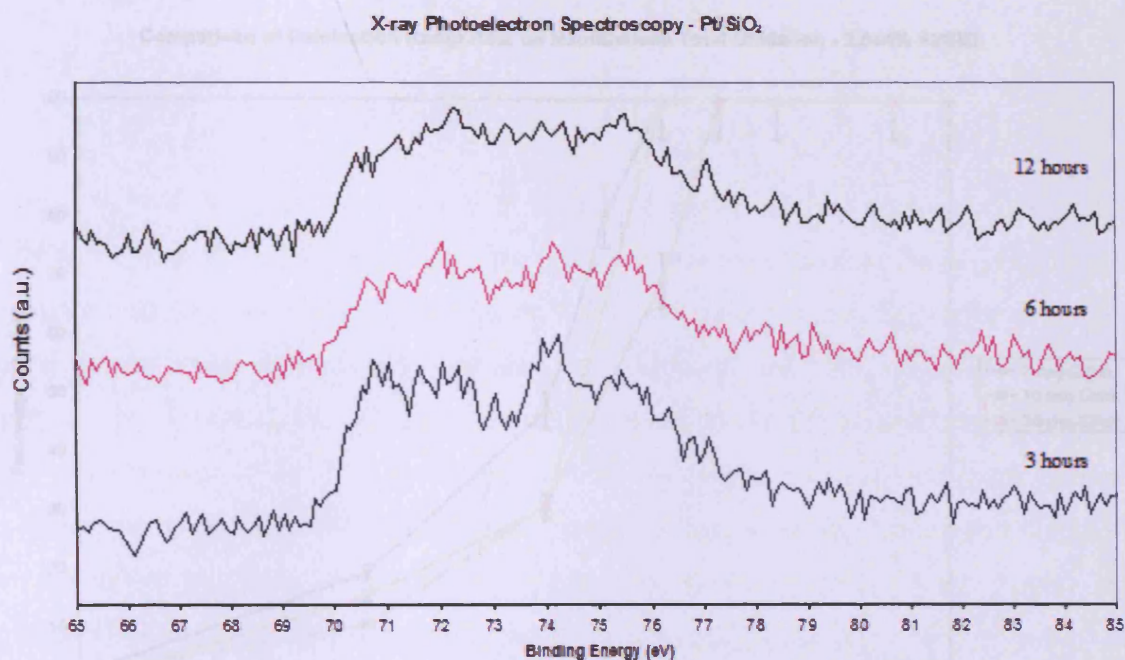
Figure 4.11. Pt 4f spectra of 2.5wt% Pt/SiO₂ calcined for different lengths of time.

Table 4.11. Pt^0:Pt^{4+} ratio for 2.5wt% Pt/SiO₂ calcined for different lengths of time determined by XPS spectra peak analysis.

Sample calcination time (h)	Pt^0:Pt^{4+} ratio
3	49:51
6	51:49
12	59:41

All spectra were observed to contain Pt^0 and Pt^{4+} (peaks at 71eV and 74eV respectively) as reported previously in this text. The most active catalyst (12 hours) gave rise to the highest degree of metallic Pt compared to oxidised Pt. Therefore the observations made previously apply here; predominantly metallic Pt with a large crystallite size and low dispersion favour naphthalene total oxidation. If the three catalysts are arranged in order of decreasing Pt^0 content, it can be seen that the resultant trend is identical to that found for T_{50} and T_{100}.

4.5 The Effect of Varying Calcination Ramp Rate on the Total Oxidation of Naphthalene

4.5.1 Activity Data
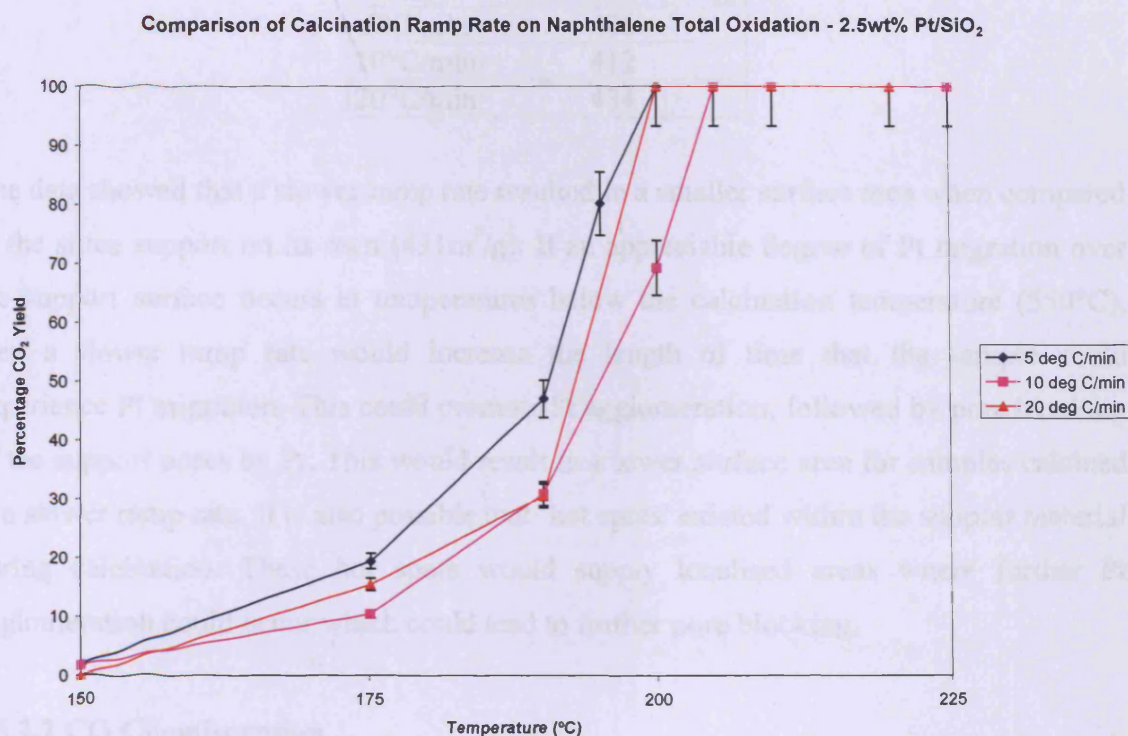
Figure 4.12. Activity data for 2.5wt% Pt/SiO$_2$ calcined at ramp rates of 5°C/min, 10°C/min and 20°C/min. Temperature range: 150 – 225°C. GHSV = 45,000h^{-1}, 100vppm naphthalene, total flow = 50mL/min. Other calcination parameters: 550°C, 12h, static air. Error bars are ± 6.7%.

The 10°C/min ramp rate gave rise to the least active catalyst. The most active catalysts were found when calcined at ramp rates of 5 or 20°C/min. The difference in the activities of these two catalysts were not completely conclusive, therefore repeat experiments were undertaken. The difference in activity for the 5 and 20°C/min catalysts were similar to the original data set, i.e. a ramp rate of 5°C/min gave rise to a more active catalyst. Both catalysts gave 100% CO$_2$ yields at 200°C whereas the 10°C/min catalyst required a slightly higher temperature (205°C) to attain a 100% CO$_2$ yield. At the T$_{50}$ point, this activity order was maintained (5°C/min > 20°C/min > 10°C/min). Therefore, it was decided that a calcination ramp rate of 5°C/min would be used in future catalyst preparations.

107

4.5.2 Characterisation

4.5.2.1 Surface Area Analysis

Table 4.12. Surface areas determined via the BET method using N_2 at 77K.

Sample	Surface Area (m²/g)
5°C/min	406
10°C/min	412
20°C/min	434

The data showed that a slower ramp rate resulted in a smaller surface area when compared to the silica support on its own (431m²/g). If an appreciable degree of Pt migration over the support surface occurs at temperatures below the calcination temperature (550°C), then a slower ramp rate would increase the length of time that the sample could experience Pt migration. This could promote Pt agglomeration, followed by pore blocking of the support pores by Pt. This would result in a lower surface area for samples calcined at a slower ramp rate. It is also possible that 'hot spots' existed within the support material during calcination. These hot spots would supply localised areas where further Pt agglomeration could occur which could lead to further pore blocking.

4.5.2.2 CO Chemisorption

Table 4.13. CO chemisorption data for 2.5wt% Pt/SiO₂ calcined at different ramp rates. Pretreatment conditions: 400°C, 1h, H_2. CO chemisorption performed at RT using 50μL pulses of CO. Sample mass used *ca.* 550mg.

Ramp Rate	Av. Crystallite Size (Å)	Dispersion (%)	Pt surface area (m²/g)
5°C/min	322	4	0.2
10°C/min	173	7	0.4
20°C/min	278	4	0.3

All the Pt/SiO₂ samples displayed large crystallite sizes and low dispersion as previously reported[1]. The most active catalyst, 5°C/min was observed to have the largest crystallite size (322Å) and the lowest dispersion (4%). The least active catalyst (10°C/min) displayed the highest dispersion (7%) and the smallest crystallite size (173Å). Therefore, it appears that the nature of the Pt crystallites in terms of dispersion and size are key

features in obtaining a highly active Pt/SiO$_2$ catalyst for the total oxidation of naphthalene in agreement with the findings of Edwin *et al*[1].

4.5.2.3 X-ray Photoelectron Spectroscopy
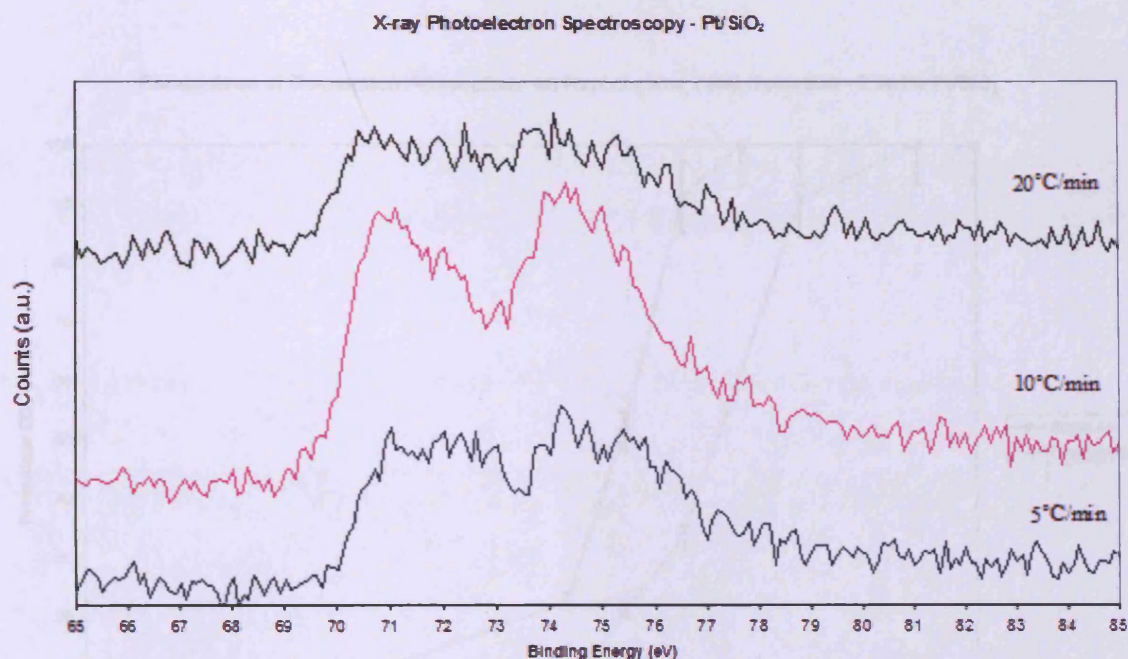
Figure 4.13. Pt 4f spectra of 2.5wt% Pt/SiO$_2$ calcined at different ramp rates.

All the spectra displayed binding energies of 71eV and 74eV as in previous studies within this text relating to Pt^0 and Pt^{4+} respectively.

Table 4.14. Pt^0:Pt^{4+} ratio for 2.5wt% Pt/SiO$_2$ calcined at different ramp rates determined by XPS spectra peak analysis.

Sample calcination ramp rate	Pt^0:Pt^{4+} ratio
5°C/min	54:46
10°C/min	49:51
20°C/min	55:45

The Pt^0:Pt^{4+} ratio reveals that the ratio was very similar for the 5°C/min and 20°C/min calcination samples where Pt^0 contents of 54% and 55% were observed for both samples. This observation can be correlated to the very similar catalytic activities of both samples. This reinforces the proposal that the amount of Pt^0 relative to Pt^{4+} was crucial to producing a highly active catalyst.

109

4.6   The Effect of Varying Calcination Atmosphere on the Total Oxidation of Naphthalene

4.6.1   Activity Data

Comparison of Calcination Atmosphere on Naphthalene Total Oxidation - 2.5wt% Pt/SiO$_2$
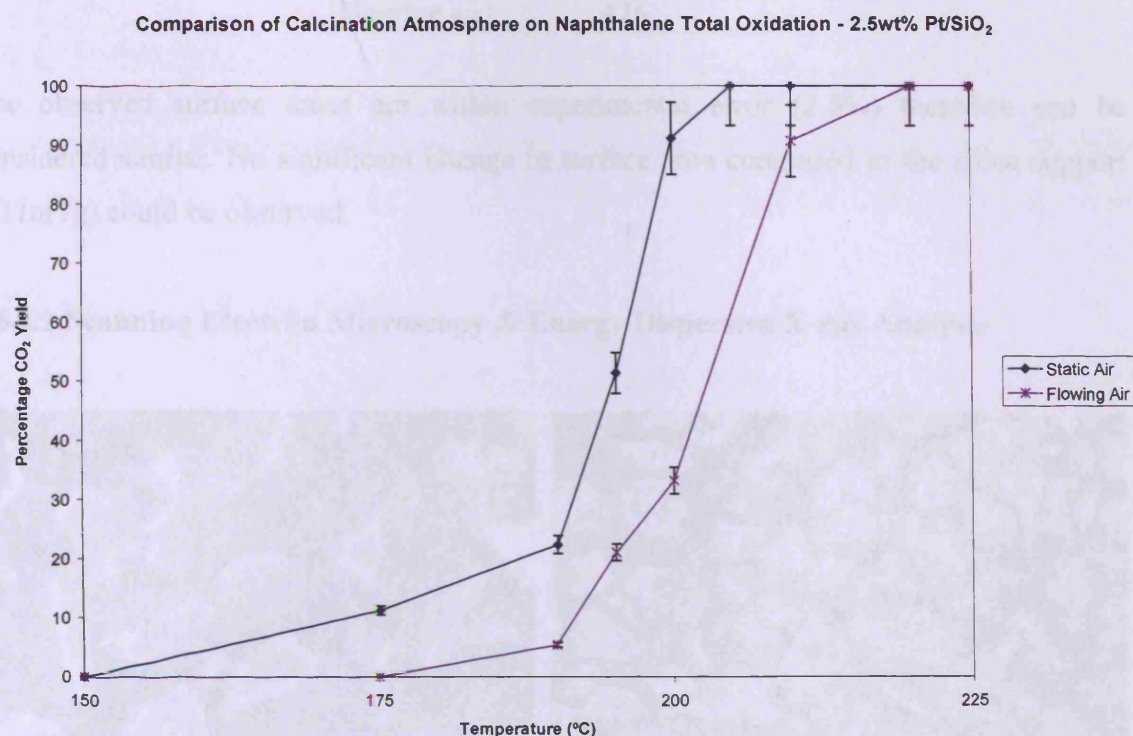
Figure 4.14. Activity data for 2.5wt% Pt/SiO$_2$ calcined in different environments. Temperature range: 150 – 225°C. GHSV = 45,000h^{-1}, 100vppm naphthalene, total flow = 50mL/min. Other calcination parameters: 550°C, 12h, 5°C/min ramp rate. Error bars are ± 6.7%.

As the above figure shows, calcination by static air gave a significantly more active catalyst. 100% CO$_2$ yields were achieved at 205°C (static air) and 220°C (flowing air). T$_{50}$ values of 194.5°C (static air) and 203°C (flowing air) were observed. Repeat experiments confirmed these findings.

110

4.6.2 Characterisation

4.6.2.1 Surface Area Analysis

Table 4.15. Surface areas determined via the BET method using N_2 at 77K.

Sample	Surface Area (m^2/g)
Static air	438
Flowing air	426

The observed surface areas are within experimental error (2.5%) therefore can be considered similar. No significant change in surface area compared to the silica support ($431m^2/g$) could be observed.

4.6.2.2 Scanning Electron Microscopy & Energy Dispersive X-ray Analysis
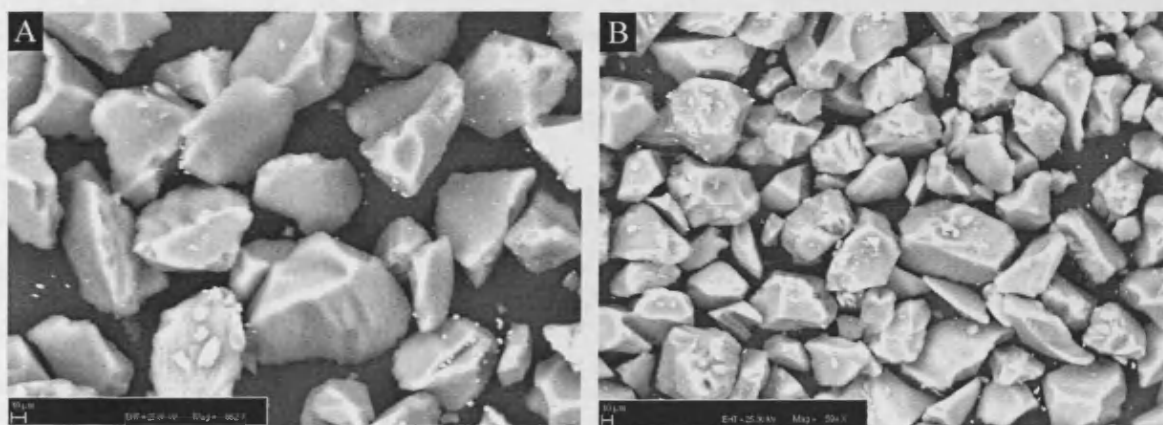
Figure 4.15. BSE based images of 2.5wt% Pt/SiO₂ calcined in different atmospheres; a) static air and b) flowing air.

If the images from the analysis of the two samples are compared, it appears that the concentration of noticeable Pt clusters is very similar. This might be considered to be slightly unusual if the catalytic activities of the two samples are considered; they were not similar. In previous studies during this investigation, significant differences in catalytic activities can correspond with differences in the imaging of the samples. It appeared that some Pt particles were isolated from the support, as the BSE image of 2.5wt% Pt/SiO₂ calcined in static air shows in the figure above. This suggests that the Pt adhesion to the support was relatively low, implying that a weak MSI between Pt and the silica existed.

111

4.6.2.3 CO Chemisorption

Table 4.16. CO chemisorption data for 2.5wt% Pt/SiO$_2$ calcined in different atmospheres. Pretreatment conditions: 400°C, 1h, H$_2$. CO chemisorption performed at RT using 50µL pulses of CO . Sample mass used *ca.* 500mg.

Atmosphere	Av. Crystallite Size (Å)	Dispersion (%)	Surface area (m^2/g)
Static air	264	4	0.3
Flowing air	245	5	0.3

Both samples were observed to have similar crystallite sizes and dispersions, although the static air was observed to have the larger Pt crystallite size and a slightly lower dispersion.

4.6.2.4 X-ray Photoelectron Spectroscopy
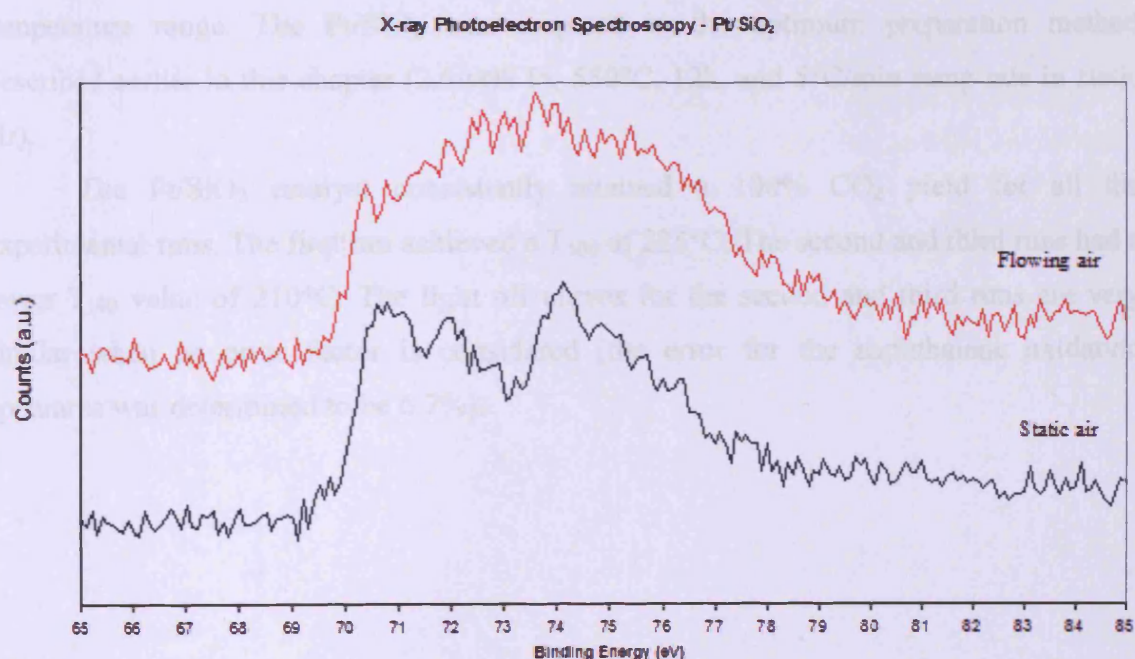
Figure 4.16. Pt 4f spectra of 2.5wt% Pt/SiO$_2$ calcined in different atmospheres.

The spectra for the static air calcination sample displayed binding energies of 71eV and 74eV as in previous studies within this text relating to Pt^0 and Pt^{4+} respectively. However, the flowing air calcination sample displayed a broad peak over a range of binding energies which consist of metallic Pt and two forms of oxidised Pt (Pt^{2+} and Pt^{4+}). This

112

suggests that the Pt contains a relatively significant amount of Pt^{2+}, which has been observed in catalysts which display poor activity for naphthalene total oxidation[1].

The static air calcination sample also acts as a control experiment since its preparation precisely follows the same preparation procedure as that undertaken in the previous section (2.5wt% Pt, 12h, 550°C, 5°C/min, static air). A $Pt^0:Pt^{4+}$ ratio of 56:44 was observed for the static air calcination sample, which is similar to that observed for the 5°C/min calcination ramp rate sample (studied in section 4.5) $Pt^0:Pt^{4+}$ ratio (54:46). Due to the lack of discrete peaks due to oxidised and metallic Pt, a Pt^0: Pt oxide ratio could not be established for the flowing air calcination sample.

4.7   Time On-Line and Catalyst Stability Studies

Pt/SiO_2 was tested for its activity over an extended period of time at high temperature. In a separate experiment, a fresh sample was subjected to repeated runs through its light-off temperature range. The Pt/SiO_2 was prepared to the optimum preparation method described earlier in this chapter (2.5wt% Pt, 550°C, 12h, and 5°C/min ramp rate in static air).

The Pt/SiO_2 catalyst consistently attained a 100% CO_2 yield for all the experimental runs. The first run achieved a T_{100} of 225°C. The second and third runs had a lower T_{100} value of 210°C. The light off curves for the second and third runs are very similar when an error factor is considered (the error for the naphthalene oxidation apparatus was determined to be 6.7%).

Stability of 2.5wt% Pt/SiO₂ for the Total Oxidation of Naphthalene
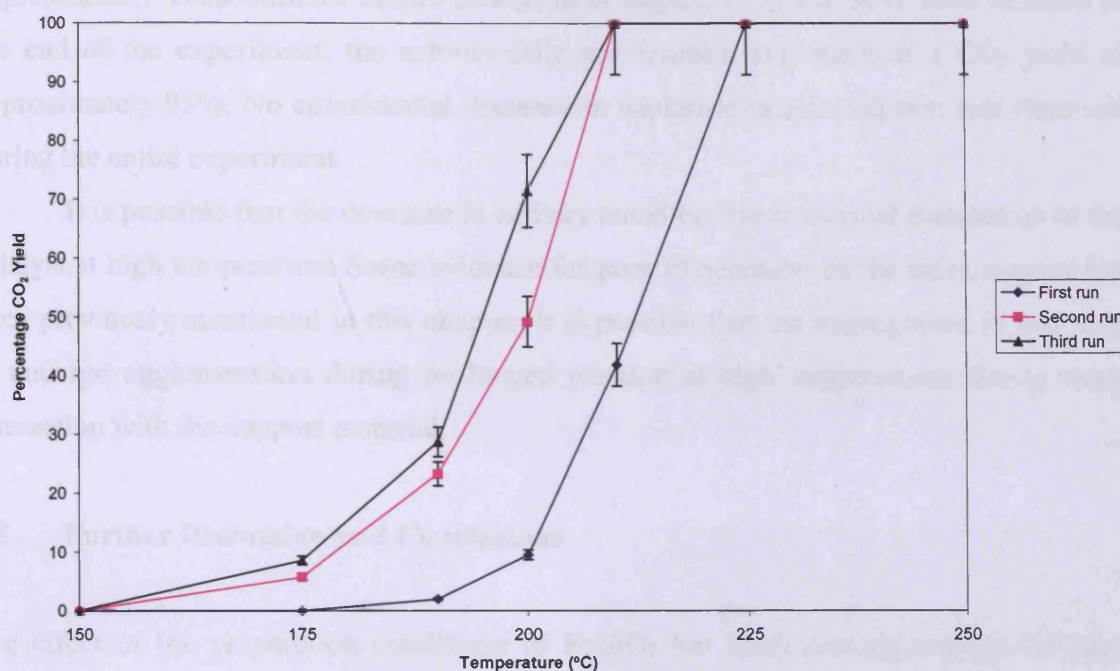
Figure 4.17. Activity data from three reaction cycles over a three day period using the same 2.5wt% Pt/SiO₂ sample. Temperature range: 150 – 250°C. GHSV = 45,000h⁻¹, 100vppm naphthalene, total flow = 50mL/min. Catalyst calcination conditions: 550°C, 12h, 5°C/min, static air. Error bars are ± 6.7%.

TOL Study (48h) - 2.5% Pt/SiO₂
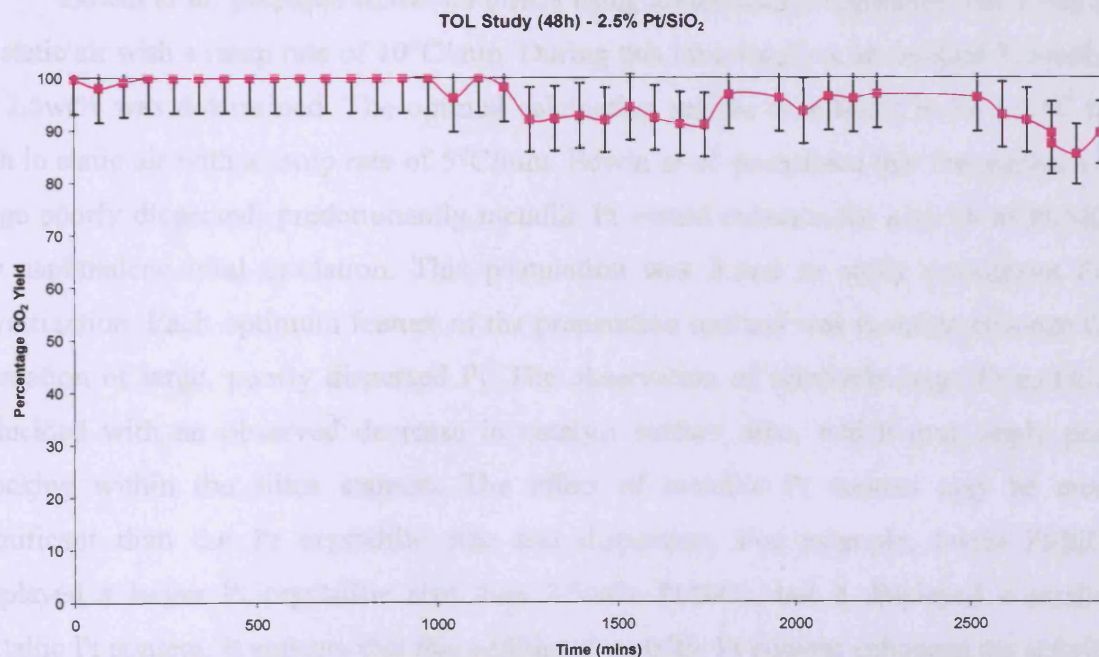
Figure 4.18. Time on-line study of 2.5wt% Pt/SiO₂ over a 48h period at 300°C. GHSV = 45,000h⁻¹, 100vppm naphthalene, total flow = 50mL/min. Catalyst preparation conditions: 550°C, 12h, 5°C/min, static air. Error bars are ± 6.7%.

114

Generally, the catalytic activity of Pt/SiO_2 remains at 100% CO_2 yield for approximately 1000 minutes before deactivation begins. Over the next 1800 minutes to the end of the experiment, the activity falls and remains consistent at a CO_2 yield of approximately 95%. No coincidental decrease in naphthalene consumption was observed during the entire experiment.

It is possible that the decrease in activity could be due to thermal destruction of the catalyst at high temperature. Some evidence for poor Pt adhesion on the silica support has been previously mentioned in this chapter; it is possible that the impregnated Pt was able to undergo agglomeration during prolonged reaction at high temperatures due to weak interaction with the support material.

4.8   Further Discussion and Conclusions

The effect of the preparation conditions of Pt/SiO_2 has been investigated for the total oxidation of naphthalene. These investigated conditions involved both the Pt content of the catalysts and the calcination regime (temperature, time, ramp rate and atmosphere). Based on a preparation procedure which was previously reported[1], each part of the preparation regime was investigated in a matrix fashion.

Edwin *et al.* prepared 0.5wt% Pt/SiO_2 using a calcination regime of 550°C for 6h in static air with a ramp rate of 10°C/min. During this investigation, an optimal Pt loading of 2.5wt% was determined. The optimal calcination regime was found to be 550°C for 12h in static air with a ramp rate of 5°C/min. Edwin *et al.* postulated that the presence of large poorly dispersed; predominantly metallic Pt would enhance the activity of Pt/SiO_2 for naphthalene total oxidation. This postulation was found to apply throughout this investigation. Each optimum feature of the preparation method was found to enhance the formation of large, poorly dispersed Pt. The observation of relatively large Pt particles coincided with an observed decrease in catalyst surface area, which may imply pore blocking within the silica support. The effect of metallic Pt content may be more significant than the Pt crystallite size and dispersion. For example, 5wt% Pt/SiO_2 displayed a larger Pt crystallite size than 2.5wt% Pt/SiO_2, but it displayed a smaller metallic Pt content. It appears that this additional metallic Pt content enhanced the activity of 2.5wt% Pt/SiO_2 so that it was more active than 5wt% Pt/SiO_2. This therefore suggests that whilst a large Pt crystallite size/low dispersion was necessary, the nature of the Pt

oxidation states needed to favour metallic Pt to fully exploit the activity of these large Pt crystallite size catalysts. The same observation was made whilst probing calcination temperature; calcination at higher temperatures (650°C and 750°C) afforded the largest Pt crystallite sizes, but the higher degree of metallic Pt produced with a calcination temperature of 550°C afforded the more active catalyst. The presence of Pt^{4+} based oxides was observed during XRD analysis of a number of samples, where a peak at approximately 35°2θ was observed[13]. All XRD patterns revealed the presence of metallic Pt as shown in the relevant figures above.

EDX analysis also consistently confirmed the presence of large Pt particles such as that shown in the EDX mapping data given in figure 4.19.
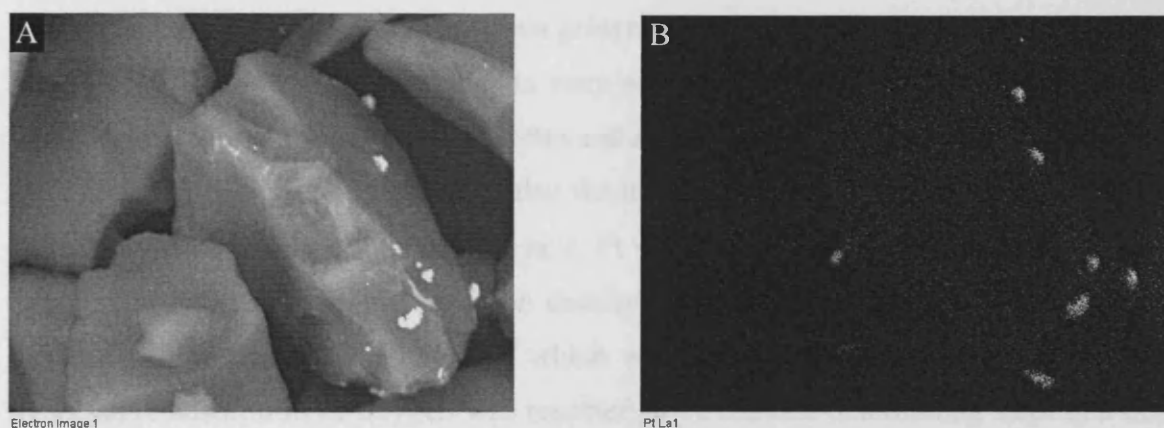
Figure 4.19. Images of 2.5wt% Pt/SiO2 calcined at 550°C for 12h at a ramp rate of 5°C/min in static air; a) BSE image and b) Pt element map.

The image on the left was obtained using a BSE detector analysing all elemental signals. The right hand side image shows the portions of the image that presented the X-ray wavelengths that related to Pt atoms. By cross referencing the two images, it can be shown that the positions of the bright spots on the BSE image and the Pt signal responses coincided. Therefore this agrees with the BSE based data presented thus far that the bright spots on the images are due to Pt clusters.

There is further scope to probe the calcination regime of Pt/SiO₂. For example, the effect of thermal treatment in an inert atmosphere has not been probed to investigate if a decrease in the amount of oxidised Pt occurs.

Some catalysts displayed mass transfer behaviour, i.e. where the rate of adsorption onto the catalyst surface is slower than the rate of oxidation. These catalysts generally had

relatively small Pt crystallites. They also displayed relatively low metallic Pt contents. This further suggests that the active site is found on metallic Pt. It has been shown previously that naphthalene oxidation can occur over Pt/γ-Al$_2$O$_3$ catalysts via either a Langmuir-Hinschelwood[14] or Eley-Rideal[15] mechanism. However, neither paper directly probed the Pt oxidation state.

Radic and co-workers performed kinetic experiments with regards to toluene oxidation over Pt/Al$_2$O$_3$[16]. The Mars van Krevelen mechanism was used to describe the kinetic data in that paper. It was reported that the oxygen chemisorption rate increased with increasing Pt crystallite size. The oxygen chemisorption activation energy also decreased with increasing Pt crystallite size which gave rise to an increased reaction rate. Relatively weak Pt-O bonds were reported to form on larger Pt crystallites. Although no data on Pt oxidation state (e.g. XPS) was presented, the authors stated their belief that the Pt was metallic since their experiments were performed at temperatures where stable Pt oxide formation was not favoured. Garetto and Apesteguía observed similar behaviour for cyclopentane[17]. The authors reported that the turnover frequency values for cyclopentane increased with increasing Pt crystallite size. Pt was cited to exist as metallic particles and larger Pt crystallite sizes increased the density of active Pt-O species and that a redox mechanism operated, the first step of which was oxidation of metallic Pt to Pt-O. The dissociative adsorption of oxygen was reported to be the rate determining step. In a time on stream experiment for cyclopentane oxidation, it was found that cyclopentane conversion increased with time. This was reported to be due to agglomeration of the Pt to larger hence more active Pt crystallites during the experiment. A similar observation was made during this study during cycled use of the same Pt/SiO$_2$ sample. The activity of the first run was noticeably less than subsequent runs. When the entire experiment was repeated, the same observation was made. Therefore one can suppose that agglomeration of the Pt occurred during the first run, optimising the Pt crystallite size for subsequent runs. In the time on line experiment, the temperature was significantly higher than that observed to achieve a 100% CO$_2$ yield. Therefore an induction period of the type reported by Garetto and Apesteguía for cyclopentane oxidation does not appear to apply here.

In the time on line experiment reported in section 4.7, a reduction in CO$_2$ yield was observed after approximately 1000 minutes. One possible explanation of this is that excessive agglomeration of the Pt clusters may occur at 300°C over an extended period of time. The plateau after approximately 1150 minutes would then imply that agglomeration

had ceased. Another possibility is that the proportion of metallic Pt decreased with time, which would reduce the number of active sites hence, activity. It was not possible to recover a sufficient quantity of the used catalyst to perform sufficient characterisation studies to probe the changes in activity in the TOL or cycled use experiments.

As Pt/SiO$_2$ has been observed to give rise to a 100% CO$_2$ yield at temperatures below 250°C, a repeat experiment at 250°C may be useful to perform. The reason for this is that Pt agglomeration may be avoided or its effect lessened during the TOL experiment.

In this study, it can be suggested that the Pt^{4+} component of the Pt/SiO$_2$ catalysts would go on to form PtO$_2$ when oxygen is present. If the relatively weak Pt-O bonds are formed during oxygen adsorption on the surface with metallic Pt and that a redox mechanism such as the Mars van Krevelen operates, then minimising Pt^{4+} content in favour of metallic Pt would be beneficial to activity. In other words, Pt^{4+} would form an oxide where the oxygen could be too tightly held, thus disallowing an interaction of the adsorbed hydrocarbon with PtO$_2$. Kinetic studies of Pt/SiO$_2$ known to predominantly contain metallic Pt would need to be performed to probe this postulation.

4.9 The Effect of the SiO$_2$ Support on the Total Oxidation of Naphthalene

Now that the calcination parameters have been optimised, attention turned to other catalyst features which may benefit from optimisation. Firstly, different types of SiO$_2$ were compared. The 60Å pore SiO$_2$ was taken as a baseline dataset and compared against two other types of SiO$_2$. One (denoted herein as nanopowder SiO$_2$) was supplied by Aldrich and used as received. The second hollow sphere SiO$_2$ support was prepared using this nanopowder SiO$_2$ by Asuncion Aranda. Full preparation details are given in section 2.1.4.6. The regime used in the preparation of these catalysts was based on the experiments performed in this chapter (i.e. a Pt content of 2.5wt% with a calcination regime of 550°C for 12h in static air at a ramp rate of 5°C/min).

4.9.1 Activity Data

Comparison of SiO$_2$ Type on Naphthalene Total Oxidation - 2.5wt% Pt/SiO$_2$
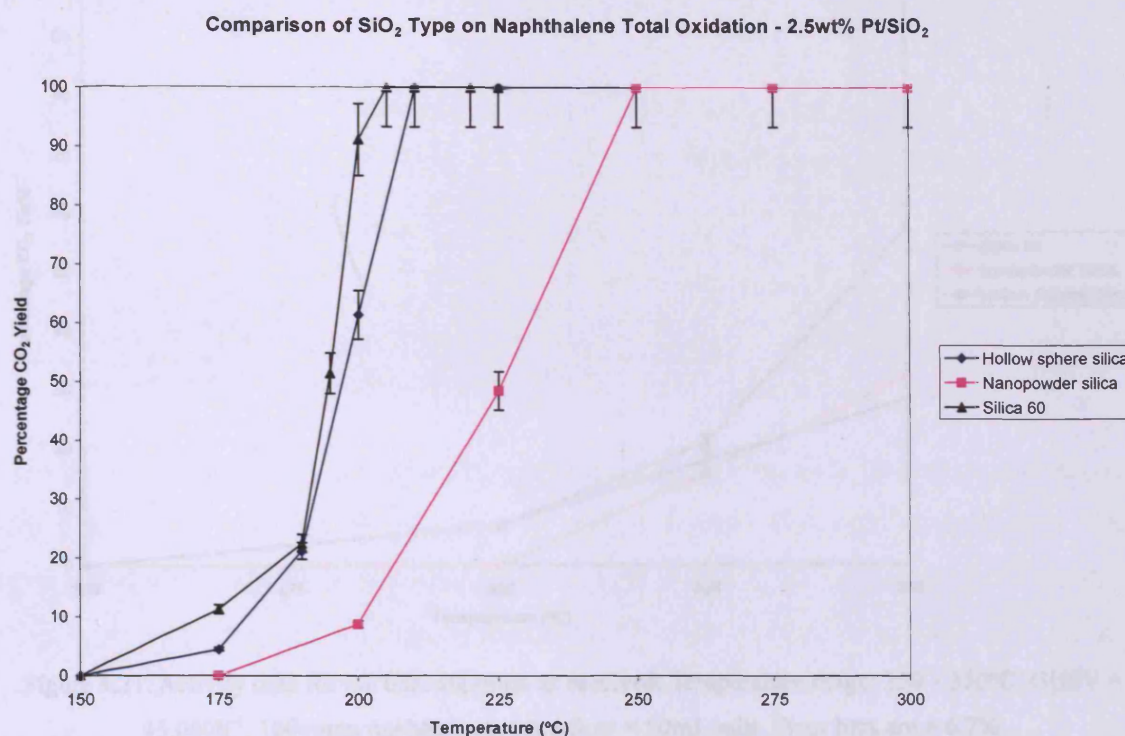
Figure 4.20. Activity data for 2.5wt% Pt/SiO$_2$ using three different types of SiO$_2$ support. Temperature range: 150 – 300°C. GHSV = 45,000h^{-1}, 100vppm naphthalene, total flow = 50mL/min. Calcination parameters: 550°C, 12h, 5°C/min ramp rate, static air. Error bars are ± 6.7%.

The 60Å pore silica as a support could not be improved upon. The hollow sphere silica did give a highly active catalyst, which suggests that large, poorly dispersed Pt particles were impregnated onto the hollow sphere silica. At this point, it was not possible to tell whether the impregnated Pt was within the hollow sphere free space, or if the hollow sphere pores were blocked by Pt, hence the Pt impregnation occurred on the exterior of the hollow spheres.

The nanopowder silica was the poorest performing support. A much higher temperature was required to reach T$_{50}$ and 100% CO$_2$ yield compared to the 60Å pore and hollow sphere silica supports. At this point, it is not possible to tell definitively why this was so; it could be due to either a highly dispersed, small particle Pt catalyst was synthesised (which so far has been demonstrated to be less active than larger, poorly dispersed Pt crystallites), or the pores of the support were too small for the large, poorly dispersed Pt crystallites, hence resulting in a significant decrease in surface area. When the supports used as prepared/received were analysed, the following data were collected.

119

Comparison of SiO$_2$ Supports on Naphthalene Total Oxidation
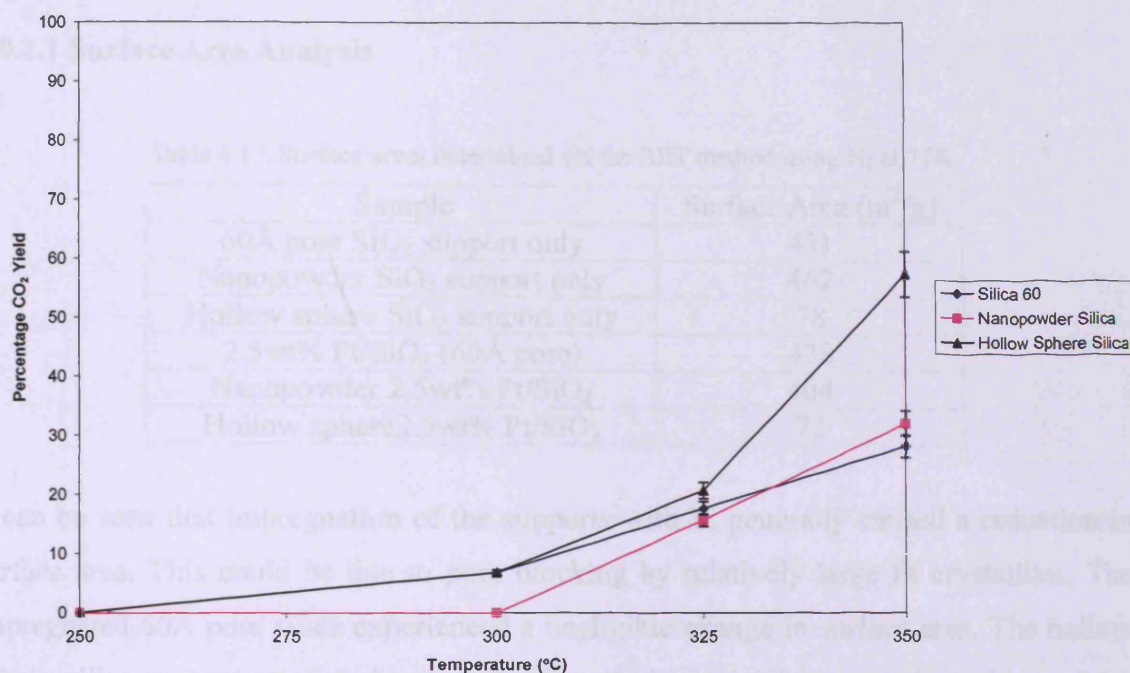
Figure 4.21. Activity data for the bare supports as received. Temperature range: 250 – 350°C. GHSV = 45,000h^{-1}, 100vppm naphthalene, total flow = 50mL/min. Error bars are ± 6.7%.

All the bare supports (as received) displayed activity for the total oxidation of naphthalene. The most active was the hollow sphere SiO$_2$ with a maximum CO$_2$ yield of 57% at 350°C. The least active catalyst (in terms of absolute CO$_2$ yield) was the 60Å pore SiO$_2$ support with a 28% CO$_2$ yield at 350°C. However, at 300°C, the 60Å pore SiO$_2$ gave a very similar CO$_2$ yield to the hollow sphere silica support (approximately 7%). The nanopowder silica was inactive at 300°C. This experiment therefore shows that the impregnation of the Pt metal was the key feature of producing a catalyst capable of obtaining a 100% CO$_2$ yield.

To conclude, the 60Å pore SiO$_2$ gave rise to the most active Pt catalyst and it was this material that was used in subsequent catalysts preparations during this study.

120

4.9.2 Characterisation

4.9.2.1 Surface Area Analysis

Table 4.17. Surface areas determined via the BET method using N_2 at 77K.

Sample	Surface Area (m^2/g)
60Å pore SiO_2 support only	431
Nanopowder SiO_2 support only	462
Hollow sphere SiO_2 support only	78
2.5wt% Pt/SiO_2 (60Å pore)	438
Nanopowder 2.5wt% Pt/SiO_2	404
Hollow sphere2.5wt% Pt/SiO_2	72

It can be seen that impregnation of the supports with Pt generally caused a reduction in surface area. This could be due to pore blocking by relatively large Pt crystallites. The impregnated 60Å pore silica experienced a negligible change in surface area. The hollow sphere silica was reported to have a significantly lower surface area than either of the other supports investigated. The surface area of the material appears to have limited consequence when correlating the activity data with the obtained surface area data. The nanopowder based Pt/SiO_2 was the least active, yet displayed a similar surface area to the most active catalyst (the 60Å pore based Pt/SiO_2). The surface areas were observed to be $404m^2/g$ and $438m^2/g$ respectively. The hs-Pt/SiO_2 had the lowest surface area ($72m^2/g$) but an activity that was comparable to that of 60Å pore Pt/SiO_2.

4.9.2.2 X-ray Diffraction
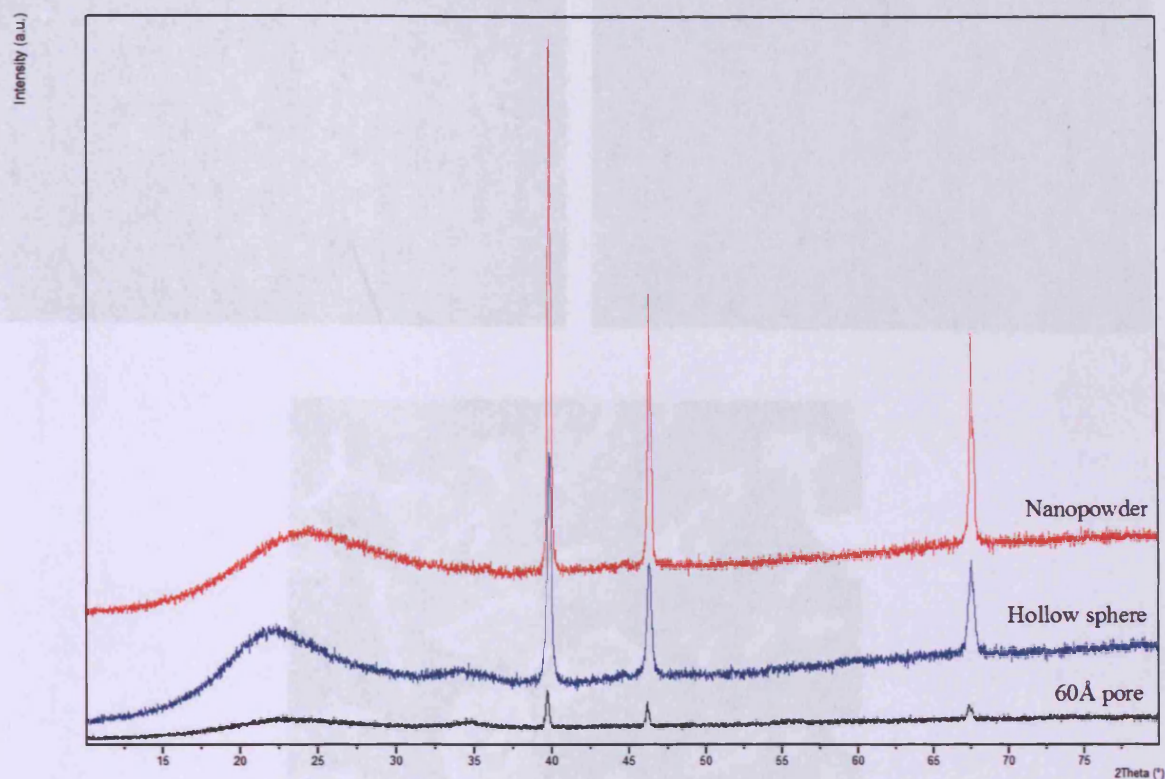
Figure 4.22. XRD patterns obtained for 2.5wt% Pt/SiO$_2$ prepared on different types of SiO$_2$.

All the Pt/SiO$_2$ samples were matched with reference cubic Pt phases as with all the Pt/SiO$_2$ samples studied thus far. No crystalline phases due to the support were observed in the impregnated catalysts, as shown in the figure above.

4.9.2.3 Scanning Electron Microscopy & Energy Dispersive X-ray Analysis

The images obtained for 60Å pore SiO$_2$ have already been presented and discussed in previous sections of this chapter. The following images are for hollow sphere and nanopowder SiO$_2$ supports doped with 2.5wt% Pt as with the previous catalyst preparations presented in this chapter. There was a distinct lack of bright spots (which have been shown to be due to Pt clusters) for the nanopowder and hollow sphere silica based samples.

122
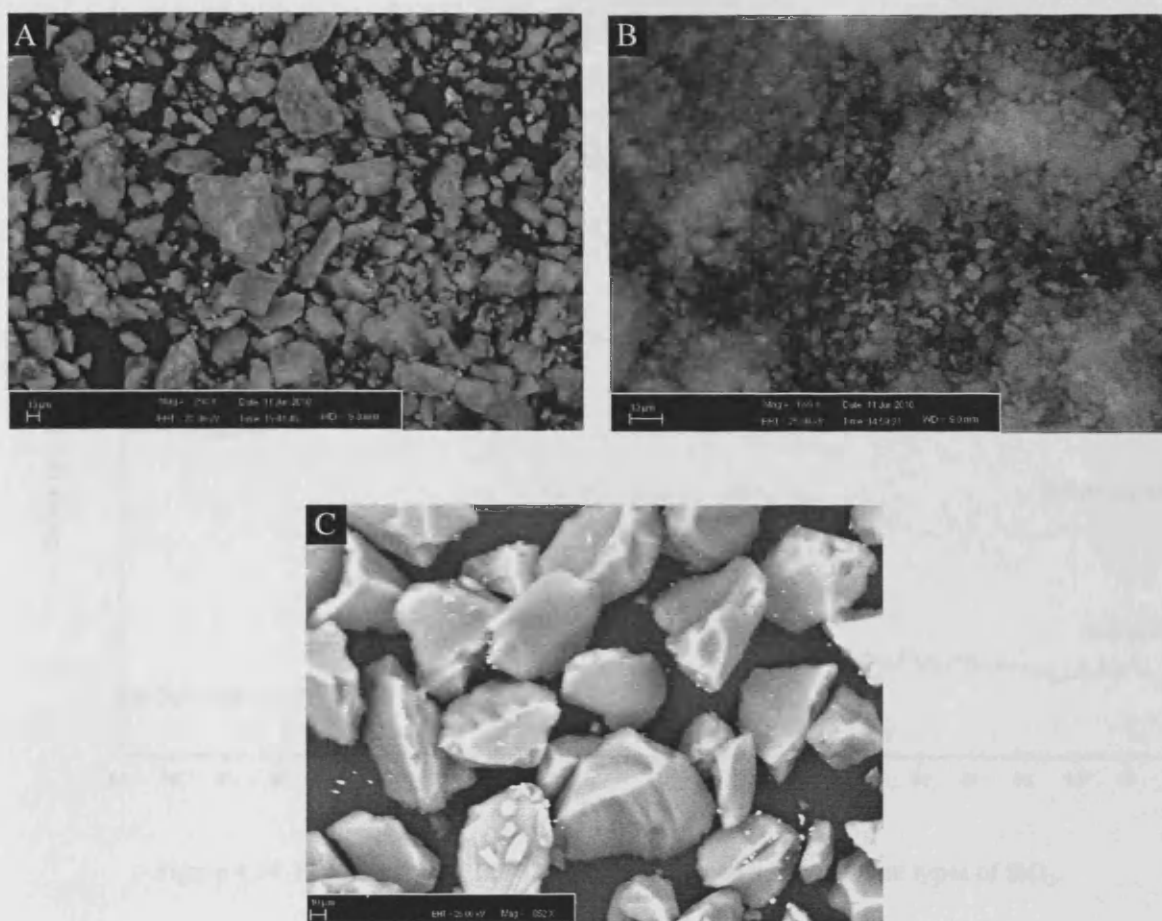
Figure 4.23. BSE images of 2.5wt% Pt/SiO₂ prepared on different types of SiO₂ support; a) hollow sphere; b) nanopowder and c) 60Å pore SiO₂.

4.9.2.4 CO Chemisorption

Table 4.18. CO chemisorption data for 2.5wt% Pt/SiO₂ prepared on different SiO₂ supports. Pretreatment conditions: 400°C, 1h, H₂. CO chemisorption performed at RT using 50µL pulses of CO. Sample mass used *ca*. 300-500mg.

SiO₂ type	Av. Crystallite Size (Å)	Dispersion (%)	Surface area (m²/g)
60Å pore	264	4	0.27
nanopowder	226	5	0.31
hollow sphere	305	3	0.22

The nanopowder based catalyst was the least active of the three catalysts investigated, yet the Pt crystallite parameters were very similar to those observed for the most active catalyst (the 60Å pore SiO₂ based catalyst). The hollow sphere catalyst was observed to have similar Pt dispersion and the largest average crystallite size.

123

4.9.2.5 X-ray Photoelectron Spectroscopy

X-ray Photoelectron Spectroscopy - Pt/SiO₂
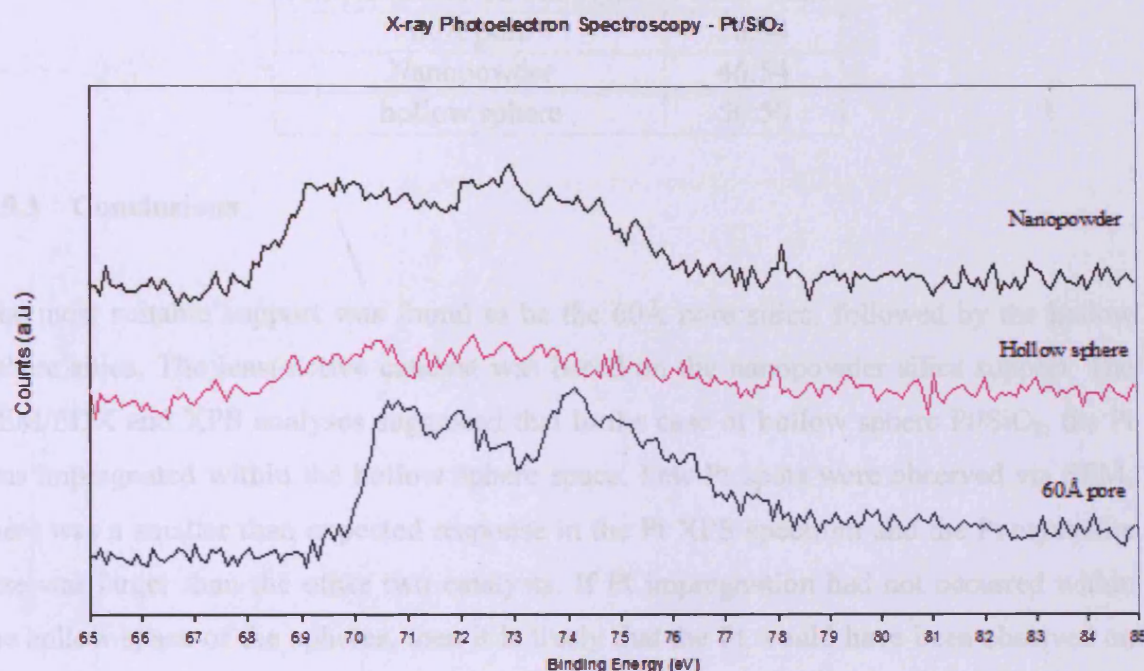
Figure 4.24. Pt 4f spectra of 2.5wt% Pt/SiO₂ prepared using different types of SiO₂.

The nanopowder and 60Å pore support based Pt/SiO₂ catalysts both displayed doublet peaks as discussed previously for Pt^0 and Pt^{4+}. The Pt signal for the hollow sphere catalyst was relatively weak, which suggests that the Pt did not interact fully with the incident analysis beam, since XPS is a surface sensitive technique. This in turn suggests that the Pt was impregnated within the hollow spheres. Milling the sample prior to analysis would give some insight into if the Pt content was significantly lower than the intended 2.5wt%. However, there was not enough sample available (due to a limited amount of the support being available for impregnation) to perform additional XPS analysis. The data presented in the table below suggests that the most active catalyst contained the highest Pt^0 ratio of the three catalysts examined. The lowest Pt^0 ratio was observed for the nanopowder Pt/SiO₂, which was the least active catalyst.

Table 4.19. $Pt^0:Pt^{4+}$ ratio for 2.5wt% Pt/SiO₂ prepared on different SiO₂ types determined by XPS spectra peak analysis.

Sample (based on SiO₂ type)	$Pt^0:Pt^{4+}$ ratio
60Å pore	56:44
Nanopowder	46:54
hollow sphere	50:50

4.9.3 Conclusions

The most suitable support was found to be the 60Å pore silica, followed by the hollow sphere silica. The least active catalyst was based on the nanopowder silica support. The SEM/EDX and XPS analyses suggested that in the case of hollow sphere Pt/SiO₂, the Pt was impregnated within the hollow sphere space. Few Pt spots were observed via SEM, there was a smaller than expected response in the Pt XPS spectrum and the Pt crystallite size was larger than the other two catalysts. If Pt impregnation had not occurred within the hollow space of the spheres, then it is likely that the Pt would have been observed on the exterior of the spheres during SEM/EDX analysis. The depth of the interaction volume of the incident electron beam interacting with the sample may not be large enough to permeate through the silica spheres, resulting in little interaction with the Pt encased in the hollow spheres. It should be noted that the same volume of the same Pt stock solution was used in all three catalyst preparations; therefore all Pt contents should be similar. Although hollow sphere Pt/SiO₂ was observed to have the more desirable Pt crystallite size and dispersion, it did not display as high a metallic Pt content as the 60Å pore Pt/SiO₂. This increased metallic Pt content seemed to enhance the activity of the 60Å pore Pt/SiO₂ more than the Pt crystallite size/dispersion enhanced the activity of the hollow sphere Pt/SiO₂. In other words, the effect of Pt oxidation state appeared to be greater than the effect of Pt crystallite size/dispersion, although both features are important to produce an active catalyst. In previous sections of this chapter, a correlation between activity and Pt crystallinity from XRD analysis has occasionally been observed; more crystalline Pt was attributed to enhanced activity. However, this appears that Pt oxidation states crystallite sizes/dispersions are the more dominant factors. The most crystalline Pt catalyst was the least active and the most active catalyst displayed the least crystalline Pt phase. Analysis via Scherrer's method showed no correlation between Pt crystallite size and activity.

4.10 The Effect of Exchanging Pt/SiO$_2$ for Pd/SiO$_2$ on the Total Oxidation of Naphthalene

4.10.1 Activity Data
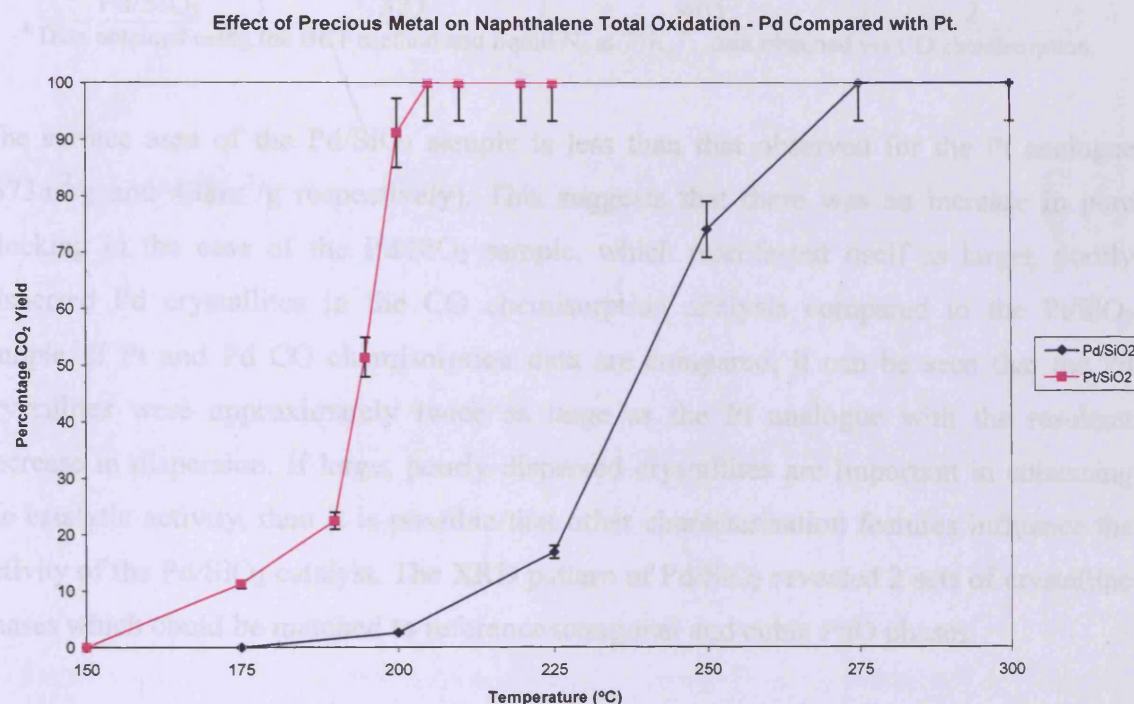
Figure 4.25. Activity data for 2.5wt% Pd/SiO$_2$ compared to 2.5wt% Pt/SiO$_2$ prepared in an identical fashion. Temperature range: 150 – 300°C. GHSV = 45,000h^{-1}, 100vppm naphthalene, total flow = 50mL/min. Calcination parameters: 550°C, 12h, 5°C/min ramp rate, static air. Error bars are ± 6.7%.

As the above figure shows, Pd/SiO$_2$ is considerably less active than the Pt analogue. A temperature of 275°C was required for Pd/SiO$_2$ to reach a CO$_2$ yield of 100% whereas the Pt/SiO$_2$ catalyst typically required a temperature of 205°C. Therefore, it was not possible during this study to synthesise a Pd catalyst that had comparable or greater catalytic activity than its Pt analogue.

4.10.2 Characterisation

Table 4.20. Characterisation data for Pd/SiO₂ calcined using the optimum conditions described above. A comparison with a Pt/SiO₂ analogue is also included.

Sample	Surface Area (m²/g)[a]	Av. Crystallite Size (Å)[b]	Dispersion (%)[b]
Pt/SiO₂	438	264	4
Pd/SiO₂	373	465	2

[a]: Data obtained using the BET method and liquid N_2 at 77K, [b]: data obtained via CO chemisorption.

The surface area of the Pd/SiO₂ sample is less than that observed for the Pt analogue ($373m^2/g$ and $438m^2/g$ respectively). This suggests that there was an increase in pore blocking in the case of the Pd/SiO₂ sample, which manifested itself as larger, poorly dispersed Pd crystallites in the CO chemisorption analysis compared to the Pt/SiO₂ sample. If Pt and Pd CO chemisorption data are compared, it can be seen that the Pd crystallites were approximately twice as large as the Pt analogue with the resultant decrease in dispersion. If large, poorly dispersed crystallites are important in enhancing the catalytic activity, then it is possible that other characterisation features influence the activity of the Pd/SiO₂ catalyst. The XRD pattern of Pd/SiO₂ revealed 2 sets of crystalline phases which could be matched to reference tetragonal and cubic PdO phases.

127
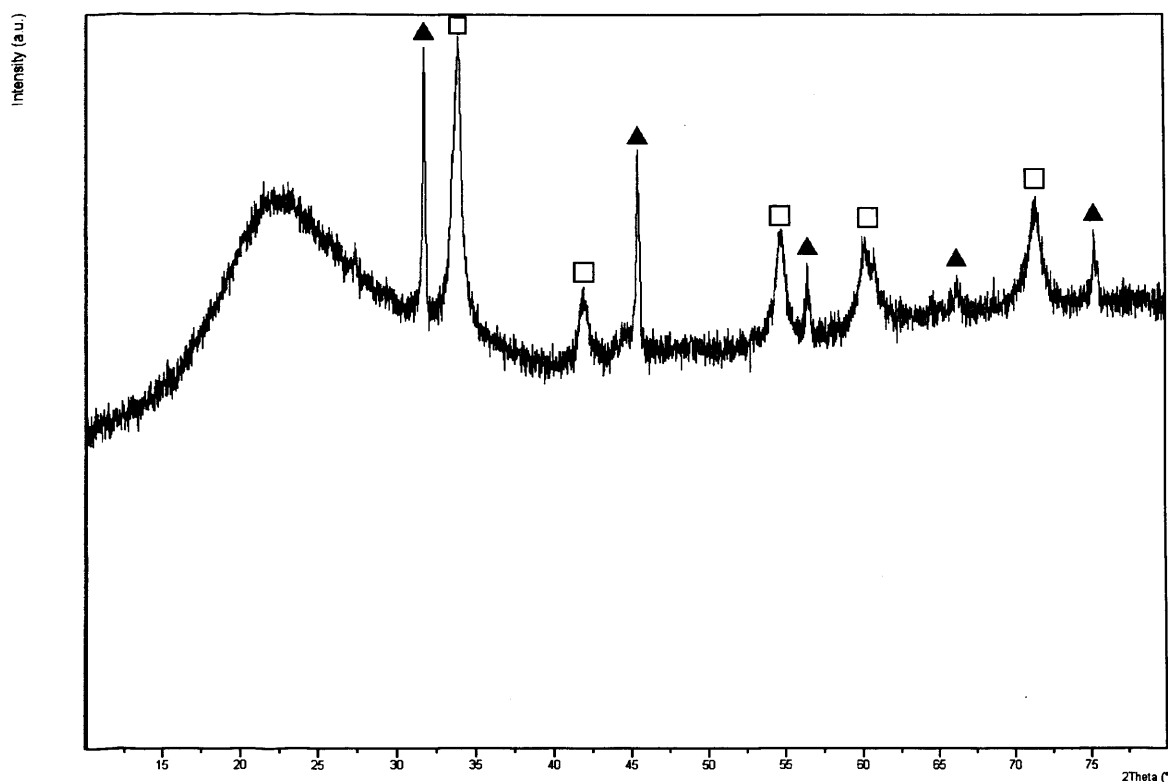
Figure 4.26. XRD pattern obtained for Pd/SiO$_2$ displaying tetragonal (□) and cubic (▲) PdO phases.

As the following figure shows, the use of the tetrachloropalladate salt resulted in the formation of block-like particles on the surface of the Pd/SiO$_2$ sample. The elemental maps revealed that these block-like structures are composed of Na and Cl. The maps also suggest that the Pd was evenly dispersed on the surface and did not display the larger Pt particles as for the 2.5wt% Pt/SiO$_2$ analogue.
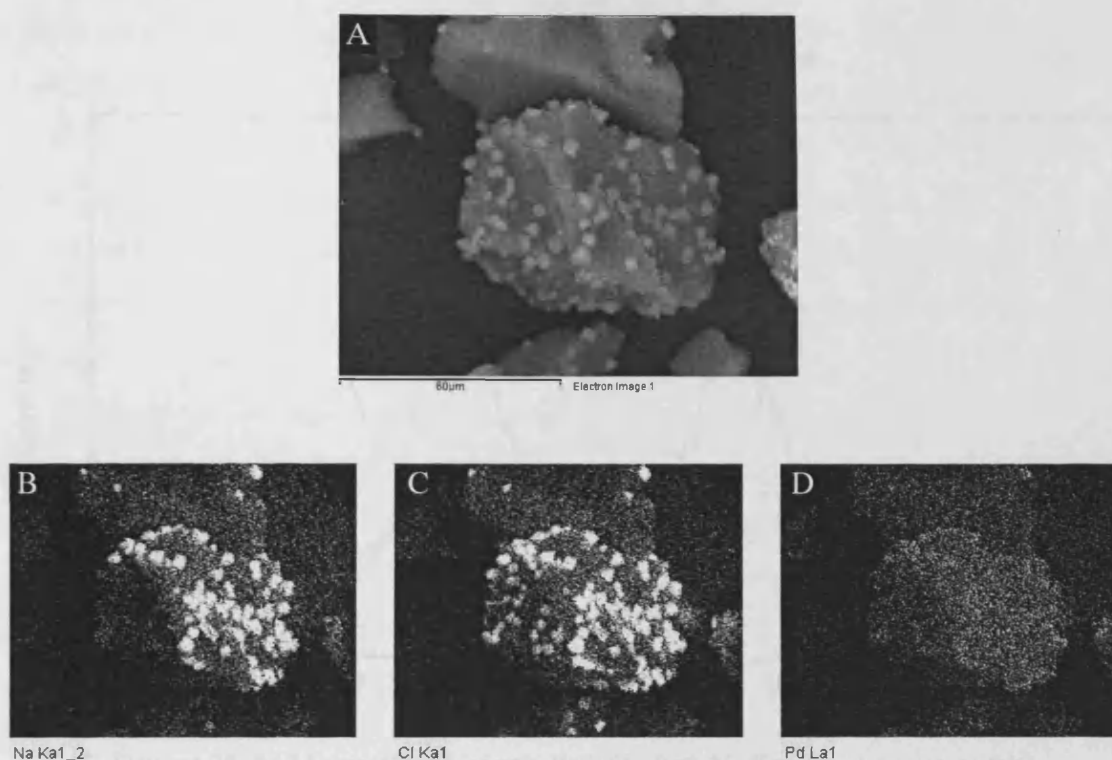
Figure 4.27. a) BSE image of Pd/SiO₂ displaying block-like formations. Elemental maps of b) Na; c) Cl; d) Pd.

XPS analysis revealed that approximately the correct amount of Pd was impregnated during the original catalyst preparation (figure 4.28 and table 4.21). As shown previously in this chapter, Pt contents were often close to the intended loading. The Pd/SiO₂ sample did display binding energies of approximately 337 and 342eV. These were assigned PdO from the Pd $3d_{5/2}$ spectrum[11, 18] and PdO from the Pd $3d_{3/2}$ spectrum respectively[19]. Little metallic Pd was observed. The presence of both Na and Cl were also detected, supporting the observations made during EDX analysis.

X-ray Photoelectron Spectroscopy - Pd/SiO₂; (Pd)
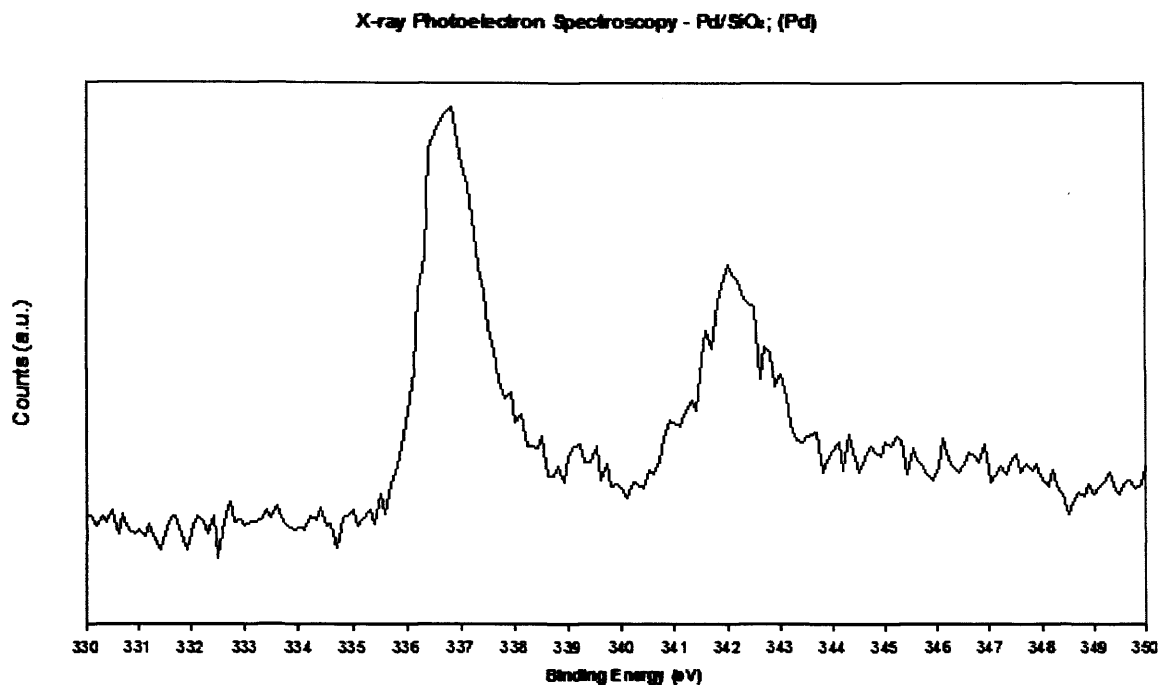
Figure 4.28. Pd 3d spectrum of 2.5wt% Pd/SiO₂. Both binding energies relate to PdO.

Table 4.21. Pd content of Pd/SiO₂ sample investigated in this study. Error of approximately 0.1wt%. Na and Cl contents were not considered during analysis.

Sample	Weight percent Pd
Pd/SiO₂	2.25

4.10.3 Further Discussion & Conclusions

It has been found that Pd/SiO₂ is less active than Pt/SiO₂ for the total oxidation of naphthalene. A difference of approximately 75°C was observed between the T_{100} values. Characterisation studies (XRD, XPS) have revealed that the Pd predominantly exists as PdO. The presence of both Na and Cl were detected via EDX analysis and both can influence the activity of a given catalyst, both positively and negatively[20]. Attempts at synthesising a Na and Cl free catalyst from Pd chloride were made but the results were unsuccessful.

Since the activity of Pd/SiO₂ is significantly higher than SiO₂, it appears that the PdO is an active site for hydrocarbon oxidation. PdO is a feature of many different oxidation reactions, e.g. propane combustion via Pd/SiO₂-Al₂O₃ catalysts[21], methane combustion[22] via Pd/Al₂O₃ and toluene combustion via Pd supported on zeolites[23]. A redox mechanism based on PdO has been proposed in the literature for methane total

oxidation by Ciuparu and Pfefferle[24]. Other studies have also postulated that hydrocarbon oxidation can occur using PdO as an active site via a redox mechanism[25, 26]. Studies where the lattice oxygen contained within an oxide support plays a direct role in the oxidation mechanism have also been published. An example of this came from Ciuparu and Pfefferle where the oxide support was found to transfer lattice oxygen from the support to the PdO[24]. However, this was observed at temperatures above that employed in this study for naphthalene total oxidation.

Assuming that a redox mechanism operates for both Pt and PdO, one could suggest that the reducibility of the PdO active site is less than that of Pt-O (fostered from metallic Pt) as discussed in section 4.8, which would cause higher activity for Pt/SiO$_2$ for the total oxidation of naphthalene. Kinetic studies would be beneficial to ascertain if these suggestions are valid.

There is the possibility that a predominantly metallic Pd active centre may enhance the activity of Pd/SiO$_2$ for the total oxidation of naphthalene. Kim and Shim found similar activities for PdO and metallic Pd supported on γ-Al$_2$O$_3$ over a variety of different VOCs[27]. Cordi and Falconer reported that metallic Pd was more active than PdO for general VOC oxidation[28]. This allows a potential avenue to follow in future experiments to see if this applies to naphthalene total oxidation.

4.11 References

1. N. N. Edwin, A. F. Carley, S. H. Taylor, *Catalysis Today*, **137**, (2008), 362-366.

2. E. Ntainjua, S. H. Taylor, *Topics in Catalysis*, **52**, (2009), 528-541.

3. K. Okumura, T. Kobayashi, H. Tanaka, M. Niwa, *Applied Catalysis B-Environmental*, **44**, (2003), 325-331.

4. J. M. Nhut, L. Pesant, N. Keller, C. Pham-Huu, M. J. Ledoux, *Topics in Catalysis*, **30**, (2004), 353-358.

5. C. Methivier, B. Beguin, M. Brun, J. Massardier, J. C. Bertolini, *Journal of Catalysis*, **173**, (1998), 374-382.

6. C. Methivier, J. Massardier, J. C. Bertolini, *Applied Catalysis A-General*, **182**, (1999), 337-344.

7. M. Conte, A. F. Carley, G. Attard, A. A. Herzing, C. J. Kiely, G. J. Hutchings, *Journal of Catalysis*, **257**, (2008), 190-198.

8.   B. Z. Tian, J. L. Zhang, T. Z. Tong, F. Chen, *Applied Catalysis B-Environmental*, **79**, (2008), 394-401.

9.   D. Briggs, M. P. Seah, *Practical Surface Analysis*, John Wiley & Sons, 1993.

10.   C. D. Wagner, *Journal of Vacuum Science & Technology*, **15**, (1978), 518-523.

11.   T. L. Barr, *Journal of Physical Chemistry*, **82**, (1978), 1801-1810.

12.   S. Hufner, G. K. Wertheim, J. H. Wernick, *Solid State Communications*, **17**, (1975), 417-422.

13.   M. P. H. Fernandez, B. L. Chamberland, *Journal of the Less-Common Metals*, **99**, (1984), 99-105.

14.   X. W. Zhang, S. C. Shen, L. E. Yu, S. Kawi, K. Hidajat, K. Y. S. Ng, *Applied Catalysis A-General*, **250**, (2003), 341-352.

15.   J. L. Shie, C. Y. Chang, J. H. Chen, W. T. Tsai, Y. H. Chen, C. S. Chiou, C. F. Chang, *Applied Catalysis B-Environmental*, **58**, (2005), 289-297.

16.   N. Radic, B. Grbic, A. Terlecki-Baricevic, *Applied Catalysis B-Environmental*, **50**, (2004), 153-159.

17.   T. F. Garetto, C. R. Apesteguia, *Catalysis Today*, **62**, (2000), 189-199.

18.   T. L. Barr, *Journal of Vacuum Science & Technology A-Vacuum Surfaces and Films*, **9**, (1991), 1793-1805.

19.   T. Tateishi, Y. Ito, Y. Okazaki, *Materials Transactions, JIM*, **38**, (1997), 78-84.

20.   M. Bowker, *The Basis and Applications of Heterogeneous Catalysis*, Oxford University Press, 1998, .

21.   Y. Yazawa, H. Yoshida, N. Takagi, S. Komai, A. Satsuma, T. Hattori, *Applied Catalysis B-Environmental*, **19**, (1998), 261-266.

22.   P. Castellazzi, G. Groppi, P. Forzatti, E. Finocchio, G. Busca, *Journal of Catalysis*, **275**, (2010), 218-227.

23.   Z. K. Zhang, L. Y. Xu, Z. L. Wang, Y. J. Xu, Y. F. Chen, *Journal of Natural Gas Chemistry*, **19**, (2010), 417-421.

24.   D. Ciuparu, L. Pfefferle, *Catalysis Today*, **77**, (2002), 167-179.

25.   D. Ciuparu, M. R. Lyubovsky, E. Altman, L. D. Pfefferle, A. Datye, *Catalysis Reviews-Science and Engineering*, **44**, (2002), 593-649.

26.   P. Castellazzi, G. Groppi, P. Forzatti, *Applied Catalysis B-Environmental*, **95**, (2010), 303-311.

27.   S. C. Kim, W. G. Shim, *Applied Catalysis B-Environmental*, **92**, (2009), 429-436.

28.   E. M. Cordi, J. L. Falconer, *Journal of Catalysis*, **162**, (1996), 104-117.

Chapter 5 – The Total Oxidation of Naphthalene and Propane Using Catalysts Prepared in Non-Aqueous Solvents

5.1   Introduction

As mentioned in chapter 1, one of the supports tested by Edwin *et al.* for the total oxidation of naphthalene was SnO_2, which is a hydrophobic material[1]. In other words, the use of an aqueous solution limited the impregnation of Pt onto the surface due to the SnO_2 undergoing a relatively poor wetting process.

Hydrophobic supports generally have low thermal and electrical conductivities. This may lead to weaker metal-support interactions, which, as described above, may be suitable for catalysts that are active for the total oxidation of naphthalene.

There have been several studies reported over the last decade regarding the use of hydrophobic supports as active catalysts for a small number of processes. However, most of these focussed on partial or synthetic oxidation rather than the total oxidation of the given starting material. No reported studies on the use of these materials as supports for the total oxidation of naphthalene where the hydrophobicity of the support has been exploited could be found. Therefore, this could lead to the discovery of novel, highly active catalysts for the total oxidation of VOCs. There have been some reports of hydrophobic supports being used for the total oxidation of light alkanes such as methane and propane. Methane total oxidation in particular has been studied relatively extensively[2-9]. The study of propane total oxidation has been less widespread.

5.1.1   Boron Nitride

Postole *et al.* performed TEM studies on Pd impregnated BN and found that the Pd crystallite size was approximately 3.8nm[10]. At a later date, Postole *et al.* studied BN as a support for oxide based active phases for the selective reduction of NO by C_2H_4 in oxidative conditions[11]. The inertness of BN was shown to hinder the reduction mechanism which suggested that the MSI of BN was very low. In the application of naphthalene total oxidation, this MSI could be considered advantageous based on the findings of Edwin *et al.*[1].

Vanadium catalysts supported on BN were studied for propane partial oxidation by Taylor *et al.*[12]. These catalysts were then compared against V/SiO_2 catalysts. Some of the studies reported in this literature review utilised the hydrophobic supports in aqueous preparations. However, Taylor *et al.* used methanol with vanadyl acetylacetonate during the preparation of the incipient-wetness impregnated V/BN catalysts. Therefore researchers were beginning to appreciate that aqueous preparations were not necessarily exploiting the advantages offered by hydrophobic supports in terms of impregnated metal properties (metal crystallite size and dispersion, etc.). In this study, it was found that V/SiO_2 catalysts were active for propane total oxidation (i.e. the major product was CO_2) but also displayed some selectivity to acrolein. The V/BN catalysts, however, caused an appreciable increase in acrolein selectivity. The chemistry of the V supported on BN was noted to differ from that observed for V/SiO_2. The authors also suggested that acrolein adsorption was reduced in the case of V/BN, preventing further oxidation of the acrolein. This reduced acrolein adsorption was achievable through the hydrophobic nature of the BN coupled with its low surface area, which was observed to be $7m^2/g$ (V/BN) compared to $194m^2/g$ (V/SiO_2).

Wu *et al.* investigated the use of Pt/BN for the oxidation of volatile gasoline and compared this data with that obtained for $Pt/\gamma-Al_2O_3$ in the same study[13]. The authors found that in a test of 2500vppm volatile gasoline with a volume hourly space velocity of $20,000h^{-1}$ produced an initial T_{50} value of 210°C. When the same catalyst sample was used for subsequent reaction cycles, it was found that the activity increased markedly. The T_{50} value reduced to 160-170°C and 95% gasoline conversion was observed below 200°C. The authors attributed this increase in activity to the metallic Pt on the fresh catalyst being oxidised to PtO. This PtO was reported to enhance the catalytic activity of the Pt/BN catalyst. Pt sintering was found to be reduced due to the high thermal conductivity of the BN support, which prevented hot spot formation and therefore areas for subsequent Pt sintering. In terms of catalyst longevity, the authors reported that Pt/BN was able to maintain high activity over a longer period than $Pt/\gamma-Al_2O_3$.

The selective hydrogenation of crotonaldehyde using PtSn/BN catalysts was reported by Wu and Chen[14]. This paper also highlights the need to use a non-aqueous preparation solvent. The PtSn was found to form crystalline PtSn and $PtSn_3$ alloys were observed in the XRD analysis. This reinforces previous observations that mobile metal phases can form on BN, since metal mobility would be required to achieve an appreciable

amount of metal alloying.

Wu published a second paper, this time with S-J Lin as the co-author in 2008 based on the same PtSn/BN catalysts for the oxydehydrogenation of propane[15]. The same XRD observations were made with respect to PtSn/BN. The authors also reported that PtSn analogues using γ-Al_2O_3 did not display PtSn alloys via XRD analysis. Therefore the PtSn alloy formations appear to be influenced by the nature of the support.

High surface area hexagonal BN (SA = 125m^2/g) when impregnated with Pt, was found to be active for preferential CO oxidation using a 1% CO/1% O_2/98% He reactant feed[16]. However, the activity was reported to be lower than Pt/γ-Al_2O_3[17, 18], although the Pt/BN catalyst was used in a reactant gas feed that contained a higher CO concentration and the Pt content was also lower than the Pt/γ-Al_2O_3 catalysts.

5.1.2 Silicon Nitride

Si_3N_4 has received a relatively high amount of coverage in the literature. Since the MSI of Si_3N_4 is relatively high, one could expect that active metal phases supported on it would be composed of small, highly dispersed metal crystallites. This would be due to an increased interaction between the metal and support, reducing the mobility of the metal phase, therefore reducing the degree of sintering the metal can undertake. Small metal particles tend to be desirable for a wide range of oxidation reactions, e.g CO oxidation by supported Au catalysts[19, 20].

One of the main protagonists in this field is J.C. Bertolini and coworkers. A variety of papers have been published by this group on the study of silicon nitride from 1999 up to the present.

One of this group's earliest papers was published in 1999 where Pd/Si_3N_4 was investigated for the total oxidation of methane[8]. The Pd was impregnated using a non-aqueous method (Pd (II) bis-acetylacetonate in toluene). A previous report described the impregnated Pd as being of a small metallic particles[21]. This catalyst was found to be active for methane total oxidation, where a 90% conversion was observed at approximately 350°C. This was similar to a Pd/α-Al_2O_3 catalyst that was prepared in the same way, albeit with a higher Pd loading (0.75% and 1.05% Pd for Pd/Si_3N_4 and Pd/α-Al_2O_3 respectively). If the catalysts were aged at 800°C for 3h under the O_2/CH_4/N_2 reactive gas flow, it was found that the silicon nitride catalyst displayed minimal catalytic

136

deactivation. On the other hand, the alumina catalyst then required a temperature of 450°C to reach 90% CH_4 conversion, therefore demonstrating deactivation. Two reasons were proposed; firstly no oxidation of the silicon nitride support occurred thereby preventing encapsulation of the active phase as observed for SiC based catalysts. Secondly, the strong metal-support interaction of the Pd and silicon nitride provided resistance to sintering.

The partial oxidation of methane was then probed using a similar catalyst, Pt/Si_3N_4[9]. Higher Pt contents were investigated and it was found that these higher Pt content catalysts (1 – 2.2wt% Pt) were less stable at high temperatures (900°C) compared to lower Pt content catalysts (0.045wt% Pt), based on metal losses. The initial dispersions of the Pt catalysts were very high (quoted to reach up to 100%) but at 900°C, Pt sintering occurred. If the particle size exceeded 1.1nm, then oxidation of the Pt to PtO_2 occurred and this PtO_2 became volatile, leading to the observed metal losses.

0.5wt% Pd/Si_3N_4 was then studied for 1,3-butadiene hydrogenation[22]. The data was compared with other non-porous supports (SiO_2, Al_2O_3 and SiC). The Pd XPS spectra revealed that the Pd binding energies were 1eV higher for Pd/Si_3N_4 compared to the other Pd catalysts, suggesting that the Pd-support interaction was higher for the Pd/Si_3N_4 catalyst. All the catalysts displayed an immediate reduction in the conversion of 1,3-butadiene. However, whilst Pd/SiC and Pd/Al_2O_3 displayed a gradual decrease in conversion, Pd/SiO_2 and Pd/Si_3N_4 displayed rapid decreases in conversion before a plateau was reached. The authors could not find a relationship between the support thermal properties and the initial catalyst deactivation.

In 2005, it was reported that increased crystallinity and increased proportions of α-Si_3N_4 was necessary to increase the catalytic activity towards the total oxidation of methane[5]. The amorphous silicon nitride support was less active. The high Pd binding energies observed in the previous discussed paper were replicated here in the case of Pd/α-Si_3N_4. This led to the conclusion that the amorphous fraction of the support undergoes more facile oxidation at higher temperatures, thus reducing activity[23]. The Pd/αSi_3N_4 was more stable when subjected to the reaction conditions.

A second paper expanding on these conclusions was published in 2006[3]. This paper came to the same conclusions as in 2005 with regards to Pd/Si_3N_4 and the amount of amorphous phase present[5]. However, they also reported an aqueous preparation which was significantly less active than the hydrophobic preparation (the same Pd source, Pd(II)

acetate was used in both preparations). Whilst the hydrophobic preparation displayed a methane conversion in excess of 80% at approximately 600°C, a temperature of 700°C was required for the aqueous preparation to display 60% methane conversion.

Some characterisation was performed on these hydrophobic and aqueous catalysts and was subject to a publication in 2009[4]. CO chemisorption studies showed that the chemisorption was weaker on the aqueous Pd/α-Si₃N₄ compared to the analogue prepared in toluene. It was observed that the aqueous preparation was more selective towards butenes in the 1,3-hydrogenation reaction. This increased selectivity was proposed to be due to the migration of Si atoms from the support to the surface of the Pd metal during the catalyst preparation leading to the observed modifications in the CO chemisorption and catalytic activity data.

In one of this group's most recent papers, they proposed that Si₃N₄ would be a suitable support for VOC abatement[24]. Although Bertolini and co-workers found that amorphous silicon nitride was a relatively poor support, Hullmann *et al.* reported that Pt impregnated amorphous silicon nitride was active for propane dehydrogenation and were selective for propane dehydrogenation compared to a reference Pt/MgO catalyst[25]. CO chemisorption data displayed extremely low Pt dispersions for the impregnated silicon nitride catalysts.

Ni/Si₃N₄ was found to be active for the partial oxidation of methane to syngas[26]. The catalyst was stable at 800°C after 200h of time on line reaction with no deactivation. The reasons cited by the authors was that the catalyst suffered from low coke deposition and a strong Ni-support interaction. The high thermal conductivity (resulting in less hot spots throughout the support) was also cited to be advantageous.

5.1.3   Silicon Carbide

SiC is widely used in laboratories as an inert material for reactors etc as exemplified by Sautel *et al.*, who used SiC as a solid dilutent to prevent large temperature gradients from being present in a reactor[27]. SiC was also used as a packing material in ethylene and propylene production by microwave irradiation by Cooney and Xi[28]. Due to its relative inertness, it could be expected that any metal-support interaction would be very weak. As discussed earlier, this may be advantageous. However, it has been noted that above 800°C, SiC was reported to be unsuitable for use in oxidation reactions in 1998, where

oxidation of the support occurred[29]. In a subsequent study, the same authors also identified that metal silicides can form during catalyst preparation if subjected to a high enough temperature[30].

In terms of using SiC as a catalyst support, one of the earliest reports concerned automotive Pt-Rh three way catalysts (TWCs) where the Al_2O_3 monolith was replaced by SiC[31, 32]. The intention of the SiC was to increase the chemical inertness, mechanical strength and thermal stability of the monolith to prevent sintering and loss of the active phase. However, initial results showed that the light off temperature for the SiC TWC was 100°C higher than that for the standard Al_2O_3 based TWC. However, standard TWCs have promoters incorporated into the catalyst (Ce, La, Ba) which the SiC test TWC did not contain[33]. The addition of Ce to the Pt-Rh/SiC TWC decreased the light off temperature gap to the standard TWC to 40-50°C[31].

SiC has found a use in the steam reformation of propane as a monolith substrate for Ru catalyst. The reaction system (H_2 production from steam reformation of hydrocarbon fuel) required reaction temperatures in excess of 800°C to prevent coking[34]. The authors reported that after 15 thermal cycles which involved temperatures of up to 1000°C, the microreactor was unaffected. After 120h of continuous reaction at 800°C, no deactivation of the catalyst could be observed.

SiC has been shown to be an effective support for the direct oxidation of H_2S into sulfur. Part of the reason the authors attributed this activity to was the partly hydrophobic nature of the SiC[35].

2wt% Pt/SiC has also been investigated for CO oxidation, where 100% CO conversion was observed at 194°C when a 1% CO/1% O_2/98% He reactant gas mixture was fed over the Pt/SiC catalyst[36]. The SiC support displayed high surface area (157m^2/g) with a relatively large pore volume (0.46cm^3/g) with a large pore size distribution.

5.1.4 Tin Oxide

As already mentioned, SnO_2 has been investigated for naphthalene oxidation via aqueous impregnation[1]. It was reported by Habuta *et al.* that V_2O_5/SnO_2 demonstrated selectivity towards CO and CO_2 when investigating the oxidation of propane. Whilst relatively high turnover frequencies for propane conversion were observed, this did not necessarily

correlate to the greatest degree of propane conversion. The authors were investigating the production of propylene, which the SnO_2 catalyst displayed the least amount of selectivity towards out of all the investigated catalysts. Instead the preferred products were that of partial and total combustion (i.e. CO_2). The SnO_2 support itself was observed to have appreciable activity for propane combustion[37].

However, Harrison et al. stated that coprecipitating rare earth metals when preparing the SnO_2 support did not enhance the catalytic activity of Cr-promoted SnO_2 for the oxidation of propane[38]. Also M^{3+}/SnO_2 (where M = La, Pr, Nd, Sm, Gd) did not enhance activity over SnO_2 only.

Oi-Uchisawa et al. reported that Pt/SnO_2 was a relatively active catalyst for soot oxidation, displaying similar activity to other oxide surfaces such as Pt/SiO_2[39]. CO oxidation and alcohol oxidation (methanol and ethanol) for fuel cell applications via catalysts prepared by supporting Pt on Sb-doped SnO_2 was reported by Lee et al.[40]. In comparison with Pt/C, it was found that a low Pt loading on the SnO_2 based support enhanced the catalytic activity over that observed for Pt/C. The authors reported that the enhanced activity was due to a more suitable Pt dispersion and the interaction between the Pt and the SnO_2 support. The stability of the SnO_2 based catalyst was also improved, proposed to be due to improved corrosion resistance.

A study by Moreau and Bond observed that Au/SnO_2 was active for CO oxidation[19]. In a similar study, Au/SnO_2 prepared by deposition-precipitation was studied in more detail by Wang et al.[41]. Preparation conditions of 2.86wt% Au calcined at 473K afforded the most active catalyst. This allowed very small Au and SnO_2 crystallites to be formed. The proportion of metallic Au also increased.

Pd/SnO_2 was observed by Okumura et al. to be a relatively poor catalyst for the total oxidation of toluene, although more active than Pd/MgO[42]. A key observation that was made was that the Pd dispersion of the Pd/SnO_2 was extremely low (1.2%). The most active catalyst, Pd/ZrO_2, displayed a Pd dispersion of 16.5%. Other active catalysts displayed similar Pd dispersions. This low dispersion may be advantageous according to the reports of Edwin et al.[1]. Low dispersions tend to be coupled with large metal crystallite sizes as noted by Edwin et al. This low Pd dispersion was enhanced by performing the Pd impregnation in an aqueous solvent, which would cause poor surface wetting.

Mitsui et al. investigated the activity of Ru/SnO_2 for the combustion of toluene,

ethyl acetate and acetaldehyde[43]. It was found that whilst other oxide based supported Ru catalysts (Ru/ZrO_2 and Ru/γ-Al_2O_3) benefited from a short thermal reduction at 400°C after calcination at 400°C, the Ru/SnO_2 catalyst activity was reduced. Pd and Pt/SnO_2 catalysts were compared for the hydrogenation of nitrate and nitrite[44]. The authors reported that the Pd/SnO_2 was more active than the Pt counterpart.

There is very little literature covering the use of hydrophobic materials as supports for active catalysts in the total oxidation of propane. For example, few published works exist on the use of boron nitride in catalytic oxidation[12, 45]. Silicon nitride has been reported for propane dehydrogenation[25]. Silicon carbide has been reported for oxidative dehydrogenation of propane[46] and general propane oxidation using non-conventional catalysts[47]. A literature search showed no reported studies concerning the use of SnO_2 in propane oxidation.

5.2   Pd, Pt, Ni, Ag and Cu Catalysts Prepared via Organic/Non Aqueous Solutions

5.2.1   Catalytic Activity

5.2.1.1 Naphthalene Total Oxidation

Figure 5.1. Catalytic activity (naphthalene total oxidation) for all Pd catalysts synthesised in this study. All Pd contents were 0.5wt%. Temperature range: 125 – 300°C. GHSV = 45,000h^{-1}, 100vppm naphthalene, total flow = 50mL/min. Error bars are ± 6.7%.

Figure 5.1 (above) shows that all the Pd catalysts were active for the total oxidation of naphthalene. The most active catalyst was Pd/SnO_2. Although the temperature where 100% CO_2 yield was achieved (T_{100}) was the same as Pd/BN (250°C), the T_{50} values were significantly different (190°C compared to 214°C). Pd/SiC displayed a similar activity to Pd/BN with similar T_{50} values (214°C and 218°C respectively). However, Pd/SiC displayed lower activity at higher temperatures compared to Pd/BN. Pd/SiC displayed a T_{100} value of 275°C compared to 250°C for Pd/BN. It could be argued that Pd/SiC was experiencing a slight limiting effect due to mass transfer. Pd/Si_3N_4 was the least active catalyst; a temperature of 300°C was required to attain a 100% yield of CO_2 and a T_{50} temperature of 252.5°C was observed. The order of activity of the Pd catalysts was found to be thus:

$SnO_2 > BN > SiC > Si_3N_4$

Figure 5.2. Catalytic activity (naphthalene total oxidation) for all Pt catalysts synthesised in this study. All Pt contents were 0.5wt%. Temperature range: 150 – 300°C. GHSV = 45,000h^{-1}, 100vppm naphthalene, total flow = 50mL/min. Error bars are ± 6.7%.

As figure 5.2 shows, the SnO_2 based catalyst was not the most active Pt catalyst observed. Pt/SiC was the most active catalyst (temperatures of 212.5°C and 250°C

required to reach T_{50} and 100% CO_2 yield (T_{100}) respectively). Pt/SnO_2 also required a temperature of 250°C to reach T_{100}, but it had a higher T_{50} temperature than Pt/SiC (231°C). The least active catalyst was the Si_3N_4 based catalyst as with a T_{100} of 275°C, which was lower than that observed for Pd/Si_3N_4 (300°C). Pt/BN may have suffered from mass transport effects during reaction at higher temperatures. Its T_{50} value was comparable to the most active Pt catalyst with a temperature of 216°C. However, T_{100} was not achieved until 275°C compared with Pt/SiC and Pt/SnO_2 which both achieved T_{100} at 250°C.

If the Pt/BN has a reduced number of active sites, then mass transfer limitations at high naphthalene conversions could occur. A potential reason for this can be attributed to the densities and masses of the catalysts. The catalysts were packed in such a way the volume of catalyst was equal for each activity test. Since the densities vary for each catalyst, their masses therefore the mass of impregnated metal, varied. A lower density would mean that the mass required for a given catalyst volume would be smaller, therefore resulting in a smaller amount of impregnated metal. The densities of BN and SiC were the lowest investigated, therefore the amount of impregnated metal would be low. Therefore, the order of activity of the Pt catalysts was found to be thus:

$SiC>SnO_2\sim BN>Si_3N_4$.

Based on a lower T_{50} value (compared to Pd/BN, Pt/SiC, Pt/BN and Pt/SnO_2), it appears that the most active catalyst from these 8 presented here was Pd/SnO_2. Both Pd/Si_3N_4 and Pt/Si_3N_4 were the poorest performers in each respective catalyst set. It has been reported by Bertolini *et al.* that Pd/Si_3N_4 appears to have an unusual MSI[4, 48]. If the Pd experienced a strong interaction with the support, it could be possible that the Pd would be less facile to undergo a chemical change (e.g. reduction of the Pd oxidation state) when impregnated on Si_3N_4 compared to a more active Pd catalyst (e.g. Pd/SnO_2).

Ni, Ag and Cu based catalysts on the same four supports were also investigated. However, these were all less active than either the Pt or Pd catalysts, as the next three figures show.

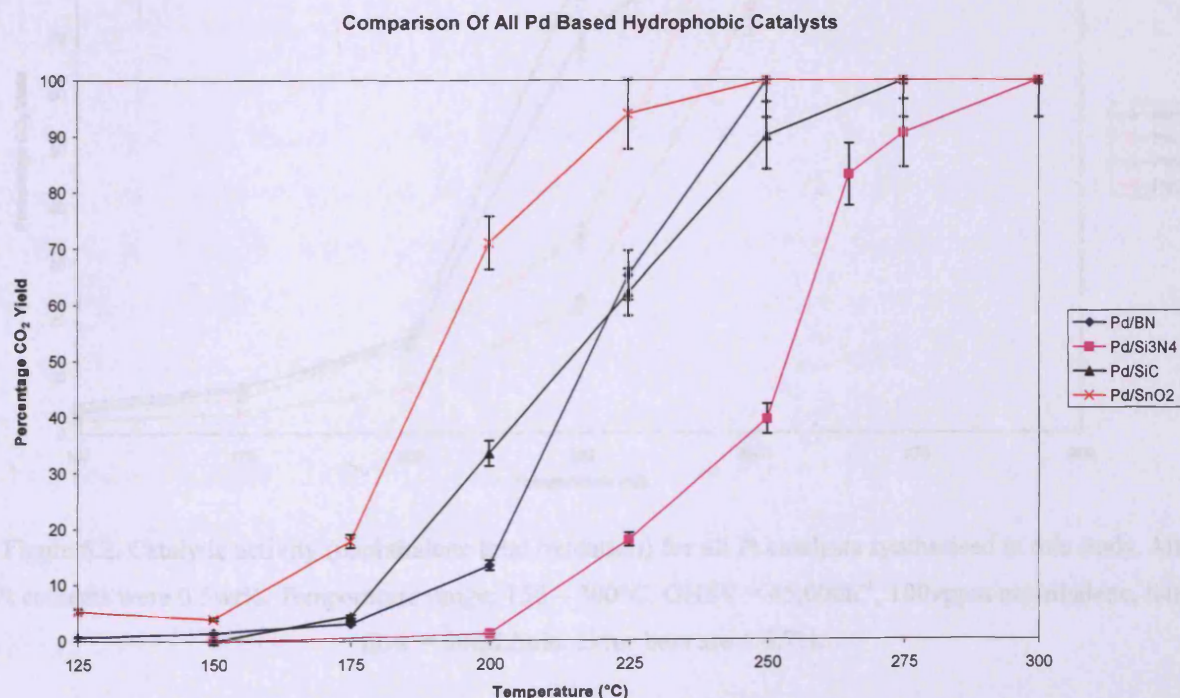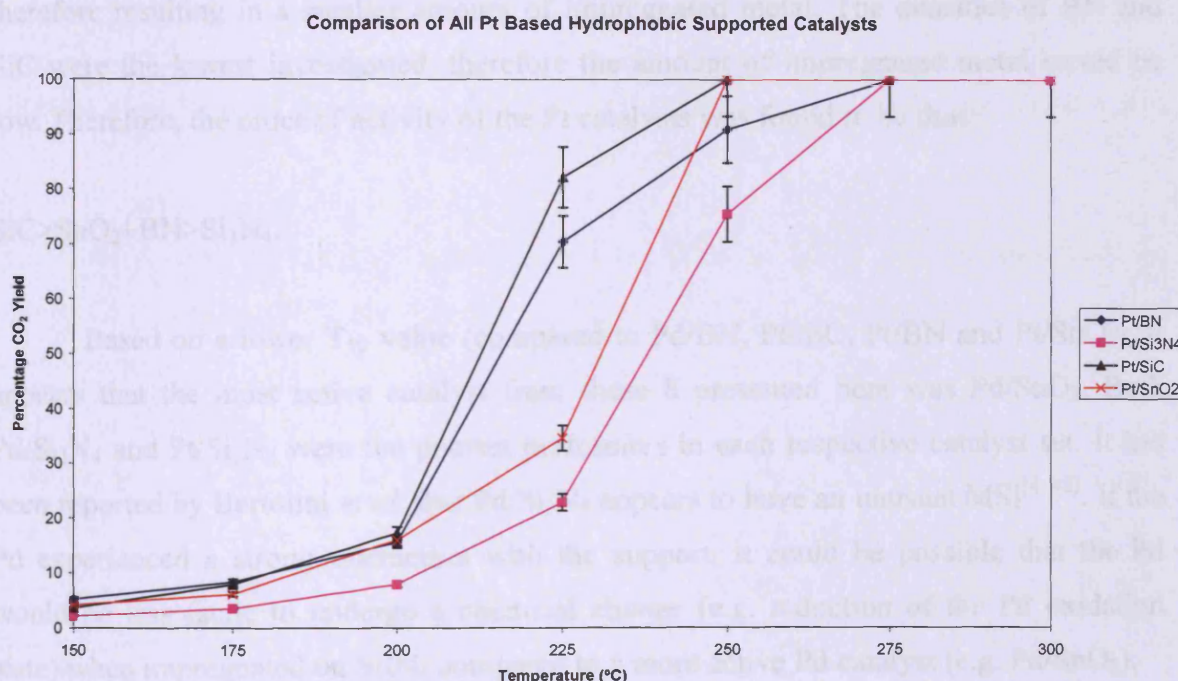**Comparison of All Ni Based Hydrophobic Supported Catalysts**

Figure 5.3. Catalytic activity (naphthalene total oxidation) for all Ni catalysts synthesised in this study. All Ni contents were 0.5wt%. Temperature range: 150 – 350°C. GHSV = 45,000h^{-1}, 100vppm naphthalene, total flow = 50mL/min. Error bars are ± 6.7%.

Here, none of catalysts achieved a CO_2 yield of 100%. Ni/BN displayed the highest CO_2 yield at 350°C but was observed to require the highest temperature to achieve a CO_2 yield of 50% (T_{50}). T_{50} was observed to be 325°C. Ni/Si$_3$N$_4$ was relatively active, with a relatively low T_{50} value of 257.5°C. The catalyst which displayed the lowest T_{50} temperature was Ni/SnO$_2$ at 254°C. However, a maximum CO_2 yield of 90% was observed. Ni/SiC was the poorest catalyst of this data series; it displayed one of the highest T_{50} temperatures (314°C) and showed a maximum CO_2 yield comparable with Ni/Si$_3$N$_4$ (approximately 88%). Based on this, the activity series can be written as:

SnO$_2$>Si$_3$N$_4$>BN~SiC.

144

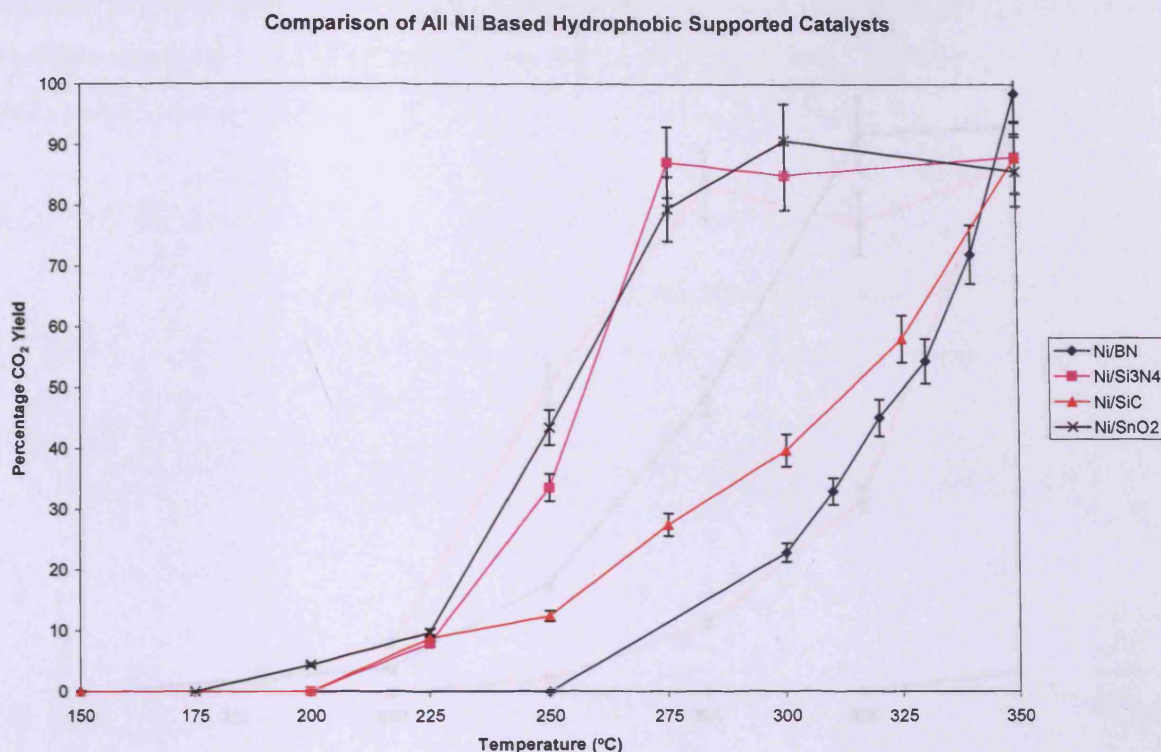**Comparison of All Cu Based Hydrophobic Supported Catalysts**

Figure 5.4. Catalytic activity (naphthalene total oxidation) for all Cu catalysts synthesised in this study. All Cu contents were 0.5wt%. Temperature range: 200 – 350°C. GHSV = 45,000h⁻¹, 100vppm naphthalene, total flow = 50mL/min. Error bars are ± 6.7%.

Cu/BN exhibited similar behaviour to Ni/BN in respect to requiring a relatively high temperature (350°C) before any activity was observed. However, where Ni/BN gave respectable activity at higher reaction temperatures, Cu/BN achieved a CO_2 yield of less than 5% at 350°C. This catalyst was one of the most inactive studied and presented here. Cu/SnO_2, as with Pd/SnO_2, was the most active of the Cu catalysts when the T_{50} values are compared. Cu/SnO_2 was observed to have the lowest T_{50} value of 274.5°C. Cu/SiC had a T_{50} value of 301°C and Cu/Si_3N_4 had a T_{50} value of 332.5°C. As Cu/BN did not exceed a maximum CO_2 yield of 5%, no T_{50} value could be determined. Cu/SiC attained the highest catalytic activity of approximately 92% at 325°C. It appears that both Cu/SnO_2 and Cu/SiC might display the effects of mass transfer. There could also have been a limited number of available active sites which would hinder catalytic activity and that the concentration of naphthalene in the reactant gas stream was too great. The drop in activity at 325°C for Cu/SnO_2 is unlikely to be correct data – a repeat experiment would need to be performed to ascertain this. However, as there were more active catalysts that

145

have already been tested (i.e. the Pd and Pt series) it was decided that the testing time available would be spent more usefully on the Pd and Pt catalysts. Therefore, the activity series can be considered as:

$SnO_2 \sim SiC > Si_3N_4 > BN$.

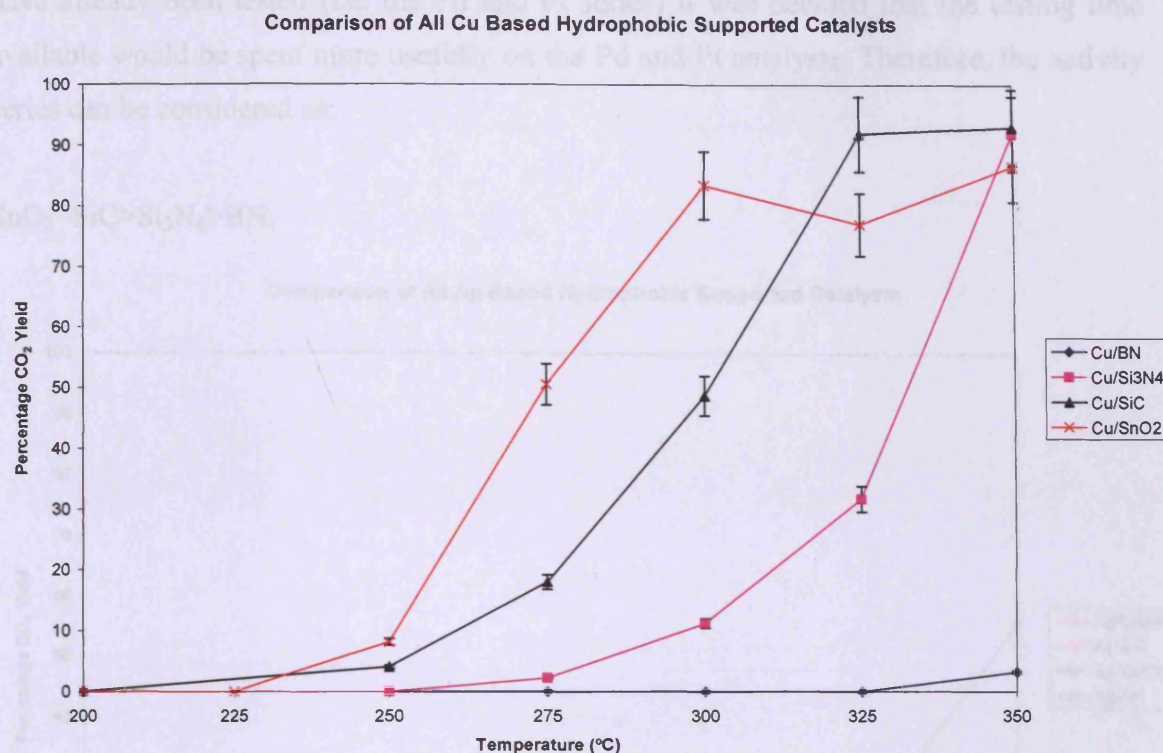**Comparison of All Ag Based Hydrophobic Supported Catalysts**
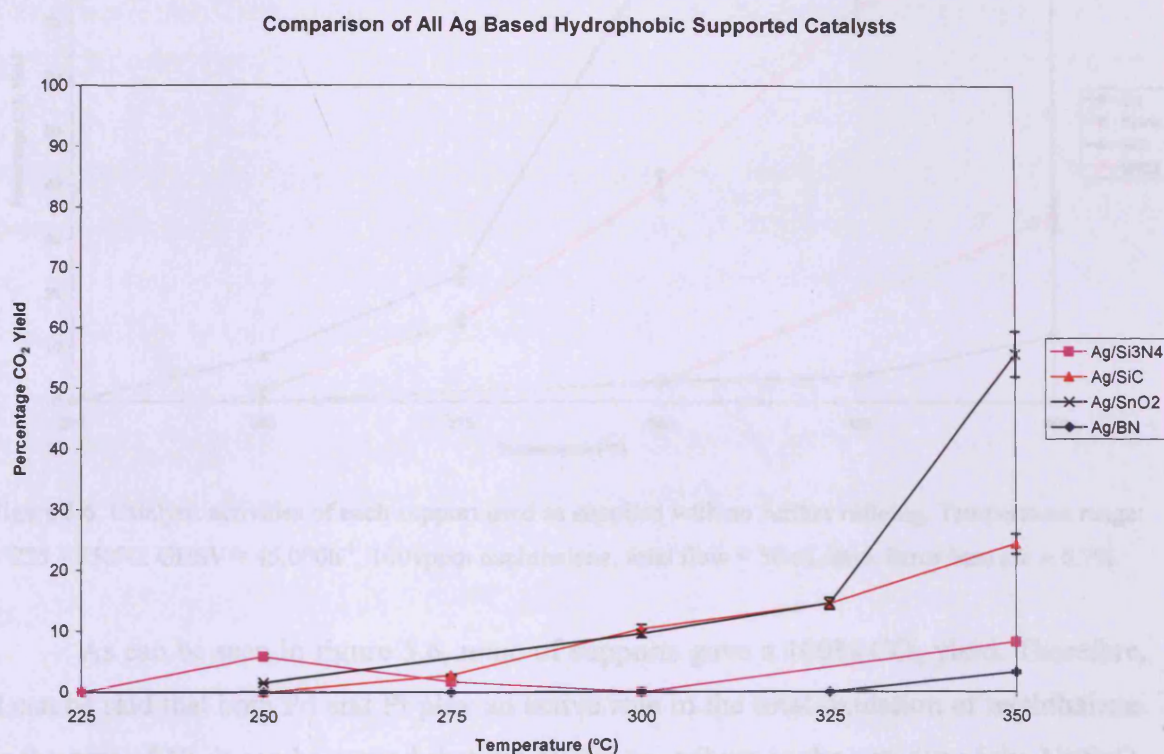
Figure 5.5. Catalytic activity (naphthalene total oxidation) for all Ag catalysts synthesised in this study. All Ag contents were 0.5wt%. Temperature range: 225 – 350°C. GHSV = 45,000h^{-1}, 100vppm naphthalene, total flow = 50mL/min. Error bars are ± 6.7%.

All of the Ag based catalysts can be considered to show poor activity for the total oxidation of naphthalene. As with the Cu analogue, Ag/BN displayed a catalytic activity of less than 5% at 350°C. The most active catalyst, achieving a maximum CO_2 yield of approximately 56% was the Ag/SnO$_2$ sample. The activity series for the Ag catalyst series is very similar to that observed for Cu, i.e.

$SnO_2 > SiC > Si_3N_4 > BN$.

If the bare supports are examined for their catalytic activities for the total oxidation of naphthalene, it would be possible to assess whether or not each metal has a

146

positive effect on the catalysts' activities.
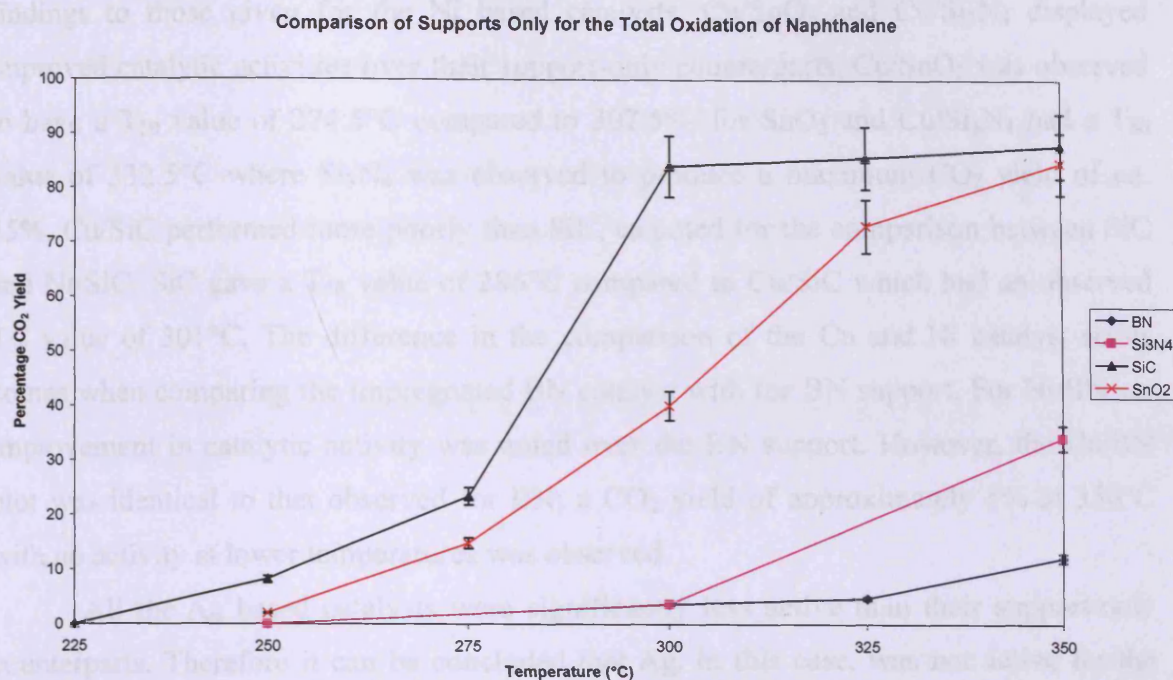
Figure 5.6. Catalytic activities of each support used as supplied with no further refining. Temperature range: 225 – 350°C. GHSV = 45,000h^{-1}, 100vppm naphthalene, total flow = 50mL/min. Error bars are ± 6.7%.

As can be seen in figure 5.6, none of supports gave a 100% CO_2 yield. Therefore, it can be said that both Pd and Pt play an active role in the total oxidation of naphthalene. In the case of Ni, it can be argued that the Ni did contribute to the activity of the Ni/SnO$_2$ catalyst since both the T_{50} value was lower for Ni/SnO$_2$ than that observed for the SnO$_2$ support (254°C and 307.5°C respectively). However, it cannot be said that Ni increases the CO_2 yield achievable by SnO$_2$ only as a plateau in activity was observed at approximate CO_2 yield of 90% for Ni/SnO$_2$. The inclusion of Ni does, however, lower the temperature at which this level of catalytic activity is shown. Ni/SnO$_2$ displayed a CO_2 yield of approximately 85-90% at 300°C. SnO$_2$ required a temperature of 350°C to achieve the same yield. Both Ni/Si$_3$N$_4$ and Ni/BN comfortably outperformed their respective Si$_3$N$_4$ and BN supports in that both Ni catalysts could have a T_{50} value attributed to them. The same could not be said for the Si$_3$N$_4$ and BN supports. It appears that Ni/SiC was a poorer catalyst than the bare SiC support and was the only Ni catalyst to perform more poorly that its support only counterpart. T_{50} values of 314°C and 286°C respectively were observed. At 300°C, the SiC support had attained a CO_2 yield of approximately 85%. Ni/SiC produced a CO_2 yield of 40% at 300°C.

147

The comparison of the Cu catalysts with the support-only testing gave similar findings to those given for the Ni based catalysts. Cu/SnO_2 and Cu/Si_3N_4 displayed improved catalytic activities over their support-only counterparts. Cu/SnO_2 was observed to have a T_{50} value of 274.5°C compared to 307.5°C for SnO_2 and Cu/Si_3N_4 had a T_{50} value of 332.5°C where Si_3N_4 was observed to produce a maximum CO_2 yield of *ca.* 35%. Cu/SiC performed more poorly than SiC, as noted for the comparison between SiC and Ni/SiC. SiC gave a T_{50} value of 286°C compared to Cu/SiC which had an observed T_{50} value of 301°C. The difference in the comparison of the Cu and Ni catalyst series comes when comparing the impregnated BN catalyst with the BN support. For Ni/BN, an improvement in catalytic activity was noted over the BN support. However, the Cu/BN plot was identical to that observed for BN; a CO_2 yield of approximately 5% at 350°C with no activity at lower temperatures was observed.

All the Ag based catalysts were significantly less active than their support-only counterparts. Therefore it can be concluded that Ag, in this case, was not active for the total oxidation of naphthalene. In fact, one could say that Ag disrupts the activity of the support significantly for the majority of the catalyst supports. The exception was the BN support, which was inactive until 350°C where the activity is then extremely poor. There are several examples in the literature where Ag supported catalysts are active for a variety of reactions[49-56], or can enhance catalytic activity when used in a bimetallic catalyst system[57-59]. To conclude, the following statements can be made.

- Pd and Pt consistently improved the catalytic activities of all the supports investigated in this study.
- Ni improved the catalytic activities of the majority of the supports, the exception being Ni/SiC.
- Cu/SnO_2 and Cu/Si_3N_4 were observed to be more active than their support-only counterparts, but Cu/BN and Cu/SiC were less active.
- All the Ag catalysts were less active than their support-only counterparts. The only possible exception was Ag/BN which displayed only a small amount of activity at very high temperatures.

Of the catalysts investigated, only the Pt and Pd based catalysts presented high activities. Therefore, the focus of the study centred on these eight Pt and Pd catalysts.

5.2.1.2 Propane Total Oxidation

Due to the findings of section 5.2.1.1, it was decided to limit the testing of these catalysts for the total oxidation of propane to just the Pt and Pd series. Figure 5.7 gives the data obtained for all the Pd catalysts. Only two catalysts, Pd/SnO_2 and Pd/SiC, gave rise to 100% C_3H_8 conversion and 100% CO_2 yield. A repeat experiment using a fresh catalyst sample confirmed this initial observation.

Figure 5.7. Catalytic activities for the Pd catalysts prepared in this study for the total oxidation of propane. Temperature range: 100 – 550°C. GHSV = 45,000h^{-1}, 0.4% propane in synthetic air, total flow = 50mL/min. Error bars are ± 6.7%.

Both the impregnated SnO_2 and SiC gave T_{100} values of 500°C. The T_{50} values were also very similar and within the experimental error of the apparatus (±6.7%). The impregnated BN and Si_3N_4 catalysts showed very similar activity profiles which were within an error margin of 6.7% as shown on the figure. In terms of an activity series, it can be drawn thus:

$SiC \sim SnO_2 > BN \sim Si_3N_4$.

The Effect of Hydrophobic Catalysts on the Total Oxidation of Propane - Platinum
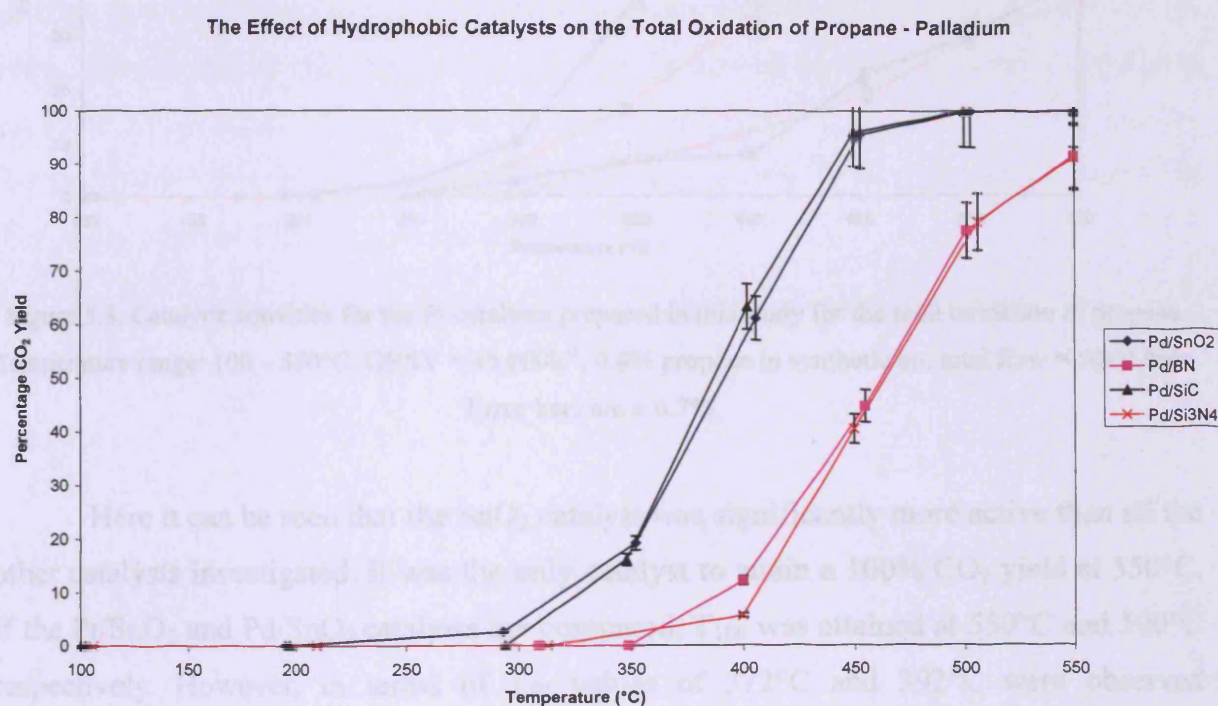

Figure 5.8. Catalytic activities for the Pt catalysts prepared in this study for the total oxidation of propane. Temperature range: $100 - 550°C$. GHSV = $45,000h^{-1}$, 0.4% propane in synthetic air, total flow = 50mL/min. Error bars are ± 6.7%.

Here it can be seen that the SnO_2 catalyst was significantly more active than all the other catalysts investigated. It was the only catalyst to attain a 100% CO_2 yield at 550°C. If the Pt/SnO_2 and Pd/SnO_2 catalysts are compared, T_{100} was attained at 550°C and 500°C respectively. However, in terms of T_{50} values of 372°C and 392°C were observed respectively. The Pt/SnO_2 catalyst suffered from mass transfer effects at higher temperatures/CO_2 yields. If low temperature activities are compared, it can be seen that the Pd/SnO_2 catalyst was less active than the Pt analogue. At 300°C, the Pd/SnO_2 catalyst produced a CO_2 yield of less than 5%. The Pt/SnO_2 catalyst produced a 10% CO_2 yield at the same temperature. The activity series for the Pt catalysts was found to be:

SnO_2>Si_3N_4>SiC~BN.

The Pt/Si_3N_4 was surprisingly active. So far in this study, the Si_3N_4 catalysts have been comparatively poor catalysts. If the Pt crystallites experience a strong interaction with the support, then small crystallites may be produced if this interaction prevents Pt sintering to the same degree as the other catalysts (SnO_2, SiC and BN) during thermal

150

treatments. Characterisation of the metal crystallites would be useful.

As the Pd/SnO_2 and the Pt/SnO_2 samples were generally highly active for the total oxidation of both polycyclic and linear hydrocarbons, it could be possible that the support may play an active role in the oxidation of the VOCs. As figures 5.6 and 5.9 show, SnO_2 offered appreciable activity when used as received from the supplier for both propane and naphthalene total oxidation. For propane total oxidation, SnO_2 was the only support to show appreciable activity. It is also the only oxide support examined in this study. It could be speculated that the bound lattice oxygen could participate directly in the oxidation reaction in a similar way to the Mars van Krevelen mechanism. The MvK mechanism (or redox behaviour) has been reported to operate for several catalytic systems for the total oxidation of naphthalene and propane, in particular CeO_2[60] and $CeZrO_2$[61, 62]. Therefore the possibility of naphthalene oxidation occurring via the MvK mechanism cannot be discounted without further mechanistic studies.
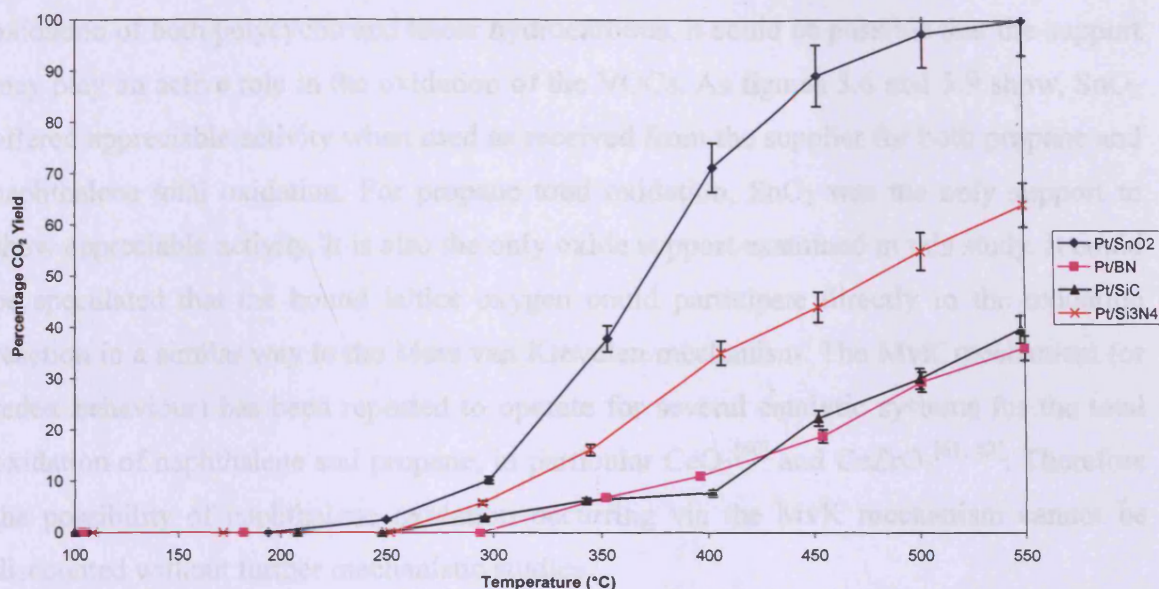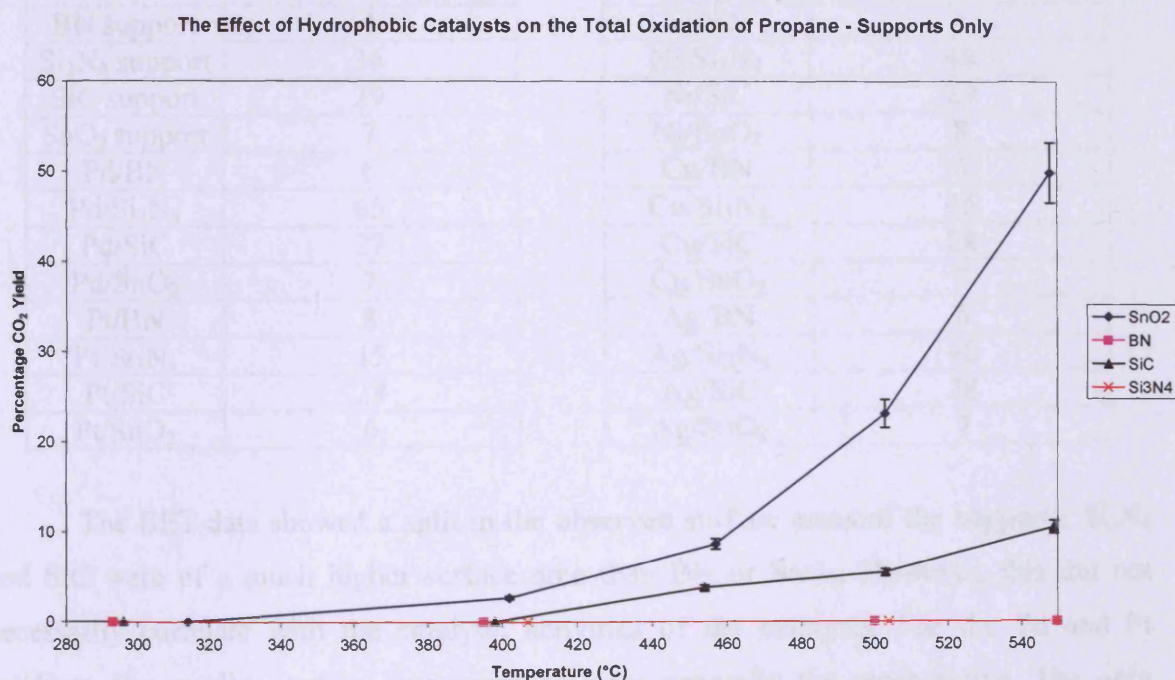

Figure 5.9. Catalytic activities for the supports used (as received) in this study for the total oxidation of propane. Temperature range: 280 – 550°C. GHSV = 45,000h^{-1}, 0.4% propane in synthetic air, total flow = 50mL/min. Error bars are ± 6.7%.

Si_3N_4 and BN supports offer no active sites whatsoever for the total oxidation of propane. Therefore, any catalytic activity would be due to the catalyst preparation and that the active sites would directly involve the impregnated metals. The same also applied to

SiC, which gave a 10% CO_2 yield at 550°C. The most active support was SnO_2, which was observed to produce a 50% CO_2 yield therefore would probably contribute towards the overall activity of an impregnated catalyst.

5.2.2 Characterisation

5.2.2.1 Surface Area Analysis

Table 5.1 shows the surface area data obtained for all the hydrophobic catalysts investigated in this study.

Table 5.1. Surface area analysis of all hydrophobic catalysts. Surface areas obtained using N_2 adsorption at 77K and the BET method.

Sample	Surface Area (m^2/g)	Sample	Surface Area (m^2/g)
BN support	4	Ni/BN	4
Si_3N_4 support	36	Ni/Si_3N_4	48
SiC support	29	Ni/SiC	29
SnO_2 support	7	Ni/SnO_2	8
Pd/BN	6	Cu/BN	4
Pd/Si_3N_4	65	Cu/Si_3N_4	45
Pd/SiC	27	Cu/SiC	28
Pd/SnO_2	7	Cu/SnO_2	7
Pt/BN	8	Ag/BN	6
Pt/Si_3N_4	45	Ag/Si_3N_4	48
Pt/SiC	28	Ag/SiC	28
Pt/SnO_2	6	Ag/SnO_2	7

The BET data showed a split in the observed surface areas of the supports; Si_3N_4 and SiC were of a much higher surface area than BN or SnO_2. However, this did not necessarily correlate with the catalytic activities of the catalysts. For the Pd and Pt catalysts, the smaller surface area catalysts were generally the more active. The only exception was Pt/SiC, which was one of the most active Pt catalysts for propane total oxidation. There was negligible reduction in surface area after impregnation for this catalyst. On the contrary, the Pd/Si_3N_4 catalyst surface area increased by almost two fold, yet this catalyst was the least active Pd catalyst. A similar observation was made regarding Pt/Si_3N_4, although the increase in surface area was not as pronounced as for the Pd analogue. Therefore, despite containing relatively high surface areas, the Si_3N_4 based catalysts were generally some of the poorest catalysts investigated in this study. For all the

other catalysts (based on BN, SiC, SnO_2), the surface areas of the supports did not change significantly after the impregnation of the metal. If the metal-support interaction between Si_3N_4 and the impregnated metal was high, then sintering of the impregnated metal can be minimised during calcination. This would lead to the formation of small metal crystallites thereby increasing the metal surface area.

5.2.2.2 Scanning Electron Microscopy

The backscattered-electron images generally did not reveal any bright spots that would correspond to the impregnated metal phase. This was not surprising as a low metal loading (0.5wt%) was used and the crystallite sizes can be small; as stated by Bertolini *et al.*[7, 8].

The morphologies of each support are very different. BN, for example, has a butterfly-like plate morphology that appears to be fairly thin. The other supports appear to have a more globular morphology, as exemplified by the SnO_2 support only image in figure 5.10 below. After impregnation, agglomeration of the spherical particles was apparent, as shown in the image obtained for Pd/SnO_2. The same also seemed to apply to Pt/SnO_2. Impregnated BN supports displayed the same butterfly-like morphology as the bare support. SiC was observed to have a similar morphology to SnO_2.
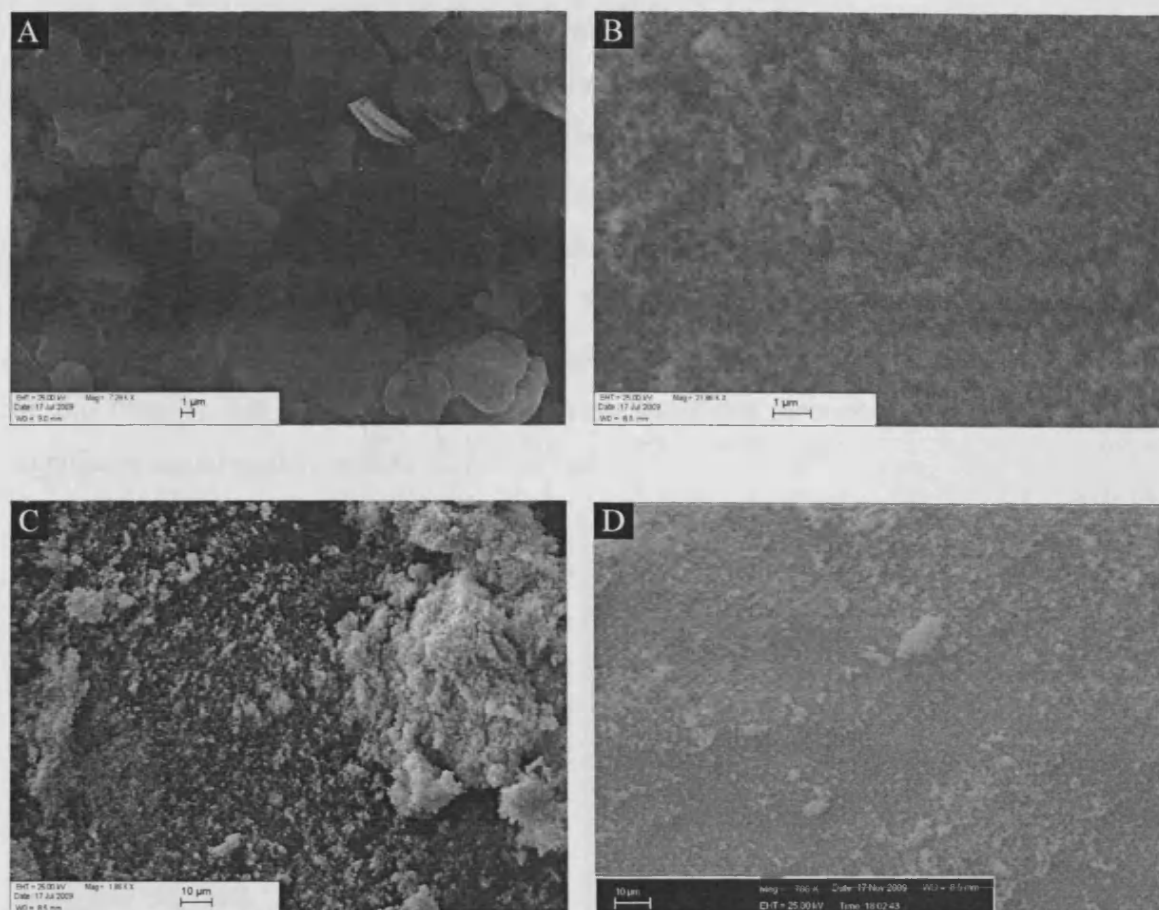
Figure 5.10. a) SEM image of BN support showing butterfly-like morphology; b) SEM image of SiC support ; c) SEM image of SnO_2 support; d) BSE image of Pd/SnO_2 showing slight support agglomeration.

5.2.2.3 Energy Dispersive X-ray Analysis

Table 5.2. Percentage weight loadings of all Pt and Pd catalysts investigated during this study via EDX. Errors calculated during analysis (±0.15%).

Sample	Metal weight loading (wt%)
Pt/SnO_2	0.5
Pd/SnO_2	0.5
Pt/BN	0.3
Pd/BN	0.2
Pt/SiC	0.3
Pd/SiC	0.7
Pt/Si_3N_4	0.3
Pd/Si_3N_4	0.4

All the SnO_2 catalysts revealed metal loadings in the region of 0.5wt% when experimental error was considered. For Pt/BN, approximately the correct Pt content was observed,

154

however Pd/BN revealed a a slightly lower bulk Pd content. No bright spots were observed for this catalyst. All other BN catalysts contained the correct metal loadings. For the SiC catalysts, a range of metal loadings were observed. Pd/SiC was observed to have a higher metal content than Pt/SiC (0.7wt% and 0.3wt% respectively). Pt/Si$_3$N$_4$ and Pd/Si$_3$N$_4$ contained similar metal contents when error was considered. Elemental mapping of some of the Pd catalysts was performed; for example, the maps obtained for Pd/SnO$_2$ are shown in the following figure. A Pd content of approximately 0.5wt% was observed for this catalyst. The Pd appeared to be evenly distributed throughout the catalyst and no significant signal agglomeration was observed.

Figure 5.11. Elemental mapping data for 0.5wt% Pd/SnO$_2$. Maps of b) Pd; c) Sn; d) O; based on a) the Pd/SnO$_2$ electron image.

5.2.2.4 CO Chemisorption

The CO chemisorption of the Pt and Pd catalysts were attempted. However, as Pd can be difficult to quantify using the apparatus available if the Pd content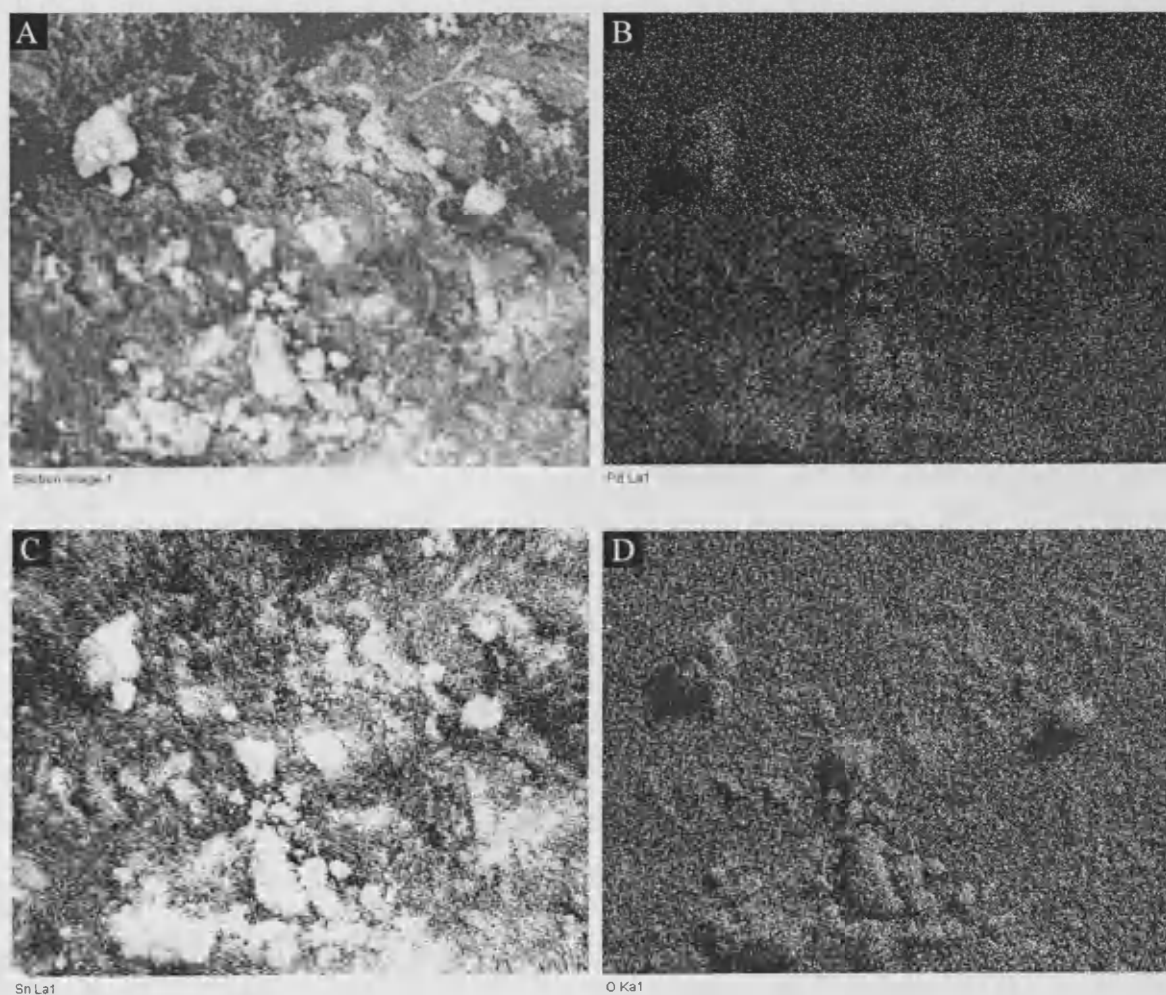 is low, it was impossible to achieve a gradual CO saturation of the Pd particles. The smallest possible pulse of CO (50µL) was used in these experiments with as large a sample mass as possible without causing undesirable effects such as gas flow backpressure. Generally Pd/CO chemisorption analysis is not impossible to perform, as data from the previous chapter (2.5wt%Pd/SiO$_2$) will confirm. However, sample pretreatment can be enhanced by use of a vacuum during the pretreatment stage to limit the formation of Pd hydride, especially for low Pd contents. However, such equipment was not available.

Table 5.3. CO chemisorption data for the most and least active hydrophobic Pt catalysts investigated in this study. Pretreatment conditions: H$_2$, 1h, 300°C. CO chemisorption performed at RT using 50µL pulses of CO.

Sample	Average Crystallite Size (Å)	Pt Dispersion (%)	Pt surface area (m^2/g)
Pt/SiC	167	7	0.08
Pt/SnO$_2$	443	3	0.03
Pt/BN	304	4	0.05
Pt/Si$_3$N$_4$	81	14	0.17

The order of the CO chemisorption data in the table above relates to the activity series in terms of naphthalene total oxidation. It appears that the same observation made by Edwin *et al.*[1] for Pt/SiO$_2$ applied in this study, i.e. large Pt crystallites with low dispersions are desirable features. This also suggests that the MSI for Pt/SiC was weaker compared to the Pt/Si$_3$N$_4$ catalyst. The Pt/SiC was the most active catalyst studied but was observed to contain smaller Pt crystallites (and the associated higher Pt dispersion) than either the Pt/SnO$_2$ or Pt/BN catalysts. However, the surface areas of Pt/SnO$_2$ and Pt/BN are significantly lower than Pt/SiC, which may explain the increased activity of Pt/SiC over Pt/BN or Pt/SnO$_2$.

The most active Pt catalyst for the total oxidation of propane was found to be Pt/SnO$_2$, followed by Pt/Si$_3$N$_4$ then Pt/BN and Pt/SiC. The high activity of the Pt/SnO$_2$ and Pt/Si$_3$N$_4$ catalysts indicate that the supports which generally interact more strongly with the impregnated metal (i.e. resulting in catalysts with a strong MSI) gave rise to more active catalysts. The two least active catalysts also generally have the weakest MSIs

156

according to the literature as discussed in the introduction of this chapter. However, the Pt crystallite size of Pt/SnO_2 was larger (hence a lower Pt dispersion) than one may expect; one would expect the Pt to be resilient to sintering during calcination when impregnated on a support with a strong MSI. Okanishi *et al.*[63] reported that XPS analysis of Pt/SnO_2 which was first calcined then reduced in $10\%H_2/N_2$ at $400°C$ revealed that the predominant Pt state was metallic Pt. Pt/SnO_2 which had been calcined but not reduced predominantly contained Pt oxides. Since the reduction step of the catalyst preparation appears to limit the Pt-Sn-O interaction, it is possible that Pt was susceptible to increased Pt sintering during thermal treatment in much the same way as a weak MSI support, e.g. SiO_2, SiC and BN.

Bertolini *et al.* reported that the preparation method used to synthesise the catalysts in this study produced small metal crystallites (therefore with relatively high dispersions)[8]. However, that was with respect to Pd impregnation and using Si_3N_4 exclusively, since the strength of the interaction between the metal and support would affect the degree of sintering during catalyst preparation. It was unfortunate that the CO chemisorption data for the Pd/SnO_2 and Pd/Si_3N_4 catalysts could not be obtained to compare the Pd characteristics for the most active catalyst and the catalyst that was investigated by Bertolini *et al.*[8]. The general metal dispersion using this preparation method could be dependent on the metal used and how resilient the metal particles are to sintering etc. during high temperature treatments (e.g. calcination).

5.2.2.5 X-ray Photoelectron Spectroscopy

Table 5.4. Comparison of metal loadings from bulk (EDX) and surface (XPS) studies.

Sample	EDX metal loading (wt%)	XPS metal loading (wt%)
Pd/SnO_2	0.5	1.5
Pd/Si_3N_4	0.4	1.9
Pt/SiC	0.3	13.5
Pt/Si_3N_4	0.3	5.2

XPS analysis of the most and least active Pd and Pt catalysts was performed. Whilst the bulk sensitive analysis (EDX) showed metal loadings similar to the theoretical loadings, the XPS analysis displayed significantly larger metal loadings. This implies that the metal was located on the surface of the support as opposed to being dispersed through the catalyst bulk, which would be expected for an impregnation catalyst preparation.

The most active Pd catalyst, Pd/SnO_2, appeared to have both Pd^0 and Pd oxide present (with binding energies of 335.2eV and 340.4eV respectively). A third binding energy of 338eV was observed in this study and has been previously attributed to be due to oxidised Pd[64, 65]. Pd oxide species have been reported by Neyestanaki *et al.* as being an undesirable species for the total oxidation of naphthalene[66]. The ratio of Pd^0 to Pd oxide was found to be approximately 57:43.

The least active Pd catalyst, Pd/Si_3N_4, displayed less intense Pd binding energies which occurred at higher values observed for Pd/SnO_2. Binding energies of 335.8eV and 341.9eV were observed.
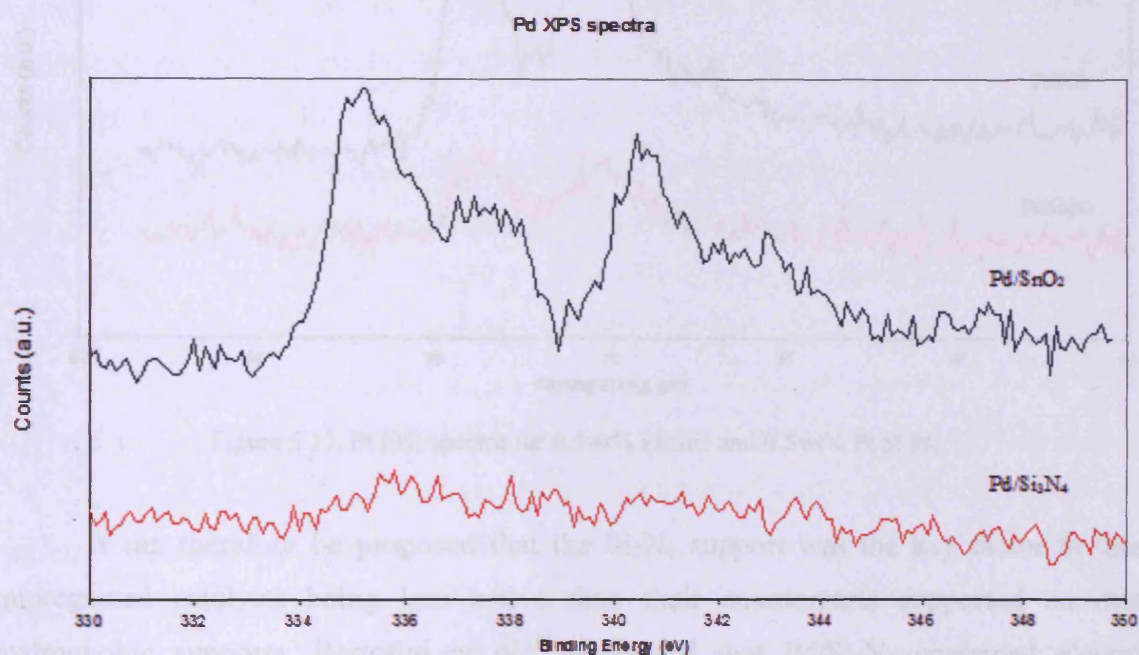
Figure 5.12. Pd (3d) XPS spectra for 0.5wt% Pd/SnO_2 and 0.5wt% Pd/Si_3N_4.

The most active Pt catalyst, Pt/SiC, contained predominantly of Pt metal, a similar observation to Edwin *et al.*[1]. Peaks corresponding to binding energies of 71eV and 74.5eV were reported by Edwin *et al.* to be due to Pt metal and Pt^{4+} (i.e. Pt oxide) respectively. A Pt^0:PtOx ratio of 54:46 was observed.

The least active Pt catalyst, Pt/Si_3N_4, displayed Pt peaks at binding energies of 71.2eV and 74.8eV. The intensities of these binding energies were significantly less than that observed for Pt/SiC, which can be used to explain the difference in catalytic activity between these two catalysts. These two main peaks appeared to be relatively broad (figure

5.13). The peak positions were at a slightly higher binding energy than Pt/SiC, which could indicate that the Pt/Si$_3$N$_4$ experienced a stronger MSI than Pt/SiC. A Pt^0:Pt^{4+} ratio of approximately 51:49 was observed, i.e. Pt/Si$_3$N$_4$ displayed less metallic Pt content than Pt/SiC.

Pt XPS Spectra
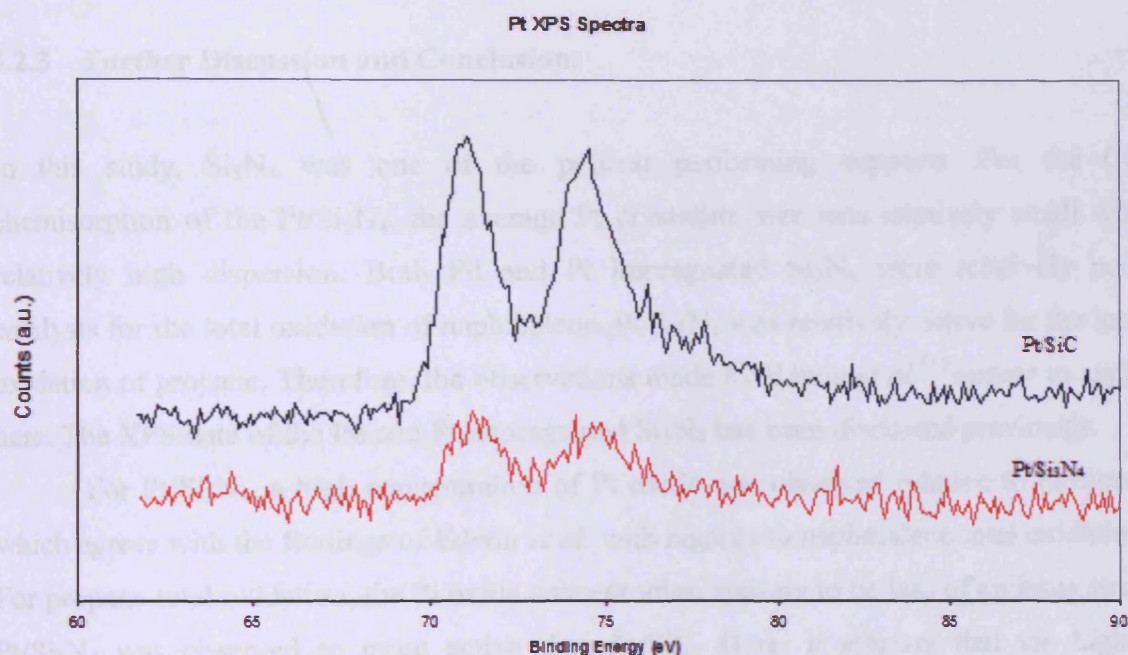
Figure 5.13. Pt (4f) spectra for 0.5wt% Pt/SiC and 0.5wt% Pt/Si$_3$N$_4$.

It can therefore be proposed that the Si$_3$N$_4$ support was the key factor to these impregnated catalysts being less active than their counterparts supported on other hydrophobic supports. Bertolini *et al.*[8] suggested that Pd/Si$_3$N$_4$ contained electron deficient Pd causing a shift in the strength of the metal-support interaction. Based on previous investigations that have been reported in the literature that a strong metal-support interaction was detrimental to catalytic activity[1], it can be suggested that the Si$_3$N$_4$ based catalysts would be less active for naphthalene total oxidation. This would influence the impregnated metal's propensity to sinter/agglomerate during thermal treatments as part of the catalyst preparation. In other words, based on the CO chemisorption data presented above, the stronger MSI of impregnated Si$_3$N$_4$ catalysts causes resilience to sintering during thermal treatment. As the total oxidation of naphthalene has so far been shown to be more facile for impregnated catalysts with large active metal crystallites with relatively poor dispersion, this stronger MSI (hence smaller

159

metal crystallites with higher dispersions) would be a disadvantage. It appears that for the total oxidation of propane, the opposite applied. The Pt/Si_3N_4 was one of the more active Pt catalysts. As the above figure shows, the Pt binding energies for Pt/Si_3N_4 shifted to slightly higher values than Pt/SiC, implying a greater metal-support interaction in line with the reports of Bertolini *et al.*

5.2.3 Further Discussion and Conclusions

In this study, Si_3N_4 was one of the poorest performing supports. For the CO chemisorption of the Pt/Si_3N_4, the average Pt crystallite size was relatively small with relatively high dispersion. Both Pd and Pt impregnated Si_3N_4 were relatively poor catalysts for the total oxidation of naphthalene. Pt/Si_3N_4 was relatively active for the total oxidation of propane. Therefore, the observations made by Edwin *et al.*[1] appear to apply here. The XPS data of the Pd and Pt impregnated Si_3N_4 has been discussed previously.

For Pt/Si_3N_4, a high concentration of Pt oxide was observed relative to Pt metal, which agrees with the findings of Edwin *et al.* with regards to naphthalene total oxidation. For propane total oxidation, the Pt oxide concentration appears to be less of an issue since Pt/Si_3N_4 was observed to more active than Pt/SiC. Here, it appears that the higher dispersion and smaller average Pt crystallite size favoured propane total oxidation.

One might expect SnO_2 to be the next poorest support for the total oxidation of naphthalene based on reports of a stronger MSI compared with BN or SiC. However, SnO_2 gave rise to highly active catalysts for both propane and naphthalene total oxidation regardless of whether Pt or Pd was impregnated upon it. The reason for this activity appears to lie in the catalyst preparation (based on the findings of Okanishi *et al.*[63] with regards to Pt/SnO_2). Okanishi *et al.* reported that calcination followed by reduction at 400°C revealed the existence of metallic Pt. If the Pt/SnO_2 was calcined but not reduced, Pt oxides were formed. The average Pt crystallite size was also found to increase if the reduction at 400°C was performed after calcination (via TEM analysis).

In this study, Pt/SnO_2 was shown (using CO chemisorption analysis) to contain large, predominantly metallic Pt particles and should therefore display high activity for naphthalene total oxidation. However, one might expect a catalyst which displayed large, poorly dispersed Pt crystallites to be relatively inactive for the total oxidation of propane. As Pt/SnO_2 was highly active for propane total oxidation, it appears that the metal

160

crystallite size/dispersion and the strength of the MSI are not the only controlling factors. If a large quantity of metallic Pt is present, then one may suggest that a redox mechanism similar to the one described in section 4.8 may operate. The Mars van Krevelen mechanism has been previously reported to operate for the total oxidation of propane, e.g. Au doped Co oxide[67]. A kinetic study would need to be performed in order to ascertain if this is the case.

Of the catalysts investigated, the Pd and Pt impregnated SnO_2 catalysts displayed the most significant H_2 uptake via TPR analysis. This reduction was observed to begin at a temperature of *ca.* 325°C for both catalysts. A low H_2 uptake was observed at 100 – 150°C for both catalysts, which is likely to be due to the reduction of residual acetylacetonate ligands from the precious metal salts used during catalyst preparation.

Therefore, the reducibility of the two SnO_2 catalysts was not a significant feature with respect to naphthalene total oxidation since 100% CO_2 yields were observed for both catalysts at temperatures below 300°C. For the total oxidation of propane, the light-off temperatures (i.e. the temperature range where CO_2 yields significantly increase) of both SnO_2 catalysts coincide with increasing H_2 uptake during TPR analysis. Previous studies indicate that this reduction is of bulk SnO_2[68]. This suggests that a redox reaction pathway involving the oxygen species from SnO_2 could be plausible for propane total oxidation by SnO_2 catalysts. The enhanced reducibility of the SnO_2 catalysts may also explain the mass transfer effect observed for Pt/SnO_2. At temperatures of 400°C and above, the influence of mass transfer on CO_2 yield can be seen. The TPR analysis showed that catalyst reducibility began to significantly increase at the same temperature. If the catalyst can undergo reduction more efficiently (hence increasing the efficiency of propane oxidation), then the mechanism for propane adsorption could become the limiting factor to catalyst activity. Pd/SnO_2 also displayed similar behaviour but not to the same severity as that observed for the platinum analogue.
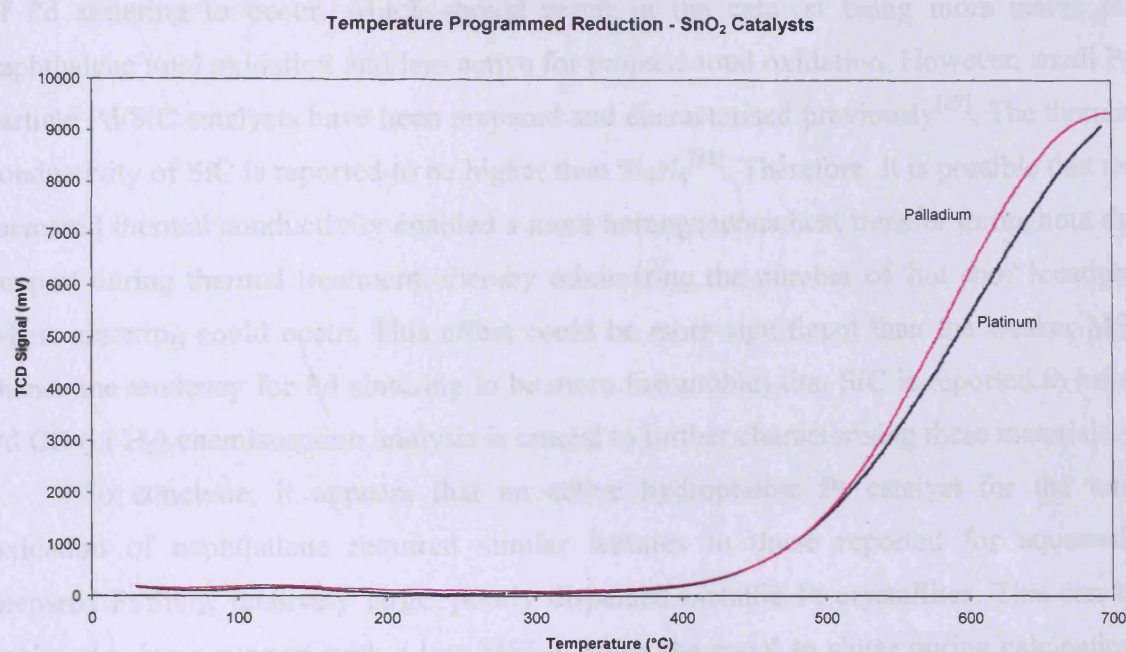
Temperature Programmed Reduction - SnO$_2$ Catalysts

Figure 5.14. Temperature Programmed Reduction data for 0.5wt% Pt/SnO$_2$ and 0.5wt% Pd/SnO$_2$. Data obtained using Thermo TPDRO1100, 10% H$_2$/Ar at 13mL/min, ramp rate of 5°C/min, temperature range of RT – 700°C studied. Sample mass – *ca.* 100mg per run.

Boron nitride was not a suitable support for propane total oxidation. The surface area of the support was very low and the formation of large metal crystallites (based on the Pt/BN CO chemisorption) appears to be unfavoured compared to smaller, more highly dispersed metal crystallites. BN was a more suitable support for the total oxidation of naphthalene. Since the lower MSI of BN allows migration of the impregnated metal (sintering), larger crystallites could be formed, as shown by the CO chemisorption data obtained for Pt/BN, which would enhance the catalytic activity in agreement with the published literature.

Pt/SiC was observed to have a larger Pt crystallite size coupled with a relatively low dispersion than Pt/Si$_3$N$_4$, but Pt/SnO$_2$ and Pt/BN displayed larger Pt crystallite sizes. This was beneficial for naphthalene total oxidation as observed for Pt/SiO$_2$. As with BN, this larger Pt crystallite size was not suitable for propane total oxidation. The lower MSI of SiC with Pt allowed sintering of the metal to occur. Pd/SiC was one of the most active Pd catalysts for the total oxidation of propane and one of the least active for naphthalene total oxidation. As described above, chemisorption data could not be obtained for the Pd catalysts. Based on the other catalysts studied here, one could conclude that the Pd may exist as relatively small crystallites. However, the weak MSI of SiC should allow a degree

162

of Pd sintering to occur, which should result in the catalyst being more active for naphthalene total oxidation and less active for propane total oxidation. However, small Pd particle Pd/SiC catalysts have been prepared and characterised previously[69]. The thermal conductivity of SiC is reported to be higher than Si_3N_4[48]. Therefore, it is possible that the increased thermal conductivity enabled a more homogeneous heat transfer throughout the support during thermal treatment, thereby minimising the number of 'hot spot' locations where sintering could occur. This effect could be more significant than the weaker MSI (hence the tendency for Pd sintering to be more favourable) that SiC is reported to have. Pd CO (or H_2) chemisorption analysis is crucial to further characterising these materials.

To conclude, it appears that an active hydrophobic Pt catalyst for the total oxidation of naphthalene required similar features to those reported for aqueously prepared Pt/SiO_2; relatively large, poorly dispersed metallic Pt crystallites. This can be achieved using a support with a low MSI to allow the metal to sinter during calcination, such as SiC. The least active catalyst, Pt/Si_3N_4, was observed to have a stronger MSI.

For propane total oxidation, it was concluded that smaller, more highly dispersed Pt crystallites were required. However, Pt/SnO_2 (with a large Pt crystallite size) was also an active catalyst, suggesting that a redox mechanism can operate as discussed previously.

For Pd catalysts and the total oxidation of naphthalene, Pd/SnO_2 was found to be the most active catalyst. Pd/Si_3N_4 was found to be the least active. Pd/Si_3N_4 was shown to have a relatively strong MSI in agreement with reported literature. Pd/SnO_2 was found to have a larger concentration of metallic Pd. Experiments to determine Pd crystallite size and dispersion could not be performed satisfactorily and is a key dataset to obtain.

For propane total oxidation, Pd/SiC and Pd/SnO_2 were observed to be the most active catalysts. Pd/Si_3N_4 was the least active alongside Pd/BN. Pd/Si_3N_4 is known to have a strong MSI and XPS binding energies suggested that the Pd was chemically influenced, e.g. there was a significant amount of non-metallic Pd in agreement with published literature. This overrode the effect of a small average Pd crystallite size and high dispersion which one would expect to be beneficial for propane total oxidation based on the Pt data. Pd/SiC can have small Pd crystallites[69] and Pd has been shown in the literature to be primarily metallic[48]. The weak MSI of SiC with Pd implied that Pd would sinter during thermal treatment. However, the high thermal conductivity of SiC appeared to reduce the number of localised hot spots considerably, thereby reducing the number of sites where Pd sintering would be encouraged.

5.3   Comparison of Pd/BN Prepared Using Aqueous and Non-Aqueous Solvents

5.3.1   Introduction

The purpose of this section is to determine if the use of a non-aqueous solution offers an improved catalyst over an aqueous preparation, based on the discussions of Edwin *et al.*[1], who stated that hydrophobic supports underwent poor surface wetting in aqueous preparations. Therefore, it could be anticipated that increasing the amount of support wetting during the catalyst preparation would be beneficial to the impregnation of the active metal species. The catalyst investigated was 0.5wt% Pd/BN.

5.3.2   Catalytic Activity

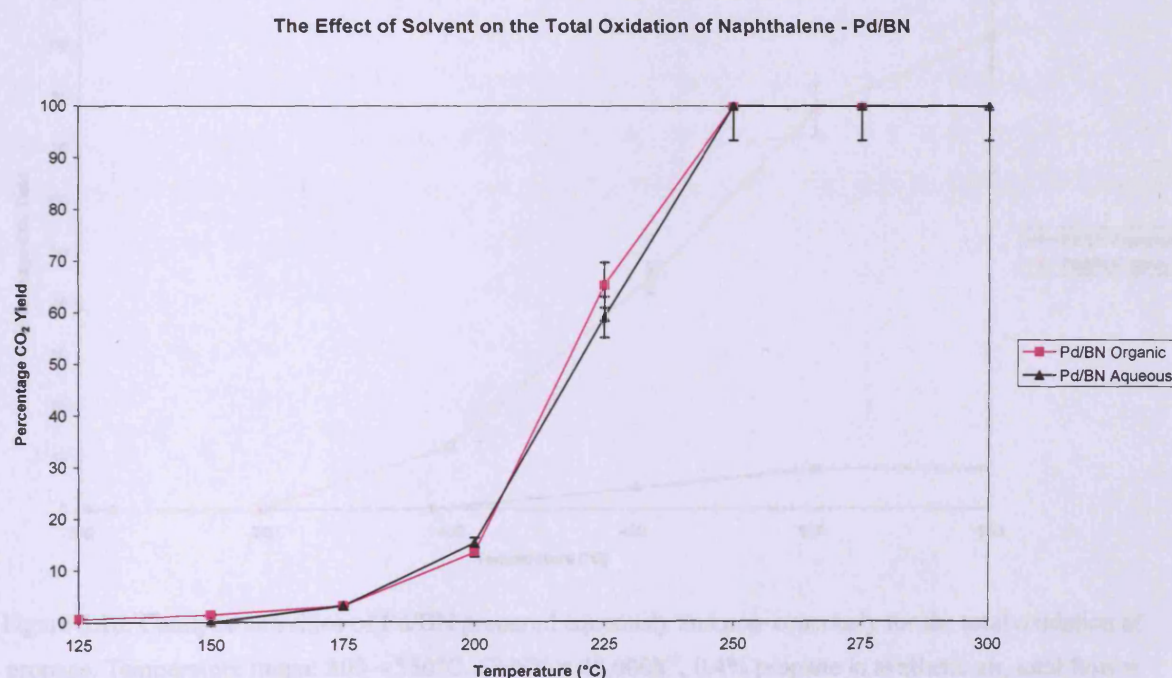### 5.3.2.1 Naphthalene Total Oxidation

Figure 5.15. Catalytic activity data for Pd/BN prepared aqueously and non-aqueously (using toluene) for the total oxidation of naphthalene. Temperature range: 125 – 300°C. GHSV = 45,000h^{-1}, 100vppm naphthalene, total flow = 50mL/min. Error bars are ± 6.7%.

As the above figure shows, there was little difference observed in the catalysts' activities.

164

Both achieved T_{100} at the same temperature (250°C) and the T_{50} values are very similar. Therefore, it appears that in the case of Pd/BN, the deposition of the Pd metal appears to be unhindered by the lack of support wetting in the case of the aqueous preparation. It is possible that the Pd crystallite sizes of the precursors were smaller than the finished catalysts, i.e. sintering occurred during the catalyst thermal treatment. However, probing this would be difficult. Since high temperatures would be required to perform CO (or H_2) chemisorption on the non-calcined catalysts, the characteristics of the impregnated metal would be likely to change (e.g. sintering). Repeat experiments were performed with respect to both the aqueous and non-aqueous Pd/BN to try and replicate the initial activity plot given in the figure above using fresh sample. Both could be replicated successfully.

5.3.2.2 Propane Total Oxidation

The Effect of Solvent on the Total Oxidation of Propane - Pd/BN
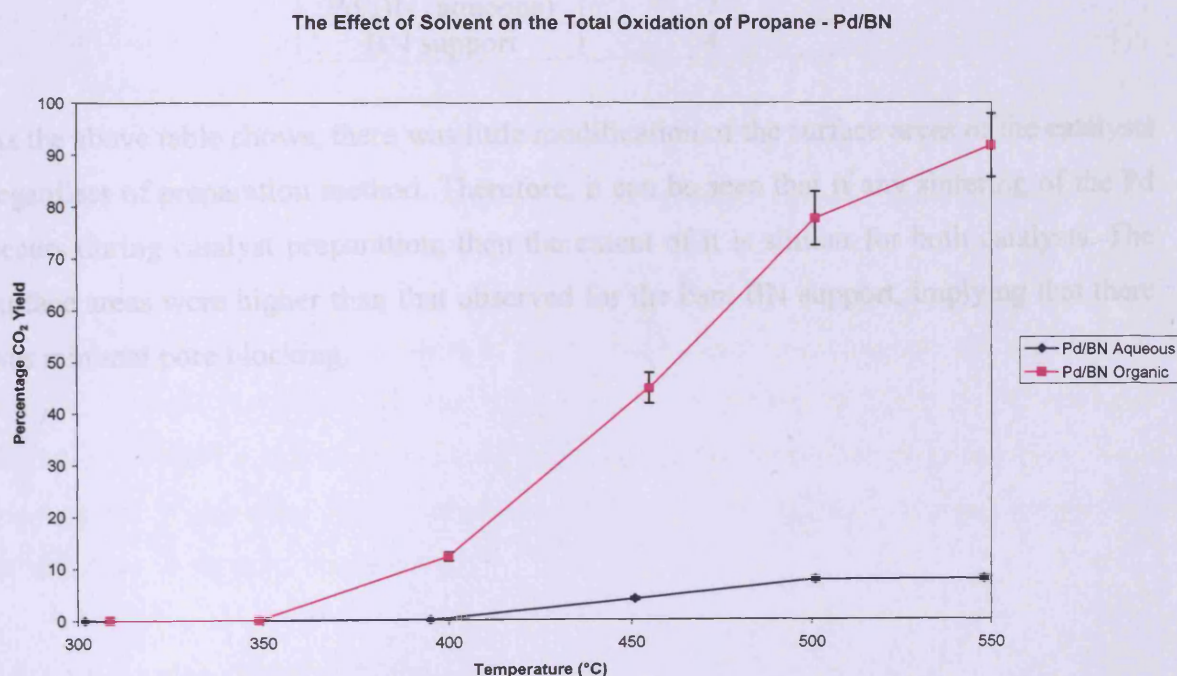
Figure 5.16. Catalytic activities of Pd/BN prepared aqueously and non-aqueously for the total oxidation of propane. Temperature range: 300 – 550°C. GHSV = 45,000h^{-1}, 0.4% propane in synthetic air, total flow = 50mL/min. Error bars are ± 6.7%.

In the above figure, it is clear to see that the use of a non-aqueous solvent (in this case, toluene) greatly benefits the catalytic activity. It has been shown that for light hydrocarbons such as methane, small supported metal crystallites with relatively high

dispersions tend to be the most active catalysts[7, 8]. Propane can be considered a light hydrocarbon since it is a small straight chained alkane, therefore it is likely that the same catalyst features for methane oxidation would apply to propane oxidation. As mentioned previously, the preparation method used in this study has been previously reported to yield small highly dispersed metal crystallites[7, 8].

5.3.3 Characterisation

5.3.3.1 Surface Area Analysis

Table 5.5. Surface area analysis of Pd/BN prepared using aqueous (water) and non-aqueous (toluene) solvents. Surface areas obtained using N_2 adsorption at 77K and the BET method. Pd loadings are 0.5wt%.

Sample	Surface Area (m^2/g)
Pd/BN(non-aqueous)	6
Pd/BN (aqueous)	7
BN support	4

As the above table shows, there was little modification of the surface areas of the catalysts regardless of preparation method. Therefore, it can be seen that if any sintering of the Pd occurs during catalyst preparation, then the extent of it is similar for both catalysts. The surface areas were higher than that observed for the bare BN support, implying that there was minimal pore blocking.

5.3.3.2 X-ray Diffraction
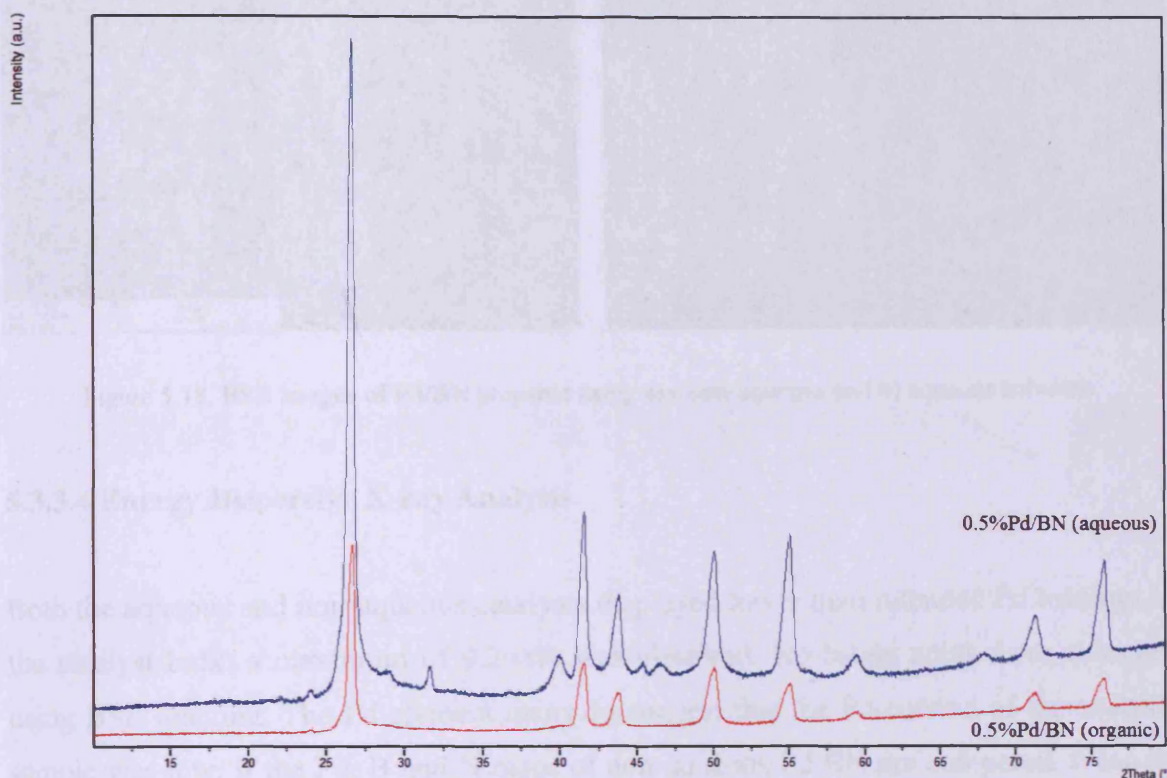
Figure 5.17. XRD patterns of 0.5wt% Pd/BN prepared using aqueous and non-aqueous/organic solvents. Cubic Pd phases observed on aqueous Pd/BN pattern.

The aqueous Pd/BN catalyst displayed extra phases that were not observed for the non-aqueous (organic) analogue. These extra phases were matched with a cubic Pd reference pattern. Therefore it can be concluded that the amount of crystalline Pd phase increased if an aqueous preparation was performed. However, this did not enhance activity for naphthalene or propane combustion.

5.3.3.3 Scanning Electron Microscopy

In terms of morphology, the BN catalyst appeared to be unmodified whether prepared using aqueous or non aqueous solvents. The same butterfly-like morphology was observed. As with the hydrophobically prepared Pd/BN, no bright spots relating to Pd could be observed.
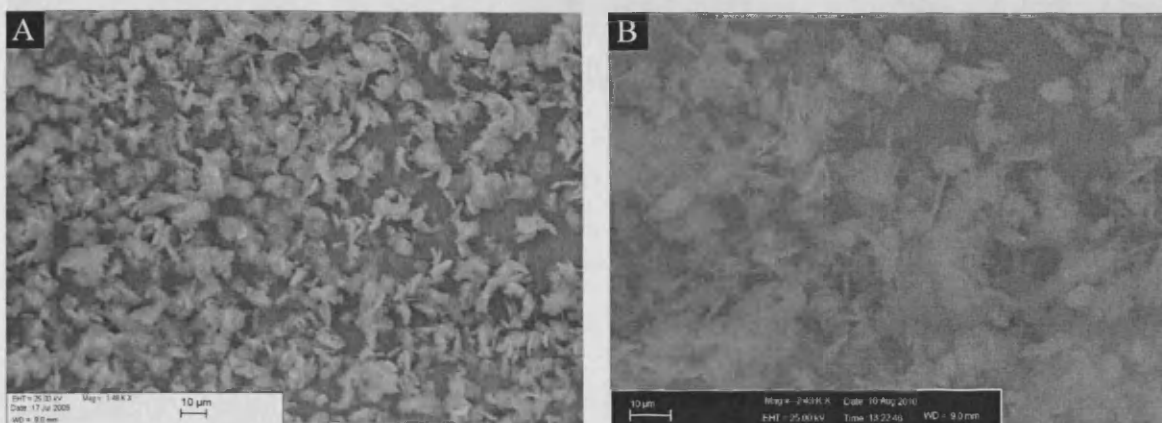
Figure 5.18. BSE images of Pd/BN prepared using a) a non-aqueous and b) aqueous solvents.

5.3.3.4 Energy Dispersive X-ray Analysis

Both the aqueous and non-aqueous catalysts displayed lower than intended Pd loadings in the catalyst bulk; a maximum of 0.2wt% was observed. No bright spots were observed using BSE imaging. The Pd element maps do suggest that the Pd content of the analysis sample was low; if the Pd, B and N maps of non-aqueous Pd/BN are compared, it can be seen that the B and N maps resemble the original electron image. The Pd map does not. The aqueous Pd/BN Pd map did show the same characteristics; however there were areas of the map which resembled the original electron image (figure 5.20).

Table 5.6. EDX data for Pd/BN prepared aqueously and non aqueously. Error measurements calculated by analyser during the analysis.

Sample	Pd content (wt%)
0.5wt% Pd/BN (non-aqueous)	0.2
0.5wt% Pd/BN (aqueous)	0.2

Figure 5.19. Elemental mapping data for non-aqueous 0.5wt% Pd/BN. Maps of b) Pd; c)B; d) N; based on a) the Pd/BN electron image.

Figure 5.20. Elemental mapping data for aqueous 0.5wt% Pd/BN. Maps of b) Pd; c) B; d) N; based on a) the Pd/BN electron image.
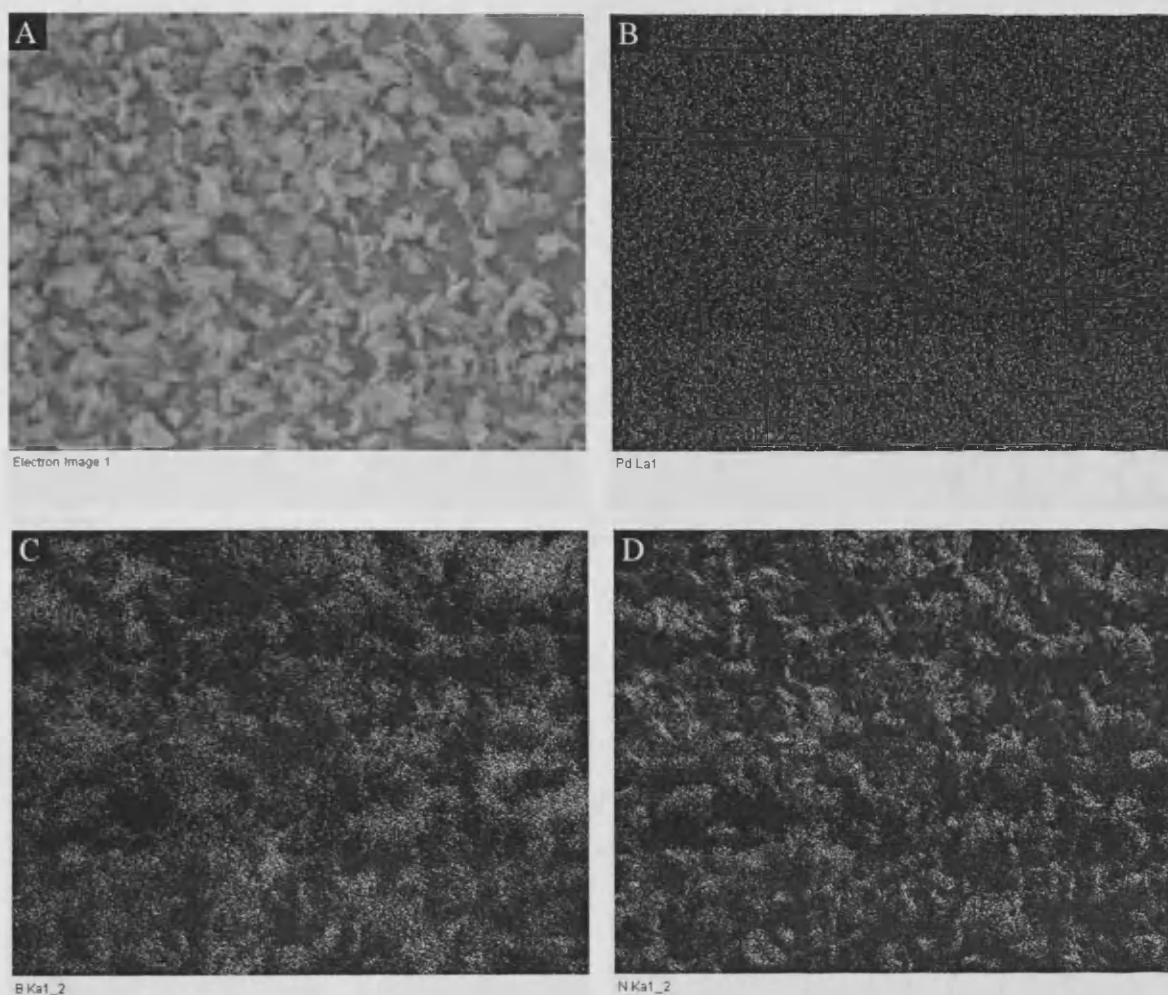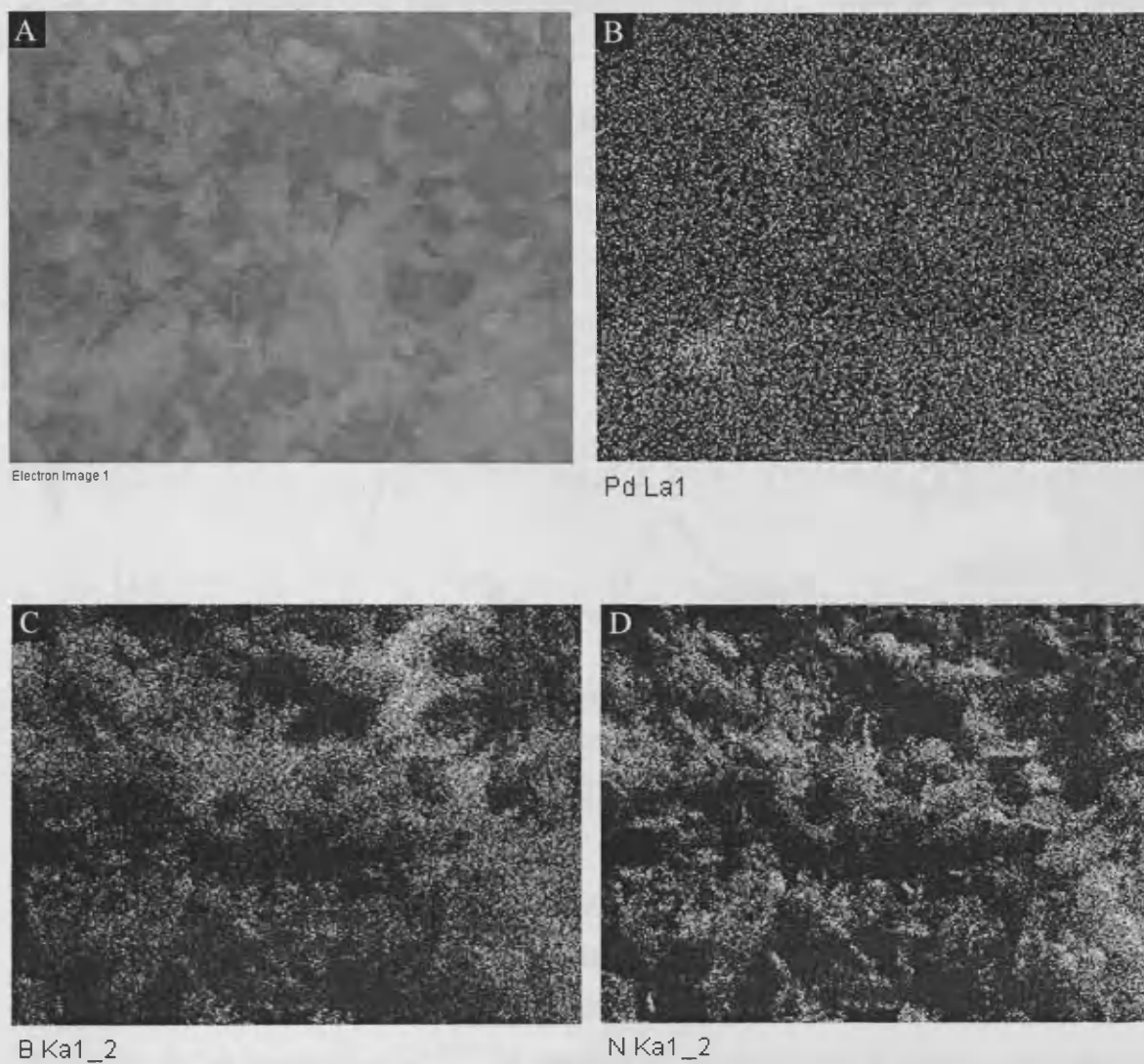
5.3.3.5 X-ray Photoelectron Spectroscopy
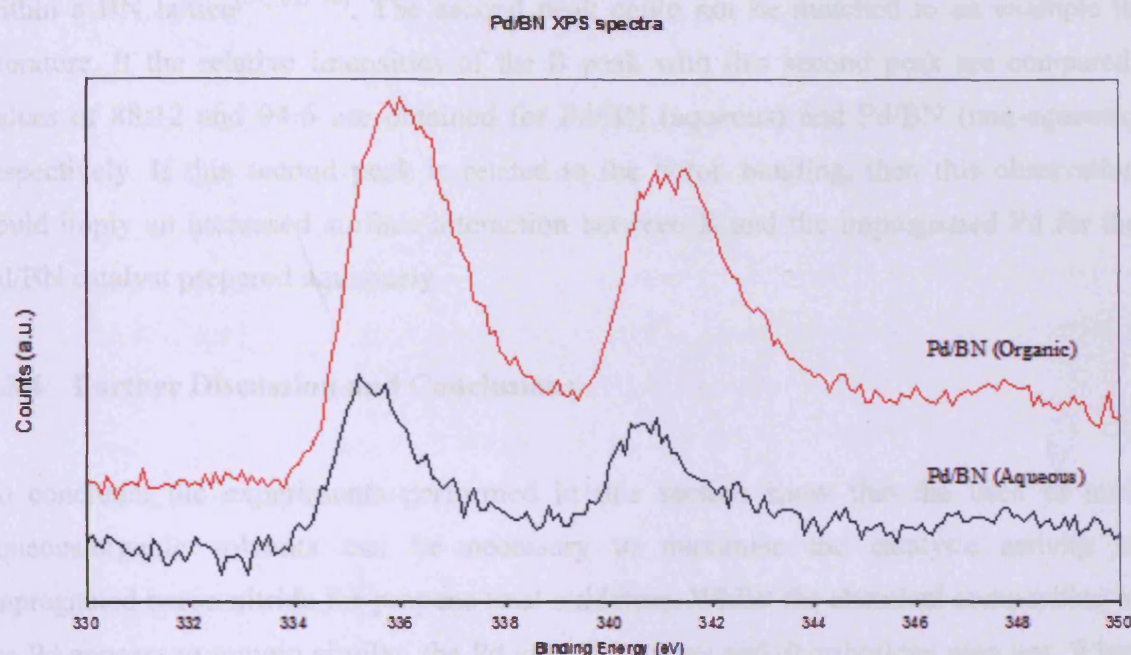
Figure 5.21. Pd 3d spectra for 0.5wt% Pd/BN prepared in aqueous and non-aqueous solvents.

The Pd/BN (aqueous) catalyst was observed to have binding energies of 335eV and 340eV, which related to Pd^0 and PdO respectively. Pd oxides have been previously reported to be disadvantageous for an active Pd catalyst (in terms of naphthalene total oxidation) by Neyestanaki *et al.*[66]. Pd contents of approximately 0.35wt% were observed for both catalysts, implying that the majority of the Pd was situated at the immediate surface. Similar binding energies were observed for the non-aqueous Pd/BN analogue, hence Pd^0 and PdO were observed.

Table 5.7. Pd^0:PdO ratio for 0.5wt% Pd/BN prepared using an aqueous and non-aqueous solvent determined by XPS spectra peak analysis.

Sample	Pd^0:PdO ratio
Pd/BN (non-aqueous)	60:40
Pd/BN (aqueous)	63:37

As the above table shows, both Pd/BN catalysts were observed to have similar ratios of catalytically active to inactive Pd states. Therefore the difference in catalytic activity was due to another catalyst feature which may not have been characterised fully e.g. Pd crystallite size and distribution.

171

In the boron 1s spectra for both Pd/BN samples, two peaks were observed. The most intense peak was observed at approximately 190.5eV which was matched to B within a BN lattice[64, 65, 70]. The second peak could not be matched to an example in literature. If the relative intensities of the B peak with this second peak are compared, values of 88:12 and 94:6 are obtained for Pd/BN (aqueous) and Pd/BN (non-aqueous) respectively. If this second peak is related to the boron bonding, then this observation could imply an increased surface interaction between B and the impregnated Pd for the Pd/BN catalyst prepared aqueously.

5.3.4 Further Discussion and Conclusions

To conclude, the experiments performed in this section show that the used of non-aqueous/organic solvents can be necessary to maximise the catalytic activity of impregnated boron nitride for propane total oxidation. Whilst the chemical composition of the Pd appears to remain similar, the Pd crystallite sizes and distributions may not. When Pt/SnO$_2$ was prepared aqueously by Edwin *et al.*, they noted that Pt impregnation was hindered by poor wetting of the support. It would not be surprising if the same applied here since SnO$_2$ and BN are hydrophobic materials. Pd-CO chemisorption would be of a great benefit but requires the use of a vacuum system to satisfactorily prepare the Pd catalysts prior to undertaking the chemisorption experiments. Surface XPS analysis suggested that Pd content was approximately correct with regards to intended loadings and that the aqueous catalyst preparation could give rise to increased Pd-B interaction at the surface. If metallic Pd is the active Pd phase, as with Pt, then this increased MSI would be undesirable.

Another differing feature associated with a change in preparation solvent is the appearance of crystalline Pd phases in the XRD pattern of Pd/BN (aqueous). Since the weight loading of both Pd/BN catalysts was similar, it may be possible that the Pd crystallite size was larger for the aqueous Pd/BN. Based on the activity data presented throughout this text, it is concluded that larger Pd crystallite size would be detrimental to the catalytic activity of Pd/BN for the total oxidation of propane. This could be caused by poor wetting in the case of aqueous Pd/BN.

5.4   Analysis of a High Surface Area Pd/SnO$_2$ Catalyst

5.4.1   Introduction

Due to the high performance of the Pd/SnO$_2$ catalyst reported in this study, an attempt at improving the catalytic activity was undertaken. Whilst the Pd/SnO$_2$ catalyst was not quite as active as aqueously prepared Pt/SiO$_2$, the surface areas are very different. The SiO$_2$ catalysts contain surface areas of approximately 400m^2/g, the Pd/SnO$_2$ catalyst reported in this study had a surface area of just 7m^2/g. Therefore there is scope to improve this surface area with the aim to increase the catalytic activity.

One way of creating high surface area supports is to use a high surface area material as a secondary support. A paper published by Wang *et al.* reported a preparation method for SnO$_2$ impregnated on a SiO$_2$ support[71]. The authors of that paper reported that XRD analysis revealed that segregated SnO$_2$ phases occurred when 16wt% of Sn was impregnated on the SiO$_2$. Therefore an analogue was prepared and then impregnated with 0.5wt% Pd as previously performed in this study.

5.4.2   Catalytic Activity

5.4.2.1 Naphthalene Total Oxidation
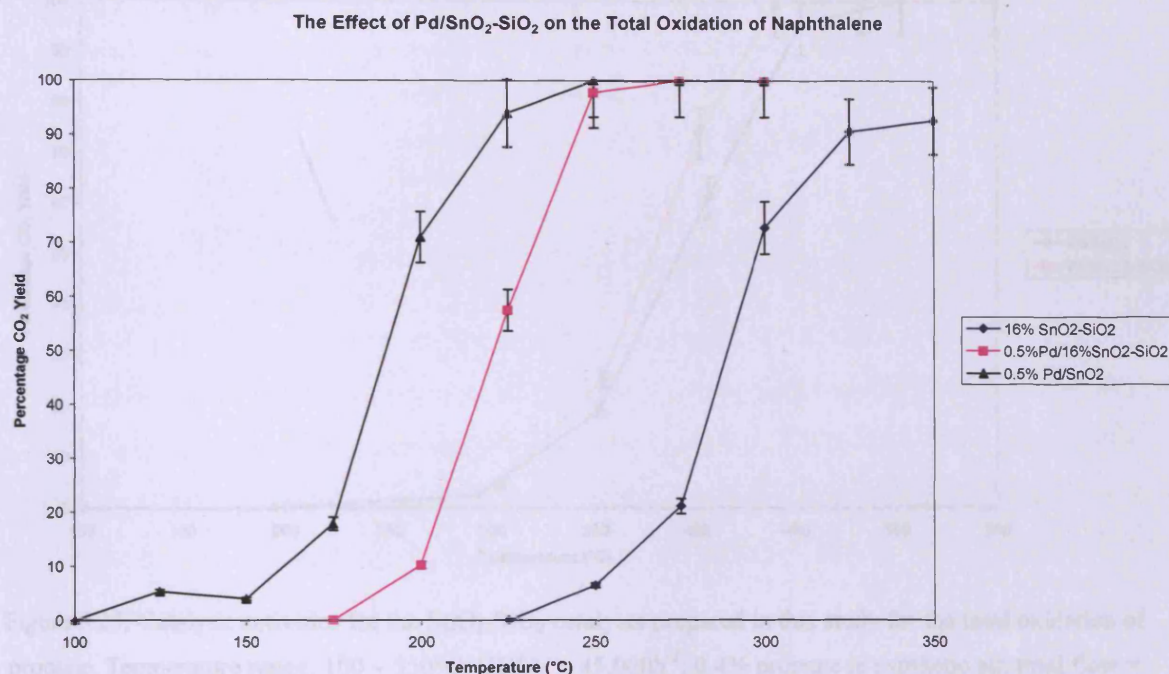
Figure 5.22. Catalytic activities for the SnO_2-SiO_2 catalysts prepared in this study for the total oxidation of naphthalene. The activity data for impregnated SnO_2 is included for comparative purposes. Temperature range: 100 – 350°C. GHSV = 45,000h^{-1}, 100vppm naphthalene, total flow = 50mL/min. Error bars are ± 6.7%.

For the total oxidation of naphthalene, it appears that the Pd/SnO_2-SiO_2 catalyst was less active than Pd/SnO_2. It is possible that the average Pd crystallite size is smaller for the SiO_2 based catalyst than the SnO_2 only analogue, which so far has been shown to be a disadvantage when preparing highly active catalysts for the total oxidation of naphthalene. The comparison of SnO_2-SiO_2 support with the Pd impregnated analogue shows that the Pd actively participates in the naphthalene oxidation. A CO_2 yield in excess of 90% (albeit at a much higher temperature than the impregnated version) was observed for 16% SnO_2-SiO_2.

174

5.4.2.2 Propane Total Oxidation

The Effect of SnO₂ Type on the Total Oxidation of Propane
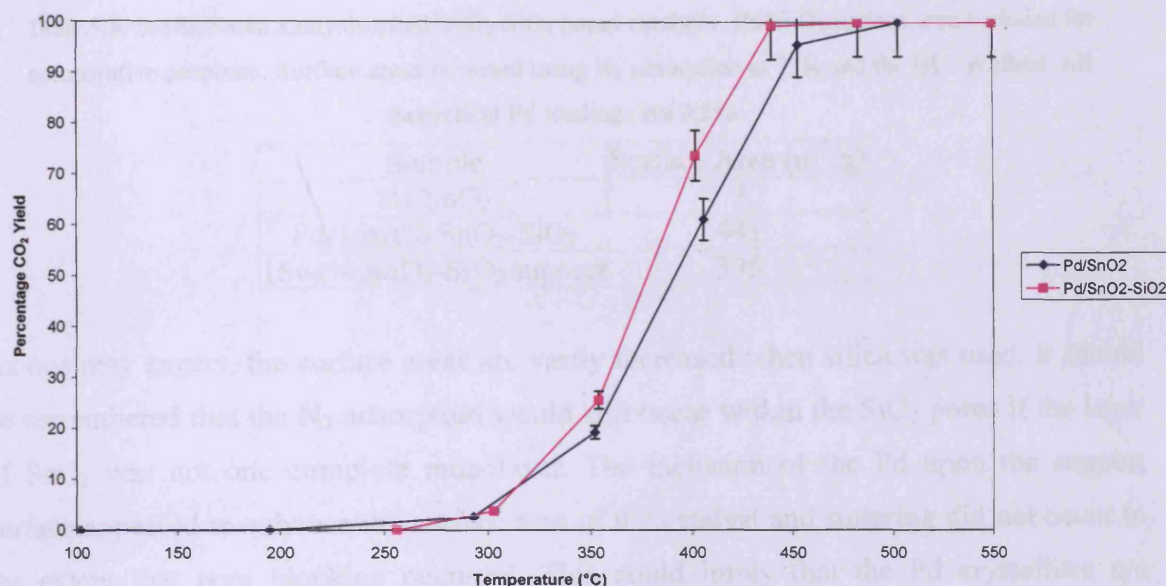
Figure 5.23. Catalytic activities for the SnO_2-SiO_2 catalysts prepared in this study for the total oxidation of propane. Temperature range: $100 - 550°C$. GHSV $= 45,000h^{-1}$, 0.4% propane in synthetic air, total flow $= 50mL/min$. Error bars are $\pm 6.7\%$.

As figure 5.23 shows, the catalytic activity for the total oxidation of propane can be improved by using SnO_2-SiO_2 as opposed to SnO_2 as the catalyst support. T_{100} was achieved at a temperature below $450°C$ for Pd/16% SnO_2-SiO_2, compared to $500°C$ for Pd/SnO_2. Pd/16% SnO_2-SiO_2 was also observed to reach T_{50} at a lower temperature ($378°C$ and $392°C$ for Pd/SnO_2-SiO_2 and Pd/SnO_2 respectively). The suggestions given in section 5.4.2.1 can also be applied here to explain why the impregnated SnO_2-SiO_2 was less active for naphthalene total oxidation compared to Pd/SnO_2, but more active than Pd/SnO_2 for propane total oxidation. 16% SnO_2-SiO_2 achieved a CO_2 yield of 25% at $550°C$.

5.4.3 Characterisation

5.4.3.1 Surface Area Analysis

Table 5.8. Surface area analysis of all SnO_2-SiO_2 based catalysts. Pd/SnO_2 surface area included for comparative purposes. Surface areas obtained using N_2 adsorption at 77K and the BET method. All theoretical Pd loadings are 0.5%.

Sample	Surface Area (m^2/g)
Pd/SnO_2	7
$Pd/16wt\%$ SnO_2-SiO_2	441
$16wt\%$ SnO_2-SiO_2 support	395

As one may expect, the surface areas are vastly increased when silica was used. It should be remembered that the N_2 adsorption would still occur within the SiO_2 pores if the layer of SnO_2 was not one complete monolayer. The inclusion of the Pd upon the support surface appeared to enhance the surface area of the catalyst and sintering did not occur to the extent that pore blocking occurred. This could imply that the Pd crystallites are relatively small.

5.4.3.2 X-ray Diffraction
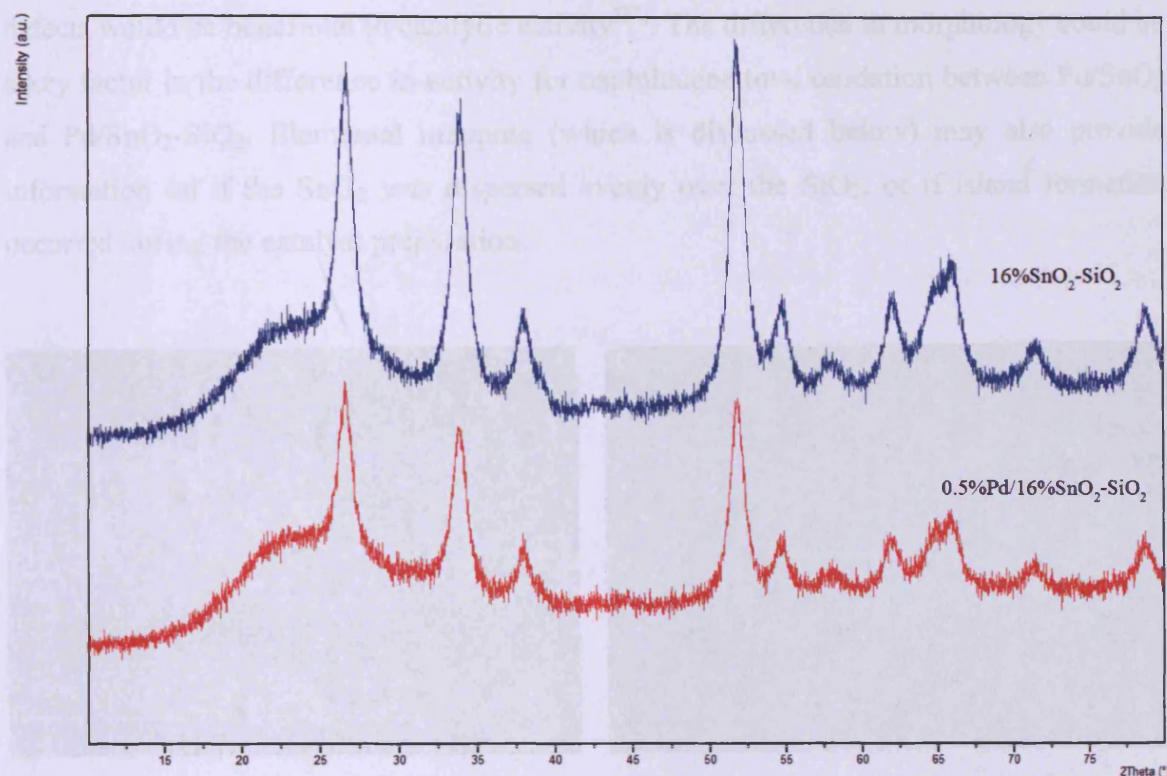
Figure 5.24. XRD patterns of 0.5wt% Pd/16wt% SnO_2-SiO_2 and 16wt% SnO_2-SiO_2.

As the above patterns show, there were no modifications made upon impregnation of the Pd in terms of new phases. As the Pd content was low, this was not surprising. The peak positions of the SnO_2-SiO_2 phases remained at approximately the same angles. The only modification made to the pattern was a loss in crystallinity when Pd was impregnated upon the SnO_2-SiO_2 support. The crystalline phases observed were all due to crystalline SnO_2 as shown by Wang *et al.*[71]. The patterns shown here are very similar to that published by Wang *et al.* which indicates that the same material was made in this study.

5.4.3.3 Scanning Electron Microscopy

If the impregnated SnO_2 and SiO_2-SiO_2 catalysts are compared, it can be seen that the morphologies are very different. The SnO_2 morphology was observed to be globular and therefore the chance of obtaining a relatively high degree of surface defects was appreciable. The SnO_2-SiO_2 based catalyst was significantly less globular; in fact the surface was observed to be fairly flat with islands of material upon it. These would

introduce surface defects but possibly not in the same number as the Pd/SnO_2 catalyst. For the total oxidation of naphthalene, it has been proposed that a high number of surface defects would be beneficial to catalytic activity[72]. The difference in morphology could be a key factor in the difference in activity for naphthalene total oxidation between Pd/SnO_2 and Pd/SnO_2-SiO_2. Elemental mapping (which is discussed below) may also provide information on if the SnO_2 was dispersed evenly over the SiO_2, or if island formation occurred during the catalyst preparation.
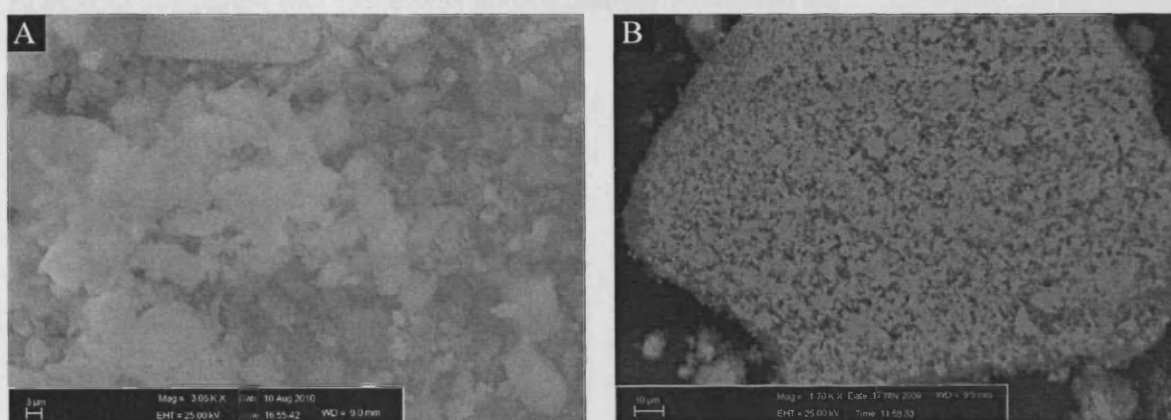
Figure 5.25. BSE images of a) 0.5wt% $Pd/16wt\%$ SnO_2-SiO_2 and b) 0.5wt% Pd/SnO_2.

5.4.3.4 Energy Dispersive X-ray Analysis

A 16wt% Sn content was desired for the SnO_2-SiO_2 support. EDX analysis suggested a Sn content of approximately 11wt% was achieved. The same data was observed upon repeated experiments. There was enough SnO_2 to display segregated SnO_2 crystalline phases in the XRD patterns, although there may be less than a monolayer coverage of the SnO_2 on the SiO_2 support.

The impregnated SnO_2-SiO_2 (i.e. 0.5wt% $Pd/16wt\%$ SnO_2-SiO_2) displayed a Pd loading of approximately 0.4wt%. This value was observed consistently over several repeated experiments. No bright spots could be observed which related to impregnated Pd.

178

Table 5.9. EDX data for 16wt% SnO_2-SiO_2 and 0.5wt% Pd/16wt% SnO_2-SiO_2. Error measurements calculated by analyser during the analysis.

Sample	Metal loading (wt%)
16wt% SnO_2-SiO_2	10.82 ± 0.08 (Sn)
0.5wt% Pd/16wt% SnO_2-SiO_2	0.41 ± 0.06 (Pd)

The elemental mapping of the 16wt% SnO_2-SiO_2 showed that the Sn was distributed evenly over the SiO_2, although the intensity of the Sn signal was less than that observed for Si, which could be expected as a relatively low Sn content was present. The EDX data suggested that there was approximately 32wt% of Si.
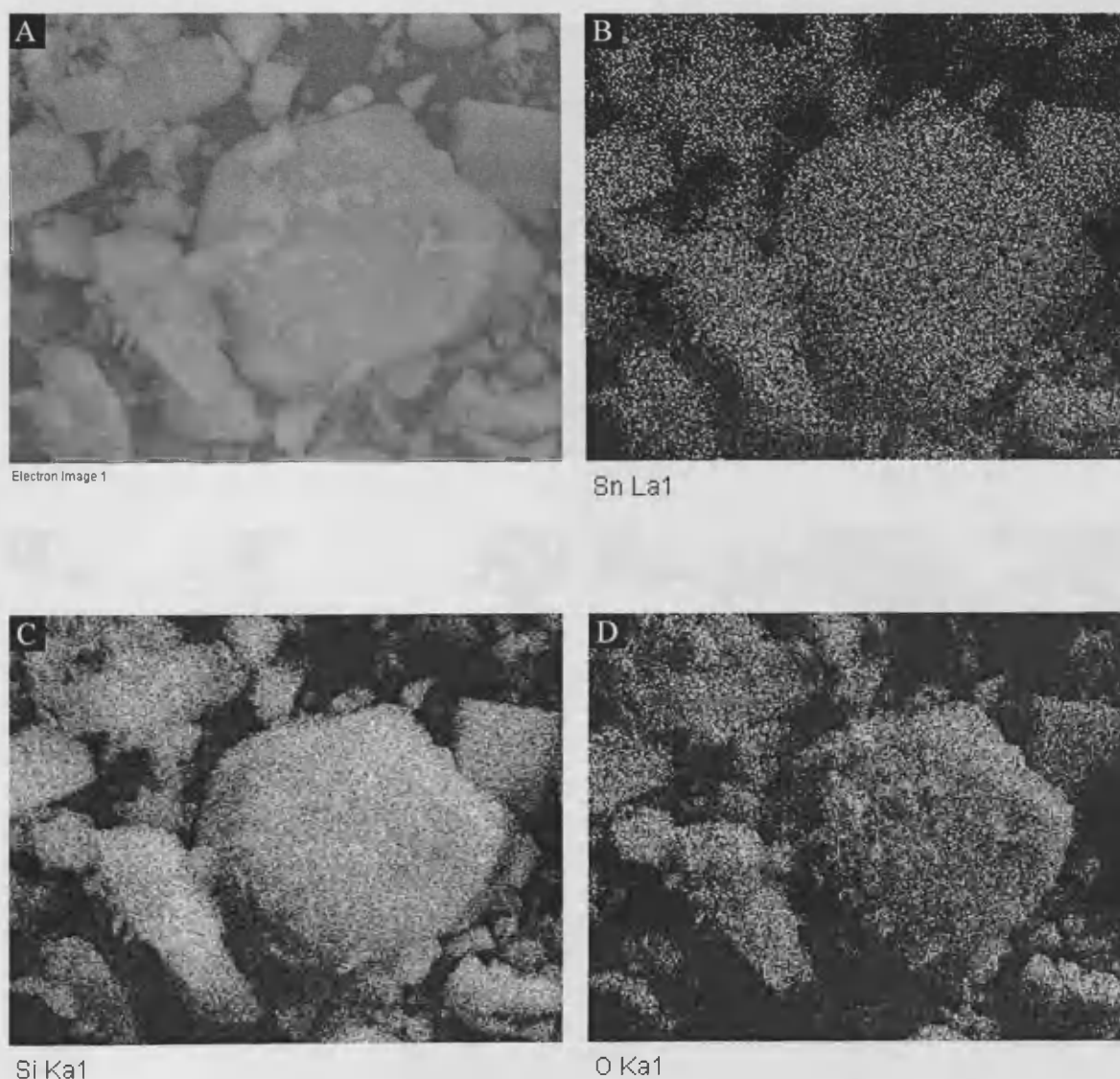

Figure 5.26. Elemental mapping data for 16wt% SnO_2-SiO_2. Maps of b) Sn; c) Si; d) O; based on a) the 16wt% SnO_2-SiO_2 electron image.
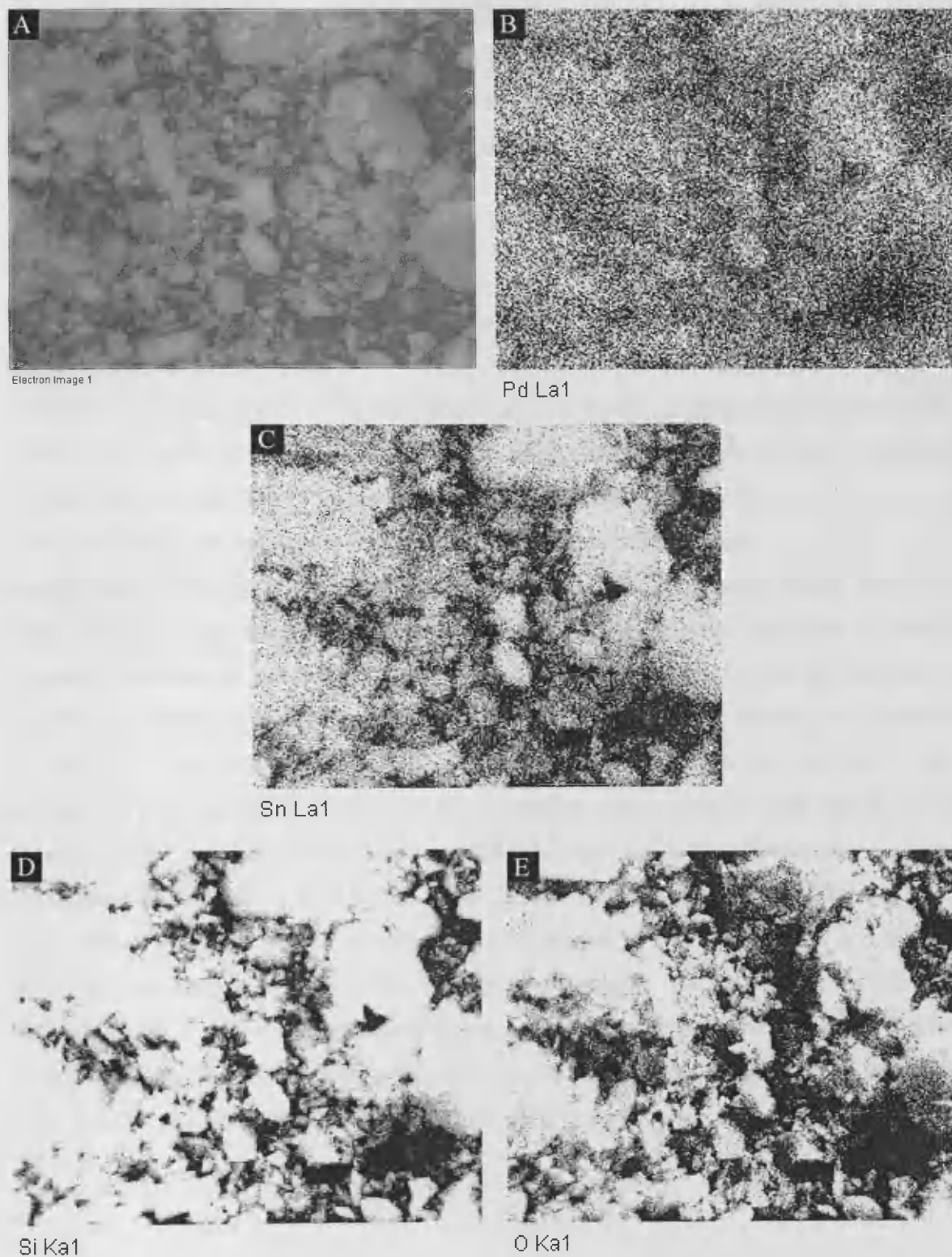
Figure 5.27. Elemental mapping data for 0.5wt% Pd/16wt% SnO_2-SiO_2. Maps of b) Pd; c) Sn; d) Si; and e) O; based on a) the 16wt% SnO_2-SiO_2 electron image.

The Pd/SnO$_2$-SiO$_2$ catalyst, as with the other Pd catalysts studied in this chapter, was evenly distributed on/through the catalyst and no islands or concentrations of Pd signal could be observed. However, there was a more significant Pd content for Pd/SnO$_2$-SiO$_2$ than for Pd/BN; the Pd map for Pd/SnO$_2$-SiO$_2$ resembled the original BSE image.

5.4.3.5 X-ray Photoelectron Spectroscopy

The XPS data of Pd/SnO$_2$ has been discussed previously. For Pd/SnO$_2$-SiO$_2$, binding energies relating to Pd^0 (335eV[64,73-77] and 340.5eV[64, 73, 76]) and PdO (336eV[64, 65 73-77], 337eV[64, 77, 78] and 342eV[64, 79]) were observed. Due to the close binding energies of two different Pd states, it was impossible to perform quantitative analysis and establish a relative ratio between the different Pd states. The spectrum observed for the Pd 3d scan is shown in the figure below. It should be noted that previous Pd catalysts studied in this chapter did not show analysis peaks overlapping each other to the same degree as they did here. In previous Pd analyses the size of the 'satellite' peaks were negligible in relative intensity compared to the Pd^0 peak at 335eV and PdO at 341eV. Due to the multiplicity observed for Pd/SnO$_2$-SiO$_2$, it is suggested that there is increased Pd-support interaction for SnO$_2$-SiO$_2$ compared to SnO$_2$ (i.e. a stronger MSI). Based on the analysis of other catalysts in this chapter, it is proposed that a catalyst with a stronger MSI would tend to favour propane total oxidation over naphthalene total oxidation. There was a second indication that SnO$_2$-SiO$_2$ does have a chemical interaction with Pd. The 3d Sn spectra for SnO$_2$-SiO$_2$ revealed a peak corresponding to SnO$_2$ at 494.5eV (3d$_{3/2}$ spectrum)[64, 79]. When Pd was impregnated upon the SnO$_2$-SiO$_2$ support, the binding energy shifted from 495.4eV to 494.5eV. This could be attributed to the formation of a bridging oxide species. A second Sn oxide binding energy was observed at approximately 487eV[64, 65] for SnO$_2$-SiO$_2$, but this remained at a similar energy after Pd impregnation.
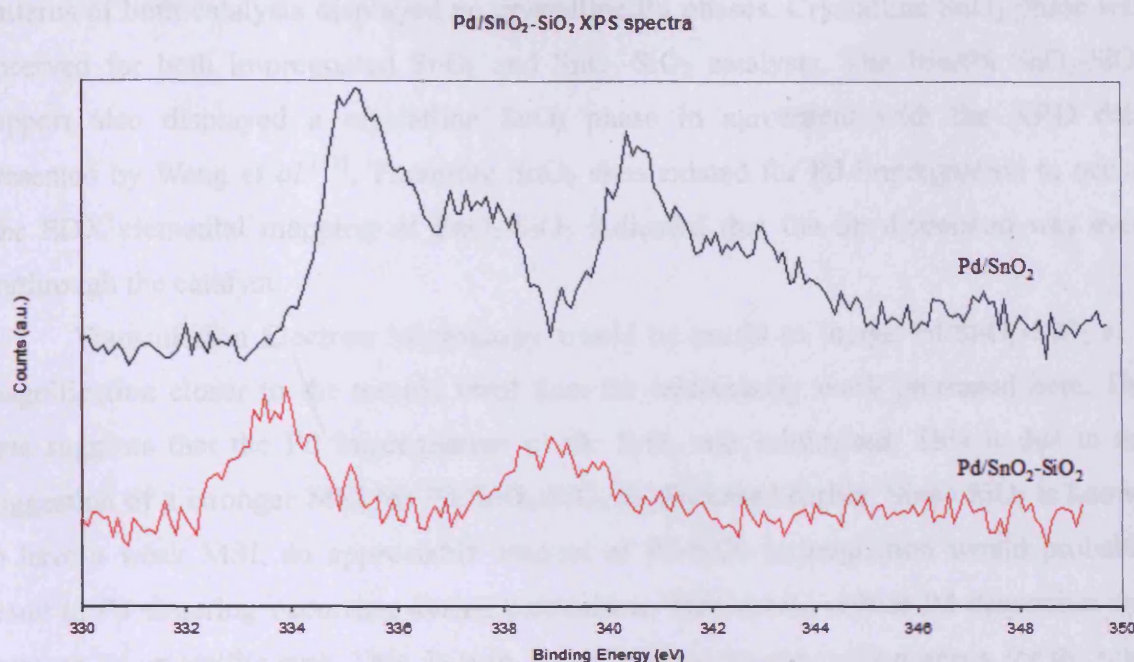
Pd/SnO₂-SiO₂ XPS spectra

Figure 5.28. Pd 3d spectra for 0.5wt% Pd/SnO₂ and 0.5wt% Pd/SnO₂-SiO₂.

5.4.4 Further Discussion and Conclusions

For the total oxidation of naphthalene, using SnO_2-SiO_2 as a support offered no benefit over the SnO_2. However, the use of SnO_2-SiO_2 over SnO_2 was beneficial for propane total oxidation. Without CO chemisorption data, it is difficult to summarise if the average Pd crystallite sizes are significantly affected and from this state if there was a significant difference between the MSI of Pd with SnO_2 and SnO_2-SiO_2. However, based on XPS data reported in this chapter, a stronger MSI may exist for Pd/SnO_2-SiO_2 compared to Pd/SnO_2. A stronger MSI usually results in higher metal dispersion and smaller metal crystallites. Of the two oxidation systems investigated in this chapter, a stronger MSI based catalyst would appear to favour propane total oxidation over naphthalene total oxidation.

A substantial increase in surface area was achieved for SnO_2-SiO_2 compared with SnO_2 and a further increase in surface area was observed after Pd impregnation. This suggested that the Pd crystallites were not sufficiently large to block SnO_2-SiO_2 pores, implying that the degree of sintering during calcination may have been limited. A stronger MSI would influence this. However, CO chemisorption would be a key analysis to perform.

The amount of crystalline Pd phase was not significantly altered since the XRD

182

patterns of both catalysts displayed no crystalline Pd phases. Crystalline SnO_2 phase was observed for both impregnated SnO_2 and SnO_2-SiO_2 catalysts. The 16wt% SnO_2-SiO_2 support also displayed a crystalline SnO_2 phase in agreement with the XRD data presented by Wang *et al.*[71]. Therefore SnO_2 sites existed for Pd impregnation to occur. The EDX elemental mapping of SnO_2-SiO_2 indicated that the Sn dispersion was even on/through the catalyst.

Transmission Electron Microscopy would be useful to image Pd/SnO_2-SiO_2 at a magnification closer to the atomic level than the microscopy work presented here. The data suggests that the Pd impregnation of the SiO_2 was minimised. This is due to the suggestion of a stronger MSI for Pd/SnO_2-SiO_2 as discussed earlier. Since SiO_2 is known to have a weak MSI, an appreciable amount of Pd-SiO_2 impregnation would probably result in Pd sintering occurring during calcination. This would reduce Pd dispersion and increase Pd crystallite size. This, in turn, would reduce the catalyst's potency for the total oxidation of propane based on the observations already discussed in this chapter. However, chemisorption analysis would need to be performed to see if this statement applies.

The XPS analysis showed that Pd existed in both metallic and oxide forms for both Pd/SnO_2 and Pd/SnO_2-SiO_2. It was also suggested that Pd and SnO_2-SiO_2 do have some sort of chemical interaction due to a shift in binding energy when the Sn 3d spectra of SnO_2-SiO_2 and Pd/SnO_2-SiO_2 are compared. The Pd/SnO_2-SiO_2 catalyst displayed peaks with a degree of multiplicity. This was not observed for Pd/SnO_2, which suggests that there was an increased amount of Pd bonding with the surface in the case of Pd/SnO_2-SiO_2 (i.e. a stronger MSI). CO chemisorption analysis would be required to see if a stronger MSI manifests itself as causing a change in the Pd crystallite size and dispersion when Pd/SnO_2 and Pd/SnO_2-SiO_2 are compared.

5.4   References

1.   N. N. Edwin, A. F. Carley, S. H. Taylor, *Catalysis Today*, **137**, (2008), 362-366.

2.   F. J. C. S. Aires, S. Ramirez, G. G. Cervantes, E. Rogemond, J. C. Bertolini, *Applied Catalysis A-General*, **238**, (2003), 289-301.

3.   F. J. C. S. Aires, I. Kurzina, G. G. Cervantes, J. C. Bertolini, *Catalysis Today*, **117**, (2006), 518-524.

4.   F. J. C. S. Aires, G. G. Cervantes, J. C. Bertolini, *Catalysis Letters*, **129**, (2009), 266-272.

5.   I. Kurzina, F. J. Cadete Santos Aires, G. Bergeret, J. C. Bertolini, *Chemical Engineering Journal*, **107**, (2005), 45–53.

6.   I. A. Kurzina, F. J. C. S. Aires, G. G. Cervantes, J. C. Bertolini, *Russian Journal of Physical Chemistry*, **80**, (2006), 1661-1665.

7.   C. Methivier, B. Beguin, M. Brun, J. Massardier, J. C. Bertolini, *Journal of Catalysis*, **173**, (1998), 374-382.

8.   C. Methivier, J. Massardier, J. C. Bertolini, *Applied Catalysis A-General*, **182**, (1999), 337-344.

9.   F. Monnet, Y. Schuurman, F. Cadete Santos Aires, J. C. Bertolini, C. Mirodatos, *Catalysis Today*, **64**, (2001), 51–58.

10.   G. Postole, M. Caldararu, N. I. Ionescu, B. Bonnetot, A. Auroux, C. Guimon, *Thermochimica Acta*, **434**, (2005), 150-157.

11.   G. Postole, A. Gervasini, M. Caldararu, B. Bonnetot, A. Auroux, *Applied Catalysis A-General*, **325**, (2007), 227-236.

12.   S. H. Taylor, A. J. J. Pollard, *Catalysis Today*, **81**, (2003), 179-188.

13.   J. C. S. Wu, Z. A. Lin, J. W. Pan, M. H. Rei, *Applied Catalysis A-General*, **219**, (2001), 117-124.

14.   J. C. S. Wu, W. C. Chen, *Applied Catalysis A-General*, **289**, (2005), 179-185.

15.   J. C. S. Wu, S. J. Lin, *Chemical Engineering Journal*, **140**, (2008), 391-397.

16.   L. X. Lin, Z. H. Li, Y. Zheng, K. M. Wei, *Journal of the American Ceramic Society*, **92**, (2009), 1347-1349.

17.   H. Liu, L. Ma, S. Shao, Z. Li, A. Wang, Y. Huang, T. Zhang, *Chinese Journal of Catalysis*, **28**, (2007), 1077 - 1082.

18.	F. C. Galisteo, R. Mariscal, M. L. Granados, M. D. Z. Poves, J. L. G. Fierro, V. Kroger, R. L. Keiski, *Applied Catalysis B-Environmental*, **72**, (2007), 272-281.

19.	F. Moreau, G. C. Bond, *Catalysis Today*, **122**, (2007), 215-221.

20.	M. Haruta, *Cattech*, **6**, (2002), 102-115.

21.	A. J. Renouprez, K. Lebas, G. Bergeret, J. L. Rousset, P. Delichere, *11th International Congress on Catalysis - 40th Anniversary, Pts A and B*, **101**, (1996), 1105-1114.

22.	G. Garcia Cervantes, F. J. Cadete Santos Aires, J. C. Bertolini, *Journal of Catalysis*, **214**, (2003), 26–32.

23.	K. Kijima, S. Shirasaki, *Journal of Chemical Physics*, **65**, (1976), 2668-2671.

24.	F. J. C. S. Aires, J. C. Bertolini, *Topics in Catalysis*, **52**, (2009), 1492-1505.

25.	D. Hullmann, G. Wendt, U. Singliar, G. Ziegenbalg, *Applied Catalysis A-General*, **225**, (2002), 261-270.

26.	R. J. Shang, W. Z. Sun, Y. Y. Wang, G. Q. Jin, X. Y. Guo, *Catalysis Communications*, **9**, (2008), 2103-2106.

27.	M. Sautel, G. Thomas, A. Kaddouri, C. Mazzocchia, R. Anouchinsky, *Applied Catalysis A-General*, **155**, (1997), 217-228.

28.	D. O. Cooney, Z. P. Xi, *Fuel Science & Technology International*, **14**, (1996), 1315-1336.

29.	R. Moene, M. Makkee, J. A. Moulijn, *Applied Catalysis A-General*, **167**, (1998), 321-330.

30.	R. Moene, E. P. A. M. Tijsen, M. Makkee, J. A. Moulijn, *Applied Catalysis A-General*, **184**, (1999), 127-141.

31.	P. H. Cuong, S. Marin, M. J. Ledoux, M. Weibel, G. Ehret, M. Benaissa, E. Peschiera, J. Guille, *Applied Catalysis B-Environmental*, **4**, (1994), 45-63.

32.	M. J. Ledoux, C. Pham-Huu, R. R. Chianelli, *Current Opinion in Solid State & Materials Science*, **1**, (1996), 96-100.

33.	M. B. Kizling, P. Stenius, S. Andersson, A. Frestad, *Applied Catalysis B-Environmental*, **1**, (1992), 149-168.

34.	M. M. Christian, P. J. A. Kenis, *Lab on a Chip*, **6**, (2006), 1328-1337.

35.	N. Keller, R. Vieira, J. M. Nhut, C. Pham-Huu, M. J. Ledoux, *Journal of the Brazilian Chemical Society*, **16**, (2005), 202-209.

36.   X. N. Shen, Y. Zheng, Y. Y. Zhan, G. H. Cai, Y. H. Xiao, *Materials Letters*, **61**, (2007), 4766-4768.

37.   Y. Habuta, N. Narishige, K. Okumura, N. Katada, M. Niwa, *Catalysis Today*, **78**, (2003), 131-138.

38.   P. G. Harrison, C. Bailey, W. Azelee, *Journal of Catalysis*, **186**, (1999), 147-159.

39.   J. Oi-Uchisawa, A. Obuchi, R. Enomoto, S. T. Liu, T. Nanba, S. Kushiyama, *Applied Catalysis B-Environmental*, **26**, (2000), 17-24.

40.   K. S. Lee, I. S. Park, Y. H. Cho, D. S. Jung, N. Jung, H. Y. Park, Y. E. Sung, *Journal of Catalysis*, **258**, (2008), 143-152.

41.   S. R. Wang, J. Huang, Y. Q. Zhao, S. P. Wang, X. Y. Wang, T. Y. Zhang, S. H. Wu, S. M. Zhang, W. P. Huang, *Journal of Molecular Catalysis A-Chemical*, **259**, (2006), 245-252.

42.   K. Okumura, T. Kobayashi, H. Tanaka, M. Niwa, *Applied Catalysis B-Environmental*, **44**, (2003), 325-331.

43.   T. Mitsui, K. Tsutsui, T. Matsui, R. Kikuchi, K. Eguchi, *Applied Catalysis B-Environmental*, **81**, (2008), 56-63.

44.   M. D'Arino, F. Pinna, G. Strukul, *Applied Catalysis B-Environmental*, **53**, (2004), 161-168.

45.   J. S. Min, N. Mizuno, *Catalysis Today*, **71**, (2001), 89-96.

46.   F. Cavani, N. Ballarini, A. Cericola, *Catalysis Today*, **127**, (2007), 113-131.

47.   L. Lefferts, K. Seshan, B. Mojet, J. van Ommen, *Catalysis Today*, **100**, (2005), 63-69.

48.   G. G. Cervantes, F. J. C. S. Aires, J. C. Bertolini, *Journal of Catalysis*, **214**, (2003), 26-32.

49.   H. A. Cong, C. F. Becker, S. J. Elliott, M. W. Grinstaff, J. A. Porco, *Journal of the American Chemical Society*, **132**, (2010), 7514-7518.

50.   D. C. Ford, A. U. Nilekar, Y. Xu, M. Mavrikakis, *Surface Science*, **604**, (2010), 1565-1575.

51.   J. H. Lee, S. J. Schmieg, S. H. Oh, *Applied Catalysis A-General*, **342**, (2008), 78-86.

52.   V. Houel, P. Millington, R. Rajaram, A. Tsolakis, *Applied Catalysis B-Environmental*, **73**, (2007), 203-207.

53. S. Sitshebo, A. Tsolakis, K. Theinnoi, *International Journal of Hydrogen Energy*, **34**, (2009), 7842-7850.

54. K. Theinnoi, A. Tsolakis, S. Sitshebo, R. F. Cracknell, R. H. Clark, *Chemical Engineering Journal*, **158**, (2010), 468-473.

55. K. Arve, H. Backman, F. Klingstedt, K. Eranen, D. Y. Murzin, *Applied Catalysis B-Environmental*, **70**, (2007), 65-72.

56. A. Satsuma, K. Shimizu, *Progress in Energy and Combustion Science*, **29**, (2003), 71-84.

57. V. A. Sadykov, R. V. Bunina, G. M. Alikina, A. S. Ivanova, T. G. Kuznetsova, S. A. Beloshapkin, V. A. Matyshak, G. A. Konin, A. Y. Rozovskii, V. F. Tretyakov, T. N. Burdeynaya, M. N. Davydova, J. R. H. Ross, J. P. Breen, *Journal of Catalysis*, **200**, (2001), 131-139.

58. H. Jeong, M. Kang, *Applied Catalysis B-Environmental*, **95**, (2010), 446-455.

59. Y. M. Jin, A. K. Datye, E. Rightor, R. Gulotty, W. Waterman, M. Smith, M. Holbrook, J. Maj, J. Blackson, *Journal Of Catalysis*, **203**, (2001), 292-306.

60. T. Garcia, B. Solsona, S. H. Taylor, *Applied Catalysis B-Environmental*, **66**, (2006), 92-99.

61. A. Bampenrat, V. Meeyoo, B. Kitiyanan, P. Rangsunvigit, T. Rirksomboon, *Catalysis Communications*, **9**, (2008), 2349-2352.

62. E. Ntainjua, S. H. Taylor, *Topics in Catalysis*, **52**, (2009), 528-541.

63. T. Okanishi, T. Matsui, T. Takeguchi, R. Kikuchi, K. Eguchi, *Applied Catalysis A-General*, **298**, (2006), 181-187.

64. http://www.lasurface.com/database/elementxps.php

65. D. Briggs, M. P. Seah, *Practical Surface Analysis*, John Wiley & Sons, 1993.

66. A. K. Neyestanaki, L. E. Lindfors, T. Ollonqvist, J. Vayrynen, *Applied Catalysis A-General*, **196**, (2000), 233-246.

67. B. Solsona, T. Garcia, G. J. Hutchings, S. H. Taylor, M. Makkee, *Applied Catalysis A-General*, **365**, (2009), 222-230.

68. R. Sasikala, S. K. Kulshreshtha, *Journal of Thermal Analysis and Calorimetry*, **78**, (2004), 723-729.

69. J. M. Nhut, L. Pesant, N. Keller, C. Pham-Huu, M. J. Ledoux, *Topics in Catalysis*, **30-1**, (2004), 353-358.

70. A. Faussemagne, P. Delichere, N. Moncoffre, A. Benyagoub, G. Marest, *Surface & Coatings Technology*, **83**, (1996), 70-73.

71. S. Wang, X. Ma, J. Gong, X. Yang, H. Guo, G. Xu, *Industrial & Engineering Chemistry Research*, **43**, (2004), 4027-4030.

72. N. N. Edwin, T. Garcia, B. Solsona, S. H. Taylor, *Catalysis Today*, **137**, (2008), 373-378.

73. A. Rochefort, M. Abon, P. Delichere, J. C. Bertolini, *Surface Science*, **294**, (1993), 43-52.

74. S. Hufner, G. K. Wertheim, J. H. Wernick, *Solid State Communications*, **17**, (1975), 417-422.

75. T. J. Sarapatka, *Chemical Physics Letters*, **212**, (1993), 37-42.

76. G. Kumar, J. R. Blackburn, R. G. Aldridge, W. E. Moddeman, M. M. Jones, *Inorganic Chemistry*, **11**, (1972), 296-300.

77. T. L. Barr, *Journal of Physical Chemistry*, **82**, (1978), 1801-1810.

78. T. L. Barr, *Journal of Vacuum Science & Technology A-Vacuum Surfaces and Films*, **9**, (1991), 1793-1805.

79. T. Tateishi, Y. Ito, Y. Okazaki, *Materials Transactions, JIM*, **38**, (1997), 78-84.

Chapter 6 – Conclusions & Further Work

6.1   Conclusions

The preparation of $CeZrO_2$ catalysts employing different Ce:Zr ratios was undertaken. The preparations were based on a co-precipitation technique using two different precipitating agents; urea and sodium carbonate. It was found that a Zr content as low as 1 molar percent increased the catalytic activity for naphthalene total oxidation compared to CeO_2. This was observed for both urea and carbonate precipitated catalysts. For carbonate precipitated $CeZrO_2$, a 99:1 Ce:Zr ratio was the most active catalyst and activity decreased with increasing Zr content. All carbonate precipitated $CeZrO_2$ catalysts were more active than carbonate precipitated CeO_2. A trend between Ce:Zr ratio and catalytic activity could not be established for the urea precipitated $CeZrO_2$ catalysts. Ce99Zr1 was also prepared using a synthesis method using supercritical CO_2. It was found to be significantly less active than the NH_4-U or NH_4-C Ce99Zr1 catalysts.

Urea precipitated Ce99Zr1 displayed resilience to deactivation through repeated use and was also resilient to deactivation during a TOL experiment for 48h at 300°C. Carbonate precipitated Ce99Zr1 was also resilient during repeated, cycled use but displayed slight deactivation during the TOL experiment.

Incorporating Zr into ceria was found to increase the reducibility of the catalysts compared to CeO_2 via TPR analysis. The reducibility increased with increasing Zr content. However, the temperature where peak H_2 consumption was observed also increased with increasing Zr content. It was suggested that the increased reduction capacity of high Zr content $CeZrO_2$ was not required for the testing parameters employed in this study. SEM and XRD studies both showed that the Ce and Zr did not exist as discrete particles, even if the Ce:Zr ratio was 50:50. XPS studies showed that Ce existed as Ce^{3+} and Ce^{4+}. Ce^{4+} was the more common oxidation state for all catalysts. Zr^{4+} was also observed for all catalysts. Previous publications cited Ce^{4+} as the more active Ce oxidation state for the total oxidation of naphthalene. It was suggested that a redox mechanism such as the Mars van Krevelen could be operating in this study in agreement with previous publications.

189

Pt/SiO$_2$ has been reported to be highly active for the total oxidation of naphthalene using a Pt content of 0.5wt%. The object of this section of work was to enhance the activity of Pt/SiO$_2$ for naphthalene total oxidation by optimising the catalyst preparation method.

The Pt content was the first parameter to be investigated. A Pt content of 2.5wt% was found to give rise to the most active catalyst. This preparation gave the highest proportion of metallic Pt and a large Pt crystallite size with a low dispersion. These three characteristics had been reported (in a previous study) to be necessary requirements in the preparation of highly active Pt/SiO$_2$ catalysts for the total oxidation of naphthalene.

The calcination parameters used as part of the preparation of Pt/SiO$_2$ were then investigated. From a calcination regime used in a previous study (550°C, 6h, 10°C/min ramp rate in static air), an improved calcination regime was reported. Each calcination parameter was investigated separately. Changing the calcination temperature from 550°C was found to have a negative effect on catalytic activity. If the calcination time was increased from 6h to 12h, the catalytic activity was enhanced. A slower ramp rate of 5°C/min was found to enhance activity over 10°C/min. Calcination in static air afforded the most active catalyst; calcination in flowing air reduced activity. Each optimal calcination parameter was found to optimise the Pt crystallite size and dispersion (large Pt crystallites with low dispersion) and increased the proportion of metallic Pt. Possible explanations for these observations were discussed.

A time on line study of the most active 2.5wt% Pt/SiO$_2$ catalyst was performed; it was found that CO$_2$ yield decreased slightly after approximately 1000 minutes of continuous reaction. No loss in activity was observed during repeated cycled use of the same sample.

Using the optimised calcination regime and optimal Pt loading, the effect of the silica support on naphthalene total oxidation was investigated. It was found that the original silica support (with a pore size of 60Å) could not be improved upon. Pt impregnation on hollow sphere silica was also reported but activity was less than that observed for the 60Å pore Pt/SiO$_2$ catalyst.

Characterisation data suggested that for the hollow sphere supported Pt catalyst, the Pt was impregnated within the free space of the hollow spheres. Generally the observations made earlier in this study with regards to the nature of the impregnated Pt applied here.

190

A Pd analogue of 2.5wt% Pt/SiO$_2$ was also prepared using the optimised calcination procedure; however the activity was found to decrease. Imaging studies revealed the presence of NaCl crystals on the catalyst surface which may have acted as a catalyst poison. The Pd was found to exist as an oxide and may therefore be less active than metallic Pt for naphthalene total oxidation.

Pt/SnO$_2$ prepared in water was reported to be an active catalyst for naphthalene total oxidation. However, there was scope to improve upon this; if Pt/SnO$_2$ was prepared using aqueous solvents, then poor wetting of the SnO$_2$ support occurred due to its hydrophobic nature. An investigation into preparing metal catalysts supported on hydrophobic materials using non-aqueous solvents was reported in this thesis. A variety of hydrophobic supports (SnO$_2$, Si$_3$N$_4$, SiC and BN) were each impregnated with 0.5wt% of metal (Pt, Pd, Ni, Cu and Ag) giving a total of twenty catalysts. These catalysts were tested for the total oxidation of naphthalene. It was found that the Pd and Pt catalysts gave rise to the most active catalysts. Fresh samples of these Pt and Pd catalysts were investigated for the total oxidation of propane. It was generally found that the silicon nitride based catalysts were the least active. Pt/SiC and Pd/SnO$_2$ were found to be the most active Pt and Pd catalyst for the total oxidation of naphthalene; Pt/SnO$_2$ and Pd/SnO$_2$ were found to be the most active Pt and Pd catalysts for the total oxidation of propane.

The effect of solvent was investigated for the preparation of Pd/BN. For naphthalene total oxidation, there was little difference in the activity of Pd/BN regardless of if it was prepared aqueously or by use of toluene as the preparation solvent. For propane total oxidation, preparing Pd/BN using an aqueous solvent significantly decreased the activity.

Since Pd/SnO$_2$ was found to be an active catalyst, attempts were made to enhance its activity by increasing its surface area. This was achieved by impregnating SnO$_2$ onto 60Å pore silica. The Pd was then subsequently impregnated on this new material. A Sn content of 16wt% was desired. EDX analysis suggested that a Sn loading of approximately 11wt% was achieved. For naphthalene total oxidation, it was found that 0.5wt%Pd/16wt%SnO$_2$-SiO$_2$ was less active than 0.5wt%Pd/SnO$_2$. However, for propane oxidation, an improvement in activity was observed. XPS analysis suggested that a stronger MSI may exist between Pd and SnO$_2$-SiO$_2$ compared with Pd and SnO$_2$.

6.2   Future Work

One of the aims of this thesis were to take catalysts which (from previous studies) are known to be active for naphthalene total oxidation and to modify them in various ways. This was done to improve the activities of these catalysts and understand which characteristics made them active. During this thesis, an improvement in activity was found for Pt/SiO_2 and $CeZrO_2$ was shown to be more active than CeO_2. Both Pt/SiO_2 and CeO_2 were amongst the most active catalysts known for naphthalene total oxidation before this study commenced.

Another aim of this thesis was to introduce other types of catalysts (in this case, 'hydrophobic' catalysts) that had not been studied previously and to evaluate their potential activity for total oxidation. In the case of naphthalene total oxidation, the activities of some of these catalysts were similar to catalysts already known to be highly active. There is the potential for improving the activities of these catalysts further, since no specific work on linking the preparation conditions with catalytic activity was performed during this thesis. There is scope for building upon the work described in this thesis in the future.

Some further characterisation and testing work would be beneficial in furthering the understanding of how $CeZrO_2$ operates for the total oxidation of naphthalene. As suggested in the text, testing conditions may exist where the increased reducibility of high Zr content $CeZrO_2$ would be beneficial. Since Ce^{4+} has been shown in this text to be more active than Ce^{3+} for naphthalene total oxidation, the synthesis and testing of pure Ce^{4+} $CeZrO_2$ may enhance the activity of these materials. Further XPS analysis could be performed on the catalyst series reported in this text to quantify the concentration of Ce^{3+} to Ce^{4+}. The Mars van Krevelen mechanism has been reported to operate for $CeZrO_2$ prepared from a Ce^{3+} source. A kinetic study of predominantly Ce^{4+} $CeZrO_2$ would need to be performed to see if the same observations apply here.

A variety of mechanisms have been proposed with respect to the total oxidation of hydrocarbons by Pt in the literature. It has been suggested that a redox type mechanism operates for metallic Pt but no mechanistic/kinetic study has been performed with respect to naphthalene combustion. Probing this would be a logical step in further one's understanding of this catalytic system. The synthesis of Pd/SiO_2 with a predominantly metallic Pd content would be interesting to compare against metallic Pt and metallic Pd

oxide. Calcination in a non-oxidative atmosphere may increase the quantity of metallic metal impregnated on the silica support. The effect of bimetallic catalysts have not been reported previously for naphthalene combustion, which presents another potential avenue for further study.

There is considerable scope for improving the preparation regime of hydrophobic support based catalysts, particularly for naphthalene total oxidation. The calcination regime used in this study, for example, is a multi-stage process. Using the calcination regime to tune the oxidation state of the impregnated metal to suit a given oxidation system has not been explored during this study. Little work in this specific area has been published, which offers a number of avenues which could be pursued. Other hydrophobic materials, or other methods for obtaining high surface area hydrophobic support materials could also be investigated.